HAL open science

Cathodoluminescence lifetime spectroscopy for efficient III-nitride LEDs

Sylvain Finot

To cite this version:

Sylvain Finot. Cathodoluminescence lifetime spectroscopy for efficient III-nitride LEDs. Physics [physics]. Université Grenoble Alpes [2020-..], 2022. English. NNT : 2022GRALY064 . tel-04002669

HAL Id: tel-04002669

https://theses.hal.science/tel-04002669v1

Submitted on 23 Feb 2023

HAL is a multi-disciplinary open access archive for the deposit and dissemination of scientific research documents, whether they are published or not. The documents may come from teaching and research institutions in France or abroad, or from public or private research centers.

L'archive ouverte pluridisciplinaire **HAL**, est destinée au dépôt et à la diffusion de documents scientifiques de niveau recherche, publiés ou non, émanant des établissements d'enseignement et de recherche français ou étrangers, des laboratoires publics ou privés.

THÈSE

Pour obtenir le grade de

DOCTEUR DE L'UNIVERSITÉ GRENOBLE ALPES

École doctorale : PHYS - Physique
Spécialité : Nanophysique
Unité de recherche : Institut Néel

Spectroscopie du temps de vie de la cathodoluminescence pour des LEDs efficaces à base de nitrure d'élément III

Cathodoluminescence lifetime spectroscopy for efficient III-nitride LEDs

Présentée par :

Sylvain FINOT

Direction de thèse :

Gwénolé JACOPIN — Directeur de thèse
Chargé de recherche, Institut Néel-CNRS

Rapporteurs :

Robert MARTIN
Professeur, University of Strathclyde
Maria TCHERNYCHEVA
Directrice de recherche, C2N-CNRS

Thèse soutenue publiquement le **14 novembre 2022**, devant le jury composé de :

Kuntheak KHENG — Président du jury
Professeur, Université Grenoble Alpes
Robert MARTIN — Rapporteur
Professeur, University of Strathclyde
Maria TCHERNYCHEVA — Rapporteur
Directrice de recherche, C2N-CNRS
Sophie MEURET — Examinatrice
Chargée de recherche, CEMES-CNRS
Ulrich SCHWARZ — Examinateur
Professeur, Technische Universität Chemnitz

Invités :

Amélie DUSSAIGNE
Ingénieur-Chercheur, CEA-LETI

Table of contents

Table of contents i

Acknowledgement v

Acronyms vii

General Introduction and Outline ix

1 Introduction 1

1.1 General properties of III-nitrides 2

1.1.1 Crystal structure 2

1.1.2 Polarization and Quantum Confined Stark Effect 4

1.1.3 Optical properties 6

1.1.4 Growth and substrates 8

1.2 Introduction to light-emitting diodes 10

1.2.1 The most efficient artificial light source 10

1.2.2 Typical LED structure 11

1.2.3 Efficiency of an LED 12

1.2.4 Recombination mechanisms 14

1.2.5 Quantum-Confined Stark Effect 16

References 18

2 Experimental tools and methods 21

2.1 Optical Spectroscopy 22

2.1.1 Photoluminescence 22

2.1.2 Cathodoluminescence 22

2.2 Time-resolved optical Spectroscopy 24

2.2.1 Principle 24

2.2.2 Time-resolved PL 26

2.2.3 Time-resolved CL 27

2.3 Hanbury Brown & Twiss effect 28

2.3.1 A brief history 28

2.3.2 Hanbury Brown & Twiss and g^2 autocorrelation function . . . 30

2.3.3 HBT experiment with a cathodoluminescence setup 31

2.4 Simulations of autocorrelation measurements 33

2.4.1 Experimental parameters and acquisition scheme 34

2.4.2 Simulations of the CL-HBT experiment 39

2.4.3 Summary 46
2.5 Experimental Setup 48
2.5.1 Initial setup 48
2.5.2 Developed setup 50
2.6 Conclusion 52
Appendices 53
2.A Origin of pile-up effect 53
2.B CL mapping as a function of the entrance slit size 55
2.C Estimation of the timing resolution 56
References 57

3 Underlayers for Efficient III-Nitride Blue LEDs 61
3.1 Introduction 62
3.2 *c*-plane QW probed by temperature-dependent TRCL . . . 63
3.2.1 Studied samples 63
3.2.2 Temperature-dependent time-resolved cathodoluminescence measurements 65
3.2.3 Conclusion 67
3.3 Point Defects and Dislocations in QWs grown on Silicon . . 67
3.3.1 Motivations 67
3.3.2 Description of the samples 68
3.3.3 Photoluminescence analysis 69
3.3.4 CL and TRCL analysis 70
3.3.5 Conclusion 71
3.4 Underlayers in core-shell InGaN/GaN microwires 72
3.4.1 Advantage of core-shell microwires LEDs 72
3.4.2 Growth and structure of core-shell microwires 73
3.4.3 Optical characterization 74
3.4.4 Time-resolved CL measurements 77
3.4.5 Role of the GaN spacer: Structural characterization 80
3.4.6 Conclusion 82
3.5 InGaN underlayers in *m*-plane QWs 82
3.5.1 Samples description 83
3.5.2 Temperature-dependent cathodoluminescence analysis 84
3.5.3 Conclusion 86
3.6 Conclusion and perspectives 87
Appendices 89
3.A Effect of the acceleration voltage on CL spectra 89
References 89

4 Surface recombination in µLEDs **95**
4.1 InGaN/GaN blue µLED. **96**
4.1.1 Introduction 96
4.1.2 Studied µLED structure 97
4.1.3 Standard cathodoluminescence analysis 97
4.1.4 SRTC-CL measurements 100
4.1.5 1D diffusion simulations 107
4.1.6 Conclusion of the study 114
4.2 Extending the method to AlGaInP red µLED **115**
4.2.1 Context 115
4.2.2 Studied sample 115
4.2.3 SRTC-CL measurements 116
4.2.4 Conclusion. 118
4.3 Conclusion and perspectives. **119**
Appendices **121**
4.A Nextnano simulations **121**
4.B Carrier density independent lifetime. **123**
4.C Derivation of the lifetime profile. **125**
4.D Additional details about simulations. **128**
References **132**

5 Core-shell GaN microwires for UV emitters **137**
5.1 III-Nitride UV Emitters **138**
5.1.1 Applications of UV LEDs 138
5.1.2 State of the Art and Challenges. 139
5.1.3 Microwires for UV emission 143
5.2 Effect of cracks on the optical properties **144**
5.2.1 Studied samples 144
5.2.2 Optical characterization of cracks 146
5.3 Mitigation of cracks. **153**
5.4 Realization and characterization of single wire LEDs. **156**
5.4.1 EBID Contacts 156
5.4.2 Realization and characterization of Ni/Au contacts 171
5.4.3 Conclusion and perspectives 177
Appendices **179**
5.A Ideality factor of an ideal diode **179**
5.B Additional details on EBIC **181**
5.C SiO_2 CL emission **183**
5.D Practical details on the lithography process **184**

References **185**

Conclusion **193**

Résumé en français **197**

Acknowledgement

I am deeply thankful to Gwénolé Jacopin, my thesis supervisor, for giving me the opportunity to work on this project and for his valuable advice. It was a real pleasure to exchange with him and I learned a lot during these last three years thanks to him. I cannot express enough gratitude to Fabrice Donatini for his expertise in developing the setup and for his support in debugging various problems.

I would like to express my gratitude to the SC2G team for their kind welcome, and to Julien Pernot for his role as both team leader and teacher. His lessons on semiconductors were a source of inspiration for me to further explore this field. I also want to acknowledge the people I shared an office with - Juliette, Jesus, Bea and Eliott - it was nice to have people to complain to about failed experiments.

The Nanofab team's support during fabrication was invaluable, and I am especially thankful to Bruno for his valuable suggestions.

I am grateful to all the collaborators who made this work possible, especially Akanksha, Vincent, Christophe and Joël.

To my friends who shared long gaming nights with me, thank you for being a source of fun and relaxation during this journey. Finally, I would also like to thank my parents and my brother for their support throughout this journey and for making the lockdown an enjoyable time. And most of all, I am forever grateful to my wife, Rita, for her unconditional love and unwavering belief in me.

Acronyms

ADC analog-to-digital converter
ALE atomic layer etching

CCD charge-coupled device
CL cathodoluminescence

DAP donor-acceptor pair

e-h electron-hole
EBAC electron-beam-absorbed current
EBIC electron-beam-induced current
EBL electron blocking layer
EDX energy-dispersive X-ray
EQE external quantum efficiency
ETD Everhart-Thornley detector

FIB focused ion beam
FWHM full width at half maximum

HAADF high-angle annular dark-field
HSQ hydrogen silsesquioxane
HVPE hydride vapor phase epitaxy

IBID ion-beam-induced deposition
ICP inductively coupled plasma
IE injection efficiency
IPA isopropyl alcohol
IQE internal quantum efficiency

LED light-emitting diode
LEE light extraction efficiency

MBE molecular beam epitaxy
MOCVD metal-organic chemical vapor deposition
MQW multiple quantum wells

PL photoluminescence
PMT photomultiplier tube

QCSE quantum-confined Stark effect
QW quantum well

RHEED reflection high-energy electron diffraction
RIE reactive ion etching

SCR space charge region
SEM scanning electron microscope
SIMS secondary ion mass spectroscopy
SL superlattice
SPAD single-photon avalanche diode
SQW single quantum well
STEM scanning transmission electron microscope

TCSPC time-correlated single photon counting
TE transverse electric
TEM transmission electron microscope
TM transverse magnetic
TRCL time-resolved cathodoluminescence

UL underlayer
UV ultraviolet

WPE wall-plug efficiency

General Introduction and Outline

Over the past two decades, gallium nitride (GaN) based light-emitting diodes (LEDs) have revolutionized the lighting field by becoming the most efficient man-made light source. Nowadays, their applications are numerous, ranging from general lighting to automotive lighting and liquid-crystal display backlighting. In order to exploit the potential of this technology, two main areas of research have received particular attention.

On the one hand, the miniaturization of blue LEDs. This research is mainly motivated by the desire to develop a new generation of displays and microdisplays, brighter, with better contrast, and more efficient, especially for smartphones, smartwatches, and virtual/augmented reality applications [Wu+18; Din+19]. Interestingly, research efforts in this area could also benefit data center facilities by replacing short and medium range electrical interconnections with optical connections for more efficient chip-to-chip communication [Pez+22]. To reduce the size of these devices, two approaches are considered:

- The *top-down* approach consists in etching µLEDs from a traditional 2D epitaxy. This approach takes advantage of the maturity of 2D layers traditionally used for lighting. However, as shown in figure 1, the etching processes introduce surface defects that drastically reduce the efficiency as the surface-to-perimeter ratio decreases. The objective here is to find ways to mitigate the impact of these surface defects by developing new etching processes or by passivating the surfaces after etching [Oli+17].
- The second approach, called *bottom-up*, consists in forming pixels from assemblies of micro or nanowires. One of the considerable advantages is the possibility to grow these wires on silicon, facilitating technological integration. More importantly, the efficiency no longer depends on the pixel size but on each wire's efficiency. Thus, the challenge is here to optimize the efficiency of such wires, which have not benefited from many years of industrial optimization [Liu+22].

On the other hand, although nitrides offer the possibility of tuning the bandgap from ultraviolet (UV) to infrared by alloying AlN, GaN and InN, only LEDs emitting in the near UV to green are efficient, as shown in figure 2. On the long wavelength side, the development is confronted with the *"green gap"*, historically referring to the fact that the efficiency of LEDs decreased considerably in the green. Today this term is used more widely to describe the general trend of reduced IQE in longer-wavelength III-nitride emitters, especially in the yellow-red range (*cf* figure 2 (a)). The origin of this phenomenon is still disputed. Recently

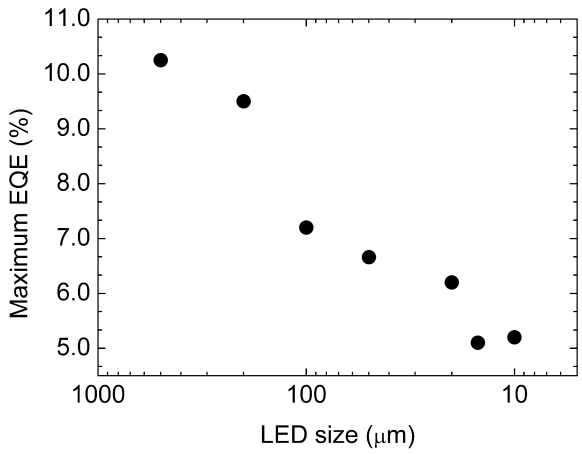

FIGURE 1: Effect of size-reduction on the maximum external quantum efficiency (EQE) of GaN-based etched μLEDs. Adapted from [Din+19].

David et al. have shown that increased incorporation of defects in wells with high indium content could be the origin of this phenomenon [Dav+20]. On the UV side, a considerable research effort is devoted to meet the growing demand for efficient, compact, and environmentally friendly sources [Ama+20]. Indeed, one of the most important features of UV light is its strong interaction with DNA molecules of bacteria, viruses, and other pathogens. These emitters are, therefore, particularly interesting for a wide range of biomedical applications, including disinfection, decontamination, water and air purification [Ama+20; RA20; Kit+21]. Unfortunately, as shown in figure 2 (b), at the present time, the efficiency collapses below ∼360 nm due to multiple issues, including the difficulty of doping AlGaN and forming UV-transparent ohmic contacts.

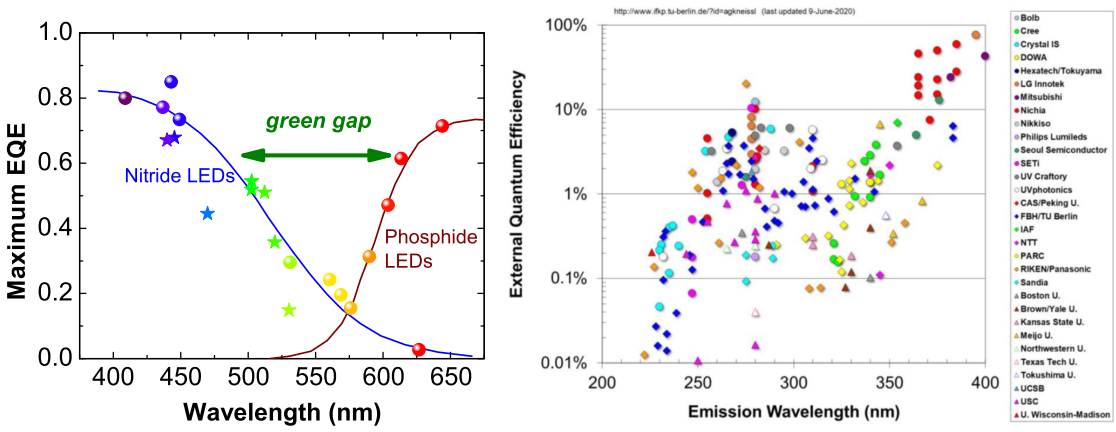

(a) (b)

FIGURE 2: External quantum efficiency as a function of wavelength in the visible (a) and UV range (b). Adapted from [Auf+16] and [Kne+19] respectively.

Therefore, the decreasing size of devices and the need to study defects has highlighted the need for optoelectronic characterization at the nanoscale, well below the diffraction limit of light. In this thesis, we used cathodoluminescence (CL),

a technique taking profit from the small wavelength of accelerated electrons to overcome the Abbe diffraction limit of light.

However, as the emitter size becomes comparable to light's wavelength or propagation length, it is difficult to distinguish the variation of light extraction from internal quantum efficiency related to the material quality. For this purpose, time-resolved techniques are often used to study the lifetime of the emitter, allowing the relative contribution of radiative and non-radiative processes to be estimated without being sensitive to changes in light extraction efficiency. Thus, this type of measurement is particularly suitable for studying the impact of various defects, such as point defects, dislocations, cracks, or surface defects, which is fundamental for early device optimization.

In this context, this thesis is focused on the study of the efficiency of III-nitride emitters. For this, we developed a method based on the study of the CL photon emission statistics. The main advantage of this technique is the ability to measure the lifetime in a conventional CL setup, *i.e.*, without modification of the electron microscope while having an excellent temporal resolution and the best possible spatial resolution.

This work is structured as follows:

Chapter 1 discusses the crystal structure, polarization, optical properties, and growth of III-nitrides. The chapter also introduces typical III-nitride LED structure and defines the different efficiencies commonly used to characterize them. Various recombination mechanisms and the Quantum-Confined Stark Effect are also introduced.

Chapter 2 introduces various optical spectroscopy techniques commonly used to study optical properties of semiconductors with a focus on the Hanbury Brown and Twiss experiment that allows the measurement of the lifetime in a standard CL setup with excellent spatial resolution. Finally, the experimental setup developed and used in this work is presented.

Chapter 3 first presents indium-containing underlayers (ULs) commonly used to increase the efficiency of "standard" *c*-plane InGaN/GaN LEDs by trapping defects before the active region. Then, we studied the relative impact of these defects compared to dislocations, known to be efficient non-radiative recombination centers, by studying quantum wells grown on silicon substrates. Then, to increase the efficiency of core-shell microwire-based LEDs, we tried to apply this process to quantum wells realized on the *m*-planes sidewalls of GaN microwires. A study was also conducted on planar *m*-plane to discriminate from the particular growth condition of microwires. Finally,

we conclude by proposing further studies that could be performed to better understand the nature of these defects.

Chapter 4 focuses on the question of surface recombinations in etched µLEDs. Thanks to the developed setup, we measure the lifetime evolution from the center of a µLED to the edge. Using a 1D diffusion model, we estimated the diffusion coefficient as well as the surface recombination velocity. The chapter then extends the method to red AlGaInP µLEDs, thus demonstrating the possibility of measuring the lifetime from UV to near-infrared.

Chapter 5 first introduces the state of the art of UV LEDs, their application, and the challenges to overcome to improve their efficiency. Then the chapter focuses on the use of GaN/AlGaN microwires for UV emitters. We characterized, in particular, the impact of cracks on the luminescence and the crucial role of strain in such devices. Finally, we show the possibility of realizing UV LEDs from these wires and demonstrate for the first time electroluminescence at 310 nm with core-shell microwires.

Finally, we conclude this work and suggest possible directions for future research.

[Ama+20] Hiroshi Amano et al. "The 2020 UV emitter roadmap". *Journal of Physics D: Applied Physics* 53.50 (Dec. 2020), 503001. DOI: 10.1088/1361-6463/aba64c.

[Auf+16] Matthias Auf Der Maur et al. "Efficiency Drop in Green InGaN/GaN Light Emitting Diodes: The Role of Random Alloy Fluctuations". *Physical Review Letters* 116.2 (2016). DOI: 10.1103/PhysRevLett.116.027401.

[Dav+20] Aurelien David et al. "Review—The Physics of Recombinations in III-Nitride Emitters". *ECS Journal of Solid State Science and Technology* 9.1 (2020), 016021. DOI: 10.1149/2.0372001jss.

[Din+19] Kai Ding et al. *Micro-LEDs, a manufacturability perspective*. 2019. DOI: 10.3390/app9061206.

[Kit+21] Hiroki Kitagawa et al. "Effectiveness of 222-nm ultraviolet light on disinfecting SARS-CoV-2 surface contamination". *American Journal of Infection Control* 49.3 (2021), 299–301. DOI: 10.1016/j.ajic.2020.08.022.

[Kne+19] Michael Kneissl et al. "The emergence and prospects of deep-ultraviolet light-emitting diode technologies". *Nature Photonics* 13.4 (Apr. 2019), 233–244. DOI: 10.1038/s41566-019-0359-9.

[Liu+22] Xianhe Liu et al. "N-polar InGaN nanowires: breaking the efficiency bottleneck of nano and micro LEDs". *Photonics Research* 10.2 (2022), 587. DOI: 10.1364/prj.443165.

[Oli+17] François Olivier et al. "Influence of size-reduction on the performances of GaN-based micro-LEDs for display application". *Journal of Luminescence* 191 (Nov. 2017), 112–116. DOI: 10.1016/j.jlumin.2016.09.052.

[Pez+22] Bardia Pezeshki et al. "LED-array based optical interconnects for chip-to-chip communications with integrated CMOS drivers, detectors, and circuitry". 1200707.March (2022), 11. DOI: 10.1117/12.2614547.

[RA20] Milad Raeiszadeh and Babak Adeli. *A Critical Review on Ultraviolet Disinfection Systems against COVID-19 Outbreak: Applicability, Validation, and Safety Considerations*. Nov. 2020. DOI: 10.1021/acsphotonics.0c01245.

[Wu+18] Tingzhu Wu et al. "Mini-LED and Micro-LED: Promising candidates for the next generation display technology". *Applied Sciences (Switzerland)* 8.9 (2018). DOI: 10.3390/app8091557.

Chapter 1

Introduction

1.1 General properties of III-nitrides 2
1.1.1 Crystal structure 2
1.1.2 Polarization and Quantum Confined Stark Effect 4
1.1.3 Optical properties 6
1.1.4 Growth and substrates 8
1.2 Introduction to light-emitting diodes 10
1.2.1 The most efficient artificial light source 10
1.2.2 Typical LED structure 11
1.2.3 Efficiency of an LED 12
1.2.4 Recombination mechanisms 14
1.2.5 Quantum-Confined Stark Effect 16
References 18

1.1 General properties of III-nitrides

Before discussing the properties of III-nitride light-emitting diodes (LEDs), it is essential to introduce the basic properties of III-nitride semiconductors.

1.1.1 Crystal structure

III-nitride is a term used to describe the binary compounds formed by one metal atom of the III group of the periodic table (Al, Ga, In) and nitrogen (N). From the three binary compounds AlN, GaN, InN, it is possible to build ternary ($Al_xGa_{1-x}N$, $In_xGa_{1-x}N$ and $Al_xIn_{1-x}N$) and quaternary ($Al_xIn_yGa_{1-x-y}N$) alloys. Depending on the choice of substrate and growth conditions, these compounds can be found in different crystal structures, such as wurtzite, zinc blende, and rock-salt. However, only the wurtzite phase is thermodynamically stable. Thus, the other two not being part of this study will not be discussed in the following.

The wurtzite structure comprises two hexagonal close-packed structures, one occupied by metal atoms and the other by nitrogen atoms. To describe hexagonal structures, the Miller-Bravais *hkil* indices are commonly used for convenience. The first three are used to describe three directions in the basal plane. As a reminder, we go from one direction to another by a 120-degree rotation. Since there are three indices for two degrees of freedom, the third can be determined by the other two: $h + k = -i$. These three directions are all associated with the same lattice parameter a. The fourth direction is the perpendicular direction with lattice parameter c. As shown in figure 1.1, the two hexagonal sub-lattices are shifted by an amount $u \times c$ along the $[0\,0\,0\,1]$-axis. In an ideal wurtzite structure, $u = 3/8$ and $c/a = \sqrt{8/3}$.

An important point to emphasize is the presence of a privileged orientation along the c-axis. Indeed, due to the presence of two hexagonal lattices, the structure loses its inversion symmetry along the c-axis. Thus, the orientation of the c-axis is defined as being aligned with the metal-nitrogen bond. The two possible configurations are often referred to as metal-polarity (resp. N-polarity) when the $[0\,0\,0\,1]$ (resp. $[0\,0\,0\,\bar{1}]$) direction is aligned with the growth direction, see figure 1.2[1]. This lack of symmetry makes possible the emergence of a spontaneous polarization in the material. This point and its implications will be discussed in a later section.

Note: The polarity is a bulk property and should not be confused with surface termination, which indicates by which atomic plane the crystal ends.

Finally, we have spoken generally of wurtzite structure without specifying the

[1] These atomic structures were drawn with *VESTA* [MI08]

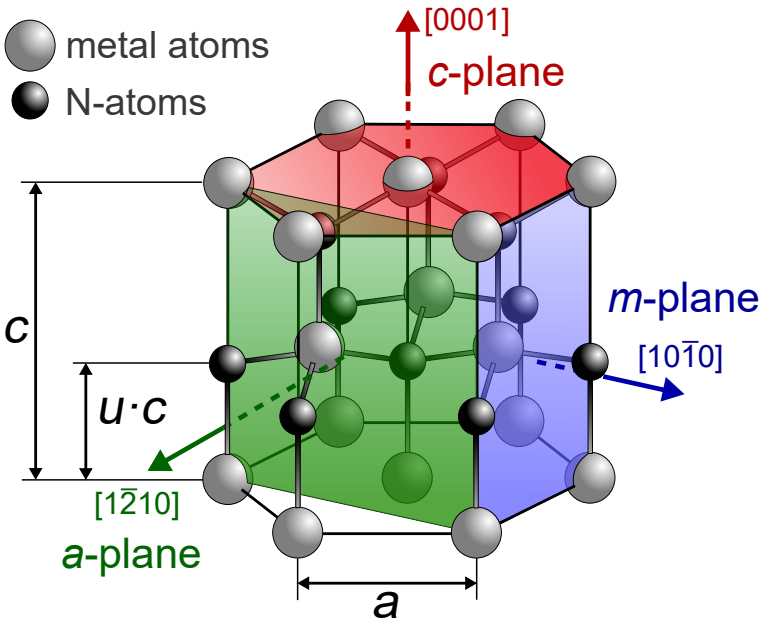

FIGURE 1.1: Representation of the wurtzite unit cell: metal (gray) and nitrogen (black) atoms, respectively, occupy a hexagonal close-packed sub-lattice. Both are displaced by the u-parameter along the [0 0 0 1]-direction. Adapted from [Ros14]

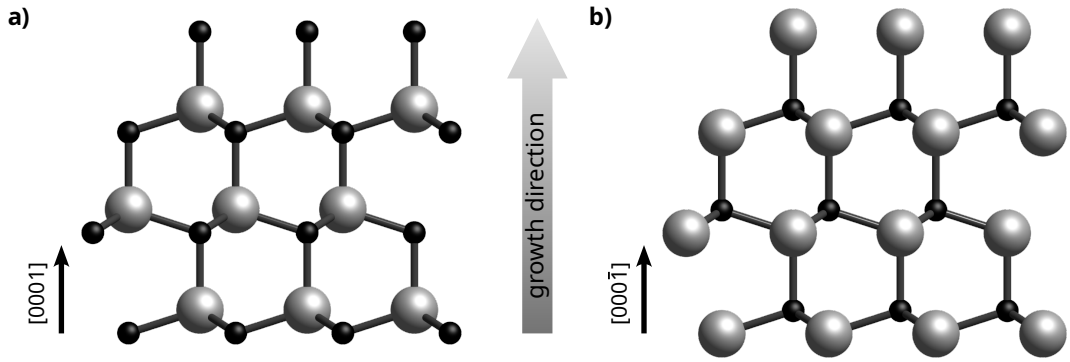

FIGURE 1.2: Illustrations of the two polarities of the wurtzite crystal. (a) Metal-polarity with the [0 0 0 1]-direction aligned with the growth direction and (b) N-polarity where metal-nitrogen bonds are opposed to the growth direction. Large gray spheres represent metal atoms, while nitrogen atoms are small dark spheres.

nature of the metal atom. However, as shown in table 1.1, the lattice parameters differ between the different binary compounds we presented above. Moreover, because of the difference in electronegativity between the metal and nitrogen atoms, c/a and u deviate from the ideal structure. Concerning ternary compounds, their lattice parameters can be determined using Vegard's law (1.1).

Parameter (T = 300K)	GaN	AlN	InN
a(Å)	3.189	3.112	3.545
c(Å)	5.185	4.982	5.703
c/a	1.6259	1.6009	1.6087
u	0.3769	0.3814	0.3787

TABLE 1.1: Room temperature lattice parameters of the different III-nitride binary compounds in their wurtzite phase. Adapted from [BG08]

$$\begin{aligned} a_{\mathrm{A}_x\mathrm{B}_{1-x}\mathrm{N}} &= x a_{\mathrm{AN}} + (1-x) a_{\mathrm{BN}} \\ c_{\mathrm{A}_x\mathrm{B}_{1-x}\mathrm{N}} &= x c_{\mathrm{AN}} + (1-x) c_{\mathrm{BN}} \end{aligned} \tag{1.1}$$

1.1.2 Polarization and Quantum Confined Stark Effect

In this section, we briefly introduce two properties of nitrides, namely pyroelectricity and piezoelectricity. The discussion is mainly based on "Effects of Polarization in Optoelectronic Quantum Structures" [BG08] and more generally by *Polarization effects in semiconductors: From ab initio theory to device applications* [WJ08].

Spontaneous Polarization

Because of the ionicity of the metal-nitrogen bond and the lack of inversion symmetry along the [0 0 0 1]-axis, the barycenters of positive and negative charges do not coincide. Thereby, a spontaneous polarization P_{sp} arises in the crystal, aligned with the [0 0 0 1]-axis. This property is referred to as pyroelectricity.

As the bond length between metal and nitrogen atoms varies with the metal atom, the spontaneous polarization also varies. Spontaneous polarization for the binary compounds are given in table 1.2. More importantly, the spontaneous polarization of ternary compounds can be calculated from these values using a modified Vegard's law (1.2)

$$P_{sp,\mathrm{A}_x\mathrm{B}_{1-x}\mathrm{N}} = x P_{sp,\mathrm{AN}} + (1-x) P_{sp,\mathrm{BN}} - x(1-x) b_{\mathrm{ABN}} \tag{1.2}$$

Materials	GaN	AlN	InN
P_{sp} ($\mathrm{C\,m^{-2}}$)	-0.034	-0.090	-0.042

TABLE 1.2: Spontaneous polarizations for the III-V nitride binary compounds. Adapted from [BG08]

where b_{ABN} the bowing parameter for the ABN ternary. Typical values are $b_{\mathrm{InGaN}} = 0.038$, $b_{\mathrm{AlGaN}} = 0.019$ and $b_{\mathrm{AlInN}} = 0.081\,\mathrm{C\,m^{-2}}$ [BG08].

The general case of the quarternary $\mathrm{Al}_x\mathrm{In}_y\mathrm{Ga}_{1-x-y}\mathrm{N}$ will not be detailed here. The reader may find additional details in [BG08, p. 473].

This effect is often considered as compensated in bulk material due to the appearance of surface charges at the crystal termination. On the other hand, in the case of heterojunction, the polarization difference between the two different nitrides results in a non-zero charge density at the interface. This particularity is notably used for the realization of AlGaN/GaN high electron mobility transistors where a 2D electron gas appears spontaneously at the interface thanks to the polarization difference. The consequences of this property on optoelectronic devices will be discussed in a forthcoming section.

Piezoelectric Polarization

In addition to the spontaneous polarization that occurs even in the absence of strain, another effect must be considered. Indeed, when the crystal lattice is subjected to deformation, the bond lengths are modified, resulting in an additional piezoelectric polarization component P_{pz}.

This piezoelectric component will depend on the basal strain $\epsilon(x)$

$$\epsilon(x) = \frac{a_{sub} - a(x)}{a(x)} \tag{1.3}$$

Where a_{sub} and $a(x)$ are the lattice parameters of the substrate and the layer considered without strain, respectively. Note that this implies a pseudomorphic growth, *i.e.*, the studied layer is constrained to have the same lattice parameter as the substrate. This does not hold if various relaxation mechanisms are involved, such as dislocations or cracks.

This way, the resulting piezoelectric polarization of binary compounds can be described by:

$$
\begin{aligned}
P_{pz,\mathrm{AlN}} &= -1.808\epsilon + 5.624\epsilon^2 \quad \text{for } \epsilon < 0, \\
P_{pz,\mathrm{AlN}} &= -1.808\epsilon - 7.888\epsilon^2 \quad \text{for } \epsilon > 0, \\
P_{pz,\mathrm{GaN}} &= -0.918\epsilon + 9.541\epsilon^2, \\
P_{pz,\mathrm{InN}} &= -1.373\epsilon + 7.559\epsilon^2
\end{aligned}
\tag{1.4}
$$

Also, the piezoelectric polarization of ternary here follows Vegard's law:

$$
P_{pz,\mathrm{A}_x\mathrm{B}_{1-x}\mathrm{N}} = xP_{pz,\mathrm{AN}} + (1-x)P_{pz,\mathrm{BN}} \tag{1.5}
$$

Thus, the total polarization can be expressed as the sum of the spontaneous and piezoelectric one:

$$
P = P_{pz} + P_{sp} \tag{1.6}
$$

The impact of this polarization on LEDs will be explained later.

1.1.3 Optical properties

In this section, we will discuss the optical properties of III-nitride materials. In particular, we will describe how the bandgap emission of III-nitride emitters can be tuned by using ternary alloys, temperature or strain engineering.

Bandgap Engineering

One of the appealing features of III-nitrides is the possibility of continuously tuning the bandgap between binary compounds using ternary alloys. Indeed, the bandgap of a ternary alloy follows a modified Vegard's law (1.7), which makes it possible to tune the bandgap from ultraviolet (UV) with AlN (∼6 eV) to infrared with InN (0.64 eV).

$$
E_{G,\mathrm{A}_x\mathrm{B}_{1-x}\mathrm{N}} = xE_{G,\mathrm{AN}} + (1-x)E_{G,\mathrm{BN}} - x(1-x)b_{\mathrm{ABN}} \tag{1.7}
$$

Where b_{ABN} is the bowing parameter of the ABN ternary. Typical values are $b_{\mathrm{InGaN}} = 1.4$, $b_{\mathrm{AlGaN}} = 0.7$ and $b_{\mathrm{AlInN}} = 2.5$ eV [VM03]. With this law and Vegard's law giving the lattice parameter as a function of the composition (1.1), it is possible to reproduce the famous figure 1.3. It should be noted, however, that these parameters vary considerably in the literature.

Although nitrides could cover a wide part of the spectrum, at present, their use is essentially limited to the blue and green part, with InGaN alloys where the indium composition does not exceed ∼25 %. Indeed, the efficiency rapidly

decreases as the indium composition increases to reach higher wavelengths. This phenomenon is known as *"green-gap"* [Dav+20]. On the other hand, research to extend the use of nitrides in UV also faces challenges where strain and resistivity of AlGaN play essential roles, severely limiting the efficiency of UV LEDs. The later points will be addressed in chapter 5, which is dedicated to this matter.

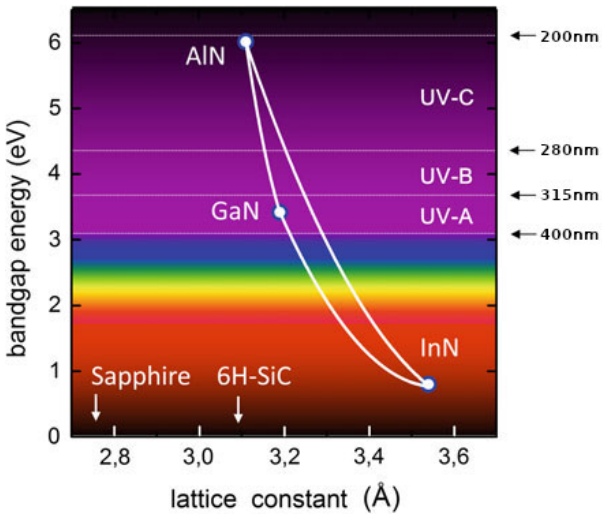

FIGURE 1.3: Bandgap as a function of the lattice constant a for the III-nitrides in the wurtzite phase. Adapted from [KR16]

Influence of the temperature

Lastly, note that bandgap changes with temperature. To describe its evolution, it is common practice to use the empirical Varshni's law (1.8), where α and β are fitting parameters and $E_G(0)$ is the bandgap at 0 K [Var67]. Typical values of α, β and $E_G(0)$ are shown in table 1.3, however, these parameters vary widely in the literature as they depend on the condition of the sample (strain, localization, heavy-doping, etc.).

$$E_G(T) = E_G(0) - \frac{\alpha T^2}{T + \beta} \tag{1.8}$$

Parameters	GaN	AlN	InN
$E_G(0\,\mathrm{K})$ (eV)	3.51	6.25	0.69
α (meV/K)	0.909	1.799	0.414
β (K)	830	1462	454
$E_G(300\,\mathrm{K})$ (eV)	3.44	6.16	0.64

TABLE 1.3: Bandgap and Varshni parameters of III-nitrides. The parameters of AlN and GaN are from [VM03] and those of InN from [Wal+04].

Effect of Strain

The considerations mentioned above are only valid in the absence of strain. When the crystal is strained, typically in the case of a heterostructure, the band structure is modified.

For an unstrained wurtzite system, the three valence bands correspond to the heavy hole (HH), the light hole (LH), and the crystal field split-off band (CH). In order to estimate the influence of strain on the band structure, a perturbative approach is often used. In this method, the effect of a small strain is treated as a perturbation to the unstrained case, involving terms proportional to the components of the strain tensor. Thus, a new hamiltonian can be written, typically the Bir-Pikus hamiltonian and the new band structure is given by the eigenvalues of this hamiltonian. Consequently, the transition energy will be modified. In addition, it is possible to observe, in some cases, a crossover (or anti-crossover) of the valence bands. As the polarization of the emitted light depends on the symmetry of the band involved, it is possible to observe a change of light polarization induced by the strain.

1.1.4 Growth and substrates

This section will briefly present different growth techniques and their characteristics. We will also discuss the problems related to the choice of substrate.

The growth of III-nitride can be achieved by three different techniques, described hereafter:

Molecular beam epitaxy (MBE) This technique is a physical vapor deposition operating under a high or ultra-high vacuum. The atoms are usually supplied by an ultra pure solid source heated to evaporation. Growth rates are typically low $\sim 1\,\mu\mathrm{m\,h^{-1}}$. The main advantage is the possibility of monitoring crystal growth down to a single atomic layer by reflection high-energy electron diffraction (RHEED).

Metal-organic chemical vapor deposition (MOCVD) Contrary to MBE, this technique relies on chemical vapor deposition. This means that the metal atoms are provided by precursors (generally triethyl or trimethyl-metal, *e.g.* trimethylgallium), and nitrogen is supplied by ammonia. Both are carried by a "carrier" gas (N_2 or H_2). The high temperature of the substrate, heated at $\sim 1000\,^{\circ}\mathrm{C}$, breaks the precursors allowing atoms to bind to the surface. Thanks to its higher growth rate than MBE, up to $\sim 10\,\mu\mathrm{m\,h^{-1}}$, and good reproducibility and scalability, this technique is widely used for mass production.

Hydride vapor phase epitaxy (HVPE) Like MOCVD, this technique relies on chemical vapor phase deposition. The main advantage here is the very high growth rate, up to a few $100\,\mu\mathrm{m\,h^{-1}}$. However, this technique cannot produce abrupt interfaces and is therefore mainly used to grow thick bulk layers that can be used as pseudo-substrates.

Note that it is possible to combine techniques, usually for research purposes. For example, it is possible to perform regrowth using MBE to take advantage of its high level of control on an array of microwires grown by MOCVD [GJD19].

If the choice of the technique is important, the choice of the substrate is perhaps even more so. Indeed, the crystalline quality and the performance of the devices will largely depend on this choice. Among the essential physical properties of the substrates, we will note the difference in lattice parameters, named lattice mismatch. A significant mismatch can, for example, result in a high density of dislocations that can act as non-radiative recombination centers or induce leakage currents. Another property, the thermal expansion coefficient, is also of primary interest. For example, since MOCVD growth occurs at high temperatures, the substrate and the layers will contract by different amounts upon cooling. This results in strain that can lead to the formation of macroscopic cracks, which is typically the case for GaN grown on silicon. Finally, other parameters that can also be considered depending on the application are thermal conductivity limiting thermal dissipation, optical transparency, or electrical conductivity. A summary of potential substrates for GaN, with some of their properties, can be found in table 1.4.

However, the choice of substrate is usually not determined solely by physical properties, and compromises must be made. For mass production, for example, the choice is influenced by the available volume, the size of the substrate, compatibility with existing manufacturing technologies, and, of course, price. For example, growing GaN on GaN is not economically viable. Nowadays, all commercial blue LEDs are grown on sapphire, which despite the difference in lattice parameters, has the advantage of being much less expensive and transparent. Similarly, despite the large thermal coefficient mismatch, silicon would be an interesting substrate as it is much cheaper, available in large quantities, and could benefit from the mature silicon-based photonic platform.

Material	Lattice mismatch (%)	Thermal mismatch (%)	Wafer size availability	Cost
GaN	-	-	2"	Prohibitive
SiC	3.5	25	2"-4"; 150mm	Very high
Sapphire	16	-34	2"-4"; 150mm; 300mm	Medium
Si	-17	54	2" to 300mm	Low

Table 1.4: Important physical properties of potential substrates. Mismatches are given relative to GaN. Adapted from [Ish+13; ZWH13]

1.2 Introduction to light-emitting diodes

In this section, we will briefly talk about LEDs and introduce the concepts necessary for the understanding of the subsequent chapters.

1.2.1 The most efficient artificial light source

In 2014, Japanese physicists Isamu Akasaki, Hiroshi Amano and Shuji Nakamura were awarded the Nobel Prize in Physics for their work in the 1990s that contributed significantly to the emergence of GaN-based blue LEDs.

> *"for the invention of efficient blue light-emitting diodes which has enabled bright and energy-saving white light sources"* The Nobel Prize in Physics 2014.[2]

As shown in figure 1.4, over the past two decades, LEDs have revolutionized the lighting field by becoming the most efficient man-made light source, ushering in a new era of energy-efficient lighting. Combined with a phosphor to emit white light, they have largely replaced conventional light sources such as incandescent bulbs and fluorescent lamps.

The applications of LEDs are not limited to lighting. Their discovery has also benefited the audiovisual and display industries. For example, LEDs also contributed to the development of more efficient displays and are now used to backlight LCDs. They also enabled the invention of a more compact data storage technology than CD and DVD: Blu-ray.

Nowadays, the research efforts continue notably in two major axes:

- The miniaturization of blue LEDs. This would open the way to new applications such as display/microdisplay (emissive display), short and medium-

[2] NobelPrize.org/prizes/physics/2014

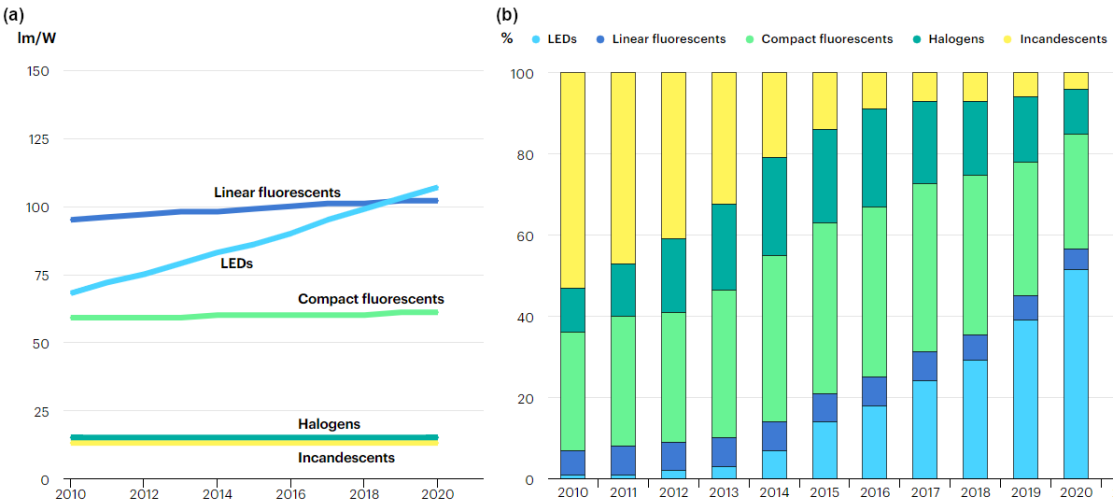

FIGURE 1.4: Global lighting efficiency (a) and sales (b) over the last decade. Adapted from International Energy Agency

range data transfer (chip-to-chip connections), or optogenetic research. However, technological challenges must be overcome to reduce the size of these LEDs without losing efficiency. This will be the subject of chapter 4.

- Emission in other wavelength ranges. Indeed, as we have seen by making alloys, it is theoretically possible to emit from UV to infrared. Without the use of phosphors for light conversion, III-nitride LEDs are now limited to blue and green emissions. The research to go to the red faces the well-known *"green-gap"* due partly to the crystalline quality that decreases for alloys rich in indium. This topic will not be discussed further in this work. Regarding UV, the efficiency decreases rapidly and drastically with decreasing wavelength to reach efficiencies of a few percent below 350 nm. The challenges are numerous and will be discussed in detail in chapter 5.

1.2.2 Typical LED structure

Although an LED could theoretically be reduced to a quantum well (QW) positioned in the space charge region (SCR) of a *p-n* junction to provide both types of carriers (electrons and holes). In practice, the structure is more complex and relies on several additional layers to address different issues, as shown in figure 1.5. Among these layers are those commonly found in III-nitride LEDs:

Nucleation layers In order to grow GaN on a foreign substrate, a nucleation layer is often grown prior to the device. This layer can be, for instance, a low-temperature AlN or GaN layer.

Buffers or gradient These layers are generally grown to accommodate the strain due to a large lattice mismatch or thermal expansion coefficient, thus improving the quality of the upper layers.

Underlayers or superlattices In the case of InGaN-based QWs, the efficiency can be significantly improved by growing an In-containing underlayer (InGaN or InAlN) before the active region. This point will be discussed later as it is the main topic of chapter 3.

Electron blocking layer (EBL) To prevent electrons from "overshooting" the active region, a layer with a larger bandgap is inserted at the interface of the last barrier and the p-doped region.

We will not discuss contact-related layers, such as current spreading layers, metal contacts themselves, or color-conversion layers (phosphor or quantum dot).

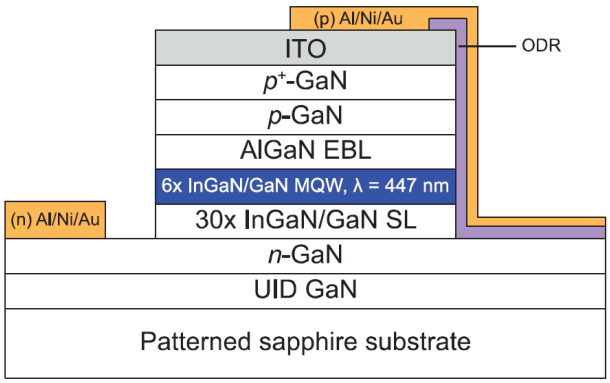

FIGURE 1.5: Typical LED structure. From bottom to top; substrate, an unintentionally doped (UID) GaN buffer, an n-GaN layer, a 30 periods superlattice (SL), the active region composed of 6 multiple quantum wells (MQW), an AlGaN EBL, a p-Gan layer, an Indium tin oxide (ITO) current spreading layer. Adapted from [Hwa+17]

1.2.3 Efficiency of an LED

This section introduces the various efficiency concepts commonly used in the study and characterization of LEDs.

Injection efficiency (IE) The injection efficiency is defined as the fraction of electron-hole (e-h) pairs injected into the device that will eventually recombine in the active region. This value can be affected by leakage current, electron overflow, and recombinations outside the active region.

$$IE = \frac{\text{Nb. of e-h pairs recombining in the active region}}{\text{Nb. of e-h pairs injected in the structure}} \tag{1.9}$$

Internal quantum efficiency (IQE) The internal quantum efficiency is defined as the number of photons generated relative to the number of e-h pairs recombining in the active region. This quantity reflects the impact of non-radiative recombinations in the active zone. The study of this quantity will be the main subject of this thesis. A more detailed description of the different recombination mechanisms in a QW will be given in a forthcoming section.[3]

$$IQE = \frac{\text{Nb. of photons emitted}}{\text{Nb. of e-h pairs recombining in the active region}} \tag{1.10}$$

Light extraction efficiency (LEE) Light extraction efficiency is defined as the ratio of the number of photons emitted into free space to those emitted from the active area. This quantity can be severely affected by the total internal reflection and absorption of substrates or other layers depending on the design of the LED.

$$LEE = \frac{\text{Nb. of photons emitted into free space}}{\text{Nb. of photons emitted}} \tag{1.11}$$

External quantum efficiency (EQE) The external quantum efficiency is the ratio of photons emitted into free space to the number of e-h pairs injected into the device. It can be expressed as the product of IE, IQE and LEE.

$$EQE = \frac{\text{Nb. of photons emitted into free space}}{\text{Nb. of e-h pairs injected in the structure}} = IE \times IQE \times LEE \tag{1.12}$$

Wall-plug efficiency (WPE) The wall-plug efficiency is a quantity useful to also account for electrical power loss. It is defined as the ratio of the LED output optical power to the LED input power.

$$WPE = \frac{P_{opt}}{P_{elec}} = \frac{E_\gamma (I/q) EQE}{IV} = \frac{E_\gamma}{qV} \times EQE \tag{1.13}$$

Where E_γ is the photon energy, q is the elementary charge, I and V are the operating current and voltage, respectively. A typical example demonstrating the importance of WPE is the case of UV LEDs, which can have a threshold voltage of up to 10–20 V for a photon energy of 4–6 eV.

[3]Note that this quantity is sometimes referred to as radiative efficiency. IQE is then defined as the product of this efficiency and IE

1.2.4 Recombination mechanisms

We will now describe the different recombination mechanisms that can take place in direct bandgap semiconductors, using GaN as an example. The discussion is mainly based on the book chapters "Optical Properties of GaN and ZnO" [Son09] and "Luminescence of excitons" [PV12]. A schematic of the mechanisms is shown in figure 1.6.

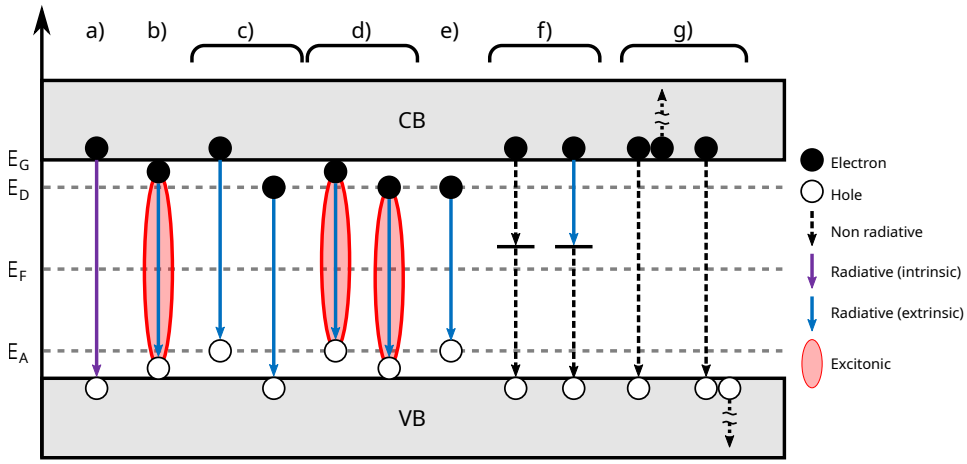

FIGURE 1.6: Different recombination mechanisms occurring in a semiconductor. See the description in the text. Adapted from [Tch15]

a) **Band to band** This recombination involves a free electron and a free hole that recombine at an energy $E = E_G + \frac{1}{2}k_BT$

b) **Free Excitons** Due to the Coulomb interaction, an electron and a hole can be attracted to each other to form a neutral pair of particles. Such a bound electron-hole pair is called an exciton. In a semiconductor, the exciton wavefunction is generally strongly delocalized, and the exciton can move freely within the crystal. This quasiparticle is called a free exciton (or Wannier exciton). The energy of its recombination can be expressed as

$$E_{FE} = E_G - \frac{E_X}{n^2} \tag{1.14}$$

Where E_X is the binding energy and n^2 the energy state ($n = 1$ for ground state). In GaN, E_X is of the order of ~28 meV. Therefore excitons are more stable at low temperatures where $k_BT \ll E_X$.

In practice, free excitons are propagating and therefore have non-zero kinetic energy and momentum, which was not taken into account in (1.14). For such excitons to emit a photon, the momentum conservation has to be

satisfied. Thus, the process involves one or more phonons (usually longitudinal or transverse optical "LO", "TO"). Thus, the luminescence spectrum can display peaks at $E_{FE} - mE_\omega$, with E_ω the energy of a phonon and m the number of phonons involved. These peaks are called phonon replica. For example, in GaN, LO phonons have an energy of ∼92 meV.

c) **Free-to-Bound** This type of transition can be observed when the semiconductor is doped and correspond to the transition from one free particle, electron e (or hole h), to a bound state, acceptor (or donor). The energy of transition is typically

$$E = E_G - E_{A,D} + \frac{1}{2}k_B T \tag{1.15}$$

Where E_A (resp. E_D) is the energy of the acceptor (resp. donor) with respect to the valence (resp. conduction) band. These transitions are enhanced when impurities are not fully ionized, usually at low temperatures. Note, however, that the acceptor level of Mg is about ∼220 meV above the valence band. Thus, even at room temperature, the acceptors are not fully ionized.

d) **Bound Excitons** Without going into details, free excitons can lower their energy by getting bound to a center. In GaN, this center can be, for example, either a shallow ionized donor[4] or a neutral impurity. Therefore, the energy of the transition is the same as that of a free exciton minus the binding energy E_B which depends on the center's nature.

$$E_{BE} = E_{FE} - E_B \tag{1.16}$$

e) **Donor-acceptor pairs (DAPs)** In compensated materials, *i.e.*, containing both donors and acceptors, electrons from the donors can be captured by the acceptors. Thus, the sample can have both ionized donors and acceptors. If the distance between the donor and acceptor is close enough, this donor-acceptor pair can act as a recombination center after capturing an electron and a hole. Due to the Coulomb interaction, the energy of this transition depends on the distance between the two impurities and can be expressed as follows

$$E = E_G - E_D - E_A - \frac{q^2}{4\pi\epsilon R} \tag{1.17}$$

Where R is the interatomic distance between the donor and the acceptor.

[4]Excitons bound to an ionized acceptor are stable only if $m_e/m_h \gtrsim 2.33$. Conversely excitons bound to an ionized donor are stable only if $m_e/m_h \lesssim 0.43$ [PV12, p. 183].

f) **Deep levels** Some defects can form deep levels, usually with energy in the middle of the bandgap. These states can either produce non-radiative recombinations or emissions at energy well below the bandgap. A famous deep level in GaN-related samples is the broad yellow band at about 2.2 eV with a full width at half maximum (FWHM) of ∼400 meV. Initially attributed to Ga or N vacancies, its origin is still debated, but more recent studies suggest carbon-related defects [LJV10; Res+18; Kat+21].

g) **Auger** Instead of emitting a photon, the energy from the recombination of an e-h pair may be transferred to a third particle, either an electron or a hole. This three-particle process is less likely and occurs at high carrier density.

1.2.5 Quantum-Confined Stark Effect

As mentioned earlier, nitrides inherently have a spontaneous polarization aligned along the [0 0 0 1]-axis that depends on the alloy composition. In addition, piezoelectric polarization arises when the lattice is deformed under the influence of strain. Thus, in a heterostructure, the polarization discontinuity between two materials results in a charge density at the interface.

In the case of a QW sandwiched between two barriers, these two charge planes will create an electric field in the [0 0 0 1] direction. Thus, free electrons and holes in the QW will be separated and confined at the two interfaces corresponding to their respective energy minima. This effect is illustrated in figure 1.7 (b) which shows the band diagram and wavefunctions of a *c*-plane (5nm)GaN/(10nm)$Al_{0.1}Ga_{0.9}N$ QW taking into account the internal electric field, based on self-consistent Schrödinger-Poisson calculations. The consequences of this electric field are twofold. First, as the radiative lifetime is inversely proportional to the square of the overlap integral, it is significantly extended. This is illustrated in figure 1.7 (a)'s inset showing 5K-time-resolved photoluminescence intensity for both a *m*-plane (non-polar) and *c*-plane (polar) QW. The lifetime of the *m*-plane is about 13 times shorter than that of the *c*-plane. Second, as the electrons and holes are at their respective energy minima, the energy of the transition is redshifted. For example, here, the emission of the GaN QW is lower than the GaN bandgap. For comparison, figure 1.7 (c) shows the same calculations for a *m*-plane (non-polar) QW.

This effect is called the quantum-confined Stark effect (QCSE). Its magnitude, both the redshift and the lengthening of the lifetimes, increases with the amplitude of the electric field and the thickness of the well.

An important point to remember is that the cause of this effect is an electric field. Consequently, the carrier density in the QW also plays a significant role. In-

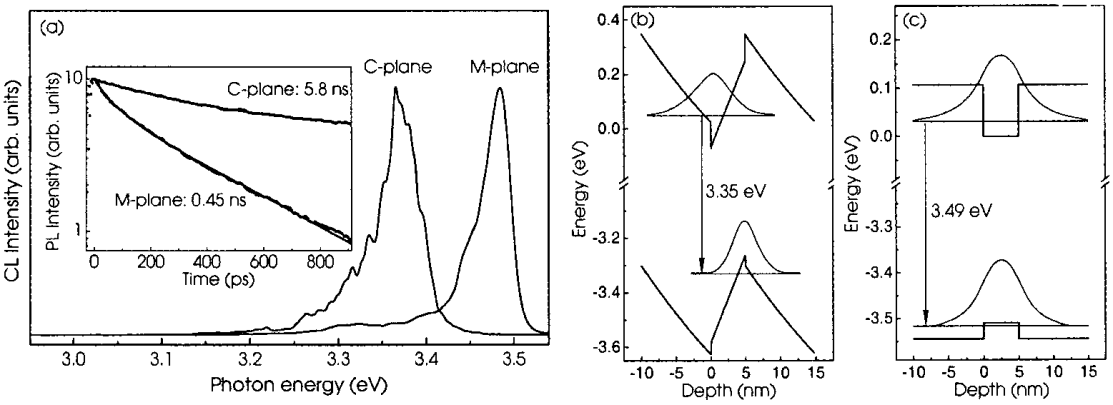

FIGURE 1.7: Impact of electrical polarization on the emission characteristics of GaN/AlGaN multiple quantum wells. a) Cathodoluminescence (CL) and time-resolved photoluminescence data demonstrating a redshift and prolonged decay times (inset) of *c*-plane wells with respect to *m*-plane wells. b), c) Band diagrams based on self-consistent Schrödinger-Poisson calculations for *c*-plane and *m*-plane wells, respectively. [Wal+00]

deed, as the carrier density increases, the internal electric field can be screened, resulting in a reduction of the QCSE. An illustration of the descreening of the electric field has been evidenced by Lefebvre et al. [Lef+04]. Figure 1.8 (a) shows the complex relaxation mechanism of a highly excited (7.8nm)GaN/(30nm)$Al_{0.15}Ga_{0.85}N$ due to the descreening of the internal electric field obtained with a streak camera with the corresponding intensity (b) and energy (c) profile as a function of time. The emission energy is initially centered around 3.4 eV and shifts rapidly as the QW empties to asymptotically reach 3.23 eV. Similarly, the intensity decays faster at early delays as the screening of the electric field enhances the wavefunction overlap. As the carrier density decreases, the increase in electric field separates the remaining carriers to the opposite side. Thus the lifetime drastically increases.

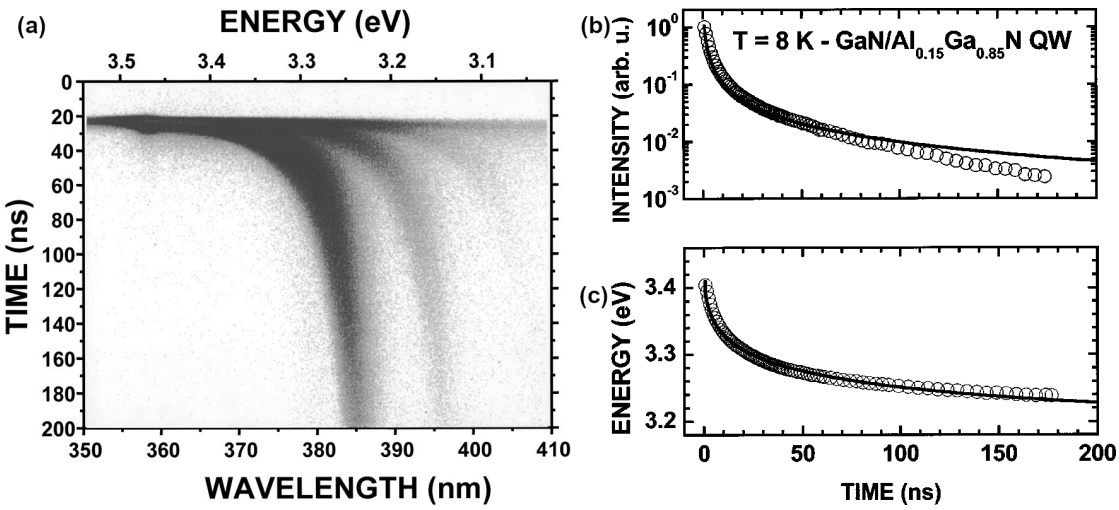

FIGURE 1.8: (a) Time evolution of the PL spectrum for a (7.8nm) $GaN/Al_{0.15}Ga_{0.85}N$ quantum well, taken at T=8 K. The maximum of laser excitation corresponds to time ∼23 ns. (b) and (c) show the PL intensity and energy obtained using a Gaussian fit. Solid lines show the result of the calculations. Adapted from [Lef+04]

References

[BG08] Raphaël Butté and Nicolas Grandjean. "Effects of Polarization in Optoelectronic Quantum Structures". *Polarization Effects in Semiconductors: From Ab InitioTheory to Device Applications*. Ed. by Colin Wood and Debdeep Jena. Boston, MA: Springer US, 2008, pp. 467–511. DOI: 10.1007/978-0-387-68319-5_9.

[Dav+20] Aurelien David et al. "Review—The Physics of Recombinations in III-Nitride Emitters". *ECS Journal of Solid State Science and Technology* 9.1 (2020), 016021. DOI: 10.1149/2.0372001jss.

[GJD19] Marion Gruart, Gwénolé Jacopin, and Bruno Daudin. "Role of Ga Surface Diffusion in the Elongation Mechanism and Optical Properties of Catalyst-Free GaN Nanowires Grown by Molecular Beam Epitaxy". *Nano Letters* 19.7 (2019), 4250–4256. DOI: 10.1021/acs.nanolett.9b00023.

[Hwa+17] David Hwang et al. "Sustained high external quantum efficiency in ultra-small blue III-nitride micro-LEDs". *Applied Physics Express* 10.3 (2017). DOI: 10.7567/APEX.10.032101.

[Ish+13] Masahiro Ishida et al. "GaN on Si technologies for power dwitching fevices". *IEEE Transactions on Electron Devices* 60.10 (2013), 3053–3059. DOI: 10.1109/TED.2013.2268577.

[Kat+21] Masashi Kato et al. "Contribution of the carbon-originated hole trap to slow decays of photoluminescence and photoconductivity in homoepitaxial n-type GaN layers". *Journal of Applied Physics* 129.11 (Mar. 2021). DOI: 10.1063/5.0041287.

[KR16] Michael Kneissl and Jens Rass, eds. *III-Nitride Ultraviolet Emitters*. Vol. 227. Springer Series in Materials Science. Springer International Publishing, 2016. DOI: 10.1007/978-3-319-24100-5.

[Lef+04] P. Lefebvre et al. "Observation and modeling of the time-dependent descreening of internal electric field in a wurtzite GaN/Al0.15Ga0.85N quantum well after high photoexcitation". *Physical Review B - Condensed Matter and Materials Physics* 69.3 (2004). DOI: 10.1103/PhysRevB.69.035307.

[LJV10] J L Lyons, A Janotti, and C G Van De Walle. "Carbon impurities and the yellow luminescence in GaN". *Applied Physics Letters* 97.15 (2010), 152108. DOI: 10.1063/1.3492841.

[MI08] Koichi Momma and Fujio Izumi. "VESTA : a three-dimensional visualization system for electronic and structural analysis". *Journal of Applied Crystallography* 41.3 (June 2008), 653–658. DOI: 10.1107/S0021889808012016.

[PV12] Ivan Pelant and Jan Valenta. "Luminescence of excitons". *Luminescence Spectroscopy of Semiconductors*. Oxford University Press, Feb. 2012, pp. 161–204. DOI: 10.1093/acprof:oso/9780199588336.003.0007.

[Res+18] M A Reshchikov et al. "Two charge states of the C N acceptor in GaN: Evidence from photoluminescence". *Physical Review B* 98.12 (Sept. 2018), 125207. DOI: 10.1103/PhysRevB.98.125207.

[Ros14] Georg Rossbach. "High-Density Excitonic Effects in GaN : Mott-Transition and Polariton Lasing". 6245 (2014), 202.

[Son09] Jung-Hoon Song. "Optical Properties of GaN and ZnO". Ed. by Takafumi Yao and Soon-Ku Hong. Vol. 12. Advances in Materials Research. Berlin, Heidelberg: Springer Berlin Heidelberg, 2009, pp. 311–349. DOI: 10.1007/978-3-540-88847-5.

[Tch15] Pierre Tchoulfian. "Propriétés électriques, optiques et électro-optiques de microfils GaN pour la réalisation de LEDs". PhD thesis. 2015.

[Var67] Y P Varshni. "TEMPERATURE DEPENDENCE OF THE ENERGY GAP IN SEMICONDUCTORS". *Physica* 34 (1967), 149–154. DOI: 10.1016/0031-8914(67)90062-6.

[VM03] I. Vurgaftman and J. R. Meyer. "Band parameters for nitrogen-containing semiconductors". *Journal of Applied Physics* 94.6 (Sept. 2003), 3675–3696. DOI: 10.1063/1.1600519.

[Wal+00] P. Waltereit et al. "Growth of M-plane GaN(1-100): a way to evade electrical polarization in nitrides". *Physica Status Solidi (A) Applied Research* 180.1 (July 2000), 133–138. DOI: 10.1002/1521-396X(200007)180:1<133::AID-PSSA133>3.0.CO;2-A.

[Wal+04] W Walukiewicz et al. "Optical properties and electronic structure of InN and In-rich group III-nitride alloys". *Journal of Crystal Growth* 269 (2004), 119–127. DOI: 10.1016/j.jcrysgro.2004.05.041.

[WJ08] Colin Wood and Debdeep Jena. *Polarization effects in semiconductors: From ab initio theory to device applications*. Springer US, Oct. 2008, pp. 1–515. DOI: 10.1007/978-0-387-68319-5.

[ZWH13] D. Zhu, D. J. Wallis, and C. J. Humphreys. "Prospects of III-nitride optoelectronics grown on Si". *Reports on Progress in Physics* 76.10 (2013). DOI: 10.1088/0034-4885/76/10/106501.

Chapter 2

Experimental tools and methods

2.1 Optical Spectroscopy 22
2.1.1 Photoluminescence 22
2.1.2 Cathodoluminescence 22
2.2 Time-resolved optical Spectroscopy 24
2.2.1 Principle 24
2.2.2 Time-resolved PL 26
2.2.3 Time-resolved CL 27
2.3 Hanbury Brown & Twiss effect 28
2.3.1 A brief history 28
2.3.2 Hanbury Brown & Twiss and g^2 autocorrelation function . . . 30
2.3.3 HBT experiment with a cathodoluminescence setup 31
2.4 Simulations of autocorrelation measurements 33
2.4.1 Experimental parameters and acquisition scheme 34
2.4.2 Simulations of the CL-HBT experiment 39
2.4.3 Summary 46
2.5 Experimental Setup 48
2.5.1 Initial setup 48
2.5.2 Developed setup 50
2.6 Conclusion 52
Appendices 53

In this chapter, we will review some commonly used optical characterization techniques. We will also see the benefit of their time-resolved variant. Then, we will look at the Hanbury Brown & Twiss interferometer, particularly how it can be coupled to a cathodoluminescence setup to measure carriers' lifetime at the nanoscale. Lastly, we will present the measurement setups developed and used in this thesis.

2.1 Optical Spectroscopy

2.1.1 Photoluminescence

Since photoluminescence (PL) is a widely used characterization technique and is not the focus of this thesis, we will not go into much detail here. The principle is based on photoexcitation, where a photon is absorbed, promoting an electron to a higher energy level. Thus, this technique inherits several properties of light:

Adjustable wavelength By choosing the excitation wavelength, it is possible to excite specific centers. For example, it is possible to generate carriers directly in a QW by pumping between the QW energy and that of the barriers.

Diffraction limited resolution The large wavelength of light limits the spatial resolution of this technique to a few hundred nanometers.

Photoexcitation Here, one probe photon generates at most one e-h pair. Thus, it is possible to estimate the resulting carrier density precisely. Moreover, it is possible to change this quantity by several orders of magnitude easily. This can be used to determine the IQE by making power-depend measurements [Dav+20].

Neutral particles It allows measurements to be made at atmospheric pressure and avoids charging problems, especially for insulating samples. However, it is complicated to deflect the beam, which makes scanning more difficult.

2.1.2 Cathodoluminescence

CL is another spectroscopy technique commonly used to study matter at the nanoscale. Since it depends on electron-matter interactions, we can briefly provide a general background on electron-microscopy-related techniques. CL measurements are usually performed in a scanning electron microscope (SEM) or a transmission electron microscope (TEM). The probe electrons, called primary electrons, can be more or less energetic with energies ranging from a few hundred eV to several tens (SEM) or even hundreds (TEM) of keV. As illustrated in figure 2.1,

the complex nature of electron-matter interactions leads to the generation of many signals.

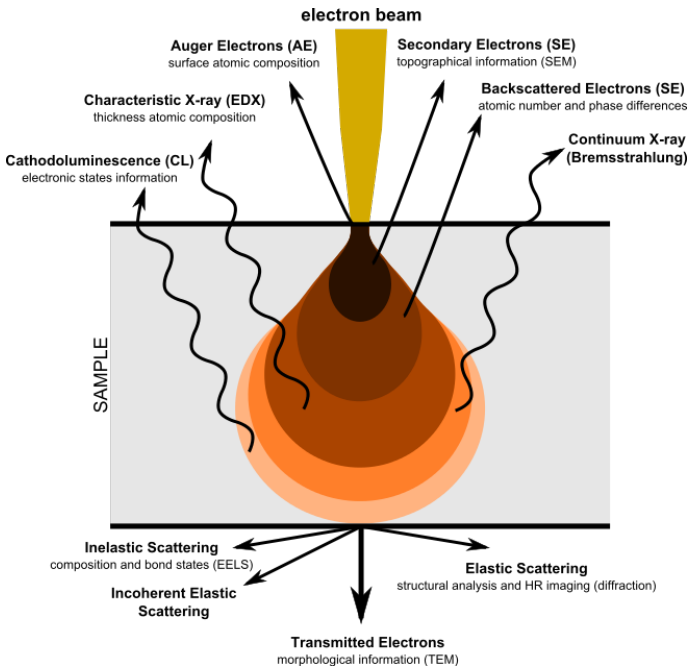

FIGURE 2.1: Electron–matter interactions and the different types of generated signals. Claudionico, Electron Interaction with Matter, CC BY-SA 4.0

Among these signals, we can briefly introduce the main ones found in a SEM:

Secondary electrons These are electrons stripped from the material. Those close enough to the surface can be collected by accelerating them with an electric field . This signal is the one mainly used in a SEM to form images and mostly gives information about the sample's topography.

Backscattered electrons These are primary electrons backscattered due to the interaction with positive nuclei. This signal is sensitive to atomic number and can be used to highlight differences in chemical elements, with heavy elements appearing brighter than light elements.

X-ray Because of the high energy of the primary electrons, it is possible to knock a core-shell electron out of an atom. A higher energy outer-shell electron can then fill this vacancy, releasing the energy difference as an X-ray whose spectrum is characteristic of the source atom. The position of the peaks in the spectrum identifies the element, while the signal intensity can be used to determine its concentration.

Cathodoluminescence When a primary electron transfers some of its kinetic energy to a sample, it creates e-h pairs. These pairs recombine according

to the various mechanisms introduced earlier. This technique is therefore mainly used to observe luminescence at the nanoscale and to extract valuable properties such as strain, doping level, and defects from its spectrum.

Since CL is at the center of this thesis, we can mention its properties, partly inherited from electron-matter interaction:

Short electron wavelength Thanks to this property, we can reach a better spatial resolution than in PL. In a SEM, depending on the acceleration voltage, the excitation volume can be of the order of a few tens of nanometers. Note that carrier diffusion (intrinsic to the material) can limit the resolution.

Voltage-dependent interaction volume As the penetration depth of primary electrons depends on their energy, it is possible (to some extent) to probe the sample at different depths .

Non-resonant excitation Accelerated electrons are a universal excitation source. However, this comes at the cost of being sensitive to changes in injection efficiency, thus making it challenging to estimate IQE quantitatively.

Complex electron-matter interactions This gives access to a unique photon statistic (described later). However, it is more difficult to precisely estimate the number of e-h generated.

Charged particles Because of this property, it is easy to deflect electrons and thus perform scans. However, this also complicates the study of insulating samples due to charging effects.

2.2 Time-resolved optical Spectroscopy

In complement to PL and CL, both techniques have their so-called time-resolved variant. First, we will briefly explain the underlying principle. Then we will discuss the concrete implementation, advantages and limitations of each technique.

2.2.1 Principle

Time-resolved photoluminescence and time-resolved cathodoluminescence (TRCL) are essentially based on the same principle: the study of the decay of the luminescence intensity after an excitation, allowing to measure carriers' lifetime. The main interest is to no longer depend on the intensity, which varies with the LEE.

There are different (more or less complicated) models to describe the luminescence intensity decay. Many are based on the assumption that the evolution of the carrier density n can be expressed as:

$$-\frac{dn}{dt} = n\left(\frac{1}{\tau_r} + \frac{1}{\tau_{nr}}\right) = \frac{n}{\tau_{eff}} \tag{2.1}$$

With τ_r the radiative lifetime and τ_{nr} the non-radiative lifetime.

For example, assuming that τ_r and τ_{nr} are constants, we obtain:

$$n(t) = n_0 \exp\left(\frac{-t}{\tau_{eff}}\right) \tag{2.2}$$

Thus, the intensity can be expressed as:

$$I(t) \propto \frac{n}{\tau_r} = \frac{n_0}{\tau_r} \exp\left(\frac{-t}{\tau_{eff}}\right) \tag{2.3}$$

This model can be used to access the IQE since it is expressed as:

$$IQE = \frac{{\tau_r}^{-1}}{{\tau_r}^{-1} + {\tau_{nr}}^{-1}} \tag{2.4}$$

$$= \frac{\tau_{eff}}{\tau_r} \tag{2.5}$$

Naturally, more complex models can be used depending on the mechanisms at play such as carrier localization [Pop+00; Han19], QCSE [Lef+04], carrier density dependent recombination [Dav21; Liu+16a; Han19], or carrier diffusion towards defects [Liu+16b].

Pile-up effect

Before talking about the techniques, it is important to mention an effect related to the acquisition that can modify the measured statistics and, therefore, the extracted lifetime. Indeed, the electronics used for acquisition (detectors and TCSPC device) are prone to dead time, *i.e.*, the time needed before the system can detect a new event. This time (up to 100 ns) is generally longer than the lifetimes we want to measure (up to ∼10 ns). Because of this, only the arrival time of the first photon is recorded after an excitation. This phenomenon will cause an over-representation of photons arriving at short delays and, consequently, an under-representation of longer delays. A general result is that exponential decay is seen as non-exponential with a shorter lifetime at the early delay [HS17; Gmb]. This effect is often referred to as *"pile-up"*. Figure 2.2,(a) shows this effect observed experimentally, where in-

creasing the count rate causes a change in the measured statistic. As an indication, if we suppose that the detection of a photon is a Poisson process with parameter λ (the mean number of photons per pulse), a monoexponential decay of lifetime τ_{eff} will be measured as (see appendix 2.A for more details on the derivation):

$$I(t) \propto \frac{e^{-\lambda}}{1-e^{-\lambda}} \frac{\lambda}{\tau_{eff}} \exp\left(\lambda e^{-t/\tau_{eff}} - t/\tau_{eff}\right) \tag{2.6}$$

This distribution is shown for different average photons per pulse λ in figure 2.2 (b). It is crucial to keep the pile-up probability low to measure a lifetime close to the actual one. Experimentally, one could take as a criterion that the count rate should not exceed 5% of the excitation frequency [HS17; Gmb].

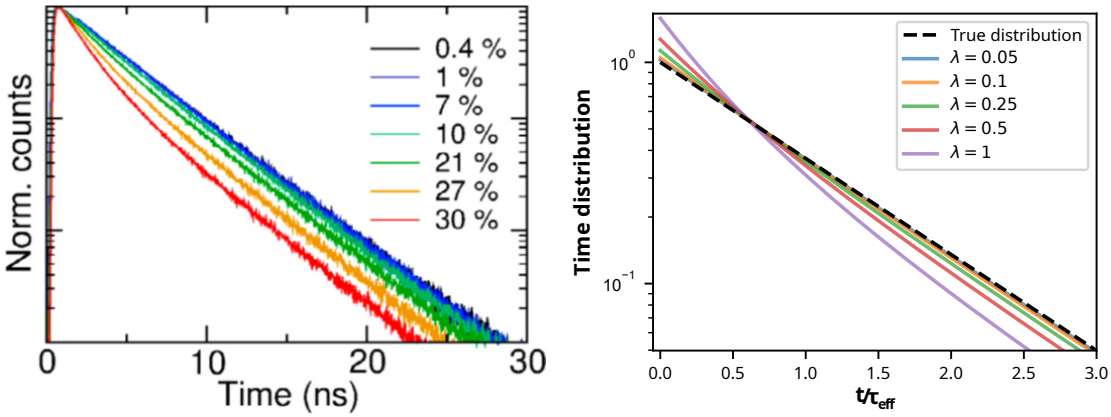

(a) (b)

FIGURE 2.2: (a) Photon pile-up of a fluorescein decay; as the count rate, expressed as a percentage of the excitation repetition rate, increases, the initially monoexponential decay becomes shorter and non-exponential. Adapted from [HS17]. (b) Calculated time distribution using equation (2.6) and assuming that on average λ photons per pulse reach the detector (solid lines). The true photon distribution (monoexponential) is indicated as a dashed black line.

Now that we have seen the fundamental principle of time-resolved spectroscopy and addressed the pile-up effect, we can discuss the advantages and limitations of time-resolved photoluminescence and TRCL.

2.2.2 Time-resolved PL

The main advantage of this technique is the possibility of studying variations of the radiative lifetime. Indeed, as we have seen, the intensity right after the excitation depends only on the carrier density (2.3). Therefore, assuming that the excitation is performed above the QW bandgap but below the barrier's energy and that the pulse is very short compared to the carrier density decay, the density just after

the pulse depends only on the power density of the pulse. This can be used to study the relative evolution of the effective and radiative lifetime as a function of temperature to determine the IQE [Lan+16; Han19].

Another advantage is the possibility to vary the carrier density over many orders of magnitude to study the dominant mechanisms (non-radiative, radiative, Auger) at different carrier densities [Liu+16a; Sha+17].

However, like PL, it is not easy to perform scans with this technique, and the spatial resolution is limited. It can also be stressed that pulsed lasers exist only at specific wavelengths and can be expensive.

2.2.3 Time-resolved CL

Like time-resolved photoluminescence, TRCL can be used to no longer depend on LEE. However, it should be noted that changes in injection efficiency have to be considered. Indeed, if the extraction efficiency does not affect the carriers' dynamic on first order, the carriers' density could [Liu+16a]. It also signifies that TRCL cannot be used to estimate variations in radiative easily. Thus, TRCL measurements do not necessarily carry the same information as time-resolved photoluminescence measurements and are mainly used when spatial resolution is required.

To perform this kind of measurement, it is necessary to generate electron pulses. Two techniques are commonly used to do this:

Laser-driven photocathode As this technique will not be used in this thesis, only a brief description is provided. Typically, these measurements are performed with a field emission gun[1]. In a field emission gun, electron emission is achieved by applying a high electric field to a tip (typically made of tungsten). To increase the emission probability the tip is heated to about 1800 K, which increases the electron population above the Fermi level[2]. With this type of setup, it is possible to lower the operating temperature of the cathode to decrease the electron extraction probability significantly. Then, a pulsed laser with an energy higher than the work function is focused on the gun tip, resulting in the emission of a photocurrent driven by the laser pulses [Meu+19]. The main advantage of this technique is an excellent time resolution while not degrading much the spatial resolution of the SEM [Meu+19]. However, it requires an optical window on the tip and an expensive pulsed UV laser. Moreover, the laser alignment on the tip is complicated.

[1] It is also possible to find cold cathodes based field emission gun, but it will not be discussed here for simplicity

[2] Also, tungsten tips are covered with a thin layer of zirconium oxide (ZrO_2), reducing the work function from 4 eV to about ∼2.7 eV.

Fast beam blanker Another way of generating electron pulses is by using a beam blanker consisting of one or more pairs of electrostatic deflector plates inserted into the microscope column. By modulating the applied bias, it is possible to deflect the e-beam. The main advantage of this technique is its ease of use and the possibility to switch from pulsed to continuous by stopping the modulation. On the other hand, this technique has a lower temporal resolution and a spatial resolution degraded mainly by the displacement of the e-beam on the sample. Note that the presence of the beam blanker also induces a loss in spatial resolution when not precisely aligned in the column. Also, note that to minimize the e-beam displacement while blanking, the midplane of the blanker has to coincide with the conjugate focal plane [Zha+20; Meu+19].

In our case, we will use the beam blanking technique, but our blanker can not be ideally positioned, thus inducing large beam displacement on the sample. We will return to this point later when describing the experimental setup. To go beyond this limitation and improve the spatial resolution, we developed a Hanbury Brown and Twiss interferometer based on the previous work of Meuret et al. This is the topic of the next section.

2.3 Hanbury Brown & Twiss effect

In addition to the time-resolved techniques we have presented, we will see that it is possible to use a Hanbury Brown & Twiss interferometer coupled to a CL setup to measure the carrier lifetime without using a pulsed electron source. Before explaining the details of the Hanbury Brown and Twiss interferometer, let us present a brief history of its origin.

2.3.1 A brief history

The development of radar during World War II led to the development of radio astronomy in the post-war period and the discovery of many extended radio sources. At that time, the technique used to measure the angular size of these objects was based on the Michelson interferometer, an amplitude interferometer. One of the main problems of this technique was the need to preserve the phase and, in particular, its sensitivity to atmospheric turbulence. Thus, with the development of radar and the decreased sensitivity to atmospheric fluctuations in the radio domain, radio astronomy experienced a boom in the 1950s. However, the angular resolution of such an interferometer is typically proportional to λ/b where λ is the source's wavelength and b is the distance between the detectors. Consequently, to

have a resolution of the order of a few milliradians in the radio domain (typically $\lambda \simeq 1.5\,\mathrm{m}$), a distance between the detectors of the order of hundreds to thousands of meters is required [Smi52; Mil52]. This was one of the fundamental limitations of this technique, given the need to preserve the phase.

In 1952, Robert Hanbury Brown published measurements of the apparent angular sizes of discrete radio sources made with *"a new type of interferometer"* designed to overcome the Michelson interferometers limitations, without giving any details about it [HJG52]. The theory involved in this new interferometer was not published until two years later by **Robert Hanbury Brown** and **Richard Quintin Twiss** [HT54]. This new interferometer would essentially consist of an intensity interferometer, eliminating the need to preserve the phase and thus being tolerant of atmospheric fluctuations and simplifying the installation of large instruments. At the end of this paper, the authors mentioned that it would be interesting to find out *"whether the principle of the new type of interferometer can in turn be applied to visual astronomy, since in this way it might be possible to increase the resolving power"*. Then, in 1956, Hanbury Brown and Twiss published 2 papers, the first on a lab experiment, analyzing the 435.8 nm emission line of a mercury-arc lamp with their interferometer. They claimed in that paper that *"photons in two coherent beams of light are correlated, and that this correlation is preserved in the process of photoelectric emission"*. They observed the now so-called "photon bunching" phenomenon, *i.e.*, that photons of a thermal light tend to be detected in close pairs [HT56b]. In the second paper, they used this type of interferometer in the visible range to measure the angular size of the star Sirius [HT56a]. However, these results caused a great debate and the idea that *"photons could interact with each other"* was considered to be in contradiction with quantum mechanics principles. Several experiments were even performed to refute them, in particular that of Brannen and Ferguson, which is at the origin of the controversy [BF56].

At the end of 1956, in response to this controversy, Edward Purcell published a paper in which he stated that *"the Brown-Twiss effect, far from requiring a revision of quantum mechanics, is an instructive illustration of its elementary principles"*. Furthermore, he showed that the observed effect could be attributed to *"fluctuations in a system of bosons"*. In the last part of his paper, he explained that the experiment published by Brannen and Ferguson to disprove this effect had not been performed under the right experimental conditions to observe it [Pur56]. The controversy did not end there, and it was not until the additional support of Richard Sillitto and the demonstration of the effect by Rebka and Pound that Hanbury Brown and Twiss were given credit [Sil57; RP57]. Then, finally, Brannen and Ferguson repeated the experiment in 1958 with a reduced

spectral width, which allowed them to observe the effect [BFW58]. The effect was then recognized, but the quantum interpretation remained disputed, leading to the emergence of modern quantum optics. Thus Hanbury Brown and Twiss contributed to the emergence of modern quantum optics by discovering the effect named after them.

2.3.2 Hanbury Brown & Twiss and g² autocorrelation function

As mentioned previously, the Hanbury Brown & Twiss interferometer, usually simply referred to as Hanbury Brown & Twiss interferometer, is an intensity interferometer. It typically consists of a beamsplitter directing light to two detectors connected to a correlator. This allows the measurement of the second order autocorrelation function $g^2(\tau)$ (2.7), which in essence is the conditional probability of detecting a photon at time $t+\tau$ on one detector given that a photon was detected at time t on the other.

$$g^2(\tau) = \frac{\langle I(t)I(t+\tau)\rangle}{\langle I(t)\rangle^2} \tag{2.7}$$

This quantity is useful to characterize the nature of the light. Indeed, we can distinguish three main cases, as illustrated in figure 2.3:

Poissonian light typically corresponds to a laser beam. The emission of photon's statistic is a Poisson process, *i.e.*, the mean time between two consecutive emissions is constant and independent of the time since the last emission. In this case $g^2(\tau) = 1\ \forall\tau$.

Super-Poissonian light typically corresponds to thermal light. Here the emission of photons tends to form bunches that spread over a time τ_c called coherence time. Thus the probability of joint detection increases at low delay. In this case $g^2(\tau)_{\tau\lesssim\tau_c} > 1$ and $g^2(\tau)_{\tau\gg\tau_c} = 1$. Note that the coherence time is of the order of $\frac{\lambda^2}{c\Delta\lambda}$.[3] Experimentally, if the time resolution is not better than τ_c, the bunching behavior cannot be observed[4], *i.e.*, $g^2(\tau) = 1\ \forall\tau$.

Sub-Poissonian light typically corresponds to single photon emitters. By definition, a single photon emitter can only emit one photon at a time. If we model this emitter by a two-level system, a ground state and an excited state, we can note τ_c (by analogy with the super-Poissonian statistics) the

[3] Example for $\lambda = 440\,\text{nm}$ $\Delta\lambda = 0.1\,\text{nm} \implies \tau_c \approx 6.5\,\text{ps}$

[4] According to Purcell, this is the main reason Brannen and Ferguson did not observe the bunching effect in their first experiment.

lifetime of this excited state. This means that the probability of having a joint detection at zero delays is zero and remains low for delays shorter than the lifetime since the emitter must relax before it can be excited and emit a new photon. This translates into $g^2(\tau)_{\tau \lesssim \tau_c} < 1$ and, in particular, $g^2(0) = 0$.

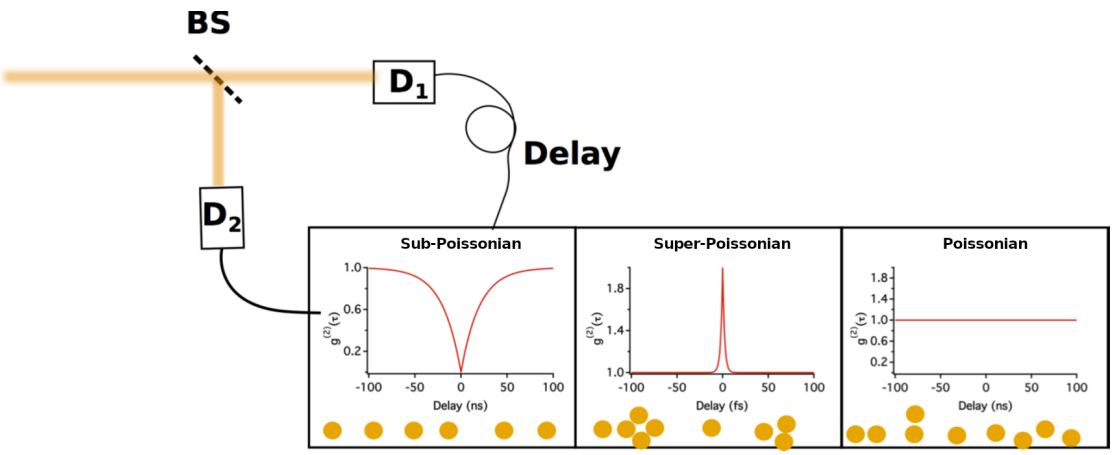

FIGURE 2.3: Basic schematic of an HBT setup illustrating different emission statistics. Adapted from [Meu16]

2.3.3 HBT experiment with a cathodoluminescence setup

In addition to the statistics described above, it is interesting to consider the emission statistics in CL. Indeed, due to the interaction between high-energy electrons and matter, it is possible to observe the phenomenon of photon bunching. This effect was first used by Borst and Liu in 1998, who used the beta particles (electrons) from a Strontium 90 source as an electron source providing short excitation pulses of about 15 ps. They used this technique, which they called *"time-autocorrelated two-photon counting"* to measure the lifetime of different plastic scintillators [BL99]. As stated by the authors, by using a Strontium source instead of a pulsed laser, their technique has *"the advantage of compact size, higher excitation energy, no radio-frequency noise, low cost, easy operation, and low maintenance"*. Recently, this effect has also been demonstrated in a scanning transmission electron microscope (STEM) and SEM [Meu+15; Meu+19]. The main advantage of this technique is that it does not require any modification of the microscope and therefore offers the same spatial resolution as in continuous CL. Note that here we will only focus on the case of photon bunching in bulk semiconductors, but it is also possible to observe anti-bunching in the case of single photon emitters [Tiz+13; Meu16].

Origin of the bunch

Unlike PL, where each probe photon has the energy to create a single e-h pair, the mechanism is different in CL. Indeed, using energetic electrons compared to the bandgap energy allows a single incident electron to create multiple e-h pairs. The underlying mechanism is the following: when a probe electron interacts with matter, it creates one or more bulk plasmons. These plasmons then rapidly create (in a few femtoseconds) several e-h pairs [Meu+15]. Thus, this process can be considered instantaneous compared to the e-h pair lifetime. Then, these e-h pairs will recombine and emit photons following an exponential law typically, as described previously.

Therefore, for each primary electron, several photons can be emitted. Using an HBT, it is possible to observe this statistic which is translated here by

$$g^2(\tau) = 1 + g_0 \exp\left(-\frac{|\tau|}{\tau_{eff}}\right) \tag{2.8}$$

Thus, by fitting the decay of the autocorrelation function it is possible to access the carriers' lifetime τ_{eff} [BL99; Meu+16; Meu+18].

Fondamental limitation on the current

In order to observe bunching, it is necessary to be in a regime where the time between each primary electron is typically larger than the width of a photon bunch, just as the excitation frequency must be low enough to allow relaxation of the system in TRCL or time-resolved photoluminescence. However, here electrons are not emitted at regular intervals but following a Poisson process with a rate parameter proportional to the e-beam current. As illustrated in figure 2.4, at *"low current"* (a), the overlap of two subsequent bunches is small. However, at higher current (b), all bunches are interlaced, leading to a strong uncorrelated background and, thus, a poor signal to background ratio.

We, therefore, want to minimize the probability that two bunches overlap. We define here the size of a bunch as equal to $3\tau_{eff}$ [5]. This probability is, therefore, the probability of having no electron ($k = 0$) in $3\tau_{eff}$ for a Poisson process with rate $\lambda = I/q$, where I is the e-beam current and q the elementary charge.

$$\begin{aligned} P(k, \lambda, t) &= \frac{(\lambda t)^k \exp(-\lambda t)}{k!} \\ P(0, \frac{I}{q}, 3\tau_{eff}) &= \exp\left(-\frac{3\tau_{eff} I}{q}\right) \end{aligned} \tag{2.9}$$

[5] This criterion is arbitrary, τ_{eff} contain on average $1 - \exp(-3) \approx 95\%$ of the bunch photons.

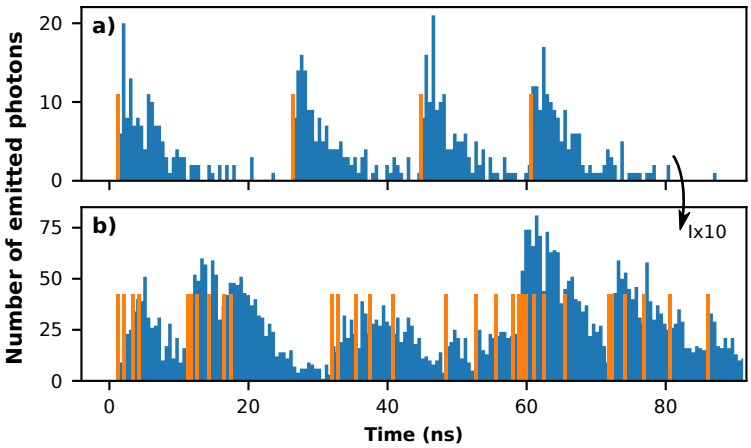

FIGURE 2.4: Illustration of the number of photons emitted over time (blue bars) for a lifetime of 5 ns and a current of (a) 8 pA and (b) 80 pA. The generation of e-h pairs, *i.e.*, electron-matter interactions, are indicated by orange bars.

So typically, we want:

$$3\tau_{eff} \lesssim q/I \tag{2.10}$$

$$I \lesssim q/3\tau_{eff} \tag{2.11}$$

Equation (2.11) can be used as a rule of thumb to select the correct operating current for a given lifetime. Several values are given in table 2.1. Therefore, the longest lifetime that can be measured depends on the smallest current that can be achieved, and the shortest lifetime depends on the time resolution of the detectors and correlator. Thus with this technique, and the typical current range of our SEM (down to ∼2 pA), we can expect to measure lifetimes up to ∼30 ns.

τ (ns)	0.1	1	10	100
I (pA)	534	53.4	5.3	0.5

TABLE 2.1: Suggested maximum e-beam current as a function of lifetime.

2.4 Simulations of autocorrelation measurements

This section aims to understand the acquisition scheme considering the photon generation process through Monte Carlo simulations. First of all, we must introduce the essential parameters and the main differences between the theoretical expression of g^2 and the measured quantity.

2.4.1 Experimental parameters and acquisition scheme

The expression of $g^2(\tau)$ given earlier (equation (2.7)) is the theoretical expression of the second-order autocorrelation but may not correspond to the measured quantity for technical reasons. Indeed, for simplicity, autocorrelation or, more generally, coincidence measurements are often performed in a histogram mode. In this scheme, absolute detection times are not recorded. Instead, the two channels of the time-correlated single photon counting (TCSPC) device are used to build a histogram directly. When an event is detected on the first channel, often referred to as the SYNC or START channel, a "clock" is started/reset. Then, when an event is detected on the second channel (STOP channel), the time difference (called delay) is stored in a histogram. Here, the TCSPC device is a PicoHarp 300, which uses a "start-multistop" scheme, meaning that multiple events on channel 2 can be recorded after a single clock start. Note, however, that the two channels are subject to dead time, *i.e.*, each channel is blind for a certain amount of time after detection.

Based on these assumptions, we will describe the simulation model. Note that we will limit ourselves to a phenomenological approach and will not address the possible optimizations related to the implementation. Also, the essential parameters are introduced and described in table 2.2.

Symbol	Description
I	Electron beam current.
N_e	Number of primary electrons generated per loop (meaningful only for the simulations, see below).
G	Electron-hole pairs generated per electron.
τ_{eff}	Effective lifetime of the sample.
$\tau_{D,detector}$	Dead time of the detectors.
$\tau_{D,TCSPC}$	Per-channel dead time of the TCSPC device.
BS	Fractions of collected photons redirected to the detector.
η	Effective efficiency of the acquisition chain, photon collected/e-h pair generated. It does not take into account dead times.
Δt	Histogram bin width
T	Total acquisition time
τ_{STOP}	Delay introduced on the STOP channel.

TABLE 2.2: Main parameters of the simulation model

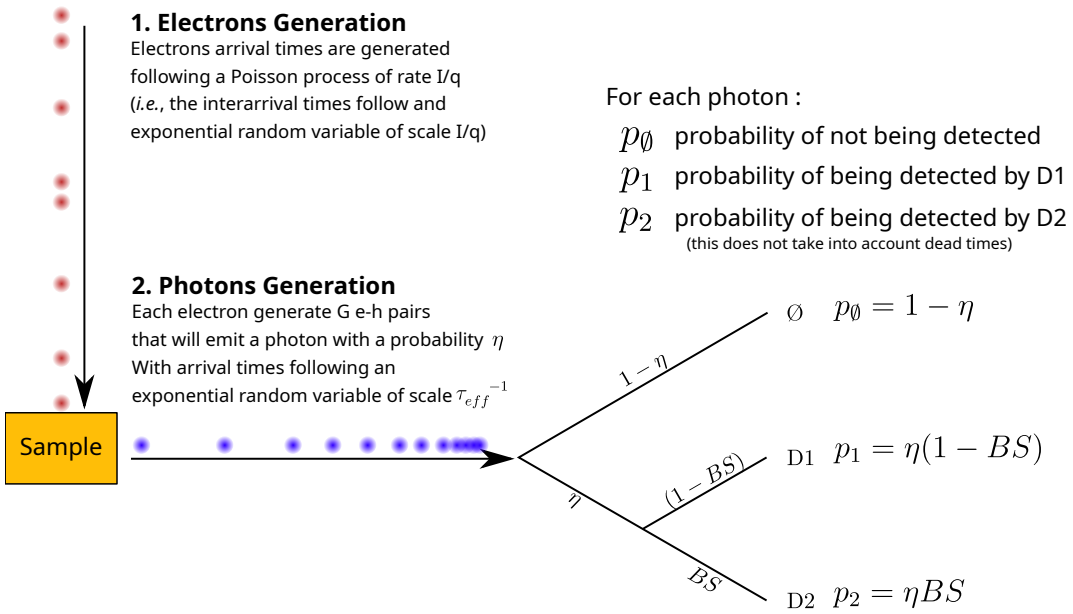

FIGURE 2.5: Illustration of the first two steps of the simulations flow.

1. **Electrons generation** First, the arrival times t_e of N_e electrons are generated following a Poisson process of rate $\lambda = I/q$.[6] This number N_e is a quantity meaningful only for the simulation. It allows parallelization of the simulation by splitting the total simulation time into smaller intervals. In our case, we choose $N_e = 10^4$, which means that it will not be possible to measure delays between photons generated by one electron and photons generated by the 10.001^{th} subsequent primary electron.[7] In the typical current range of our SEM (1 pA to 1 nA) it is not a problem as it corresponds to delays between electrons of the order of 1.6 ms to 1.6 µs which is much more than the lifetimes we want to measure (at most, a few tens of ns).

2. **Photons generation** For each primary electron, N_γ photons are generated, with N_γ being a binomial random variable with parameters (G, η), G the number of e-h pairs created per primary electron, and η is the probability that such a pair recombines into a detectable[8] photon. Thus, η includes the EQE of the sample, and the collection and detection efficiency of the optics and detectors. Then, the arrival times of these photons are generated following exponential random variables of parameter $1/\tau_{eff}$.

3. **Dead times application** In order to apply the different dead times, we first sort the arrival times of the photons and split them in two groups, according

[6] *I.e.*, interarrival times are exponential random variables with parameter $\lambda = I/q$
[7] Assuming that no photon would have reset the clock in the meantime.
[8] The term "detectable" here refers to the fact that a photon reaching the detector could be missed because of the dead time.

to BS, *i.e.*, $BS \times N_\gamma$ are sent to the detector connected to the STOP channel of the TCSPC device and $(1 - BS)N_\gamma$ to the SYNC channel. Then, for a given photon (initially the first one to arrive), all subsequent photons in an interval smaller than the dead time are rejected until a new valid photon is found. This step is repeated until all photons are processed. Also, note that an additional delay is added to the photons of the STOP channel to be able to measure negative delays.

4. **Start-Multistop** Now that we have sorted and removed undetectable photons, we associate each photon of the STOP channel to the SYNC photon preceding it and record the time difference in a histogram. Note that this differs from the theoretical autocorrelation function, which is usually obtained by calculating the delay between each photon and <u>all</u> the others.

These four steps are repeated $N_{loop} = \lfloor I/q \times T/N_e \rceil$ times[9] to obtain a duration length approximately equal to $T \pm \delta T$, with $\delta T = q/(2I) \times N_e < 1\,\text{ms}$.[10]

We can note here that a more complex analytical model could also be used [Sol+21]. In this model, G is no longer constant, but the product of two Poisson random variables, b_i and m_i, the number of bulk plasmons created per primary electron and the number of e-h per plasmon, respectively. So our model would essentially consist of taking $G = cst = \mathrm{E}[b_i \times m_i]$. As it follows the logic of emission and detection, it is relatively simple to add different features if needed (filters, jitter, noise, chained dead times), which cannot be done easily analytically.

Now that we have defined our model and before performing various simulations of CL-HBT, we can first verify the implementation in a more straightforward case, that of a Poisson process, *i.e.*, laser emission.

Histogram vs. g^2

First, we can compare a histogram obtained via simulation of laser emission to the one obtained experimentally by Meuret [Meu16].

Figure 2.6 (a) shows a HBT histogram obtained a laser emission. The parameters given are the count rates of each detector ($N_1 = 1.5 \times 10^5$ and $N_2 = 9.2 \times 10^4\,\text{cps}$), the bin width of the histogram ($\Delta t = 512\,\text{ps}$) and the total acquisition time ($T = 50\,\text{s}$). Here, in a Poisson process, photons are randomly distributed in time. Therefore, the number of event per bin is simply $TN_1N_2\Delta t = 353.28$. Note that the value calculated by Meuret is 400.38, which could be explained by a typing error. Indeed this value is obtained with $N_1 = 1.7 \times 10^5\,\text{cps}$.

[9] $\lfloor x \rceil$: round to nearest integer

[10] This rounding error could be removed by changing the implementation, however it is, in the worst case, less than 1 ms

To simulate such a measurement with our model, we assume $\eta = 1$ so the count rate of the two detectors (N_1+N_2) can be translated into a current, $I = (N_1+N_2)q$ and $BS = N_2/(N_1 + N_2)$.[11] Here, no dead time is applied. It is valid because the count rates are low. Thus the time between photons is long compared to typical dead times so that dead times can be neglected. Figure 2.6 (b) shows the simulated histograms both with N_1=1.5×10^5 (blue) and 1.7×10^5 cps (orange). We can see that the simulations match the data well.

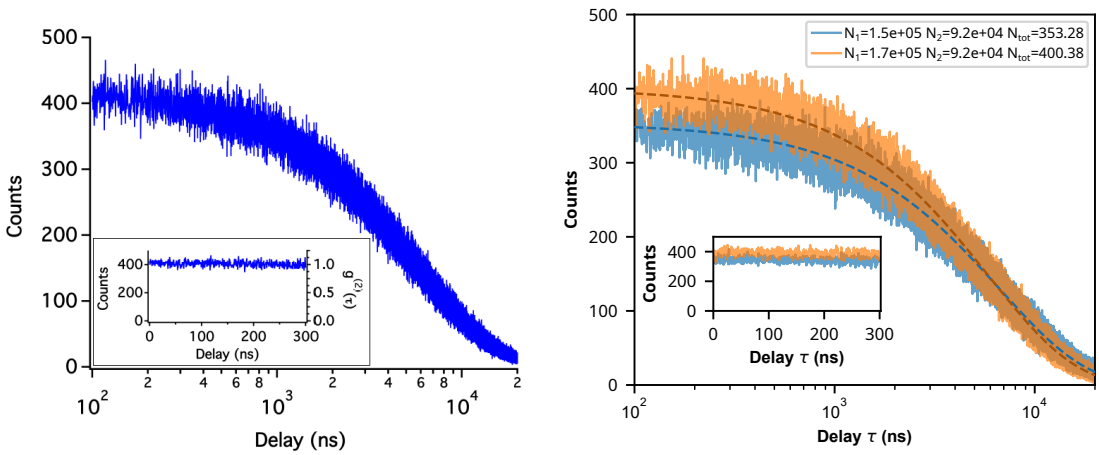

(a) (b)

FIGURE 2.6: (a) HBT histogram of the signal coming from a laser [Meu16]. (b) Simulated HBT histogram of a laser for two different sets of count rates. Expected counts for a Poisson process recorded in a start-multistop mode are indicated as dashed lines.

Now concerning the shape of the histograms, we note that they are decreasing with longer delays, which is not expected for the "true" g^2, where the delays between each photon and all the others are calculated. This difference is due to the fact that, here, the clock is reset if a photon is detected on the SYNC channel. Thus the probability of recording events at a long delay decreases with the SYNC channel count rate. The probability that an event is recorded at delay τ is proportional to the probability that the clock is not reset before. In the case of a Poisson process of rate λ, we recall that interarrival times follow an exponential random variable [RR98]. Thus, the probability is expected to be proportional to :

$$1 - P_{\text{reset}}(t < \tau) = 1 - \int_0^\tau \lambda e^{-\lambda t} dt = e^{-\lambda \tau} \tag{2.12}$$

This phenomenon is illustrated in figure 2.6 (b), where $TN_1N_2\Delta t \times \exp(-N_1\tau)$ is shown as a dashed line for $N_1 = 1.5 \times 10^5$ and $N_1 = 1.7 \times 10^5$ cps, in excellent agreement with the simulations.

[11] We could have chosen a different η and taken $I = (N_1 + N_2)q/\eta$ to get the same result.

Dead time

One other difference between the commonly considered g^2 and the measured quantity could be attributed to the dead time of the detectors and the TCSPC device. Usually, two types of dead times are considered. They are classified depending on the response to an event happening during the dead time τ_D : first, non-extended or *non-paralyzable*, the event is ignored; second, extended or *paralyzable*, the dead time is extended for an additional τ_D [Mül73]. In our case, extended dead times will not be considered as we will be confronted only with non-extended dead times.

Now when it comes to the effects of a dead time, we can first mention the lowering of the count rate by the loss of events. For a single non-extended dead time in the case of a Poisson process, the measured count rate N_{measured} can be expressed as a function of the actual count rate N_{actual} [Mül73]:

$$N_{\text{measured}} = \frac{N_{\text{actual}}}{1 + N_{\text{actual}} \times \tau_D} \tag{2.13}$$

Thus, the measured count rate for such a dead time is expected to saturate around τ_D^{-1}. However, this loss of event is hard to estimate since the actual count rate is unknown in practice. This can still be used to check the implementation of the simulation. For example, figure 2.7 (a) shows theoretical measured count rate vs. actual count rate for different dead times as well as simulations performed with a dead time of 90 ns with our model in the case of a Poisson process.

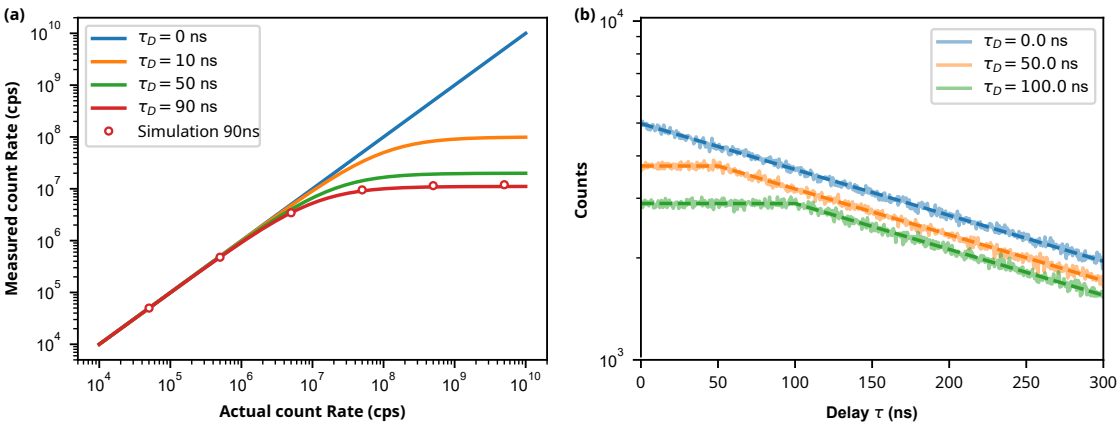

FIGURE 2.7: (a) Theoretical relation between the measured count rate and the actual count rate for various dead times. A simulation of a 90 ns dead time is also shown. (b) Simulated histogram of a Poisson process for different dead times (continuous line) and the estimated shape based on the probability that the clock is not reset (dashed line).

Another consequence of dead time is a change in the time distribution. Again, we will illustrate this for a Poisson process with a single dead time. We have already shown that the probability of recording an event at a delay τ is proportional to

the probability that the clock is not reset before. Because of the dead time, the probability that the clock is reset before τ_D is now zero. Thus, the probability that the clock is not reset before τ is now a piecewise function:

$$1 - P_{\text{reset}}(t < \tau) = \begin{cases} 1, & \text{if } \tau < \tau_D \\ e^{-\lambda(t-\tau_D)}, & \text{otherwise} \end{cases} \tag{2.14}$$

This phenomenon is illustrated in figure 2.7 (b), where simulated histograms with a count rate of $\sim 3.12 \times 10^6$ cps on each detector are shown for various dead times applied. For comparison, $\bar{H} \times (1 - P_{\text{reset}}(t < \tau))$, where $\bar{H}$ is the mean counts for $\tau < \tau_D$ is shown as dashed lines. As expected, histograms are flat for delays smaller than the dead time, and for bigger delays, we retrieve the exponential decay already observed in figure 2.6.

2.4.2 Simulations of the CL-HBT experiment

Now that we have shown that our simulations behave as expected in relatively simple cases, we can use them to investigate more complex situations, with $G > 1$, where photon bunching is expected.

In order to simplify the explanations, let us first introduce a simple model that can be used to describe the histograms obtained in this kind of measurement [Meu16]:

$$H(\tau) = A \exp\left(-\frac{|\tau - \tau_{\text{STOP}}|}{\tau_{eff}}\right) + B \tag{2.15}$$

With A the amplitude at zero delay, B the baseline, τ_{STOP} the delay introduced on the stop channel, and τ_{eff} the effective lifetime assuming a monoexponential decay.

Number of e-h pairs per primary electron

In our model, the number of detectable photons per pulse (without taking into account the dead time) reaching the STOP (resp. SYNC) channel is a binomial random variable with parameters $(G, \eta BS)$ (resp. $(G, \eta(1 - BS))$). Therefore, on average, there will be $G\eta BS$ photons per electron on the STOP and $G\eta(1 - BS)$ on the SYNC channel. For this reason, it seems natural to investigate the effect of G while keeping the same average photon number, that is $G\eta = cst$ and $BS = cst$.

For this, we perform various simulations by keeping $G\eta = 5 \times 10^{-2}$, $BS = 0.5$, and a current of $I = 1\,\text{pA}$ while increasing G from 1 to 1024 in powers of 2. For each of the simulations the count rates were identical $N_{SYNC} \approx N_{STOP} \approx$

1.5×10^5 cps $\approx (I/q)G\eta BS$, as expected. Note that it is essential to keep $G\eta BS$ and $G\eta(1 - BS)$ low to avoid pile-up effects, similar to those observed in time-resolved measurements, but we will return to this point later.

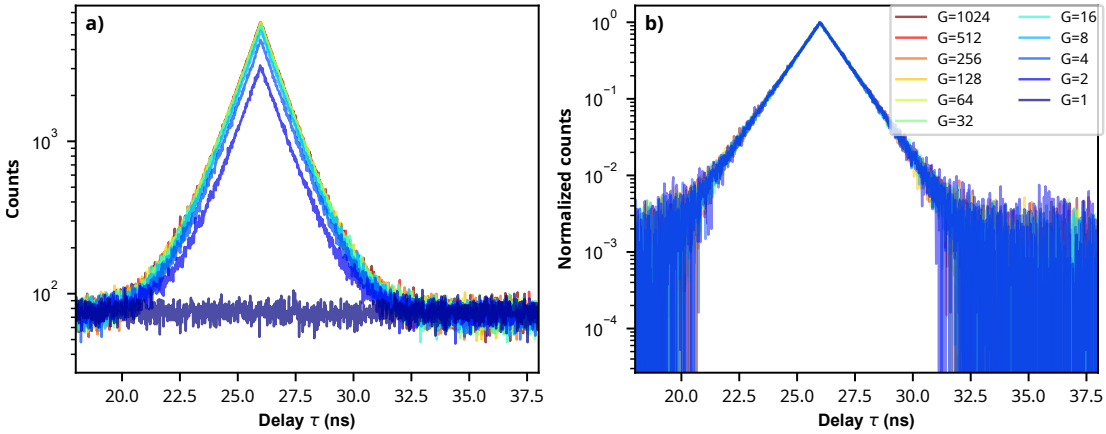

FIGURE 2.8: (a) Various simulations performed with $G\eta = 5 \times 10^{-2}$ for different number of e-h pairs generated per primary electron with constant count rate $N_{SYNC} \approx N_{STOP} \approx 1.5 \times 10^5$ cps. (b) Corresponding histograms after subtracting the baseline (B) and dividing by their amplitude (A). Note that $G = 1$ is not shown as $A = 0$.

Figure 2.8 (a) shows the obtained histograms. When $G = 1$, we find the situation of the laser described previously. When G is greater than 1, we notice the presence of a bunch as expected. This corresponds to the situation where at least one photon is detected on each channel from one primary electron. The amplitude A of this bunch increases slightly with G to reach a limit. We can ascribe this phenomenon to the fact that the binomial distribution of parameter (G, η) tends towards the Poisson distribution of parameter $G\eta$ when G is large and $G \times \eta$ kept constant.

More importantly, as we are mainly interested in this technique to measure lifetimes, we can verify that this change in statistics does not affect the decay of the bunch. Figure 2.8 (b) shows that the normalized histograms ($(H(\tau) - B)/A$) overlap perfectly, confirming that the lifetimes can be extracted without being affected.

Pile-up effect in HBT measurements

One other effect that could affect the lifetime is pile-up. It is then crucial to investigate this effect here for autocorrelation measurements.

Assuming that the number of detectable photons per bunch follows a Poisson distribution and that each bunch can be treated independently, it is possible to

show that the pile-up probability given that at least one photon has been detected on each detector is identical to the probability that pile-up occurs in time-resolved given that a photon has been detected (see appendix 2.A).

$$P_{HBT}(\text{pile-up}|\text{correlation}) = P_{TR}(\text{pile-up}|\text{detection}) \tag{2.16}$$

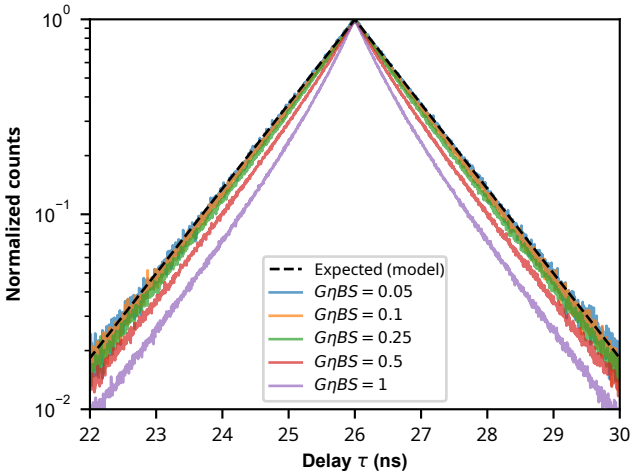

FIGURE 2.9: Normalized histograms of HBT simulations with a current of 1 nA, a lifetime of 1 ns, a delay of 26 ns, and a 1:1 beamsplitter ($BS = 0.5$) for different average photon numbers per primary electron.

Thus, to quantify the effect of pile-up, we performed simulations. Figure 2.9 shows normalized histograms for different average numbers of photons per bunch ($G\eta BS$). All the simulations were performed with an effective lifetime of 1 ns, an e-beam current of 1 pA and $BS = 0.5$. Similarly to time-resolved measurements, the distribution is modified and becomes non-exponential with increasing $G\eta BS$. Therefore, to avoid this artifact, we will take as criterion $G\eta BS < 0.05$ and $G\eta(1-BS) < 0.05$. Experimentally it means that the count rate on each channel should not exceed a threshold proportional to the current:

$$N_{STOP}, N_{SYNC} < \frac{0.05I}{q} \tag{2.17}$$

For reference, this corresponds to 3×10^5 cps on each channel for an e-beam current of 1 pA.

Effect of the current

As we mentioned earlier, by increasing the current, the bunches will not be separated anymore. Therefore the probability that delays between photons originating from two different (*i.e.*, uncorrelated) electrons is measured increases with the

e-beam current. On the other hand, the probability of recording a correlation (assuming no dead time) does not depend on the current, as it is the probability that at least one photon is detected on each channel for one primary electron. Thus, the uncorrelated count rate increases more than linearly with the current, whereas the correlated count rate increases linearly.

This has already been observed experimentally [Meu+17; Sol+21] and is typically quantified by looking at the histograms divided by their baseline:

$$h(\tau) = A/B \exp\left(\frac{-|\tau - \tau_{\text{STOP}}|}{\tau_{eff}}\right) + 1 \tag{2.18}$$

As the current increases, A/B should tend toward zero. According to Sola-Garcia et al., without taking into account dead times, we should obtain:

$$h(\tau_{\text{STOP}}) - 1 \propto I^{-1} \tag{2.19}$$

To verify this, here, taking into account the dead time of the TCSPC device, we performed simulations by keeping all the parameters constant (see below) except for the current, varying from 1 pA to 100 pA.

- $G = 20$
- $\eta = 2.5 \times 10^{-3}$
- $\tau_{eff} = 5\,\text{ns}$
- $BS = 0.5$
- $\tau_{D,TCSPC} = 90\,\text{ns}$
- $T = 10\,\text{s}$
- $\tau_{\text{STOP}} = 26\,\text{ns}$
- $\Delta t = 512\,\text{ps}$

Figure 2.10 (a) shows the obtained histograms. As the detection probability ($G\eta$) is constant, the count rate increases with the current. As a result, the effect of dead time can be seen for currents above 5 pA. We here retrieve the behavior observed in the case of the laser emission with a baseline flat for delays shorter than the dead time and then exponentially decreasing. To compare the effect of the current figure 2.10 (b) shows the normalized histograms, *i.e.*, divided by their baseline (2.18). As expected, the amplitude decreases with the current. More precisely, as shown in figure 2.10 (c), the amplitude decreases as I^{-1} as found by Sola-Garcia et al.

Signal to noise ratio

An important point that has been left out for the moment is the SNR. We are going to estimate this quantity based on simple considerations and compare it to "classical" TRCL measurements. First, we assume that the dark counts can be neglected (this will be the case with our setup, as the dark counts will be less than 100 cps relative to the signal in the 10^4–10^5 cps), so only shot noise is considered.

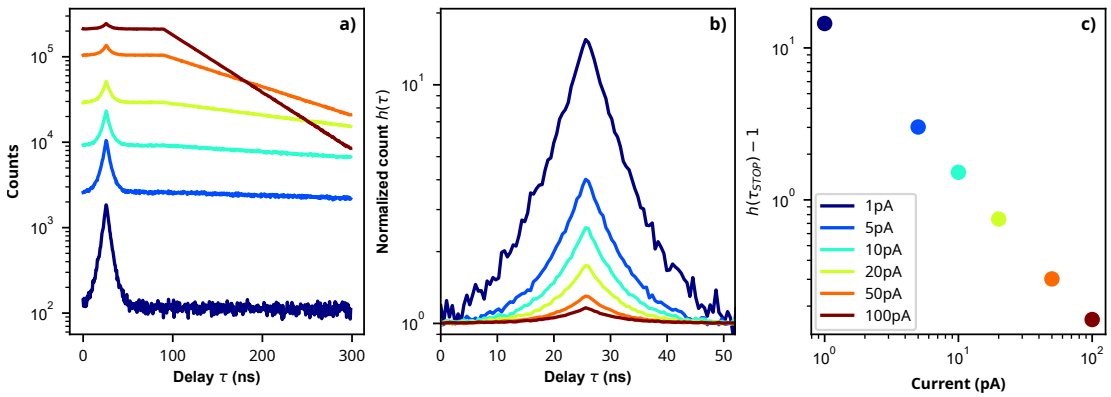

FIGURE 2.10: Simulations performed with different current ranging from 1 pA to 100 pA. (a) The obtained HBT histograms. (b) Histograms are divided by their baseline, showing a decreasing bunching amplitude as the current increases. (c) Amplitude of the bunch $A/B = h(\tau_{\text{STOP}} - 1)$ as a function of the current. The lines of (a) and (b) are color-coded according to the legend of (c)

In this case, we defined the SNR as the square root of the number of counts N as it is usually done. Then, we assume that the average number of photons detected per electron, here in HBT measurements, or per excitation in TRCL follows a Poisson distribution.

In the case of TRCL, we have,

$$\text{SNR}_{\text{TRCL}} = \sqrt{N} = \sqrt{n_{\text{TRCL}} f T} \tag{2.20}$$

With n_{TRCL} the average number of photons detected per excitation, f the repetition rate and T the acquisition time.

In autocorrelation, the probability of recording an event for one primary electron is the product of the average photon number per channel.

$$\text{SNR}_{\text{HBT}} = \sqrt{N} = \sqrt{n_{\text{START}} n_{\text{STOP}} I/qT} \tag{2.21}$$

Thus, we can now compare those quantities. For an equal acquisition time T:

$$\frac{\text{SNR}_{\text{HBT}}}{\text{SNR}_{\text{TRCL}}} = \sqrt{\frac{n_{\text{START}} n_{\text{STOP}} I/q}{n_{\text{TRCL}} f}} \tag{2.22}$$

Assuming $I/q \approx f$, in the best-case scenario, the count rates are limited to avoid pile-ups $n_{\text{START}} = n_{\text{STOP}} = n_{\text{TRCL}} \approx 5 \times 10^{-2}$. We can also consider the case where the count rates are limited by the overall efficiency: $n_{\text{START}} = n_{\text{STOP}} \approx 0.5 n_{\text{TRCL}}$ and $n_{\text{TRCL}} \leq 5 \times 10^{-2}$.

In those conditions, we can deduce:

$$\frac{\mathrm{SNR_{HBT}}}{\mathrm{SNR_{TRCL}}} = \begin{cases} \sqrt{n} \approx 0.22 & \text{Best case} \\ \sqrt{n}/2 < 0.11 & \text{Efficiency limited} \end{cases} \tag{2.23}$$

Thus, for an equal acquisition time, the SNR will be at best approximately 5 times lower compared to TRCL when pile-up is the limiting factor and more than 10 times lower when the overall efficiency is the limiting factor. An alternative way to interpret this is to consider the time required to obtain an identical SNR. Again assuming $I/q \approx f$, we can write

$$\begin{aligned} \sqrt{n_{\mathrm{START}} n_{\mathrm{STOP}} T_{\mathrm{HBT}}} &= \sqrt{n_{\mathrm{TRCL}} T_{\mathrm{TRCL}}} \\ \implies T_{\mathrm{HBT}} &= \frac{n_{\mathrm{TRCL}}}{n_{\mathrm{START}} n_{\mathrm{STOP}}} T_{\mathrm{TRCL}} \end{aligned} \tag{2.24}$$

$$T_{\mathrm{HBT}} = \begin{cases} \frac{1}{n} T_{\mathrm{TRCL}} = 20 & \text{Best case} \\ \frac{4}{n} T_{\mathrm{TRCL}} > 80 & \text{Efficiency limited} \end{cases} \tag{2.25}$$

In other words, to obtain a comparable SNR, the acquisition time has to be 20 times longer when the pile-up is limiting and more than 80 times when the efficiency is limiting.

Thus, this could be the main limitation when studying low-efficiency samples.

First measurements vs. simulations

Now that we have studied the effect of various parameters on the measured histograms, we can compare our simulations to real data. To do so, we measure a sample already extensively studied: a core-shell m-plane InGaN/GaN quantum well grown on the sidewalls of a GaN microwire. Note that this sample will be described later (referred to as sample #2 in chapter 3). For now, we will focus only on the autocorrelation measurements and simulations. Without giving more details here, due to wire-to-wire dispersion, the effective lifetime was estimated by TRCL to be between ∼160 ps and ∼190 ps[12], with a mean of 174 ps.

The setup will be described in the next section; however, we still need to introduce some key parameters related to the detectors and the TCSPC device. First, the TCSPC device is a PicoHarp 300 with non-extended dead time of less than

[12] These values are the first and third quartile respectively

90 ns according to the datasheet. Using the plateau present in the histograms at high count rates, we extracted a dead time of 86 ns. Concerning the detectors, two PMA Hybrid 06 from PicoQuant were used. According to a PicoQuant representative, these detectors have no dead time in the strict meaning of the term. However, the response of a photon produces an output pulse with a width of 650 ps. If another photon is detected within this time, *"the output pulses will add up, so it is not easily possible to discriminate"*. Thus, in a way, we could consider a 650 ps dead time, but as this value is more than two orders of magnitude lower than the dead time of the PicoHarp, we will neglect it. Another important parameter is the resolution of these detectors. Here we did not estimate it, but according to the datasheet, time resolution can be approximated by a FWHM of <50 ps. Lastly, for the delay introduced on the STOP channel, we used a few meters of coaxial cable resulting in a ∼26 ns delay.

Current (pA)	2.4	9.6	37.2	121	405	364
Acquisition time (s)	469	210	65	108	91	89

TABLE 2.3: Current and acquisition time.

Figure 2.11 (a) shows the measured histograms for different currents ranging from 2.4 pA to 405 pA with a 5 kV acceleration voltage. As each histogram's acquisition times differ (see table 2.1), we display histograms divided by their acquisition time here. In agreement with what has been shown previously, the amplitude of the bunch decreases with increasing current. We can notice two peaks at about 3 ns. Since this reflection was also present in TRCL measurements with a different optical path, we attributed it to reflections between the sample and the sapphire window of SEM.

To simulate these histograms, we need to know the essential parameters. Some are controlled and well-known, such as the acquisition time T, the bin width Δt, and the e-beam current I. Concerning the others, we already estimated the dead time and the delay, so we need to estimate G, η τ_{eff}, and BS. First, we used equation (2.15) to estimate τ_{eff} to be around 183 ps for all the currents, which match the lifetime measured in TRCL for this sample. Then, we defined BS as the ratio of the count rate on the STOP channel over the total count rate, as we previously did for the laser histogram. Finally, we assumed that G is large enough and η small so that the binomial distribution can be approximated by a Poisson distribution with parameter $G\eta$. Thus, we arbitrarily fixed G to 50 and estimated $G\eta$ as the ratio of the total count rate and I/q, giving $\eta \approx 1.12 \times 10^{-4}$.

Figure 2.11 (b) shows the simulated histograms, also divided by the acquisition time. They are in excellent agreement with the data. However, we can note some

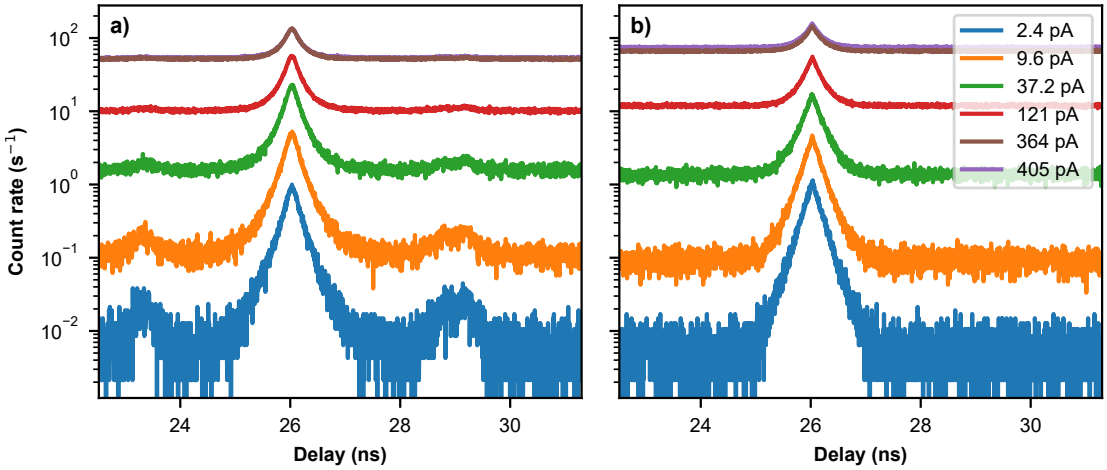

FIGURE 2.11: (a) Count rate of HBT histograms (*i.e.*, histograms divided by the acquisition time) acquired on an InGaN/GaN core-shell microwire for various e-beam current and the corresponding simulations (b).

differences:

1. Of course, the simulations do not reproduce the bump due to reflections.

2. The simulated histograms are sharper than the measured ones. This is undoubtedly because we did not consider the detectors and TCSPC device impulse responses.

3. We can see that the simulations tend to overestimate the count rates at higher currents. By taking a closer look at the measurements, we can see that those performed at 364 and 405 pA overlap. Several hypotheses could explain this behavior. First, it is possible that at a high current, the sample becomes charged, thus deflecting some of the electrons. The current measured with a Faraday cup may be higher than the injected current. Second, we have observed a decrease in intensity during prolonged or repeated measurements on this type of wire, possibly due to irradiation damage. Thus, the efficiency may have decreased between the measurement performed at 2.4 pA and 405 pA as measurements were performed in the order of increasing current.

Nevertheless, the shape of the histograms is very well reproduced, and the simulations are in satisfactory agreement with the data. Thus, our simple model seems to be sufficient to describe the experimental data.

2.4.3 Summary

In conclusion, we have introduced a simple model explaining the bunching behavior observed in the autocorrelation measurements performed in CL. First, we have

applied our model to a simple case: a laser emission. We were able to reproduce acquired data and retrieve the expected behavior when dead time is present. We then used this model to understand the influence of different parameters when the number of possible photons per primary electron is greater than one. In particular, we highlighted two essential conditions to measure lifetimes correctly. First, one should limit the current to satisfy equation (2.11). This condition can be relaxed if necessary in exchange for a larger background (typically if the e-beam current cannot go below it). Then, as the dead time also applies here, to measure the correct lifetime, it is crucial to limit the count rate on each channel below 5% of the electron rate (2.6). Finally, it is advised to keep the count rate less than half of the inverse dead time (2.26) [HS17] since above this threshold, events are usually lost. All these criteria are summarized in figure 2.12. Figure 2.12 (a) shows the maximal suggested current for a given lifetime and figure 2.12 (b) the maximal count rate per channel as a function of the current for different dead time value.

$$I < \frac{q}{3\tau_{eff}} \tag{2.11}$$

$$N_{STOP}, N_{SYNC} < \frac{0.05I}{q} \tag{2.17}$$

$$N_{STOP}, N_{SYNC} < \frac{1}{2\tau_D} \tag{2.26}$$

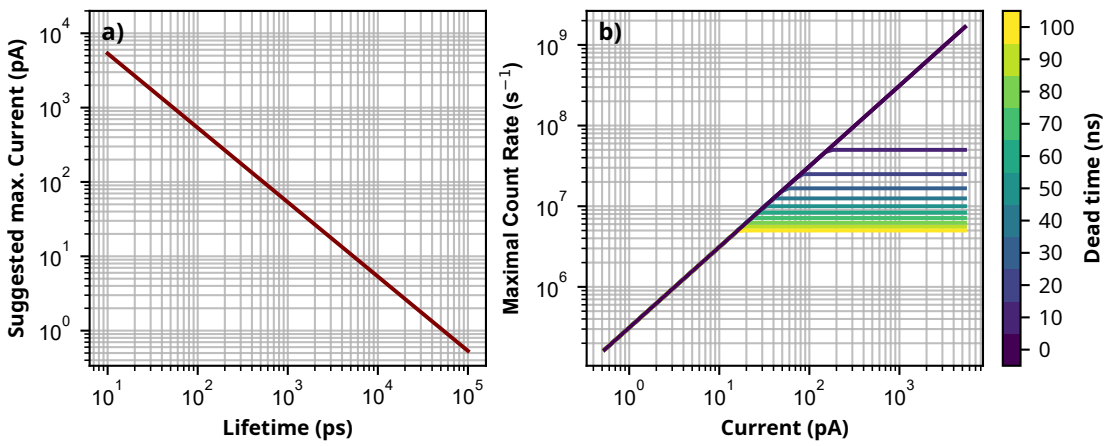

FIGURE 2.12: (a) Suggested maximal e-beam current for lifetimes ranging from 10 ps to 100 ns, based on equation (2.11). (b) Maximal useful count rate per channel taking into account dead time and pile-up for different dead time, based on equations (2.17) and (2.26).

Second, we have shown that this technique inherently suffers from a much lower SNR than time-resolved techniques, which could be the main limitation in studying defective samples.

Finally, we have shown that our simple model reproduces the histograms ob-

tained in the autocorrelation measurements for different currents using only one free parameter. This confirms that the emission statistics is well described and that this method can be used to access the carriers' lifetime. Note, however, that it is possible to complexify this model to describe the generation of e-h pairs as a sequence of two stochastic processes, first the generation of plasmons and second, for each plasmon, the generation of electron-hole pairs, both described by Poisson distributions.

2.5 Experimental Setup

Now that we have seen the different characterization techniques and their principle, we will describe the initial setup and the part developed during this thesis. A complete schematic is shown in figure 2.13.

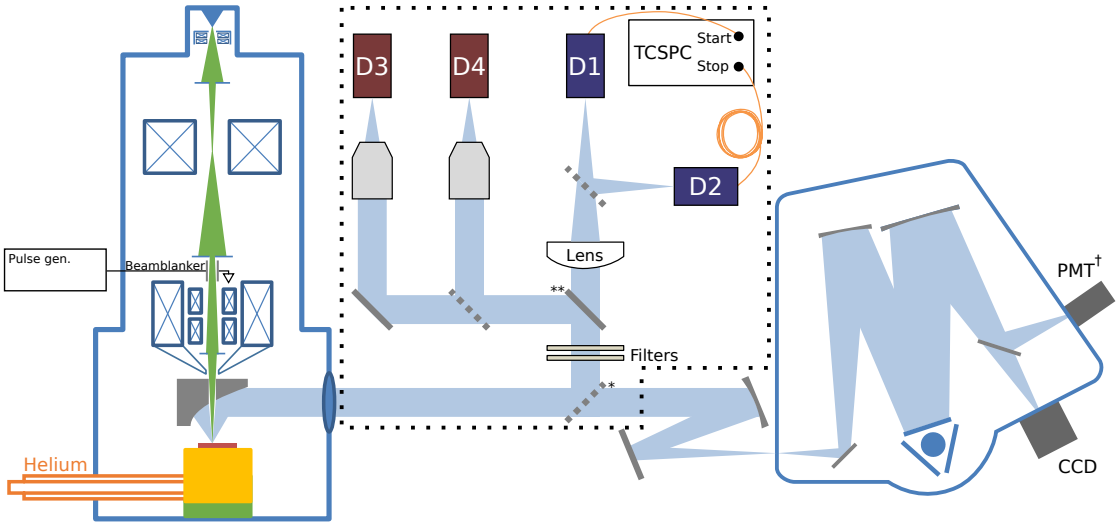

FIGURE 2.13: Schematic of the experimental setup. The part developed during this thesis is enclosed in a dotted box. * This beam splitter is only present when using one of the two Hanbury Brown & Twiss interferometers and can be replaced by a mirror if the sample is not bright enough. ** This mirror can be removed to switch from Visible-HBT to UV-HBT. † This photomultiplier tube (PMT) can be easily replaced by a hybrid PMT (D2) to perform TRCL measurements. Note that the beam blanker is present only when performing TRCL measurements.

2.5.1 Initial setup

The CL setup consists of an FEI Inspect F50 SEM equipped with a cryogenic stage allowing to work from 6 to 320K. A parabolic mirror with a focal length of 12 mm was internally designed and is controlled by piezoelectric actuators, allowing fine positioning. The light is then focused on the entrance slit of a Horiba iHR550

spectrometer using a second parabolic mirror with a focal length of 300 mm. This duet of mirrors acts as a microscope with a 25x magnification. This high magnification helps to make a precise alignment of the parabolic mirror. However, it must be kept in mind that this may limit the light collection. Typically, a 100 µm entrance slit allows a homogeneous collection on only 4 µm on the sample. When the slits are wide open, *i.e.*, 7 mm, it allows a collection on 280 µm. This phenomenon is illustrated in figure 2.B.1 (page 56) where two mapping are performed under identical conditions with 100 µm and 1 mm slits. Therefore as the entrance slit also determines the spectral resolution, there is typically a trade-off between the field of view and spectral resolution.

The spectrometer is equipped with several gratings. Unless explicitly mentioned, a 600 gr/mm grating will be used for the rest of the manuscript. Also, two exit ports are available. On the first one, an Andor Newton DU940 BU2 charge-coupled device (CCD) is mounted and is used for optical alignment, spectra acquisition, or hyperspectral mapping, *i.e.*, the e-beam scans a grid (or line) of points and a spectrum is recorded at each point. Assuming that the intensity is not the limiting factor, the dwell time can be as low as ∼25 ms, corresponding to 90 s for a 60 x 60 image. In this configuration, drift can be a problem, so a full secondary electron image (typically 1024x884 pixels) is acquired before and after the mapping, as well as the Everhart-Thornley detector (ETD) voltage forming a real-time low-resolution secondary electron image. It thus possible to correct the drift, assuming a constant drift velocity during acquisition.

On the second exit port, it is possible to mount either a Peltier-cooled[13] Hamamatsu R10699 PMT to acquire CL images with the same resolution as the secondary electron image. However, note that the spatial resolution of CL images is limited by the interaction volume and carrier diffusion. One of the advantages here is the possibility to use a fast analog-to-digital converter (ADC) converter (NI-5734 from National Instrument) to acquire both secondary electron and CL simultaneously. Instead of the PMT, it is also possible to adapt a fast detector (in our case a hybrid PMT (PMA Hybrid 06 from PicoQuant) to perform TRCL measurements. In order to generate electron pulses, a beam blanker with a different air gap (100, 200, or 500 µm) has to be inserted in the SEM column. This significantly reduces the spatial resolution, mainly introducing astigmatism. In addition, there is a trade-off between spatial and time resolution here. A smaller air gap provides higher time resolution at the cost of lower spatial resolution. A fast pulse generator (PG-1072 rev. B from Active Technologies) is used to drive the beam blanker polarization and as a trigger for the TCSPC device (PicoHarp 300 from PicoQuant).

[13]The cooling is performed by a thermoelectric cooler (C14761 from Hamamatsu)

2.5.2 Developed setup

In order to complement the existing TRCL setup, two Hanbury Brown & Twiss interferometers have been designed during this thesis. The main objective of these setups is to preserve the spatial resolution while achieving a time resolution of the order of 50 ps. The first one is designed to operate in the UV/blue part of the spectrum, and the second one addresses the rest of the visible spectrum. Figure 2.14 shows a 3D sketch of the two Hanbury Brown & Twiss interferometers. We can see a first common part consisting of two filter sliders and a cage cube containing a removable right-angle mirror for selecting the Hanbury Brown & Twiss interferometer. Note also that both setups use the same TCSPC device (not shown here).

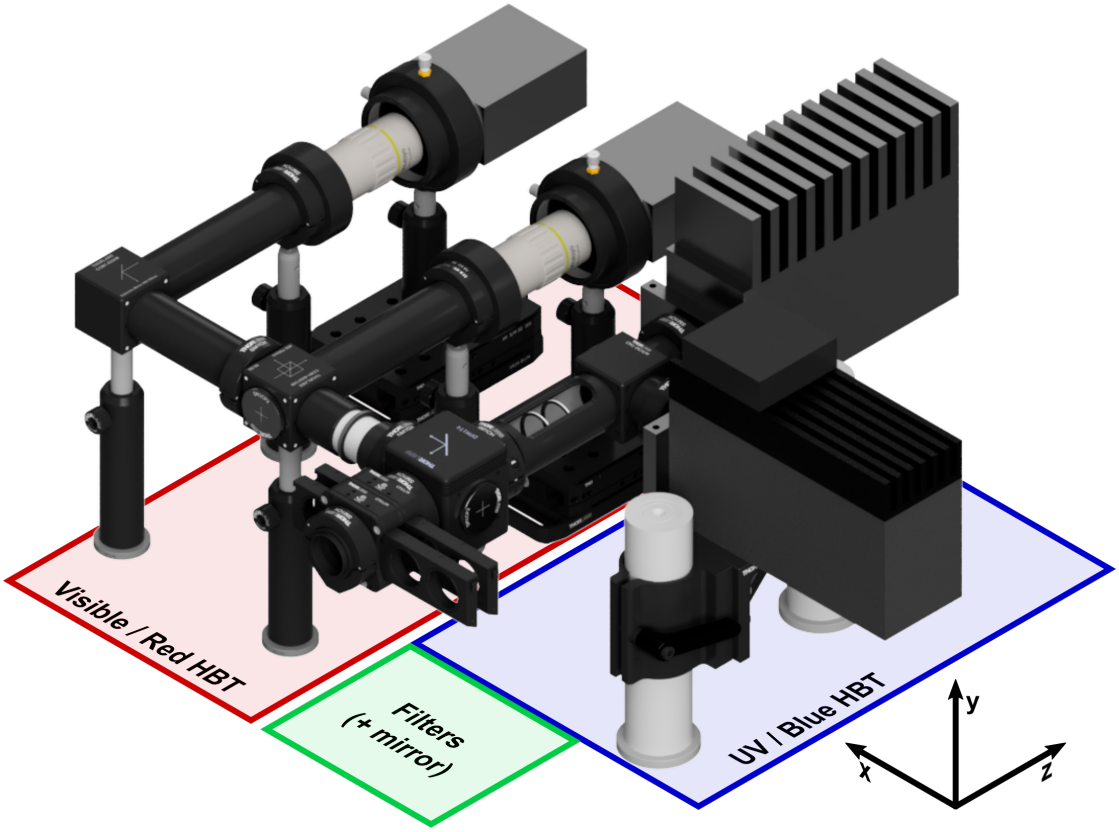

FIGURE 2.14: 3D sketch of the two Hanbury Brown & Twiss interferometers

UV-HBT

The design of this HBT is relatively simple. It is essentially composed of a plano-convex lens ($f = 200$ mm) mounted in a slotted lens tube. Then a 1:1 beamsplitter is used to direct the light to two fast PMTs, with a time resolution better than 50 ps (PMA Hybrid 06 for PicoQuant). This simplicity can be achieved thanks to the large active area of the detectors (6 mm in diameter). This eliminates the need

for fine optical alignment. This system, combined with the parabolic mirror inside the SEM, has a magnification of $200/12 \approx 16.67$. Thus, 6 mm on the detectors correspond to 360 µm on the sample. Note that the time resolution of this setup has been estimated to be around 40 ps using a sample with a short lifetime. More details can be found in appendix 2.C.

As shown in figure 2.15, the detectors (PMA Hybrid 06) have a peak efficiency of about 30% between 300 and 400 nm. Above 500 nm, the detection efficiency degrades rapidly with increasing wavelength. Therefore, a second Hanbury Brown & Twiss interferometer has been designed to cover wavelengths above 500 nm.

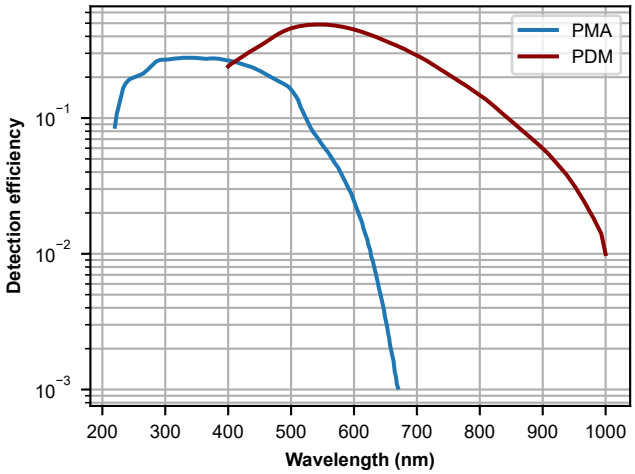

FIGURE 2.15: Detection efficiency of the detectors used in the different Hanbury Brown & Twiss interferometers.

Visible-HBT

To extend the studies to the rest of the visible spectrum, especially in the red, we received a small grant to develop a new setup.

This Hanbury Brown & Twiss interferometer relies on two Peltier-cooled single-photon avalanche diodes (SPADs) (PDM-050-CTD from Micro Photon Devices). They have a peak efficiency of 40% and their efficiency remains above 30% between 450 and ∼700 nm. Compared to hybrid PMTs of the UV-Hanbury Brown & Twiss interferometer, these detectors are much cheaper, with comparable dark count and time resolution[14], but at the cost of a much smaller active area (50 µm in diameter).

To deal with this small size, the two arms of the interferometer are independent. They are composed of a Mitutoyo plan apochromat objective with an effective focal length of 20 mm and a working distance of 34 mm. Each detector is mounted on a 2-inch XY translator, which is itself mounted on a linear translation stage,

[14]The time resolution of these detectors was measured by Micro Photon Devices and was about 27 ps at 675 nm.

allowing fine alignment along all three axes. The light proofing between the fixed part, *i.e.*, the objective, and the detector is assured by rubber bellows (not shown in figure 2.14). Here the magnification is 20/12, so 30 µm on the sample correspond to 50 µm in the focal plane, which is the diameter of the detectors.

2.6 Conclusion

In conclusion, in this chapter, we have presented different characterization techniques. In our case, we will work essentially in cathodoluminescence. The various photoluminescence measurements will be performed by collaborators. In addition, we have introduced the benefit of time-resolved measurements to probe IQE variations without being sensitive to LEE variations. To perform such measurements in CL, we have introduced three techniques:

- using a beam blanker, relatively easy to implement but with greatly reduced spatial resolution
- using a laser-driven photocathode, which requires a particular setup, including an optical window on the FEG tip and an expensive pulsed UV laser
- using an HBT setup which has the advantage of working in a classical CL setup with unchanged spatial resolution but which suffers from a significantly reduced signal-to-noise ratio compared to other methods

Finally, we have introduced our experimental setup, including a beam blanker when spatial resolution is not of primary interest, and the two developed HBT setups.

Appendices

2.A Origin of pile-up effect

Pile-up effect in time-resolved measurements

The pile-up effect is the distortion of the time distribution measured in time-resolved measurements, typically resulting in an over-representation of short delays. To understand how this effect appears, it is necessary to break down what happens in such measurements.

After a pulsed excitation (laser or e-beam), a certain number of photons N will reach the detector. When the dead times of the detectors and correlators are larger ($\sim$100 ns) than the lifetime that we want to measure ($\lesssim$ 10 ns), only the arrival time of the first photon will be recorded. This will cause an artifact in the measured time distribution.

To simplify the calculations, we consider the time between two consecutive pulses very large compared to the lifetime, to be able to consider each pulse independently. Also, we consider first a fixed number N of photons reaching the detector for each pulse. Assuming that the arrival time of photons relative to the pulse can be modeled by an exponential random variable of parameter ${\tau_{eff}}^{-1}$ ($T_i \sim \mathrm{Exp}({\tau_{eff}}^{-1})$), if N photons reach the detector, the recorded time R will follow:

$$R \sim \min\{T_i, \ldots, T_N\} \tag{2.27}$$

$$\sim \mathrm{Exp}(N{\tau_{eff}}^{-1}) \tag{2.28}$$

It can be shown that equation (2.27) follows an exponential random variable with parameter $N \times {\tau_{eff}}^{-1}$ [RR98]. In other words, if N photons per pulse reach the detectors, the measured lifetime will be τ_{eff}/N.

In practice, N is not constant. Therefore, from equation (2.27), if we assume the probability that $n > 0$ photons reach the detector $P(N = n|n > 0)$, the distribution of R becomes:

$$R \sim \sum_{n=1}^{\infty} P(N = n|n > 0)\frac{n}{\tau_{eff}} \times \exp\left(-t\frac{n}{\tau_{eff}}\right) \tag{2.29}$$

Assuming here that N is a Poisson random variable with parameter λ, R can

be expressed as:

$$R \sim \frac{e^{-\lambda}}{1-e^{-\lambda}} \sum_{n=1}^{\infty} \frac{\lambda^n n}{n!\,\tau_{eff}} \exp\left(-t\frac{n}{\tau_{eff}}\right) \tag{2.30}$$
$$\sim \frac{e^{-\lambda}}{1-e^{-\lambda}} \frac{1}{\tau_{eff}} \sum_{n=1}^{\infty} \frac{(\lambda e^{-t/\tau_{eff}})^n n}{n!}$$

We recall

$$\sum_{n=1}^{\infty} \frac{x^n n}{n!} = \frac{d}{dx}\left[\sum_{n=1}^{\infty} \frac{x^n}{n!}\right] x = \frac{d}{dx}\left[\sum_{n=0}^{\infty} \frac{x^n}{n!} - 1\right] x = e^x x$$

Thus,

$$R \sim \frac{e^{-\lambda}}{1-e^{-\lambda}} \frac{\lambda}{\tau_{eff}} \exp\left(\lambda e^{-t/\tau_{eff}} - t/\tau_{eff}\right) \tag{2.31}$$

Figure 2.A.1 illustrates the distribution of R, *i.e.*, the measured time distribution for different average numbers of photons per pulse (λ) assuming that the true photon time distribution is exponential. As expected, short delays are overrepresented and long delays underrepresented, resulting in a non-exponential distribution [HS17].

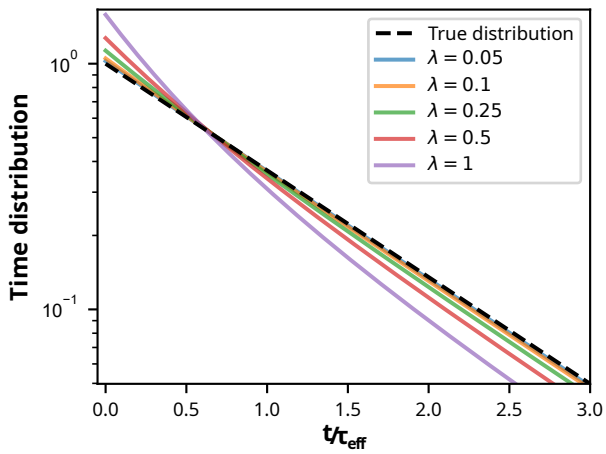

FIGURE 2.A.1: Measured time distribution assuming that on average λ photons per pulse reach the detector ($N \sim \text{Poisson}(\lambda)$) (solid lines). The true photon distribution is indicated as a dashed black line

Another useful quantity is the probability that this effect occurs given that a photon has been recorded, which can be expressed as :

$$P(N > 1|N > 0) = \frac{P(N > 1)}{P(N > 0)} \tag{2.32}$$
$$= \frac{1 - e^{-\lambda}(1+\lambda)}{1 - e^{-\lambda}} \tag{2.33}$$

Therefore, to avoid this artifact, one must limit the average number of photons

per pulse (λ) low. Experimentally, this means limiting the count rate to λf, with f the excitation frequency. By convention, it is generally recommended to limit the count rate to 5 % of the excitation frequency, giving $P(N > 1|N > 0) \approx 2.5\,\%$ [Gmb; HS17].

Pile-up effect in autocorrelated measurements

Here, we will only be interested in the frequency at which this phenomenon occurs relative to the probability that a correlation is recorded. For simplicity, we will only consider positive delays, *i.e.*, detector photons recorded after a clock photon, and that the time between two consecutive primary electrons is long enough. Hence, no cross-correlation between different bunches occurs. This probability is the probability of having at least one photon on the first channel and more than one photon on the second one given that there is at least one photon on each channel:

$$P = \frac{P(N_1 > 0)P(N_2 > 1)}{P(N_1 > 0)P(N_2 > 0)} \tag{2.34}$$

$$= \frac{P(N_2 > 1)}{P(N_2 > 0)} \tag{2.35}$$

This probability is identical to the one found for time-resolved measurements (equation (2.33)). Thus, we can expect pile-up to play an important role in autocorrelation measurements.

2.B CL mapping as a function of the entrance slit size

In CL, the choice of the entrance slit size of the spectrometer must be carefully considered. Indeed, its aperture determines the spectral resolution and the field of view. A small slit will give a better spectral resolution, but the light collection will be a problem for a large object. Conversely, a slit that is too large will not resolve any fine lines that may be present in the spectrum, but the field of view will be wider.

Figure 2.B.1 shows the CL mapping of an InGaN/GaN wire[15] with a 100 µm (a) and 1 mm (b) entrance slit. We can see that with a narrow entrance slit, the intensity rapidly decreases as a distance to the origin, where the focus was done.

[15] This kind of sample will be studied in chapter 3

With a larger slit, the collection is homogeneous on the whole wire, so we can see that the actual intensity profile is radically different.

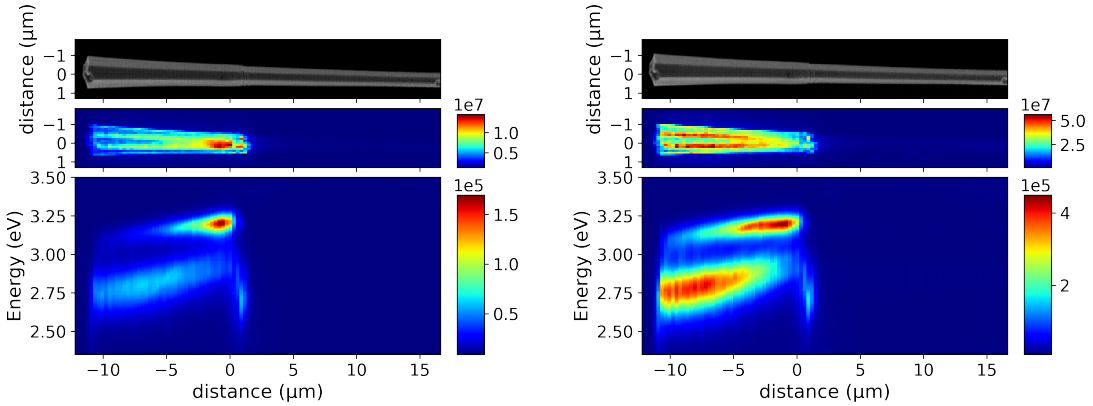

(a) 100 µm slit (b) 1 mm slit

FIGURE 2.B.1: Hyperspectral CL mapping of the same wire with two different entrance slit sizes: (a) 100 µm and (b) 1 mm. The origin of the x-axis roughly corresponds to the position where the focus was done.

2.C Estimation of the timing resolution

The full width at half maximum (FWHM) of the transit time of one detector (PMA Hybrid 06 from PicoQuant) is given in the datasheet as less than 50 ps. Therefore, if we take the worst-case scenario, assuming that each detector has a FWHM of 50 ps, the resulting timing resolution for the correlation should be $\sqrt{2} \times 50 \approx 71$ ps.

Here, we have estimated the resolution by fitting measurements done at 300 K, *i.e.*, with a short lifetime, using an exponential decay convolved with a Gaussian. Data have been fitted with several fixed FWHM (dashed lines) and without fixing the FWHM (red solid line). We can see that a 70 ps FWHM is too broad at a lower delay and declines too rapidly. On the other hand, it is not easy to distinguish between 20 and 40 ps. Therefore, the resolution should be typically better than 40 ps.

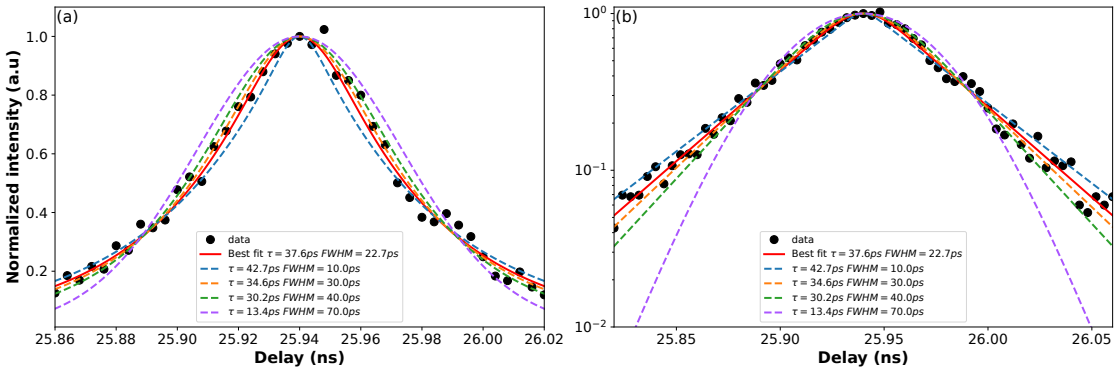

FIGURE 2.C.1: Normalized histogram obtained with the HBT setup at 300 K in linear scale (a) and in logscale (b). Data (black circles) are fitted with an exponential decay convolved with a Gaussian. Data have been fitted with several fixed FWHM (dashed lines) and without fixing the FWHM (red solid line).

References

[BF56] Eric Brannen and H. I. S. Ferguson. "The Question of Correlation between Photons in Coherent Light Rays". *Nature* 178.4531 (Sept. 1956), 481–482. DOI: 10.1038/178481a0.

[BFW58] E. Brannen, H. I. S. Ferguson, and W. Wehlau. "PHOTON CORRELATION IN COHERENT LIGHT BEAMS". *Canadian Journal of Physics* 36.7 (July 1958), 871–874. DOI: 10.1139/p58-093.

[BL99] Walter L. Borst and Lin I. Liu. "Time-autocorrelated two-photon counting technique for time-resolved fluorescence measurements". *Review of Scientific Instruments* 70.1 PART II (1999), 41–49. DOI: 10.1063/1.1149540.

[Dav+20] Aurelien David et al. "Review—The Physics of Recombinations in III-Nitride Emitters". *ECS Journal of Solid State Science and Technology* 9.1 (2020), 016021. DOI: 10.1149/2.0372001jss.

[Dav21] Aurelien David. "Long-Range Carrier Diffusion in (In,Ga) N Quantum Wells and Implications from Fundamentals to Devices". *Physical Review Applied* 15.5 (May 2021), 054015. DOI: 10.1103/PhysRevApplied.15.054015.

[Gmb] Picoquant Gmbh. *PicoHarp 300: Time-Correlated Single Photon Counting System User ' s Manual and Technical Data*. Tech. rep., pp. 1–70.

[Han19] Andreas Hangleiter. *Recombination dynamics in GaInN/GaN quantum wells*. June 2019. DOI: 10.1088/1361-6641/ab2788.

[HJG52] R. Hanbury Brown, R. C. Jennison, and M. K.Das Gupta. "Apparent angular sizes of discrete radio sources: Observations at Jodrell Bank, Manchester". *Nature* 170.4338 (Dec. 1952), 1061–1063. DOI: 10.1038/1701061a0.

[HS17] Liisa M. Hirvonen and Klaus Suhling. *Wide-field TCSPC: Methods and applications*. Jan. 2017. DOI: 10.1088/1361-6501/28/1/012003.

[HT54] R. Hanbury Brown and R.Q. Twiss. "LXXIV. A new type of interferometer for use in radio astronomy". *The London, Edinburgh, and Dublin Philosophical Magazine and Journal of Science* 45.366 (1954), 663–682. DOI: 10.1080/14786440708520475.

[HT56a] R. Hanbury Brown and R. Q. Twiss. "A test of a new type of stellar interferometer on Sirius". *Nature* 178.4541 (Nov. 1956), 1046–1048. DOI: 10.1038/1781046a0.

[HT56b] R. Hanbury Brown and R.Q. Twiss. "Correlation between Photons in two Coherent Beams of Light". *Nature* 177.4497 (Jan. 1956), 27–29. DOI: 10.1038/177027a0.

[Lan+16] Torsten Langer et al. "Radiative and nonradiative recombination mechanisms in nonpolar and semipolar GaInN/GaN quantum wells". *Physica Status Solidi (B) Basic Research* 253.1 (2016), 133–139. DOI: 10.1002/pssb.201552353.

[Lef+04] P. Lefebvre et al. "Observation and modeling of the time-dependent descreening of internal electric field in a wurtzite GaN/Al0.15Ga0.85N quantum well after high photoexcitation". *Physical Review B - Condensed Matter and Materials Physics* 69.3 (2004). DOI: 10.1103/PhysRevB.69.035307.

[Liu+16a] W. Liu et al. "Carrier-density-dependent recombination dynamics of excitons and electron-hole plasma in m -plane InGaN/GaN quantum wells". *Physical Review B* 94.19 (2016). DOI: 10.1103/PhysRevB.94.195411.

[Liu+16b] W. Liu et al. "Exciton dynamics at a single dislocation in GaN probed by picosecond time-resolved cathodoluminescence". *Applied Physics Letters* 109.4 (July 2016), 042101. DOI: 10.1063/1.4959832.

[Meu+15] S. Meuret et al. "Photon bunching in cathodoluminescence". *Physical Review Letters* 114.19 (May 2015). DOI: 10.1103/PhysRevLett.114.197401.

[Meu+16] Sophie Meuret et al. "Lifetime Measurements Well below the Optical Diffraction Limit". *ACS Photonics* 3.7 (July 2016), 1157–1163. DOI: 10.1021/acsphotonics.6b00212.

[Meu+17] Sophie Meuret et al. "Photon bunching reveals single-electron cathodoluminescence excitation efficiency in InGaN quantum wells". *Physical Review B* 96.3 (July 2017), 035308. DOI: 10.1103/PhysRevB.96.035308.

[Meu+18] Sophie Meuret et al. "Nanoscale Relative Emission Efficiency Mapping Using Cathodoluminescence g(2) Imaging". *Nano Letters* 18.4 (Apr. 2018), 2288–2293. DOI: 10.1021/acs.nanolett.7b04891.

[Meu+19] S. Meuret et al. "Complementary cathodoluminescence lifetime imaging configurations in a scanning electron microscope". *Ultramicroscopy* 197 (Feb. 2019), 28–38. DOI: 10.1016/j.ultramic.2018.11.006.

[Meu16] Sophie Meuret. "Expérience de Hanbury Brown et Twiss dans un microscope électronique à transmission à balayage : sa physique et ses applications". PhD thesis. UNIVERSITE PARIS-SACLAY, 2016.

[Mil52] B. Y. Mills. "Apparent angular sizes of discrete radio sources: Observations at Sydney". *Nature* 170.4338 (Dec. 1952), 1063–1064. DOI: 10.1038/1701063a0.

[Mül73] Jörg W. Müller. "Dead-time problems". *Nuclear Instruments and Methods* 112.1-2 (Sept. 1973), 47–57. DOI: 10.1016/0029-554X(73)90773-8.

[Pop+00] M. Pophristic et al. "Time-resolved photoluminescence measurements of InGaN light-emitting diodes". *Materials Science Forum* 338.24 (May 2000), 1623–1626. DOI: 10.4028/www.scientific.net/msf.338-342.1623.

[Pur56] E. M. Purcell. "The Question of Correlation between Photons in Coherent Light Rays". *Nature* 178.4548 (Dec. 1956), 1449–1450. DOI: 10.1038/1781449a0.

[RP57] G. A. Rebka and R. V. Pound. "Time-correlated photons". *Nature* 180.4594 (Nov. 1957), 1035–1036. DOI: 10.1038/1801035a0.

[RR98] RL and Sheldon M. Ross. *Introduction to Probability Models*. Vol. 93. 441. 1998, p. 411. DOI: 10.2307/2669658.

[Sha+17] M Shahmohammadi et al. "Enhancement of Auger recombination induced by carrier localization in InGaN/GaN quantum wells". *Physical Review B* 95.12 (2017), 125314. DOI: 10.1103/PhysRevB.95.125314.

[Sil57] Richard M. Sillitto. "Correlation between events in photon detectors". *Nature* 179.4570 (June 1957), 1127–1128. DOI: 10.1038/1791127a0.

[Smi52] F. G. Smith. "Apparent angular sizes of discrete radio sources: Observations at Cambridge". *Nature* 170.4338 (Dec. 1952), 1065. DOI: 10.1038/1701065a0.

[Sol+21] Magdalena Sola-Garcia et al. "Photon Statistics of Incoherent Cathodoluminescence with Continuous and Pulsed Electron Beams". *ACS Photonics* (Dec. 2021). DOI: 10.1021/acsphotonics.0c01939.

[Tiz+13] Luiz Henrique Galvão Tizei et al. "Spatially and spectrally resolved cathodoluminescence with fast electrons: A tool for background subtraction in luminescence intensity second-order correlation measurements applied to subwavelength inhomogeneous diamond nanocrystals". *Physica Status Solidi (A) Applications and Materials Science* 210.10 (2013), 2060–2065. DOI: 10.1002/pssa.201300044.

[Zha+20] Lixin Zhang et al. "Beam displacement and blur caused by fast electron beam deflection". *Ultramicroscopy* 211.January (2020), 112925. DOI: 10.1016/j.ultramic.2019.112925.

Chapter 3

Underlayers for Efficient III-Nitride Blue LEDs

3.1 Introduction . . . 62
3.2 *c*-plane QW probed by temperature-dependent TRCL . . . 63
3.2.1 Studied samples . . . 63
3.2.2 Temperature-dependent time-resolved cathodoluminescence measurements . . . 65
3.2.3 Conclusion . . . 67
3.3 Point Defects and Dislocations in QWs grown on Silicon . . . 67
3.3.1 Motivations . . . 67
3.3.2 Description of the samples . . . 68
3.3.3 Photoluminescence analysis . . . 69
3.3.4 CL and TRCL analysis . . . 70
3.3.5 Conclusion . . . 71
3.4 Underlayers in core-shell InGaN/GaN microwires . . . 72
3.4.1 Advantage of core-shell microwires LEDs . . . 72
3.4.2 Growth and structure of core-shell microwires . . . 73
3.4.3 Optical characterization . . . 74
3.4.4 Time-resolved CL measurements . . . 77
3.4.5 Role of the GaN spacer: Structural characterization . . . 80
3.4.6 Conclusion . . . 82
3.5 InGaN underlayers in *m*-plane QWs . . . 82
3.5.1 Samples description . . . 83
3.5.2 Temperature-dependent cathodoluminescence analysis . . . 84
3.5.3 Conclusion . . . 86
3.6 Conclusion and perspectives . . . 87
Appendices . . . 89

In this chapter, we will study the effects of underlayers (ULs) on the efficiency of InGaN/GaN QW. In particular, the study will focus on the role of indium (In) containing UL for the suppression of point defects created during the high-temperature growth of GaN. First, we will present a review of the literature on this subject. Then we will look at various QW configurations such as *c*-plane on sapphire or silicon, *m*-plane on core-shell GaN microwire, and planar *m*-plane on GaN. Finally, we will discuss the potential formation mechanisms of these defects.

3.1 Introduction

Nowadays, III-nitride blue LEDs are widely commercialized for solid-state lighting and can have an IQE well above 80% [Dav+20]. To achieve such performance, it is well known that an InGaN UL prior to the growth of the QWs greatly increases the efficiency of the active region [Dav+20]. These ULs can be either a continuous layer or a superlattice (SL). Furthermore, this can also be extended for near-UV InGaN-based LED, particularly thanks to InAlN which can be lattice-matched with GaN at a high In concentration (∼18 %) and a bandgap of 4.6 eV, thus being transparent even in the UV [Hal+19].

Although this empirical practice has been known for a long time, the underlying physics has only been recently studied in detail and is still under debate. Several mechanisms have been proposed to explain the improvement of LED efficiency[1]. Li et al. proposed the screening of the internal field due to partial strain relaxation [Li+13]. Some studies reported a reduction of the dislocations density [Tör+08], or the formation of V-shaped pits (V-pits) at the dislocation surface termination that would create a potential barrier preventing carriers from reaching them [Che+98; Han+05]. However, by performing studies on low dislocation density *c*-plane free-standing GaN substrate and observing a comparable enhancement of the IQE, the role of the dislocations and strain has been ruled out [Hal+17]. Other studies have shown that the growth of InGaN UL considerably reduces the density of defects in the QW located close to the mid-gap [Arm+15; Piv+21; Pol+20]. This point has been investigated in detail recently. In particular, Haller et al. have shown that defects are generated during the high-temperature (typically $T > 900\,°\mathrm{C}$) growth of GaN and remain on the GaN surface even after low-temperature regrowth [Hal+18]. However, these defects are incorporated into layers proportionally to the indium content to form non-radiative centers. Thus the role of an In-containing UL is to trap these defects before the growth of InGaN QWs. A schematic of the proposed mechanism is shown in figure 3.1.

[1] A more extensive review of the literature can be found in [Hal+17]

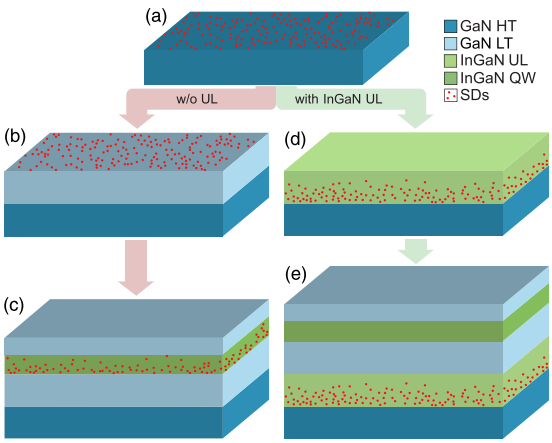

FIGURE 3.1: (a) Surface defects (SDs) are formed during the growth of high-temperature GaN. (b) These defects strongly segregate even during low-temperature growth of GaN. (c) SDs react with In atoms and are eventually trapped in the InGaN QW, creating non-radiative recombination centers. (d) InGaN underlayer in which SDs are trapped due to their interaction with In atoms. (e) After the InGaN underlayer, the GaN surface is free of defects leading to high-efficiency InGaN/GaN QW. Adapted from [Hal+19]

To this day, the origin of these defects is still under debate. Secondary ion mass spectroscopy (SIMS) studies have revealed no evident correlations between the decrease in IQE and the presence of any element among Li, C, O, Na, Mg, P, K, Ca, Cr, Fe, Ni, Zn, and Mo [Hal+18; Che+21]. More recently, based on first principle calculations, Chen et al. have proposed that these defects are most likely nitrogen vacancies [Che+21].

3.2 *c*-plane QW probed by temperature-dependent TRCL

This section aims to reproduce and study the effect of an InGaN UL on a standard structure composed of a single InGaN QW grown on *c*-plane sapphire substrate through temperature-dependent TRCL measurements.

3.2.1 Studied samples

Two similar samples were grown on *c*-plane sapphire substrates. Figure 3.2 shows schematics of the samples' structures. Sample A (see figure 3.2 (a)) consists of a large (1 µm) GaN buffer grown at high temperature (1000 °C) followed by 20 nm of GaN grown at 800 °C, 5 nm of GaN at 750 °C, a single InGaN quantum well of about 2 nm with a target indium composition of 18%. Finally, the structure

is capped with 5 nm of GaN grown at 800 °C. The second sample (sample B) is identical, except that a 50 nm InGaN UL with a target composition of 4% was grown after the GaN buffer to incorporate the surface defects generated during buffer growth.

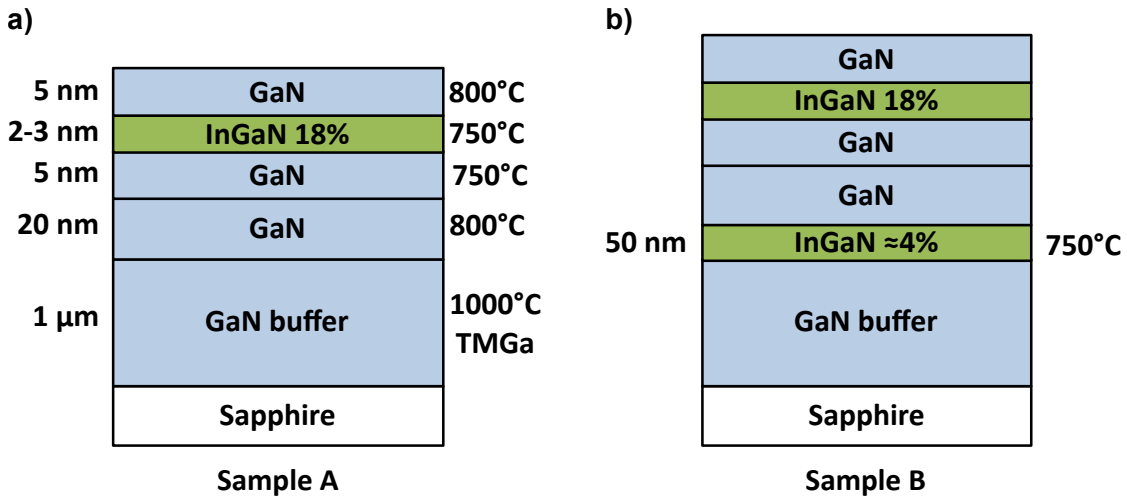

FIGURE 3.2: Schematic of the samples structures without (a) and with (b) an InGaN underlayer.

Figure 3.3 shows a quick comparison of the PL of the two samples at room temperature. The excitation was done with a frequency-doubled argon laser ($\lambda = 244\,\mathrm{nm}$) with an estimated power density of $\sim 1\,\mathrm{W\,cm^{-2}}$. We can see that the intensity of the sample without an UL is much lower, by almost two orders of magnitude, as observed by Haller et al. [Hal+17].

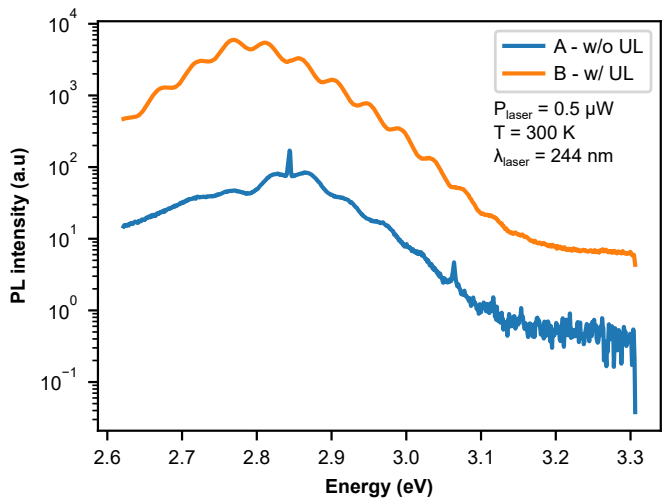

FIGURE 3.3: Room-temperature photoluminescence spectra of the two samples acquired with a 244 nm laser. The power density is estimated to be around $1\,\mathrm{W\,cm^{-2}}$.

3.2.2 Temperature-dependent time-resolved cathodoluminescence measurements

In order to have a clearer idea of the importance of radiative and non-radiative recombinations, we propose to study the effective lifetime as a function of temperature. The TRCL setup is the one described earlier with a fast PMT (PMA Hybrid 06 from PicoQuant) mounted at the output of the spectrometer.

By fitting the luminescence decay with a monoexponential decay, we can obtain the effective lifetime τ_{eff}:

$$\begin{cases} I(t) = I_0 \exp\left(-\dfrac{t}{\tau_{eff}}\right) \\ \tau_{eff}^{-1} = \tau_r^{-1} + \tau_{nr}^{-1} \end{cases} \tag{3.1}$$

With τ_r the radiative and τ_{nr} the non-radiative lifetime.

An interesting thing to note is that τ_r and τ_{nr} evolve differently with temperature. The radiative contribution can also be separated into two parts. One is constant with temperature and depends on the energy and density of localized states in the sample. The other part, the 2D radiative lifetime, increases linearly with temperature.[2] Concerning the non-radiative lifetime, τ_{nr} decreases with temperature and generally exhibits a thermal activation behavior[3]. More details can be found in [Sha+17; Ros+14; Han+18]. Thus, as illustrated in figure 3.4, the effective lifetime profile can take various shapes depending on the primary mechanism at each temperature.

Figure 3.4 (a) and (b) show the lifetime profiles of efficient QWs. The two structures are similar, except that the localization is more important in figure 3.4 (b) due to an increased In content in the QW. As a consequence, the lifetime stays constant, almost up to room temperature. On the contrary, with lower localization and low non-radiative recombination rate, the effective lifetime in figure 3.4 (a) is constant till 100 K and then rapidly increases to reach about 3 ns at room temperature. The third QW presented in figure 3.4 (c) is radically different; however, it has a similar radiative lifetime. We can see that the effective lifetime follows the radiative lifetime at low temperatures, indicating less localization. However, due to the thermal activation of non-radiative processes, the effective lifetime rapidly decreases, forming a bell-shaped curve. One last possibility, not illustrated here, is that non-radiative recombinations dominate even at low temperatures. The

[2] More generally the radiative lifetime depends on the dimension d of the sample $\tau_r \propto T^{d/2}$ [RV02]. Localized states are just 0D states, hence their lifetime does not depend on the temperature.

[3] $\tau_{nr} \propto \exp\left(\dfrac{-E_a}{k_B T}\right)$

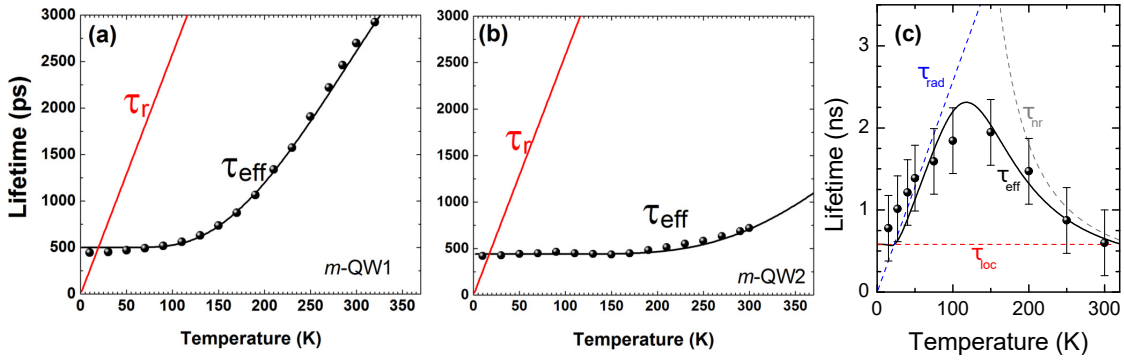

FIGURE 3.4: Effective lifetime as a function of temperature for different samples with similar radiative lifetime. The difference between (a) and (b) is the higher fraction of localized carriers in (b), resulting in a constant lifetime almost up to room temperature. The structure in (b) is different but still has a comparable radiative lifetime. The main difference lies in the non-radiative recombinations, which are predominant here and lead to a decrease of the effective lifetime. (a) and (b) are adapted from [Sha+17] and (c) from [Ros+14].

resulting effective lifetime is then decreasing with temperature.

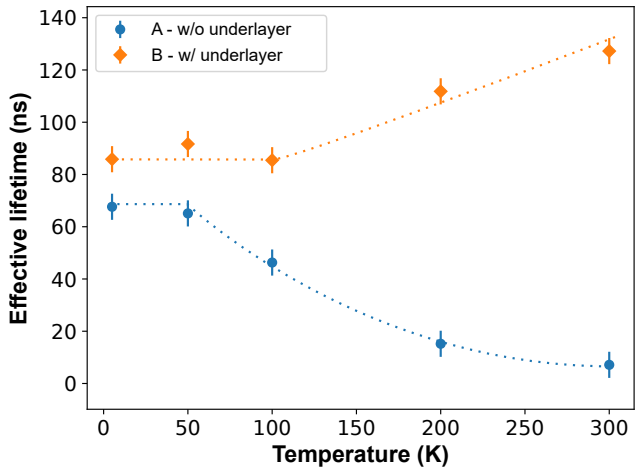

FIGURE 3.5: Effective lifetime as a function of temperature for sample A and B (without and with an underlayer). Dotted lines represent guides to the eye.

Figure 3.5 shows the effective lifetime of the samples with and without UL as a function of temperature. The TRCL measurements were done at 5 kV, with an e-beam current of about 50 pA, a repetition rate of 400 kHz and a duty cycle of 50%. As expected, the lifetime profile is radically different between the two samples. We can see that the effective lifetime increases from 86 ns at 5 K to 127 ns at room temperature for the sample with a UL, sign that radiative recombinations are preponderant. On the contrary, without UL, the lifetime decreases from 68 ns to ∼7 ns at room temperature. This significant decrease is the consequence of

thermally activated non-radiative processes.

These results are in line with a recent study where Weatherley et al. demonstrated a reduction in point defect density in thin QWs as a function of the number of periods of the InAlN (2.1 nm) /GaN (1.75 nm) SL [Wea+21]. An interesting result is the evolution of the effective photoluminescence lifetime as a function of temperature for different numbers of periods. The lifetime changes from a state dominated by non-radiative recombinations up to 8 periods to a behavior following the radiative lifetime with 16 periods or more.

Note that if we assume identical radiative lifetime and localization, we can directly compare samples by their effective lifetime at room temperature, as done in [Hal+18].

3.2.3 Conclusion

In conclusion, as expected, the growth of an InGaN UL before the active region drastically improves the QW IQE. It results in drastically different effective lifetime profiles as a function of temperature. Without UL, the effective lifetime experiences a sharp decrease due to the activation of non-radiative defects, while in the presence of a UL, the lifetime increases with the temperature.

3.3 Point Defects and Dislocations in QWs grown on Silicon

After the effect of UL has been reported on planar structures grown on sapphire and free-standing GaN, this work aims to study the effect of InGaN UL in the case of planar samples grown on silicon. In particular, it allows putting into perspective the relative impact of dislocations and point defects as non-radiative recombination centers. This study was conducted in collaboration with the EPFL, in particular with Pierre Lottigier, PhD student, who was in charge of the growth of the samples and the PL analysis.

3.3.1 Motivations

Extending the growth of III-nitride optoelectronic devices on silicon substrates is a desirable asset for expanding the applications offered by the silicon-based photonics platform. However, due to the large difference in lattice parameter and thermal expansion coefficient between Si (111) and GaN, a very high dislocation density ($>10^{10}\,\mathrm{cm}^{-2}$) is generated at the interface between the two materials. Although III-nitrides are relatively tolerant to dislocations compared to other III-V

semiconductors, a dislocation density higher than $10^8\,\mathrm{cm}^{-2}$ dramatically reduces the efficiency of QWs [KM03]. Therefore thick GaN buffer ($\gtrsim 1\,\mu\mathrm{m}$) or AlN-GaN SL are usually engineered to reduce the dislocation density in the 10^8–$10^9\,\mathrm{cm}^{-2}$ range. On the other hand, we have seen that point defects introduced during the high-temperature growth of GaN almost suppress the luminescence of *c*-plane QWs. Thus, we propose to study the relative impact of dislocations and point defects in the case of samples grown on Si (111).

3.3.2 Description of the samples

The growth of the samples starts with a 50 nm-thick AlN layer followed by a 150 nm or a 600 nm-thick GaN buffer grown at high temperature. The active region consists of a single 3 monolayer-thick $In_{0.17}Ga_{0.83}N$ QW sandwiched between two GaN layers with a thickness of 25 nm and 10 nm, respectively. The growth is terminated by a 5 nm-thick $Al_{0.05}Ga_{0.95}N$ cap to avoid surface recombination. Samples U_{150} and U_{600} have a UL grown between the GaN buffer and the active region that consists of a lattice-matched 16-period $In_{0.18}Al_{0.82}N$(2.1 nm)/GaN(1.75 nm) SL, which was shown to be an efficient UL [Hal+19; Wea+21]. All the layers were grown at 750 °C, except for the AlN layer and the GaN buffer that were grown at 970 °C. Schematics of the samples are shown in figure 3.6.

(a) Samples U and X (*i.e.*, with and without UL)

(b) Sample V_{600}, similar to sample U_{600} except that the UL has been replaced by a 50 nm-thick GaN layer

FIGURE 3.6: Schematic of the investigated samples.

We estimated a lower bound on the density of threading dislocations as V-pits are formed at their termination [Wu+98]. Thus the dislocation density is estimated to be around $5.5\times10^{10}\,\mathrm{cm}^{-2}$ for the samples with a 150 nm GaN buffer and close to $3.5\times10^{10}\,\mathrm{cm}^{-2}$ when the buffer is 600 nm thick. However, we observed a difference in V-pits diameters depending on the presence or absence of the UL. Typically,

with a UL (U samples), their diameter is close to 25 nm against 15 without (X samples). In order to differentiate any effect of V-pit size [Han+05], a new sample, named V_{600}, similar to U_{600}, is grown. To obtain comparable V-pit diameters, the UL is replaced by 50 nm of GaN grown at 750 °C.

3.3.3 Photoluminescence analysis

First, we performed a PL analysis. However, it is important to note that the intensity of the different samples cannot be compared directly. Indeed, here the thickness of the GaN is comparable to the emission wavelength. Therefore the samples are subject to microcavity effects, drastically changing the LEE.

After verifying that all samples emit at the same energy (∼3 eV at room-temperature), we performed power-dependent PL measurements. From these measurements, we extracted the relative IQE of the different samples, defined as the ratio of the integrated PL intensity over the laser irradiance as a function of the laser irradiance, see figure 3.7. Note that the lower the irradiance at which the IQE reaches its maximum value, the higher the absolute IQE [Dav+20]. In figure 3.7 (a), we can observe a general trend: the profiles are mainly determined by the presence of the UL. Indeed, we can see that whatever the thickness of the GaN buffer, the samples without a UL (samples X_{150} and X_{600}) display a similar profile, with a maximum close to 10^4 W/cm^2. Similarly, samples U_{150} and U_{600} have their maximum considerably shifted toward lower irradiance, in the 10^1–10^2 W/cm^2 range, indicating a higher IQE. At this point, we cannot conclude on the effect of the UL. As mentioned earlier, the presence of the UL also leads to larger V-pits compared to samples without UL. Thus, one could ascribe the higher

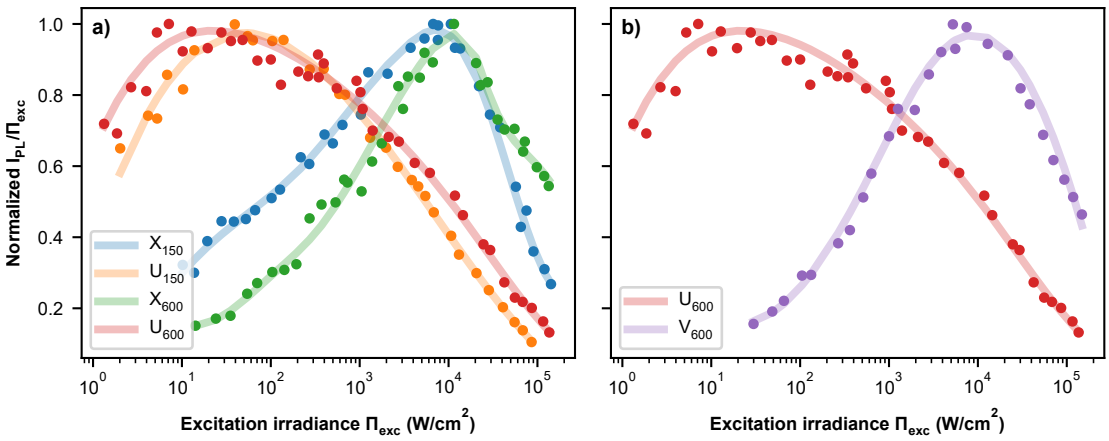

FIGURE 3.7: Relative IQE, defined as the normalized ratio of the integrated PL intensity over the excitation irradiance Π_{exc}, as a function of Π_{exc}. The solid lines are guides for the eyes.

relative IQE to a larger V-pit diameter [Oka+15].

To separate the effect of the UL and the diameter of the V-pits on the efficiency of the samples, we compare sample U_{600} with sample V_{600}, *i.e.*, without UL, which was grown to obtain similar V-pits. Although both samples have a comparable density of V-pits of equal diameter, their relative IQE profiles are radically different (see figure 3.7 (b)). The maximum IQE of V_{600} is reached at about 10^4 W/cm^2, as the samples without UL and smaller V-pits. Consequently, we can conclude that the larger V-pits cannot explain the improved efficiency and that the introduction of a UL plays a decisive role in the efficiency of these samples, even in the presence of an important dislocation density.

3.3.4 CL and TRCL analysis

In addition to the PL measurements, we performed a temperature-dependent TRCL analysis to measure the evolution of the effective lifetime, as done previously. These measurements were done in our CL setup, here with a 5 kV acceleration voltage, a e-beam current of 40 pA, a repetition rate of 10 MHz and a pulse width of 10 ns. Also, the measurements have been average over $10 \times 10\,\mu m^2$ area in order to be less sensitive to local fluctuation of the density of dislocations and to reduce the e-beam exposure.

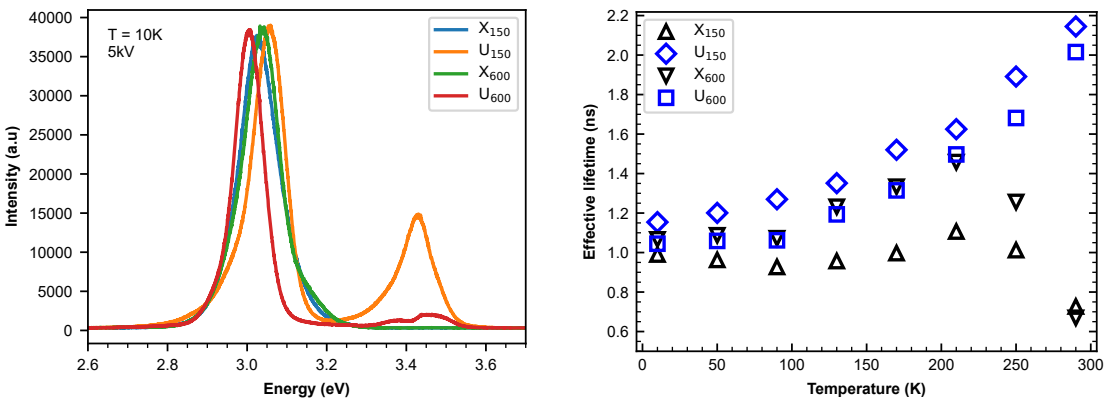

(a) (b)

FIGURE 3.8: (a) 10 K-CL spectra. (b) Effective lifetime as a function of temperature

First, figure 3.8 (a) shows CL spectra acquired at $T = 10$ K for each samples. We can see that, for the studied areas, all samples emit between 3.00 and 3.06 eV. Note that the emission energy was not homogeneous on the whole 2-inch wafer, which could account for the observed spreading. We highlight the presence of a contribution at about 3.45 eV only for the samples with SL. Note that this is not the near-band-edge luminescence of InAlN since it has a bandgap of about

4.6 eV. However, it could be attributed to the luminescence of the SL, acting as GaN/InAlN QWs [Lia+16].

Figure 3.8 (b) shows the effective lifetime as a function of the temperature for the different samples extracted with a monoexponential decay. First, we can note that all lifetimes are close to 1 ns at $T = 10\,\mathrm{K}$. Then, the lifetime profile seems to be governed mainly by the presence or not of a UL. In particular, in the presence of a UL, the lifetime increases monotonically regardless of the buffer thickness. On the other hand, without UL, the lifetime drastically decreases above 210 K, characteristic of the strong non-radiative contribution of the point defects.

These results are in line with the power-dependent PL measurements presented previously.

3.3.5 Conclusion

Despite a high density of dislocations, point defects still play an important role. If we want to be more quantitative and compare their relative impact, it is necessary to estimate the surface density of these point defects.

According to Haller et al., the density of defects incorporated in an In-containing layer can be well modeled by [Hal+17]:

$$[SD]_{Layer} = \theta_0(1 - (R_{GaN} - xp)^N) \times \frac{1}{L} \tag{3.2}$$

With:

θ_0 the defects density created at the surface of the GaN buffer, depending essentially on the growth temperature [Che+21]

R_{GaN} the segregation coefficient of the point defects in GaN (empirically $R_{GaN} = 0.9991$).

x the In content in the layer

p the interaction efficiency between In atoms and the defects (empirically $p = 0.7$)

N the thickness of the layer in number of monolayers

L the thickness of the layer

According to this model, the defect density depends mainly on the growth temperature of the buffer layer, the In content, and the thickness of the layer. Here, the samples have similar growth temperature, thickness, and an In content close to the samples studied by Weatherley et al. [Wea+21]. In their study, they estimated the point defect density to be around $10^{16}\,\mathrm{cm}^{-3}$ for 3 monolayers-thick $In_{0.15}GaN_{0.85}N$ SQW. Hence, the defect density should be similar, leading to a surface defect density of roughly $10^{16} \times 0.26 \times 10^{-7} \times 3 \approx 8 \times 10^{8}\,\mathrm{cm}^{-2}$.

Therefore, according to this estimation, point defects continue to play an essential role, although their density is 1 to 2 orders of magnitude lower than that of dislocations. Thus, while the role of dislocations as non-radiative centers is well established and cannot be neglected, it appears to be less critical than that of point defects.

3.4 Underlayers in core-shell InGaN/GaN microwires

After showing that ULs were effective for various *c*-plane structures, we will examine the influence of such ULs on the efficiency of core-shell *m*-plane InGaN/GaN single quantum wells (SQWs) grown on the sidewalls of GaN microwires. This study was performed as part of Akanksha Kapoor's thesis[4]. The interested reader can find additional details about growth conditions and, more generally, about InGaN/GaN core-shell microwires in her thesis. Before diving into the study of the influence of InGaN and GaN ULs on the efficiency of core-shell microwire LEDs, let us first discuss the attractiveness of such LEDs.

3.4.1 Advantage of core-shell microwires LEDs

We here briefly present some advantages of *m*-plane core-shell InGaN/GaN microwires LEDs over standard *c*-plane planar LEDs. Among these we can note :

A large choice of substrates GaN wires can be grown on various substrates, such as sapphire, silicon, and graphene, regardless of the lattice mismatch.

A reduced dislocation density In this geometry, dislocations created at the interface with the substrates bend toward the sidewalls, thus resulting in a low dislocation density upper part [KI15].

A higher emitting surface Because of the geometry, the emitting surface, *i.e.*, *m*-planes, is higher for an equivalent substrate area.

Non-polar QWs Here, in the case of *m*-plane core-shell QWs, the absence of QCSE allows for higher modulation speeds that can be useful for visible light communication applications or for chip-to-chip communications [Pez+22].

[4] Akanksha Kapoor. "Core-shell InGaN / GaN wire for Flexible LEDs". PhD thesis. Université Grenoble Alpes, 2020.

Size-independent IQE In addition, GaN microwires are a promising candidate for making LEDs with size-independent IQE[5]. This feature is particularly interesting for the realization of microdisplays and combined with the ability to grow the wires on silicon, is the main strength of Aledia[6], which develops and manufactures a microLED display technology based on GaN nanowires on silicon.

Flexible LEDs Finally, the possibility of realizing flexible LEDs [Dai+15; Kap20] by peeling the wires from their growth substrate and encapsulating them in a polymer is also an attractive feature and could be used for flexible display applications or in optogenetic research.

3.4.2 Growth and structure of core-shell microwires

Here, we introduce the growth conditions of the studied samples. Again, for further details the interested reader may refer to [Kap20, chapter 2], which is entirely dedicated to the growth of InGaN/GaN core-shell wires by metal-organic vapor phase epitaxy.

Self-assembled GaN wires are grown on nitridated c-plane sapphire substrates along the $\bar{c}$-direction (*i.e.*, N-polar) by catalyst-free metal-organic vapor phase epitaxy. The growth starts with the deposition of a thin SiN_x film on the substrate. This film acts as a partial mask for the growth. The wire geometry is favored by a high silane flux ($\sim$200 nmol min^{-1}), a low V/III ratio ($\sim$50), a high growth temperature (1040 °C), and a high pressure (800 mbar). The high silane flux injection for 300 s results in an 18 µm heavily doped GaN wire ([Si]$\sim 10^{20}$ cm^{-3}), here named n^{++}-GaN. Then, the silane flux is switched off, and the GaN wire continues to grow for another 300 s resulting in an unintentionally doped part (but with strong residual doping, in the order of 10^{18} cm^{-3}), named n-GaN. This part is approximately 12 µm long. In the following, three different samples based on this wire geometry are studied (see figure 3.9).

The first sample consists of an InGaN SQW grown directly around the core, followed by the growth of a GaN barrier (see sample #1, figure 3.9 (a)). Note that the m-plane SQW grows only around the unintentionally doped part of the wire because of the presence of a SiN_x passivation layer on the n^{++} part formed under the high silane flux [Eym+12]. The second sample is similar to the first one, except that a GaN spacer is inserted before the growth of the SQW (see figure 3.9 (b)). Finally, the third sample is based on the second one. An InGaN

[5]Etched planar LEDs suffer from surface recombination at the etched sidewalls and therefore experience a severe IQE drop with decreasing size. This will be the main topic of chapter 4.

[6]aledia.com

UL with a targeted indium composition of about 3-5% and an estimated thickness of 150 nm is grown after the GaN spacer. Then, a 25 nm-thick GaN layer is grown, followed by the InGaN/GaN SQW.

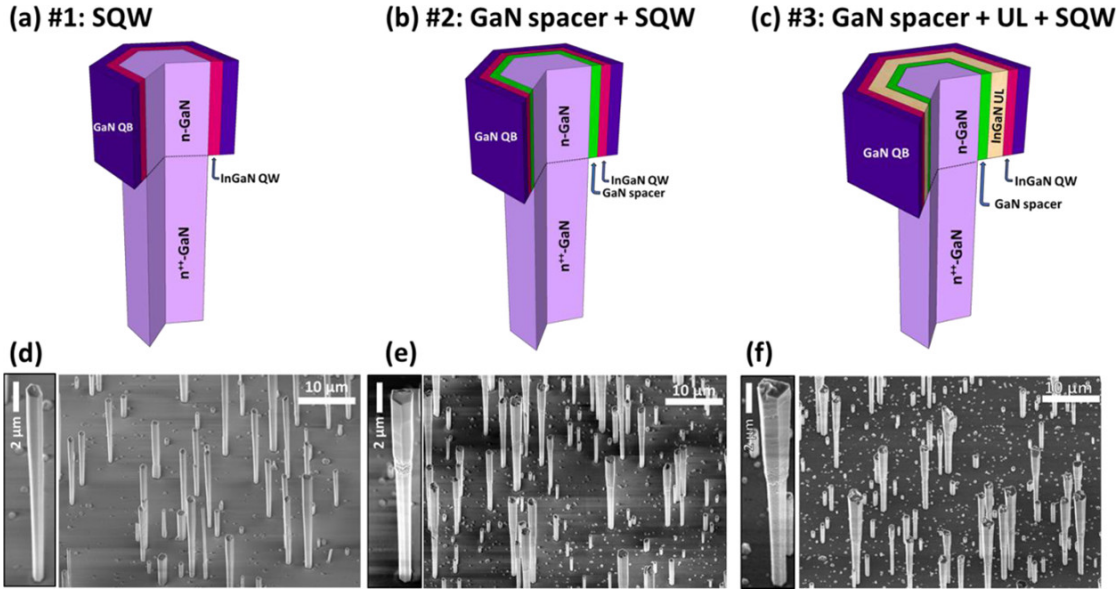

FIGURE 3.9: Schematics of the three core-shell heterostructures grown on $\bar{c}$-oriented GaN wires: (a) #1 InGaN single quantum well (SQW), (b) #2 with the addition of a GaN spacer prior to SQW, (c) #3 with the adding of an InGaN underlayer (UL) between the GaN spacer and the SQW. 30°-tilted secondary-electron images of as-grown wires: (d), (e) and (f) correspond to (a), (b) and (c) heterostructures respectively along with enlarged views on single wires. [Kap20]

Figure 3.9 (d–f) shows 30°-tilted secondary electron images of the three samples. The core-shell geometry located in the upper part of wires is visible for all samples with wires having diameter in the 0.7–2 µm range and length in the 25–30 µm range. The transition between the lower part and the core-shell region is also distinguishable by the presence of roughness on the sidewalls, indicating the end of the passivation layer.

3.4.3 Optical characterization

To measure the influence of UL and spacer on the SQW emission, the room temperature optical properties of the samples were studied. First, PL measurements were performed by Akanksha Kapoor with a frequency-doubled argon laser ($\lambda = 244$ nm) to excite the as-grown wires with a power density of 21 W cm^{-2}. The spectra were acquired with a CCD camera mounted on a spectrometer equipped with a 600 grooves/mm grating. The CL measurements were performed with a 5 kV acceleration voltage and a probe current of about 1 nA. We recall here that

in CL, the aperture of the spectrometer entrance slit is crucial as it determines the spectral resolution and the field of view. In this type of sample, as no fine emission lines are present, the entrance slit is set to 1 mm, which allows uniform light collection along the length of the wire (see appendix 2.B for CL mappings with different slit aperture).

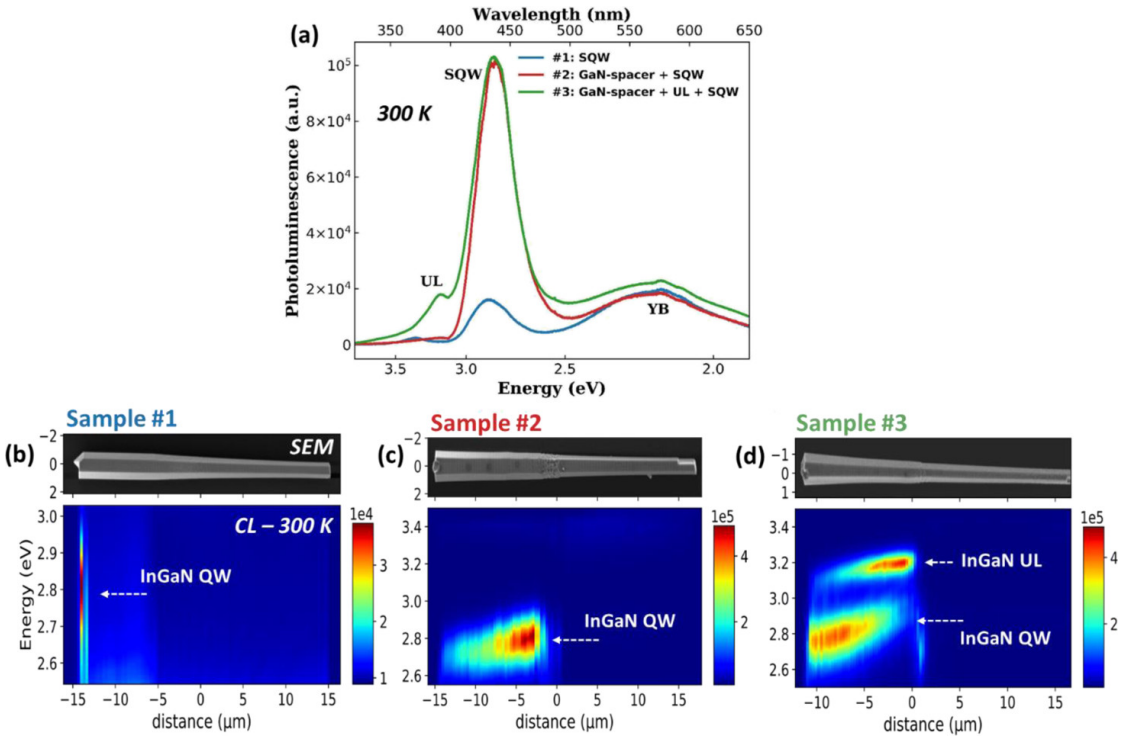

FIGURE 3.10: Room-temperature optical measurements: (a) PL spectra by exciting the samples at 244 nm for the three as-grown wires heterostructures, (b–d) CL spectra mapping of the emission with the SE image view of the measured wires for sample #1, #2 and #3 respectively. Adapted from [Kap+20]

Figure 3.10 (a) shows the PL spectra of the three samples acquired under the same experimental conditions. Figure 3.10 (b–d) show secondary electron images of a wire of each sample with their corresponding CL spectra mapping.

For all samples, we can see the InGaN QW emission close to 440 nm in the PL spectra. Despite a comparable wire density and identical experimental conditions, the QW emission of sample #1 is much weaker than that of the other two samples. From CL spectra mapping, we observed no emission on the *m*-plane sidewalls (see figure 3.10 (b)). Measurements on other wires of the same sample confirmed that the SQW emission is negligible on the *m*-plane and only the weak emission of the top facet can be observed. By performing CL mapping with a better resolution, we can attribute this emission to *c*-plane facets or semipolar facets present at the junction between *c*-plane and *m*-plane surfaces (see figure 3.11). Thus we can conclude that the emission seen in PL originates from the top facet, as the

measurements were performed on as-grown wires, *i.e.*, laser aligned with the wires.

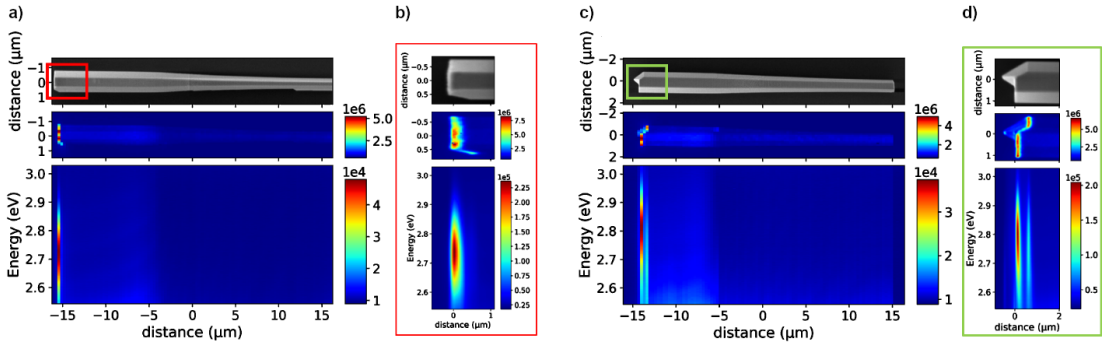

FIGURE 3.11: CL spectra mapping for sample #1 (a,c) with an enlarged view on the right side (b,d). The first wire (a-b) has a relatively flat top probably related to single N-polar phase, whereas pyramidal growth related to a mixed polarity is visible in (c-d)

CL mappings of samples #2 and #3, *i.e.,* containing a GaN spacer without and with an InGaN UL, clearly show an intense QW emission from the *m*-plane sidewalls (see figure 3.10 (c) and (d)). This emission shifts to lower energy from the bottom to the top of the wires, as it is usually observed for similar structures [Sha+16; Liu+18]. The origin of this shift could be a change in the indium content but more probably a change in the thickness of the QW. In particular, as observed in secondary electron images (c) and (d), there is typically an increase in shell thickness on top of the wires suggesting an increase in the QW thickness. Also, we can see the UL emission at 3.2 eV in figure 3.10 (d), confirming its presence on the entire sidewall. According to its emission energy, we can estimate the indium content to be around 5%. Additionally, we note a decreased UL intensity towards the top of the wire accompanied by an increase in the QW intensity. This can be explained by the increased shell thickness, which changes the excitation distribution between the UL and the QW. At the beginning of the core-shell region, more e-h pairs are generated in the GaN core and in the UL. At the wire top, the increased thickness limits the carrier generation into the GaN core and UL favoring the emission of the SQW. Similarly, the intensity ratio between UL and SQW at a given point changes with the acceleration voltage since the latter controls the e-beam excitation depth. A brief study of the influence of the acceleration voltage on the CL spectra is presented in appendix 3.A.

In addition to the QW emission, all samples presented a broad yellow band centered at ∼575 nm, which is quite common in GaN samples [RM05; Koe+10]. In this type of sample, this emission comes from the unintentionally doped part of the wire (here named *n*-GaN) [Koe+10; Kap+18].

According to these results, the GaN spacer is essential for obtaining lumines-

cence on m-plane sidewalls and the UL has no significant effect. This could suggest that the thickness of the UL is not optimal. Therefore a new series of samples based on sample #3 but with different UL thicknesses has been grown. Figure 3.12 shows the PL spectra of these different samples. Again, under the same conditions, no significant improvement was observed. Although direct comparison of PL or CL intensity between different samples can be criticized, the change in intensity induced by UL on c-plane QW is typically several orders of magnitude, as shown in the previous section and reported in [Hal+17; Hal+18].

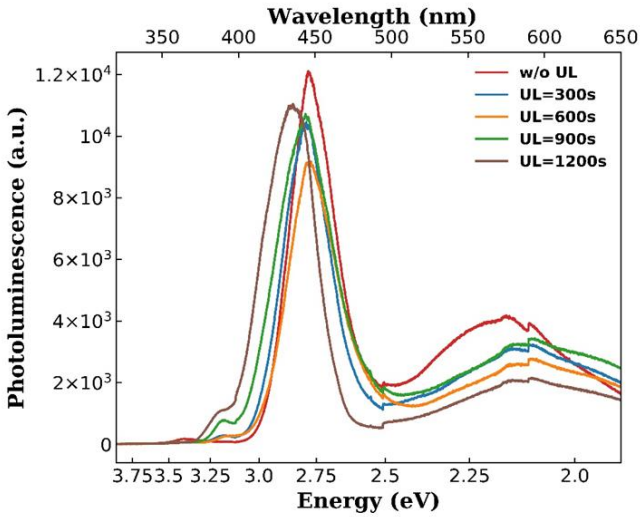

FIGURE 3.12: PL spectra for a series of samples similar to sample #3 but with varying thickness of InGaN UL by changing the growth time from 300 to 1200s [Kap20]

In addition to these measurements, temperature-dependent PL measurements were performed by Akanksha Kapoor. Details can be found in [Kap+20]. Briefly, as shown in figure 3.13, the results of this study point in the same direction, the drop in intensity with temperature, characterized by the ratio I(300K)/I(5K), is about 15% for samples #2 and #3 and less than 4% for sample #1

3.4.4 Time-resolved CL measurements

Considering that PL and CL's intensity can be affected by a change in extraction or collection efficiency, we performed a TRCL analysis to estimate the change in efficiency.

Due to the spatial resolution of the measurements, in order to make sure that the effective lifetime does not depend on the position along the wires, we first measured the lifetime on a single wire of sample #2. Figure 3.14 (a) shows the wire with its CL spectra mapping and the corresponding effective lifetime at the

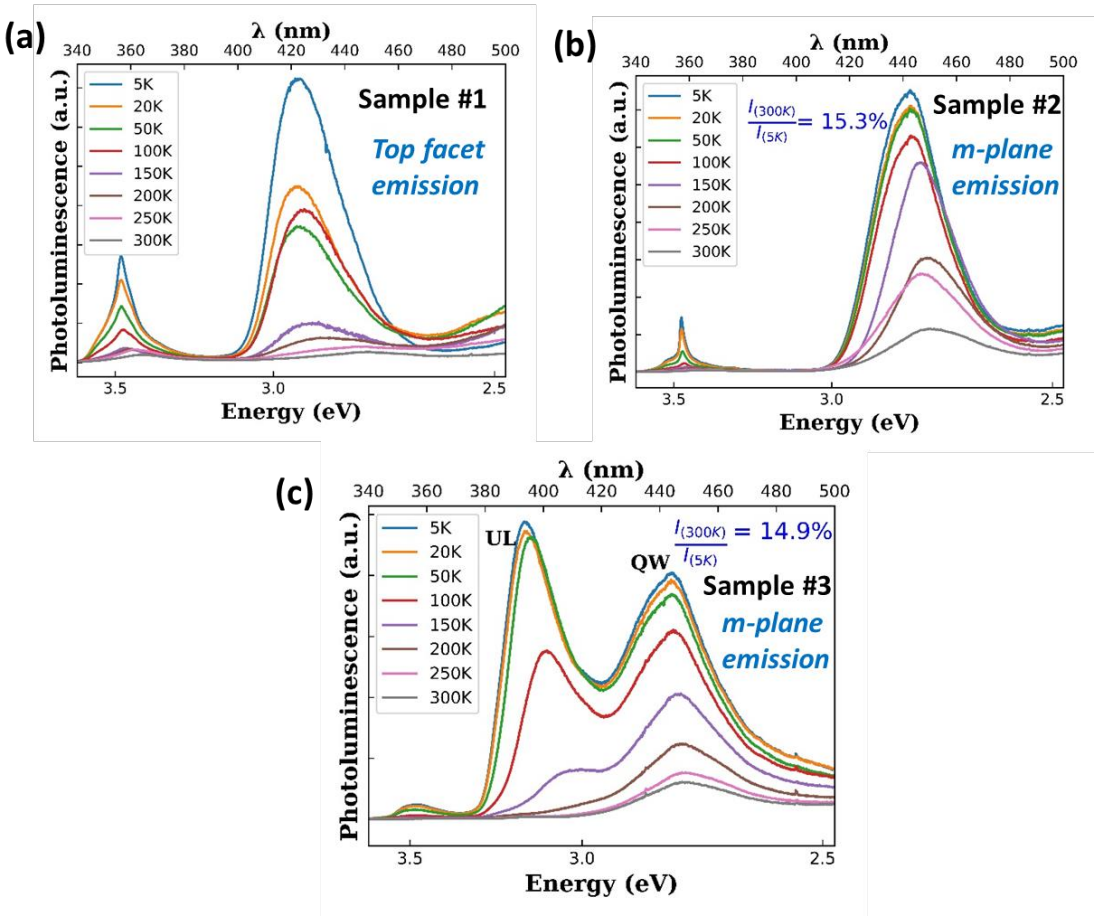

FIGURE 3.13: Temperature dependent PL spectra for the three as-grown samples. [Kap20]

QW energy along the wire at 5 K (b). As observed, the overall lifetime is typically between 220 and 270 ps.

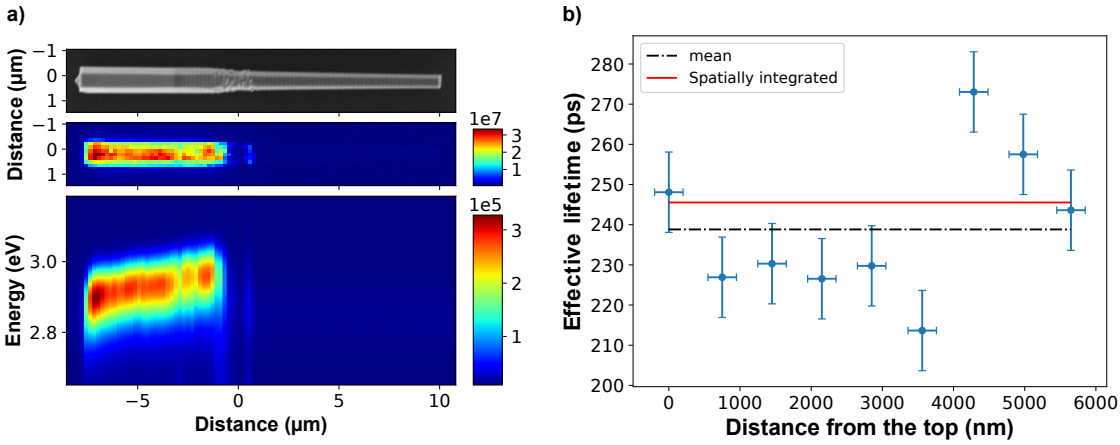

FIGURE 3.14: (a) CL spectra mapping on a wire from sample #2, (b) TRCL measurements performed on this wire along the length at the QW energy.

Then, we performed measurements at different temperatures on a single wire from sample #2, *i.e.,* with a GaN spacer but no UL, as shown in figure 3.15 (a). A solid line indicates the corresponding effective lifetime in figure 3.15 (b). The overall trend suggests that non-radiative recombinations dominate the lifetime. In order to compare the two samples, we first compare τ_{eff} at low temperature.

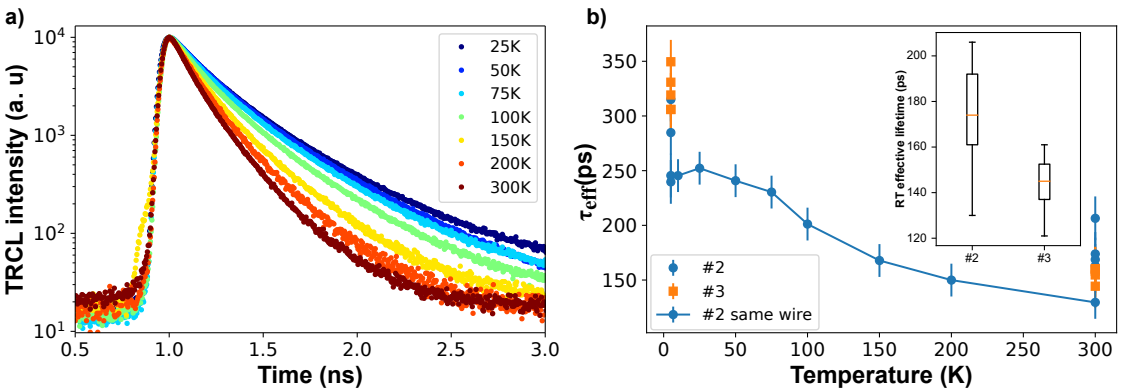

FIGURE 3.15: (a) TRCL Intensity decay curves as a function of temperature for sample #2, (b) effective lifetime (τ_{eff}) at 5 and 300 K measured on five different wires coming from sample #2 and #3. A solid line also indicates the effective lifetime extracted from (a). The inset compares $\tau_{eff}(300K)$ for 12 wires of each sample.

As shown in figure 3.15 (b), the lifetime of the sample with UL is slightly higher, but a more important statistic would be necessary to discriminate a variation from wire to wire. Similarly, we measured the lifetime of these same wires at room temperature. Here we observed the reverse phenomenon: the samples with

a UL have a slightly shorter lifetime. We confirmed this by measuring the room temperature lifetime of 12 wires of each sample. The statistic is shown in the inset of figure 3.5 (b). The observed difference is far from what has been reported in the literature, where typically, the lifetime goes from several nanoseconds with UL to about 100 ps without for *c*-plane QWs [Hal+18].

Lastly, to account for the wire-to-wire dispersion, room-temperature time-resolved photoluminescence measurements were also performed on dispersed wires by Akanksha Kapoor with the help of Joël Bleuse, CEA-IRIG. They were performed with a 366 nm laser operating with a power density of 1.73 W cm^{-2} and a repetition rate of 76 MHz. The obtained results were similar with an average lifetime of 133 and 145 ps without and with UL, respectively [Kap+20]. In addition, to discard any effect of the strong background doping [Liu+16a], we also performed the same measurements on similar samples except with the QW placed in the space charge region of a *pin* structure [Kap+20]. These experiments lead to similar conclusions.

Thus we can conclude that the presence of an InGaN UL does not improve the efficiency of *m*-plane core-shell InGaN QWs. Note that the effect of ULs in the case of *m*-plane QWs grown on GaN substrates will also be studied later (section 3.5), but before, we will briefly discuss the critical role of the GaN spacer.

3.4.5 Role of the GaN spacer: Structural characterization

This section briefly summarizes the findings reported in [Kap+20; Kap20]. They are the result of a collaboration with Vincent Grenier, who prepared the lamellae by focused ion beam (FIB), Catherine Bougerol, who performed STEM observations, and Eric Robin, who carried out quantitative energy-dispersive X-ray (EDX) analysis. Also, as before, the samples were made by Akanksha Kapoor and Christophe Durand.

To understand the influence of the GaN spacer on the growth of the InGaN QW, two additional core-shell samples with and without GaN spacer were studied by STEM and EDX. Thin cross-section slices of the wires, either in longitudinal or transversal mode (*i.e.*, cutting along and perpendicular to the *c*-axis, respectively), were prepared by FIB. Figure 3.16 (a) and (c) show low magnification STEM images acquired at 200 kV with a high-angle annular dark-field (HAADF) detector. The InGaN QWs here appear bright. A significant number of bright lines corresponding to extended defects originating from the first QW are visible in figure 3.16 (a) when the QWs are directly grown on the wire sidewalls. In contrast, no defects are visible when growing the QW on the GaN spacer figure 3.16 (c). It demonstrates that the presence of GaN spacer prevents the formation of extended

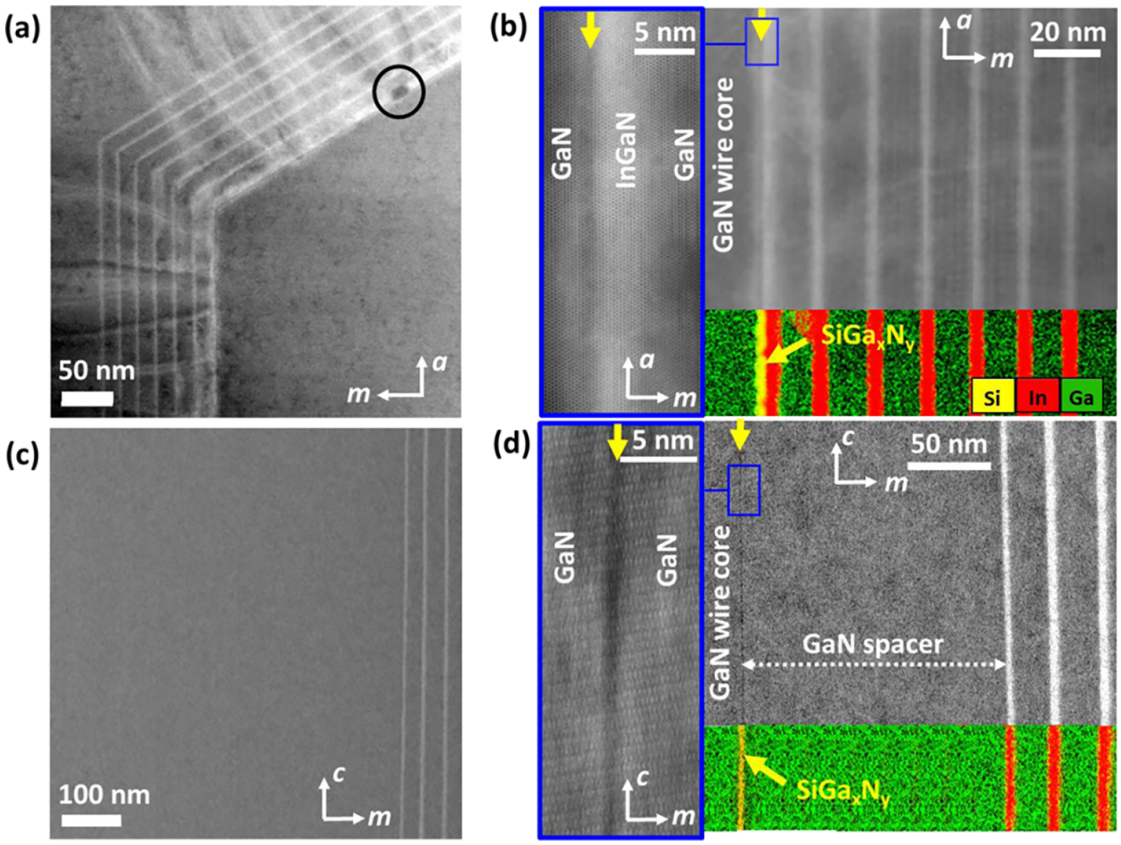

FIGURE 3.16: STEM-HAADF images at low (a,c) and high magnification (b,d) for samples without (a,b) and with (c,d) GaN spacer (150 nm thick) of core-shell InGaN/GaN MQW systems. EDX maps complete the high-magnification observation. (a,b) Transversal cross-sectional STEM-HAADF images taken along the [0 0 0 1] zone axis. The enlarged image [left image in (b)] corresponding to the blue square of the right image shows the presence of a dark line at the interface between the GaN core (yellow arrow) and the first QW, and STEM-EDX elemental mapping of Ga (green), In (red), and Si (yellow) (bottom image in (b)) indicates that the dark line is a Si-enriched layer; (c,d) longitudinal cross-sectional STEM-HAADF images taken along the [1 0 $\bar{1}$ 0] zone axis. The enlarged image [left image in (d)] and STEM-EDX elemental mapping [bottom image in (d)] show that the Si-enriched layer (dark line) is located at the interface between the GaN core and the GaN spacer, far away from the first InGaN QW. [Kap+20]

defects that cause the degradation of the QW properties.

Figure 3.16 (b) and (d) show STEM images with EDX mapping of Si (yellow), In (red), and Ga (green) for the samples without and with GaN spacer. In figure 3.16 (d) the GaN spacer with a thickness of about 150 nm can be easily identified since a dark line (indicated by a yellow arrow) is present at the GaN core-GaN spacer interface. EDX mapping shows that this dark line contains Si. In the high-resolution STEM image, the thickness of this residual layer is about 1 nm. This $SiGa_xN_y$ layer seems to spontaneously form around the GaN wire even when the silane is stopped. It is probably due to residual silane that may still be present in the reactor due to the high silane injection used to passivate the sidewalls during the first stage of GaN wire growth. The presence of this unintentional layer is detrimental to the first QW grown directly on the GaN core, exhibiting rough interfaces, a large thickness gradient, and the nucleation of a high density of extended defects. Thus, the growth of GaN spacer allows burying the unintentional $SiGa_xN_y$ layer in order to prevent defect formation inside InGaN QWs stacks.

3.4.6 Conclusion

In conclusion, we have seen that in the case of core-shell wires, the GaN spacer is critical to burying the residual SiGaN layer. The formation of this layer is probably due to the residual silane after the strong injection to promote vertical growth and reduces the quality of the InGaN QWs, thus preventing any luminescence of the sidewalls.

Another important finding is that contrary to planar *c*-plane QWs, adding an InGaN UL prior to the QW does not increase its efficiency. At this point, we cannot tell if this is related to the particular growth condition of wires. In particular, we can highlight a very low V/III ratio (50) for the growth of the high-temperature GaN core, as well as a strong silane injection ($\sim$200 nmol min^{-1}). In order to answer this question, we will focus on QWs grown on *m*-plane GaN substrates.

3.5 InGaN underlayers in *m*-plane QWs

In this section, we want to study the effect of InGaN ULs on the efficiency of QWs grown by metal-organic vapor phase epitaxy on *m*-plane GaN substrates. The main idea is to have identical growth conditions except for the substrate orientation.

This work was done in collaboration with Amélie Dussaigne from CEA-LETI who grew the samples.

3.5.1 Samples description

In order to study the effect of the UL, two samples were grown on *m*-plane GaN substrate. They consist of a high-temperature GaN buffer grown at 1010 °C followed by an InGaN QW grown at 750 °C sandwiched between two GaN barriers grown at 815 °C. The second sample is identical except for the presence of a 31 periods InGaN(2.5 nm)/GaN(5 nm) SL grown at 815 °C right after the GaN buffer. The In content in the SL is estimated to be around 3–5 % based on *c*-plane samples.[7]

In addition, we grew two additional samples similar to the one without SL, one on *c*- and the other on *m*-plane with increased growth time for each layer. These samples, with a 100 nm-thick InGaN layer were intended for SIMS analysis, as impurity incorporation may change depending on the growth orientation [Lun+19].

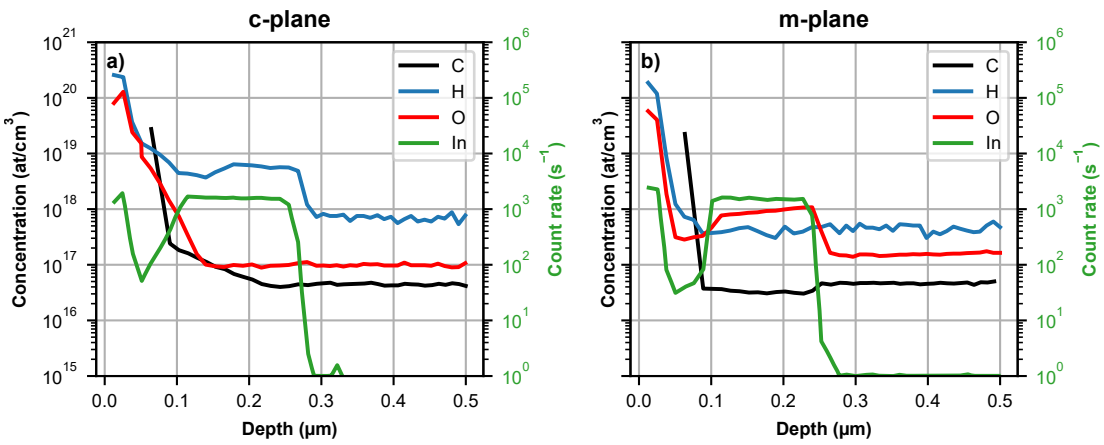

FIGURE 3.17: SIMS analysis showing carbon, hydrogen and oxygen concentration for *c* (a) and *m*-plane (b). The uncalibrated indium profile, *i.e.*, count rate, is also displayed for reference.

As shown in figure 3.17, the SIMS analyses showed differences. First, for the *c*-plane structure, the hydrogen concentration is higher in the InGaN layer ($\sim 5 \times 10^{18}\,\mathrm{cm}^{-3}$) than in GaN ($7 \times 10^{17}\,\mathrm{cm}^{-3}$). Concerning the *m*-plane structure, the hydrogen incorporation is about $4 \times 10^{17}\,\mathrm{cm}^{-3}$ in the whole structure. Secondly, the opposite effect occurs for oxygen. Its incorporation is constant in the *c*-plane structure with a level of about $10^{17}\,\mathrm{cm}^{-3}$, while on *m*-plane, the concentration is about $2 \times 10^{17}\,\mathrm{cm}^{-3}$ in GaN and $10^{18}\,\mathrm{cm}^{-3}$ in InGaN. This last point is particularly important and has to be kept in mind since oxygen is an efficient *n*-type dopant [KW00]. This has already been reported for similar samples, with carrier density estimated to be around $10^{18}\,\mathrm{cm}^{-3}$ by capacitance-voltage measurement [Liu+16a].

[7]Note that the effect of this SL has also been studied on *c*-plane, leading to a significant improvement of the PL intensity, as already demonstrated.

3.5.2 Temperature-dependent cathodoluminescence analysis

To compare the two samples, we performed temperature-dependent CL and TRCL analysis. For the CL measurements, the current was about 50 pA, and the acceleration voltage was set to 5 kV. Note that the measurements were averaged over $5 \times 5\,\mu m^2$ area.

Figure 3.18 (a) and (b) show normalized CL spectra acquired roughly every 10 K from 5 K to room temperature for the samples without and with UL. We can see that the emission of the sample with the SL is redshifted. Figure 3.18 (c) shows the mean energy as a function of temperature. The shift is typically 60 meV on the whole temperature range and could be attributed to a small variation (∼1 %) in indium content. Also, we can note the presence of a plateau below 60 K, which could be a sign of localization.

As a first comparison, we can study the intensity drop as a function of temperature for both samples.

$$\frac{\int I_{300K}(\lambda)d\lambda}{\int I_{10K}(\lambda)d\lambda} \tag{3.3}$$

If we assume that the non-radiative recombinations are negligible at low temperature and that the transfer of the carriers generated in the barriers into the QW does not depend on the temperature, this ratio is equal to the IQE. Although these conditions are not necessarily met in our case, this ratio provides an initial estimate of the IQE. Here, being equal to 55% for both samples, it suggests no improvement and a probably high IQE in both cases.

Additionally, we performed TRCL measurements in the same experimental conditions except for the modulation of the beam-blanker to create electron pulses of 10 ns with a repetition rate of 10 MHz. Figure 3.18 (d) shows the effective lifetime as a function of the temperature. The lifetimes were obtained by fitting the decay of the CL intensity with a single exponential. Overall, they increase with temperature for both samples, indicating a relatively high IQE. However, we can note a singular behavior at low temperatures. Indeed, below 60 K, the lifetimes are relatively constant, which is expected in the presence of localization, but, above 60 K, we notice a drop for both samples, which is quite unusual. To explain this drop, we tentatively assumed that, up to 60 K, carriers are localized on shallow levels[8] with a longer lifetime. With increasing temperature, the carriers would then be delocalized with a shorter lifetime, before following the expected

[8] If we assume that the localization takes place until 60 K, the energy of the state is roughly $E \sim k_B T \approx 5\,\text{meV}$

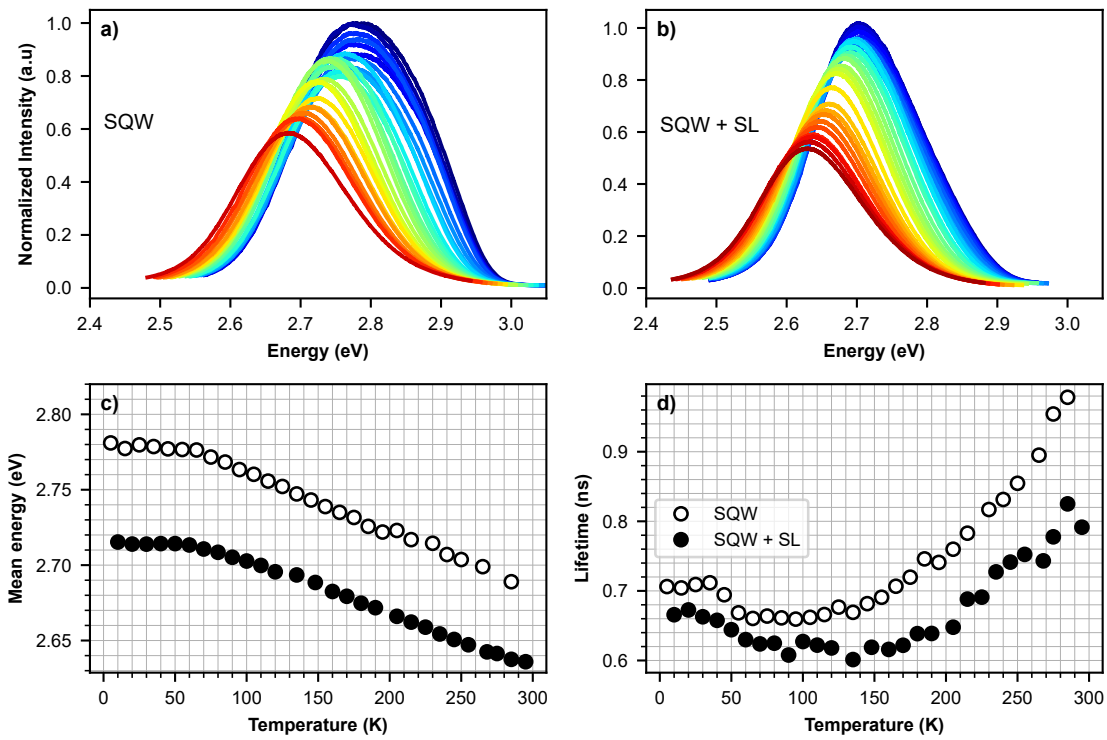

FIGURE 3.18: Temperature-dependent: normalized CL spectra (a–b), mean energy (c) and effective lifetime (d) for the samples without and with an InGaN superlattice.

monotonic increase, characteristic of samples dominated by radiative lifetime.

Before we can conclude, we have to comment on the effect of the higher doping level. First, let us assume that the intensity ratio is close to the IQE. According to equation (3.4), with an IQE of 55% and an effective lifetime approximately equal to 1 ns, we have $\tau_{nr} = 2.2\,\text{ns}$ and $\tau_r = 1.8\,\text{ns}$

$$\begin{cases} \text{IQE} = \dfrac{\tau_{eff}}{\tau_r} \\ \tau_{eff}^{-1} = \tau_r^{-1} + \tau_{nr}^{-1} \end{cases} \Longrightarrow \begin{cases} \tau_r^{-1} = \text{IQE}\ \tau_{eff}^{-1} \\ \tau_{nr}^{-1} = (1 - \text{IQE})\ \tau_{eff}^{-1} \end{cases} \tag{3.4}$$

Now, we recall that usually, both τ_{nr} and τ_r depend on the background doping. In particular, both processes rely on the recombination of an electron and a hole (whether the recombination is direct or assisted by a defect). Therefore, these processes become more likely by increasing the concentration of one of the two types of carriers [Dav+20]. Thus here, the IQE may not accurately reflect the one of an LED, where the QW is in the depletion region, *i.e.*, with no free carriers.

However, we can note that the studies performed by Haller et al. were done on highly doped structures ([Si]$\sim 3\times 10^{18}$ cm^{-3}) except for the QW which was undoped [Hal19, p. 41]. We can assume that the carrier density was high in the QW, as no space charge region was present to deplete it. Despite that, they manage to observe a huge change in lifetime, from $\sim$170 ps to 20 ns by adding a UL for a 2.7 nm InGaN QW grown on *c*-plane GaN substrate. This very short lifetime at 300 K can be equated to the non-radiative lifetime. Although the comparison is not straightforward between their sample and ours, we can still point out that in our case, we estimated the non-radiative lifetime to be in the nanosecond range, that is one order of magnitude longer. Moreover, we observed no drastic change in the lifetime profile by adding a UL. For these reasons, it seems reasonable to think that the UL is not necessary in the case of *m*-plane InGaN QW.

In any case, to remove any ambiguity, it would be interesting to design new samples with the QW placed in the middle of the space charge region to suppress the effect of background doping.

3.5.3 Conclusion

In conclusion, we studied the effect of substrate orientation on the necessity of InGaN UL. First, we observed by SIMS analysis that impurities incorporation differs between the *m* and *c* planes. In particular, for the *m*-plane, the oxygen concentration was one order of magnitude higher in the InGaN layer than in GaN. Then, we studied two *m*-plane samples with and without UL by temperature-dependent CL and TRCL analysis. We could show that both samples had similar properties. In particular, the intensity ratio between low and high temperature is about 55% and the lifetimes increased with temperature for both samples. These two signs indicate a relatively high IQE and suggest that the presence of the UL is not as critical as for *c*-plane samples.

In order to explain this difference, we can make several hypotheses. For example, it is possible that defects created during the growth of high-temperature *c*-plane GaN are not formed on *m*-planes. Indeed, a difference in stability is expected between *m* and *c*-planes. In particular, different surface energy, *i.e.*, the energy required to create one unit of surface areas is predicted by calculations [Ber17, p. 153]. In addition, Zettler et al. observed a strong anisotropy in the thermal decomposition rate of GaN nanowires [Zet+16]. Another possibility could be that these defects form but do not segregate on *m*-planes, therefore considerably reducing their density in *m*-plane QW. Finally, assuming that these defects are extrinsic, their incorporation may depend on the crystallographic orientation, as we have shown. This last point has already been reported, for example, depending

on the nitrogen or gallium polarity of *c*-plane QW [Lun+19].

3.6 Conclusion and perspectives

In conclusion, in this chapter, we have studied the effect of In-containing ULs on the efficiency of QWs for different structures. We have first reproduced the effect observed in the literature and studied the evolution of the effective lifetime as a function of temperature for QWs grown on *c*-plane sapphire substrate. As expected, in the absence of UL, the effective lifetime decreases, a sign that non-radiative recombinations dominate. Conversely, adding a UL changes this profile drastically, with an effective lifetime that increases with temperature, characteristic of the radiative lifetime of a QW.

Then, we have shown that these ULs also work in the case of QWs grown on Si (111). In particular, by comparing both the relative IQE as a function of the excitation power density and the effective lifetime as a function of temperature, we were able to highlight that point defects continue to play a significant role even if their density is typically 1–2 orders of magnitude lower than that of threading dislocations.

We were then interested in the case of core-shell microwires where the active region is grown on the *m*-plane sidewalls of GaN microwires. We have shown that these InGaN ULs do not improve efficiency, whereas a GaN spacer was needed for obtaining *m*-plane emission. Its role is to bury a $SiGa_xN_y$ layer induced by the high silane injection, forming extended defects detrimental to the QWs. In order to understand why InGaN ULs were not needed and to discriminate a possible effect of the particular growth conditions of core-shell microwires, we also studied QWs grown on *m*-plane GaN substrates. Here again, no significant difference could be observed. Moreover, the lifetime as a function of temperature increased monotonically, suggesting that radiative recombination dominates even in the absence of UL, and thus a relatively high IQE. Several hypotheses could explain this difference:

Point defects do not form on *m*-planes Indeed, we have briefly mentioned that a difference in stability between the different planes of the wurtzite crystal is expected, first by calculations that predict higher surface energy for *c*-planes [Ber17, p. 153]. Additionally, a strong anisotropy in the thermal decomposition rate of GaN was observed experimentally [Zet+16]. Also, several studies evidenced that the thermal decomposition reaction of GaN, and thus its stability, depends both on the substrate orientation and off-cut angle [May+02; Yos+19]. At this point, it is worth remembering that the growth temperature of high-temperature

GaN (typically $\gtrsim 900\,°C$) is comparable to the GaN thermal decomposition temperature ($\sim 950\,°C$) [Sto+08].

Thus, based on this analysis, we can note several experiments that could shed light on the mechanism responsible for the formation of these defects.

- According to Arita et al. and Stonert et al., AlGaN, even with an Al content as low as 5%, is much more stable than GaN [Ari+12; Sto+08]. Consequently, it could be interesting to study whether an In-containing UL is necessary if the high-temperature GaN is replaced by $Al_{0.05}Ga_{0.95}N$. Note that the question here is not whether an Al-containing layer could incorporate defects as In does, but rather whether these defects are created in AlGaN. Indeed, Haller has already shown in her thesis that AlGaN layers are not stopping the defects segregation [Hal19, p. 90].

- Also, as the thermal stability of GaN seems to depend on the surface orientation, it could be interesting to study the role of ULs on the efficiency of N-polar QWs. It should be noted that special attention must be paid to the incorporation of impurities, as N-polarity QWs are reported to have more impurities than Ga-polarity QWs [Lun+19].

- Another possibility would be to increase the growth temperature of the *m*-plane GaN buffer to test whether it is possible to create these defects intentionally, as was done by Haller et al. on *c*-plane [Hal+18]. However, this could be complicated because *m*-plane substrates are expensive, and the required temperature could be very high and far from the typical growth temperature or even outside the operating range of the reactor (Zettler et al. reported a tenfold ratio in the decomposition rate between the *m*-plane and the *c*-plane [Zet+16]).

Point defects are incorporated differently Beyond the formation mechanism of these defects, we can also assume that their incorporation differs depending on the surface orientation. Thus, we can consider two different situations:

- These defects would not remain on *m*-plane surfaces. It would mean that these defects would be effectively buried by a thin layer of GaN grown at a low temperature.

- Conversely, we can consider that these defects remain on the surface of the *m*-planes, including in the InGaN. Thus they would not be incorporated in the quantum wells, thus not forming non-radiative centers.

Appendices

3.A Effect of the acceleration voltage on CL spectra

In CL, the acceleration voltage determines both the lateral extension and the depth of the excitation volume. By varying it, it is possible to probe the different layers. Figure 3.A.1 shows CL spectra normalized to QW intensity (a) and the UL/QW intensity ratio (b) for acceleration voltages ranging from 500 V to 30 kV. At low acceleration voltages, the excitation volume is very close to the surface, so the main contribution comes from the QW. By increasing it, typically between 500 V and 10 kV, the relative intensity of the UL increases with the depth of excitation. Above 10 kV, the yellow band's intensity increases drastically, and the UL intensity decreases, indicating that the excitation is mainly located in the unintentionally doped GaN core.

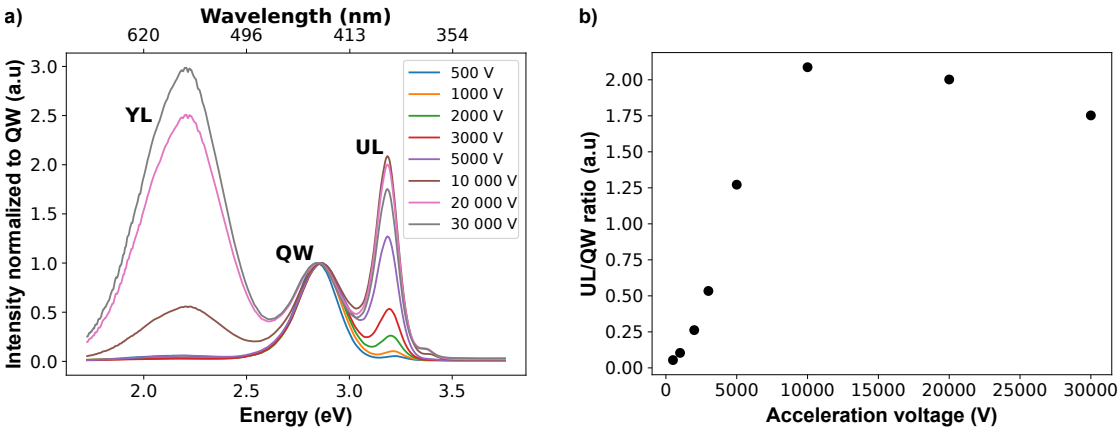

FIGURE 3.A.1: Cathodoluminescence analysis of single wires from sample #3. (a) Room temperature CL spectra as a function of the acceleration voltage. (b) CL intensity ratio between InGaN UL and QW emission as a function of the acceleration voltage.

References

[Ari+12] Munetaka Arita et al. "Fabrication of AlGaN two-dimensional photonic crystal nanocavities by selective thermal decomposition of GaN". *Applied Physics Express* 5.12 (2012). DOI: 10.1143/APEX.5.126502.

[Arm+15] Andrew M. Armstrong et al. "Defect-reduction mechanism for improving radiative efficiency in InGaN/GaN light-emitting diodes using InGaN underlayers". *Journal of Applied Physics* 117.13 (Apr. 2015), 134501. DOI: 10.1063/1.4916727.

[Ber17] V. M. Bermudez. "The fundamental surface science of wurtzite gallium nitride". *Surface Science Reports* 72.4 (2017), 147–315. DOI: 10.1016/j.surfrep.2017.05.001.

[Che+21] Yao Chen et al. "GaN buffer growth temperature and efficiency of InGaN/GaN quantum wells: The critical role of nitrogen vacancies at the GaN surface". *Applied Physics Letters* 118.11 (2021), 111102. DOI: 10.1063/5.0040326.

[Che+98] Y Chen et al. "Pit formation in GaInN quantum wells". *Applied Physics Letters* 72.6 (1998), 710–712. DOI: 10.1063/1.120853.

[Dai+15] Xing Dai et al. "Flexible Light-Emitting Diodes Based on Vertical Nitride Nanowires". *Nano Letters* 15.10 (Oct. 2015), 6958–6964. DOI: 10.1021/acs.nanolett.5b02900.

[Dav+20] Aurelien David et al. "Review—The Physics of Recombinations in III-Nitride Emitters". *ECS Journal of Solid State Science and Technology* 9.1 (2020), 016021. DOI: 10.1149/2.0372001jss.

[Eym+12] J Eymery et al. *Process for catalyst-free selective growth on a semiconductor structure*. 2012.

[Hal+17] C. Haller et al. "Burying non-radiative defects in InGaN underlayer to increase InGaN/GaN quantum well efficiency". *Applied Physics Letters* 111.26 (Dec. 2017). DOI: 10.1063/1.5007616.

[Hal+18] C. Haller et al. "GaN surface as the source of non-radiative defects in InGaN/GaN quantum wells". *Applied Physics Letters* 113.11 (Sept. 2018), 111106. DOI: 10.1063/1.5048010.

[Hal+19] Camille Haller et al. "InAlN underlayer for near ultraviolet InGaN based light emitting diodes". *Applied Physics Express* 12.3 (Feb. 2019), 034002. DOI: 10.7567/1882-0786/ab0147.

[Hal19] Camille Haller. "Elucidating the role of the InGaN underlayer in the efficiency of InGaN based light-emitting diodes". PhD thesis. Ecole Polytechnique Federale de Lausanne, 2019.

[Han+05] A Hangleiter et al. "Suppression of nonradiative recombination by V-shaped pits in GaInN/GaN quantum wells produces a large increase in the light emission efficiency". *Physical Review Letters* 95.12 (2005). DOI: 10.1103/PhysRevLett.95.127402.

[Han+18] Andreas Hangleiter et al. "Internal quantum efficiency of nitride light emitters: a critical perspective". February 2018 (2018), 59. DOI: 10.1117/12.2290082.

[Kap+18] Akanksha Kapoor et al. "Green Electroluminescence from Radial m-Plane InGaN Quantum Wells Grown on GaN Wire Sidewalls by Metal-Organic Vapor Phase Epitaxy". *ACS Photonics* 5.11 (2018), 4330–4337. DOI: 10.1021/acsphotonics.8b00520.

[Kap+20] Akanksha Kapoor et al. "Role of Underlayer for Efficient Core-Shell InGaN QWs Grown on m-plane GaN Wire Sidewalls". *ACS Applied Materials and Interfaces* 12.16 (Apr. 2020), 19092–19101. DOI: 10.1021/acsami.9b19314.

[Kap20] Akanksha Kapoor. "Core-shell InGaN / GaN wire for Flexible LEDs". PhD thesis. Université Grenoble Alpes, 2020.

[KI15] Katsumi Kishino and Shunsuke Ishizawa. "Selective-area growth of GaN nanocolumns on Si(111) substrates for application to nanocolumn emitters with systematic analysis of dislocation filtering effect of nanocolumns". *Nanotechnology* 26.22 (June 2015). DOI: 10.1088/0957-4484/26/22/225602.

[KM03] Sergey Yu Karpov and Yuri N. Makarov. "Dislocation effect on light emission efficiency in gallium nitride". *Applied Physics Letters* 81.25 (Dec. 2003), 4721–4723. DOI: 10.1063/1.1527225.

[Koe+10] R. Koester et al. "Self-assembled growth of catalyst-free GaN wires by metal-organic vapour phase epitaxy". *Nanotechnology* 21.1 (Jan. 2010), 015602. DOI: 10.1088/0957-4484/21/1/015602.

[KW00] R Y Korotkov and B W Wessels. "Electrical properties of oxygen doped GaN grown by metalorganic vapor phase epitaxy". *Materials Research Society Symposium - Proceedings* 595 (2000). DOI: 10.1557/proc-595-f99w3.80.

[Li+13] T Li et al. "The effect of InGaN underlayers on the electronic and optical properties of InGaN/GaN quantum wells". *Applied Physics Letters* 102.4 (2013), 41115. DOI: 10.1063/1.4789758.

[Lia+16] Gediminas Liaugaudas et al. "Optical properties of nearly lattice-matched GaN/(Al,In)N quantum wells". *Journal of Applied Physics* 119.20 (2016), 205708. DOI: 10.1063/1.4951711.

[Liu+16a] W. Liu et al. "Carrier-density-dependent recombination dynamics of excitons and electron-hole plasma in m -plane InGaN/GaN quantum wells". *Physical Review B* 94.19 (2016). DOI: 10.1103/PhysRevB.94.195411.

[Liu+18] W. Liu et al. "Spatially dependent carrier dynamics in single InGaN/GaN core-shell microrod by time-resolved cathodoluminescence". *Applied Physics Letters* 112.5 (Jan. 2018), 052106. DOI: 10.1063/1.5009728.

[Lun+19] Cory Lund et al. "Properties of N-polar InGaN/GaN quantum wells grown with triethyl gallium and triethyl indium as precursors". *Semiconductor Science and Technology* 34.7 (2019). DOI: 10.1088/1361-6641/ab1204.

[May+02] Miho Mayumi et al. "Influence of lattice polarity on wurzite GaN {0 0 0 1} decomposition as studied by in situ gravimetric monitoring method". *Journal of Crystal Growth* 237-239.1 4II (2002), 1143–1147. DOI: 10.1016/S0022-0248(01)02072-3.

[Oka+15] Narihito Okada et al. "Controlling potential barrier height by changing V-shaped pit size and the effect on optical and electrical properties for InGaN/GaN based light-emitting diodes". *Journal of Applied Physics* 117.2 (2015), 25708. DOI: 10.1063/1.4905914.

[Pez+22] Bardia Pezeshki et al. "LED-array based optical interconnects for chip-to-chip communications with integrated CMOS drivers, detectors, and circuitry". 1200707.March (2022), 11. DOI: 10.1117/12.2614547.

[Piv+21] Francesco Piva et al. "How does an In-containing underlayer prevent the propagation of defects in InGaN QW LEDs?: identification of SRH centers and modeling of trap profile". *Gallium Nitride Materials and Devices XVI*. Ed. by Hadis Morkoç, Hiroshi Fujioka, and Ulrich T. Schwarz. March. SPIE, Mar. 2021, p. 56. DOI: 10.1117/12.2578123.

[Pol+20] A. Y. Polyakov et al. "Deep traps in InGaN/GaN single quantum well structures grown with and without InGaN underlayers". *Journal of Alloys and Compounds* 845 (2020). DOI: 10.1016/j.jallcom.2020.156269.

[RM05] Michael A. Reshchikov and Hadis Morko. "Luminescence properties of defects in GaN". *Journal of Applied Physics* 97.6 (Mar. 2005), 061301. DOI: 10.1063/1.1868059.

[Ros+14] G. Rossbach et al. "High temperature Mott transition in wide-band-gap semiconductor quantum wells". *Physical Review B - Condensed Matter and Materials Physics* 90.20 (Nov. 2014), 201308. DOI: 10.1103/PhysRevB.90.201308.

[RV02] Emmanuel Rosencher and Borge Vinter. *Optoélectronique*. Vol. 1. Cambridge University Press, 2002, p. 621.

[Sha+16] M. Shahmohammadi et al. "Excitonic Diffusion in InGaN/GaN Core-Shell Nanowires". *Nano Letters* 16.1 (Jan. 2016), 243–249. DOI: 10.1021/acs.nanolett.5b03611.

[Sha+17] M Shahmohammadi et al. "Enhancement of Auger recombination induced by carrier localization in InGaN/GaN quantum wells". *Physical Review B* 95.12 (2017), 125314. DOI: 10.1103/PhysRevB.95.125314.

[Sto+08] A Stonert et al. "Channeling study of thermal decomposition of III-N compound semiconductors". *Nuclear Instruments and Methods in Physics Research, Section B: Beam Interactions with Materials and Atoms* 266.8 (2008), 1224–1228. DOI: 10.1016/j.nimb.2007.12.054.

[Tör+08] P. T. Törmä et al. "Effect of InGaN underneath layer on MOVPE-grown InGaN/GaN blue LEDs". *Journal of Crystal Growth* 310.23 (2008), 5162–5165. DOI: 10.1016/j.jcrysgro.2008.07.031.

[Wea+21] Thomas F.K. Weatherley et al. "Imaging Nonradiative Point Defects Buried in Quantum Wells Using Cathodoluminescence". *Nano Letters* 21.12 (June 2021), 5217–5224. DOI: 10.1021/acs.nanolett.1c01295.

[Wu+98] X H Wu et al. "Structural origin of V-defects and correlation with localized excitonic centers in InGaN/GaN multiple quantum wells". *Applied Physics Letters* 72.6 (1998), 692–694. DOI: 10.1063/1.120844.

[Yos+19] Kento Yoshida et al. "Dependence of thermal stability of GaN on substrate orientation and off-cut". *Japanese Journal of Applied Physics* 58.SC (2019). DOI: 10.7567/1347-4065/ab0f14.

[Zet+16] Johannes K. Zettler et al. "Observation of Dielectrically Confined Excitons in Ultrathin GaN Nanowires up to Room Temperature". *Nano Letters* 16.2 (Feb. 2016), 973–980. DOI: 10.1021/acs.nanolett.5b03931.

Chapter 4

Surface recombination in µLEDs

4.1 InGaN/GaN blue µLED. 96
4.1.1 Introduction 96
4.1.2 Studied µLED structure 97
4.1.3 Standard cathodoluminescence analysis 97
4.1.3.1 Effect of the acceleration voltage in the bulk 97
4.1.3.2 CL mapping near a mesa edge 99
4.1.3.3 Summary 100
4.1.4 SRTC-CL measurements 100
4.1.4.1 Experimental setup and first results 101
4.1.4.2 Averaged measurements 104
4.1.5 1D diffusion simulations 107
4.1.5.1 Introduction of the diffusion model 107
4.1.5.2 Validation of the model 111
4.1.5.3 IQE estimation using radial simulations 112
4.1.5.4 Guidelines towards efficient µLEDs 114
4.1.6 Conclusion of the study 114
4.2 Extending the method to AlGaInP red µLED 115
4.2.1 Context 115
4.2.2 Studied sample 115
4.2.3 SRTC-CL measurements 116
4.2.4 Conclusion 118
4.3 Conclusion and perspectives. 119
Appendices 121

In this chapter, we will study non-radiative surface recombinations at the etched sidewalls of micro-LEDs (µLEDs). The study will focus on blue InGaN/GaN-based µLEDs. First, we will show some limitations of classical CL measurement. Then we will introduce a methodology to quantify these recombinations thanks to a Hanbury Brown & Twiss interferometer and 1D diffusion model. We will then show the effect of a passivation technique. Finally, we will briefly show that this technique can be extended to other emitters such as red AlGaInP µLEDs.

4.1 InGaN/GaN blue µLED

The following study is mainly adapted from a published article [Fin+22], which is the result of a collaboration with CEA-LETI, particularly with David Vaufrey and Corentin Le Maoult, a former PhD student who performed the etching and passivation.

4.1.1 Introduction

After more than 30 years of development, III-nitride-based LEDs are now widely used for general lighting. Thanks to their high efficiency, this technology is now considered as a promising candidate for µLED display applications. However, the size reduction brings various challenges that are currently preventing their commercialization. In particular, as the surface-to-volume ratio increases, non-radiative surface recombinations at the sidewalls become significant, which greatly limits the efficiency of µLEDs [Oli+17a]. To mitigate such effects, different passivation techniques have been proposed such as thermal annealing [Tia+12], chemical treatment [Bor+00; Cho+14; Won+19] and oxide deposition [Won+18; Won+19].

Due to the reduced dimensions of such µLEDs, dedicated optical characterization techniques have been specifically implemented. First, the optical properties have been probed by micro-photoluminescence (µ-PL) [Bor+00; Ott+15], and electroluminescence spectroscopy [Oli+17a; Tia+12; Ley+20]. In addition, CL spectroscopy has been used to study precisely the edge effects with an excellent spatial resolution [Xie+12]. However, if these techniques are well suited to characterize the variation in EQE, they do not allow changes in IQE, LEE or IE to be disentangled. Thus, to directly estimate the influence of size reduction on Shockley-Read-Hall recombinations and to be only sensitive to IQE variation, time-resolved photoluminescence spectroscopy [Oli+17a; Bou+21] has been employed. The spatial resolution of such technique, however, does not allow to directly quantify the surface recombination velocity. Therefore, there is a need for a characterization technique that combines both high spatial and high temporal

resolution, in order to assess the changes in IQE induced by the sidewalls without being influenced by changes in IE [Oli+17b] or LEE [Ley+20; Jin+00; Cho+03].

4.1.2 Studied µLED structure

The studied structure is an InGaN/GaN blue LED commercially grown on *c*-plane GaN on sapphire template. The structure's composition was deduced during Corentin Le Maoult's thesis by STEM, SIMS, and PL analyses [Le 21, p. 68].

The LED stack would essentially consist of a thick *n*-GaN buffer ([Si]$\sim 1.4 \times 10^{19}\,\mathrm{cm}^{-3}$) followed by 200 nm of unintentionally doped GaN (*i*-GaN). Then, 6 periods of InGaN(6.5nm)/GaN(15nm) are present, doubtlessly to act as a UL as described in chapter 3. The active region, referred to hereafter as MQW, consists of 9 InGaN QWs of about 3 nm, with barriers of 15 nm. This one is followed by an AlGaN EBL of 20 nm. Finally, the structure is covered with 200 nm of *p*-GaN ([Mg]$\sim 4.5 \times 10^{19}\,\mathrm{cm}^{-3}$).

To define the µLED mesa, 1 µm of SiO_2 was deposited to be used as a hard mask. Squared mesas with lateral sizes ranging from 2 to 100 µm were then defined by Cl_2/Ar inductively coupled plasma (ICP) etching. A typical secondary electron image of a $4 \times 4\,\mu\mathrm{m}^2$ LED after dry etching is depicted in figure 4.1.

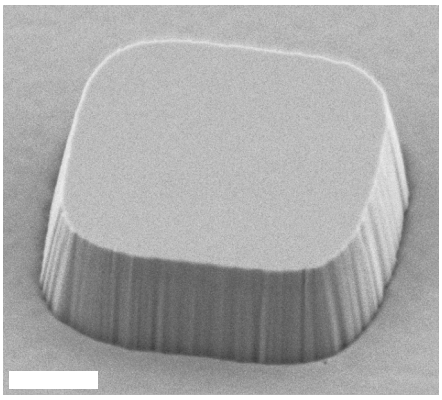

FIGURE 4.1: Bird's-eye view secondary electron image of a $4 \times 4\,\mu\mathrm{m}^2$ LED after ICP dry etching and hard mask removal. The scale bar is 1 µm long.

4.1.3 Standard cathodoluminescence analysis

4.1.3.1 Effect of the acceleration voltage in the bulk

Due to the non-resonant nature of the excitation process, the acceleration voltage must be chosen carefully. As we will see, the choice of this parameter is of critical importance here, in the presence of an EBL. Figure 4.2 shows room temperature

spectra acquired in the middle of a $100 \times 100\,\mu m^2$ mesa for different acceleration voltages.

At low acceleration voltages, typically below 6 kV, only a broad band running from about 390 to 500 nm, assigned here to the blue line (BL) of the GaN:Mg and the near band edge emission (NBE) at 364 nm can be clearly identified [RM05]. Because of the presence of the EBL, carriers generated in the GaN:Mg cannot diffuse into the MQW, therefore no emission of the MQW is observed.

At 6 kV, the MQW emission starts to appear. Additionally, a weak emission (UVL) around 380 nm, attributed to electron to acceptor transitions in the GaN:Mg is visible [RM05]. This band is better resolved at slightly higher acceleration voltage, with the intensity of the broad BL band decreasing in favor of the thinner MQW emission.

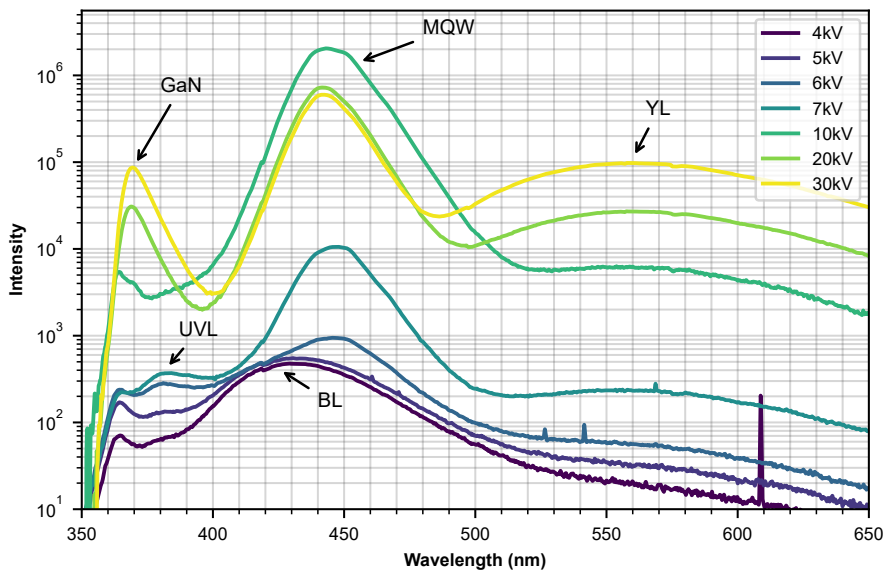

FIGURE 4.2: Room temperature spectra acquired in the center of a $100 \times 100\,\mu m^2$ mesa for different acceleration voltages

Note about BL & UVL emission Both BL and UVL emissions have already been observed in PL spectra of GaN:Mg. In particular, the BL band has been reported as the dominant PL band in heavily doped GaN, with a concentration of Mg typically above $10^{19}\,cm^{-3}$ [RM05; Mon+14; RGD18]. This is in agreement with the assumption that mainly the GaN:Mg is probed below 6 kV.

By increasing the acceleration voltage further, we can see that the MQW emission increases drastically. In particular, the intensity is multiplied by ∼200 between 7 kV and 10 kV. This corresponds to the situation where the primary electrons are injected deep enough to excite the MQW directly.

Note that at 10 kV, a peak appears at 369 nm, associated with the NBE emis-

sion of the *i*-GaN or *n*-GaN. Above 10 kV, as the acceleration voltage further increases, the intensity of the MQW doesn't increase much whereas the broad yellow luminescence (YL) band intensity at 560 nm increases and the GaN:Mg NBE is replaced by the i- or *n*-GaN NBE. This is a clear sign that the excitation mainly takes place below the MQW.

Note about YL It has been reported that the intensity of the YL band usually vanishes with Mg doping [RM05]. Again, this is in agreement with our measurements where this band is mainly visible at high acceleration voltages where *i*-GaN or *n*-GaN are excited compared to lower acceleration voltages where only GaN:Mg is excited.

4.1.3.2 CL mapping near a mesa edge

In addition to the spectra presented previously, we performed CL mapping of a $4 \times 4\,\mu m^2$ mesa. Figure 4.3 (a-d) shows normalized CL images at the MQW energy for different acceleration voltages.

On the top surface of the mesa, the CL intensity of the MQW is ruled by the presence of the EBL. However, we can see that even at low acceleration voltage, a thin emission is present at the edges of the mesa (figure 4.3 (a, b)). To understand the origin of this emission, it is necessary to take a closer look at the geometry of the samples.

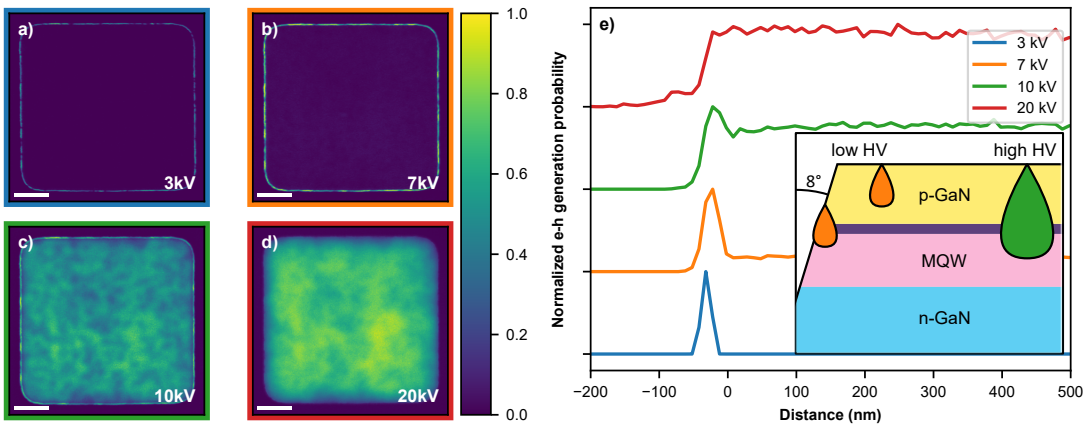

FIGURE 4.3: (a-d) CL images of the same pixel at the quantum well energy (440 ± 10 nm) for different acceleration voltages. The scale bar is 2 µm long. (e) Normalized e-h pair generation probability in the active region simulated with CASINO. (inset) Schematic of the interaction volume at low (orange) and high acceleration voltage (green).

From side-view secondary electron images (not shown here), we observed that the etched sidewalls are tilted by about 8°. This allows carriers to be injected

directly into the active region when the electron beam hits the inclined sidewalls even at low acceleration voltage, as illustrated in figure 4.3 (e)'s inset.

By increasing the acceleration voltage, the penetration depth of the primary electrons increases, allowing the generation of e-h pairs in the MQW from the top surface. However, we should keep in mind that in CL spectroscopy, the energy of the incident electrons determines not only the penetration depth but more generally the interaction volume and therefore the spatial resolution. Consequently, a loss of spatial resolution is clearly visible in figure 4.3 (c-d), where spatial fluctuations in CL intensity are smoothed by increasing the acceleration voltage from 10 kV to 20 kV. There is therefore a trade-off between spatial resolution and the MQW luminescence intensity.

To confirm these interpretations, we performed 3D Monte-Carlo simulations with the software CASINO [Dem+11]. Figure 4.3 (e) shows the normalized e-h pair generation probability in the active region, defined as the ratio of the energy deposited in the active region and the total deposited energy, for different acceleration voltages as a function of edge distance. Note that this definition is relevant here because of the presence of the EBL, which prevents carriers generated above from diffusing in the MQW.

First, we find that the simulations are in good agreement with CL images. Secondly, the results suggest that the injection efficiency is not necessarily constant over the whole sample. Moreover, it depends not only on the geometry of the sample but also on the acceleration voltage. For all these reasons, the CL intensity does not necessarily reflect the influence of surface recombination near the sidewalls.

4.1.3.3 Summary

We have seen that the choice of the acceleration voltage is very important. In particular, as it determines the penetration depth and spatial resolution, there is a trade-off between spatial resolution and intensity.

We have also highlighted that the injection efficiency is not constant over the whole surface of the mesa. It implies that the CL intensity does not necessarily reflect the influence of surface recombination near the sidewalls and thus cannot be used to accurately measure changes in IQE. Thus, we will perform lifetime measurements to investigate the impact of sidewalls on the IQE.

4.1.4 SRTC-CL measurements

As we have already seen, the CL intensity can be expressed as the product of the internal quantum efficiency (η_{IQE}), the light extraction efficiency (η_{LEE}), and the

injection efficiency (η_{inj}) (4.1).

$$I_{CL} \propto \eta_{inj} \times \eta_{IQE} \times \eta_{LEE} \tag{4.1}$$

$$\tau_{CL} = \eta_{IQE} \times \tau_{rad} \tag{4.2}$$

For this reason, to be sensitive only to the local change in IQE, a more appropriate approach is to probe the carrier lifetime (τ_{CL}), as it depends only on the IQE and the radiative lifetime (4.2).

In the following, we will see how we can use spatially-resolved time-correlated cathodoluminescence measurements to quantify the influence of surface recombinations in µLEDs.

4.1.4.1 Experimental setup and first results

In order to probe the CL lifetime with the best possible spatial resolution, we here use our HBT setup. Figure 4.5 (a) shows a schematic of the experimental setup. As the two detectors are not at the output of the spectrometer, we use a combination of a shortpass ($\lambda < 500\,\text{nm}$) and longpass ($\lambda > 400\,\text{nm}$) filters to select the emission coming from the MQW (see figure 4.5 (b)). Both filters are tilted to avoid reflections, which are a problem in time-resolved or time-correlated measurements as they add a delayed signal in addition to the main signal.
Note that the spectra displayed in figure 4.5 were taken in a large area containing both the mesa and the surrounding etched region. From additional CL mapping, it is clear that the GaN NBE and YL mainly arise from the etched region (figure 4.4 (b) and (d)) while the MQW CL comes from the mesa itself (figure 4.4 (c)).

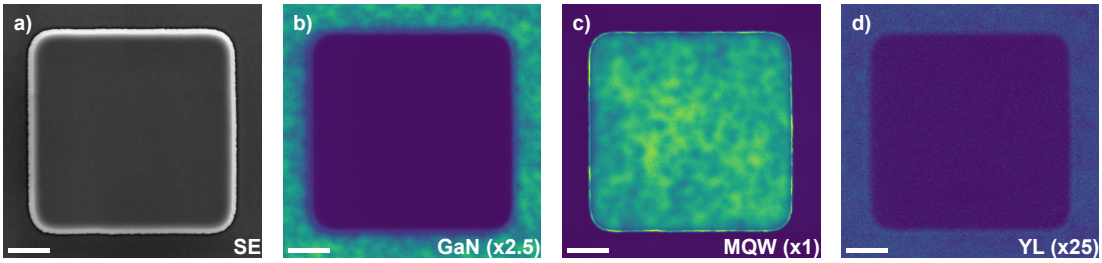

FIGURE 4.4: (a) SE image of a $10 \times 10\,\mu\text{m}^2$ mesa with its corresponding monochromatic CL images at : (b) the GaN NBE energy, (c) the MQW energy, and (d) the YL energy. Note that the intensity of the GaN NBE has been multiplied by 2.5 and the YL by 25. All measurements were performed at 10 kV.

Here again, the spatial resolution is mainly determined by the acceleration

voltage, as discussed earlier. To achieve the best possible spatial resolution while still efficiently probing the MQWs, we fixed the acceleration voltage to 10 kV for the rest of the study. Also, the probe current has been set to 4 pA, which is the lowest current possible at 10 kV in our setup.[1]

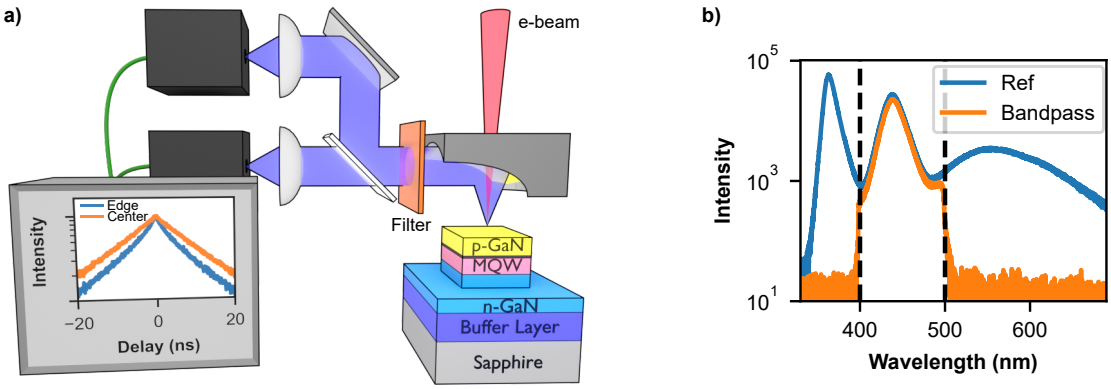

FIGURE 4.5: (a) Schematic of the SRTC-CL experimental setup. (b) CL spectra obtained at 10 kV with and without bandpass filter ($\lambda = 450 \pm 50$ nm)

We first investigated the carrier lifetime evolution across a single mesa. Figure 4.6 shows an SE image (a) of a 3-µm large mesa together with its simultaneously acquired CL image (b). In analogy to time-resolved measurements, we display normalized autocorrelation functions for positive delays in figure 4.6 (c). The corresponding scanning spots are color-coded and indicated in figure 4.6 (a) and (d).

From figure 4.6 (c), we can see that the intensity does not follow a mono-exponential decay, especially near the edges. This is probably related to both fluctuations in bulk [Pop+00] and surface recombinations. This matter will be discussed in more detail later. Here, to extract quantitative information, we fitted the g^2 decays with the autocorrelation of a stretched exponential [Sol+21]:

$$g^2 \propto \int_0^\infty f(t) f(t+t') dt' \tag{4.3}$$

With

$$f(t) = \exp\left(-(t/\tau)^\gamma\right) \tag{4.4}$$

where τ is the CL lifetime and γ is the stretching exponent.

The CL lifetime across the mesa is displayed in figure 4.6 (d). It roughly follows a bell-shaped curve with a maximum of ∼10.5 ns in the mesa center. As

[1] We recall that the time between two consecutive probe electrons must be large enough to allow the e-h pair to recombine in order to observe the bunching.

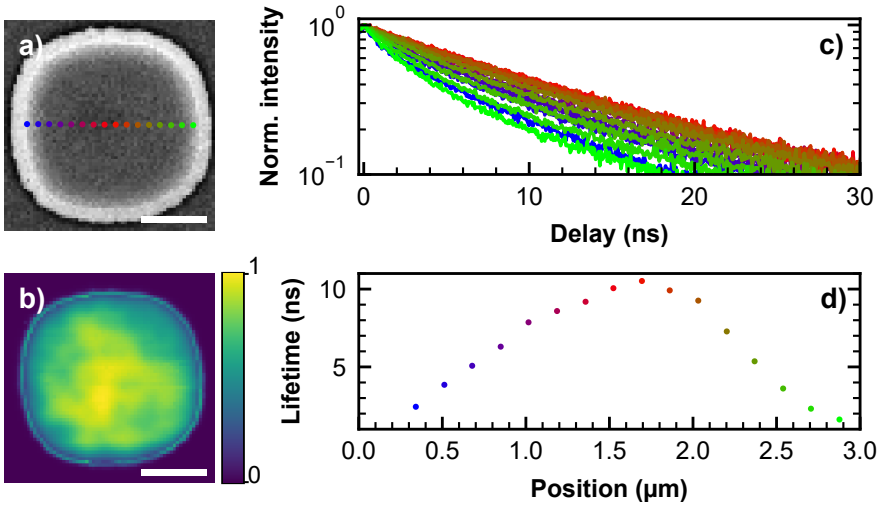

FIGURE 4.6: (a) SE image of a 3-µm large mesa and (b) the corresponding CL image at MQW energy. The scale bar is 1-µm long. (c) Normalized g^2 for different positions (colored dots in (a)) on the mesa. (d) CL lifetime as a function of the position across the mesa.

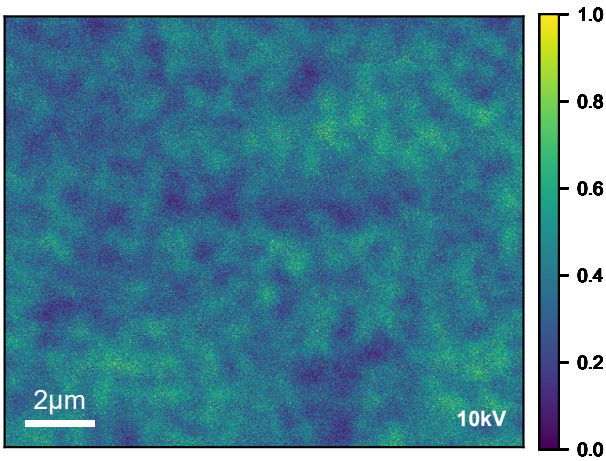

FIGURE 4.7: CL image at the quantum well energy ($440 \pm 10\,\mathrm{nm}$) acquired at $10\,\mathrm{kV}$ in the middle of a $2 \times 2\,\mathrm{mm}^2$ mesa

the electron beam approaches the sidewalls, the CL lifetime decreases. Near the sidewalls, the carrier lifetime is less than 3 ns, highlighting the detrimental role of non-radiative surface recombinations, as discussed in the following.

However, it should be noted that the shape of the curve may suggest that the surface recombinations have an impact even in the middle of the mesa. Moreover, the left and right edges do not seem to behave in the same way. The left edge appears to impact the carrier lifetime on a wider area. This effect can be linked to the inherent spatial fluctuations of CL intensity of the MQW (see figure 4.3 (c)). Indeed, even in the absence of any etching, the IQE of the active area can vary locally due to the presence of non-radiative centers such as dislocations or point defects. For example, see figure 4.7 for a CL image acquired in the middle of a $2 \times 2\,\mathrm{mm}^2$ mesa showing similar fluctuations. Due to the nanoscale resolution of SRTC-CL, this may locally modify the probed CL lifetime.

In order to average these fluctuations without compromising the spatial resolution, it is necessary to average the signal in the parallel direction to the sidewalls. Thus, instead of measuring the CL lifetime point by point, it is necessary to integrate the CL signal parallel to an edge.

4.1.4.2 Averaged measurements

To accurately measure the effect of surface recombinations, we now focus our investigation on the center of a single edge of a 100 µm large mesa, with the same experimental conditions as above (*i.e.,* a 10 kV acceleration voltage and 4 pA probe current).

Figure 4.8 shows a SE image (a) with its simultaneously acquired CL image (b) at the MQW energy near a sidewall. As discussed above, we noticed a local CL intensity enhancement when the e-beam is on the sidewall due to an increase in e-h pair generation in the active region. In addition, we observe random spatial fluctuations in the mesa itself due to the presence of non-radiative defects.

In figure 4.8 (c), different averaged profiles are displayed. First, "SE real-time" and "CL real-time" correspond to the images (a) and (b) integrated vertically. By averaging, the intensity fluctuations are smoothed out, and the surface-related effects are becoming more apparent. We observe that the maximum of the CL intensity is reached in the vicinity of the sidewall. More precisely, it matches a dip in the SE signal. This dip is assigned to the presence of the AlGaN EBL. As expected from our Monte-Carlo simulations, this corresponds to the situation where the overlap between the interaction volume and the active region is maximum. It should be noted that even after averaging, the CL signal still shows some

[2] To be precise, these measurements were performed on a passivated sample (KOH + Al_2O_3), see more details in an upcoming subsection.

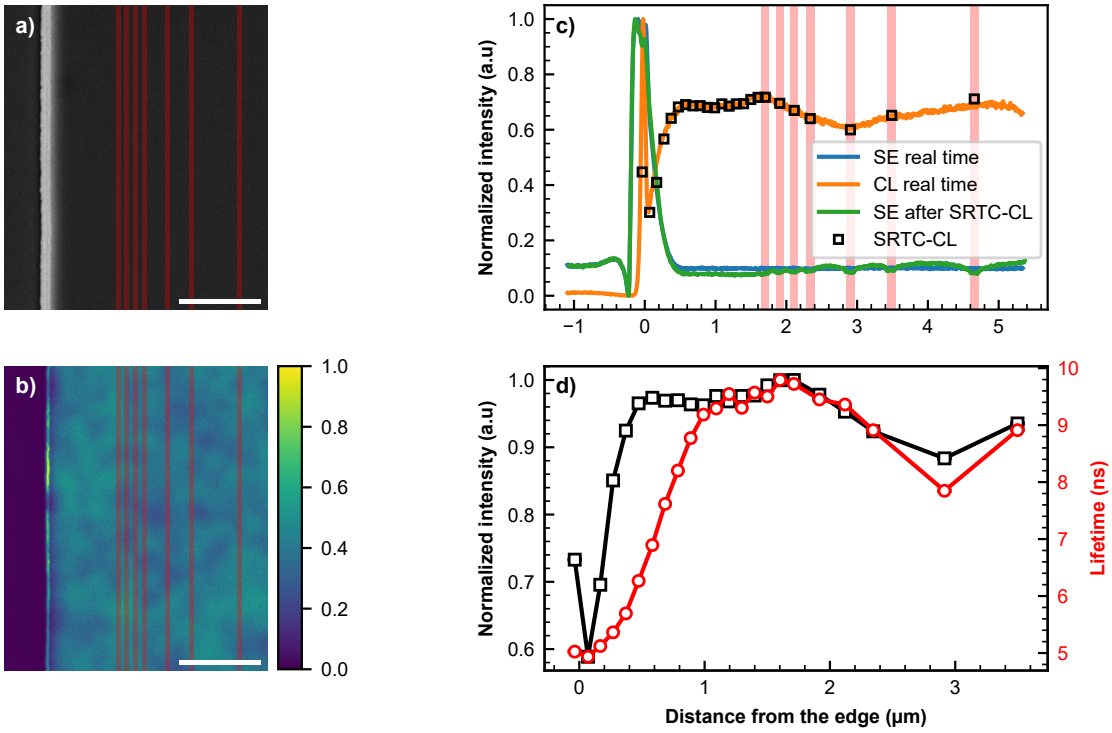

FIGURE 4.8: (a) SE image near an edge of a 100-µm large mesa[2] and (b) the corresponding CL image at MQW energy (440±10 nm). The scale bar is 2-µm long. (c) Various SE and CL profiles averaged parallel to the edge. (d) Normalized CL intensity (black squares) and CL lifetime (red circles) as a function of the distance from the edge simultaneously acquired with the SRTC-CL setup. Examples of acquisition rectangles are displayed as red stripes on (a), (b), and (c).

small fluctuations in intensity away from the edge but these are limited to ∼5 %. Finally, we observe that from a distance of about 450 nm from the edge, the CL signal decreases due to surface recombinations.

For SRTC-CL measurements, in order to maintain the spatial resolution while averaging, we shaped the e-beam in a rectangle with a width of 100 nm and a height of ∼7 µm. Examples of such rectangles are shown in red in figure 4.8 (a) and (b). The normalized CL intensity and the CL lifetime, both acquired with the SRTC-CL setup, are shown as a function of the distance from the edge in figure 4.8 (d).

Before going into the interpretation of the results, let us summarize the entire acquisition procedure:

1. A SE and CL image are simultaneously acquired with the standard CL setup (a) and (b). The averaged profiles are shown in figure 4.8 (b) as "SE real-time" and "CL real-time".

2. CL intensity and lifetime are measured in different rectangles with the SRTC-CL setup. The results are displayed in (d). In addition, some acquisition

rectangles are shown in red in (a) and (b). The acquisition time is in the order of 2 minutes per rectangle.

3. To measure the drift relative to the first image (a), and correct it if necessary, a new SE image is taken. The corresponding profile is visible on (b) "SE after SRTC-CL". The new positions (*i.e.*, drift-corrected) of SRTC-CL measurements are then computed assuming a linear drift over time.

4. Lastly, we can ensure that the drift correction is correct by verifying that the scanned rectangles' positions match the dips induced by the surface contamination in "SE after SRTC-CL." Also, we can verify that the intensity profile measured with the SRTC-CL setup is in agreement with the one measured with the PMT at the beginning of the measurements (black squares and orange line on (c)).

Concerning the CL lifetime, two regimes can be identified. First, far from the edge, the variations of CL lifetime are correlated with CL intensity variations. In this region, both the CL lifetime and CL intensity reflect the local change in IQE. However, in a ∼1 µm band close to the etched surface, the situation is different. Indeed, between 450 nm and 1 µm from the edge, the CL lifetime decreases while the CL intensity remains almost unaffected. The CL intensity decreases significantly when the distance from the e-beam to the edge is less than 450 nm.

Here, we can exclude the possibility of measurement error by pointing out that the intensity and lifetimes presented in figure 4.8 (d) are acquired simultaneously. Moreover, the intensity measured with the SRTC-CL setup is perfectly superimposed on the one measured with the PMT (see figure 4.8 (c) orange line and black squares).

Therefore, it is clear that the CL intensity and CL lifetime do not carry the same information near the surface. This can be understood as we previously saw that :

$$I_{CL} \propto \eta_{inj} \times \eta_{IQE} \times \eta_{LEE} \tag{4.1}$$

$$\tau_{CL} = \eta_{IQE} \times \tau_{rad} \tag{4.2}$$

We can see that a change in CL intensity could be attributed to either a local change of η_{LEE}, η_{IQE}, or η_{inj}. On the other hand, τ_{CL} only depends on η_{IQE} and τ_{rad}. Hence, the observed decrease of τ_{CL} could be linked to a reduction of radiative lifetime or IQE near the surface.

First, concerning the radiative lifetime, τ_{rad} could be affected by a local change in the internal electric field induced by the strain relaxation. To quantify this effect, we performed 6×6 k.p simulations, taking into account the strain relaxation and

the electric field with the software nextnano3 [Bir+07]. The parameters used for the simulations can be found in [VM03]. We observed that the change in spatial e-h overlap is limited, with on average, a maximum variation of 20 % within the first 200 nm from the edge depending on the QW (see appendix 4.A). This cannot explain the trend followed by τ_{CL}. Thus, we conclude that the variation of τ_{CL} is mainly dominated by non-radiative recombinations at the sidewall surface. From the CL lifetime profile near the edge, it is clear that surface recombination plays a role up to 1 µm which already gives an estimation of the lateral diffusion length in the MQW region.

Therefore, if the IQE is decreasing near the sidewall, to explain the near-constant CL intensity between 450 nm and 1.1 µm from the edge, either η_{inj} or η_{LEE} has to increase in this region. However, no local variation of η_{inj} is expected from our Monte-Carlo simulations (figure 4.3 (e)). As a result, the different trend between CL lifetime and intensity in this region certainly arises from a local increase in LEE. The origin of this increase could be explained by light scattering at the sidewalls [Cho+03], increased sidewall emissions [Ma+12] or total internal reflections which could redirect the light to a more favorable angle for extraction [Ley+20].

To extract quantitative information from lifetime profiles, we then develop a 1D diffusion model taking into account non-radiative surface recombinations.

4.1.5 1D diffusion simulations

This section introduces the diffusion model that we developed to describe our results. Then, thanks to this model, we will study the effect of a surface passivation technique already reported in the literature.

4.1.5.1 Introduction of the diffusion model

Our model is based on Fick's second law of diffusion with an additional term to take into account bulk recombinations (4.5).

$$\begin{cases} \dfrac{dn}{dt} = D\left(\dfrac{\partial^2 n}{\partial x^2}\right) - \dfrac{n}{\tau_{bulk}} & (4.5) \\ D\left(\dfrac{dn}{dx}\right)_{x=0} = Sn(x=0) & (4.6) \end{cases}$$

where n is the local carrier density, D is the ambipolar diffusion coefficient, and τ_{bulk} the bulk effective lifetime. It is important to note that in our case, we assume that τ_{bulk} does not depend on the carrier concentration. This holds here because

the nature of the measurement relies on very low excitation (one electron every few lifetimes) to observe the bunching effect. A more detailed justification of this assumption can be found in appendix 4.B.
In addition, an adapted boundary condition (4.5) is used to take into account the surface recombination velocity S at the edge. Also here, as we are interested in the effect of a single edge, the simulation domain is taken sufficiently large (>10 µm) to simulate a semi-infinite pixel.

As for the initial condition, an initial carrier concentration profile following a Gaussian distribution centered at the excitation position x_0, with a standard deviation of 150 nm, corresponding to the excitation volume's lateral extension at 10 kV, is generated. Then, the model is numerically integrated both in space and time by finite differences. Technical details about the implementation, performance and possible optimizations can be found in appendix 4.D.

With this model, for a given excitation position x_0, we obtain for each time step the carrier density profile over the whole sample. We extract a lifetime by fitting the decay of the carrier density integrated over the whole simulation domain N to a stretched exponential

$$N(t) = \int n(x,t)dx$$
$$N(t) \propto \exp\left(-(t/\tau_{eff})^{\gamma}\right)$$

We have chosen a stretched exponential because the decay of the carrier density depends on the diffusion and is therefore not constant in time. Figure 4.9 shows the decay of the normalized carrier density for different surface recombination velocity at (a) 100 nm and (b) 1000 nm from the edge. For carriers generated near the edge (a), the decay is faster at the beginning because they are exposed to surface recombination, and slower afterwards, because some of them diffuse away from the edge ($\gamma/\gamma_{bulk} < 1$). On the contrary, for carriers generated at a certain distance from the edge (b), initially no carriers are close to the edge thus the decay rate doesn't depend on S, then the decay rate increases as the carriers start to reach the edge due to diffusion ($\gamma/\gamma_{bulk} > 1$).

We should note, however, that the stretched exponential does not accurately reproduce the simulated decay far from the edge (figure 4.9 (b)), especially at low delay where the carriers initially experience bulk-like recombination dynamics. In other words, an increase of γ is not the most appropriate way of describing the delay induced by the diffusion. Nevertheless, we can still use the stretched exponential model as a metric to compare simulations and data. This can be seen in figure 4.10, where the trend followed by γ is observed both in the simulations and in experimental data. Additionally, we note that even at a distance of 5 µm to the

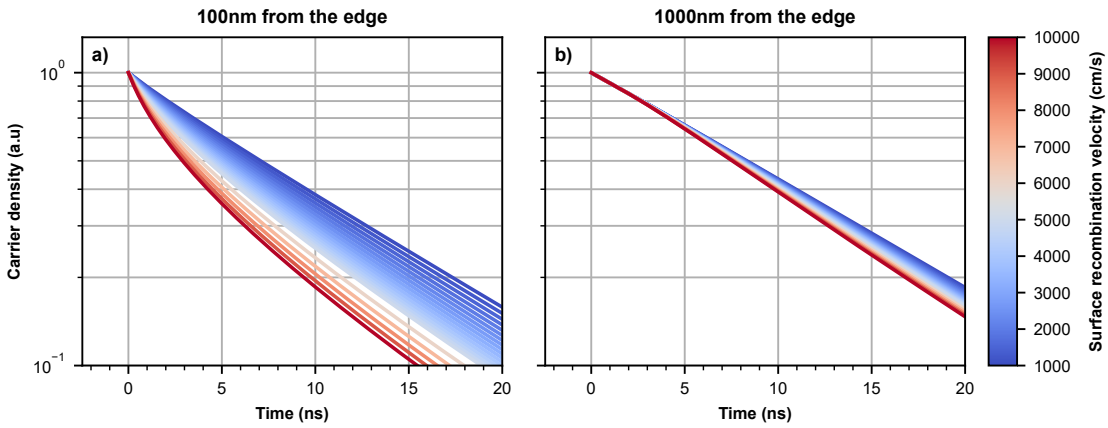

FIGURE 4.9: Decay of the normalized carrier density for different surface recombination velocity at (a) 100 nm and (b) 1000 nm from the edge.

edge, γ is not equal to 1 for the experimental data. This is probably due to the role of carrier localization in the recombination carrier dynamics, as already described by Pophristic et al. [Pop+00], hence the choice of the stretched exponential.

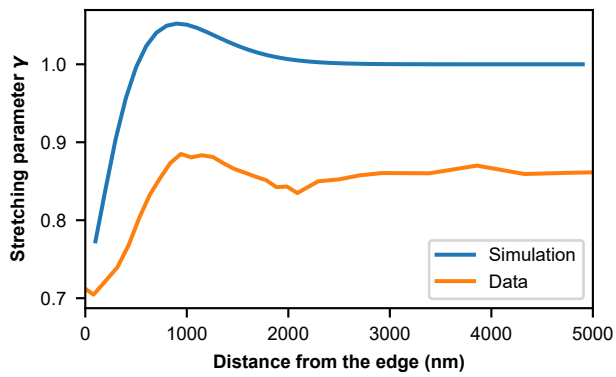

FIGURE 4.10: Stretching parameter as a function of the distance to the edge for simulation and experimental data.

In figure 4.11 the role of the diffusion coefficient D and the surface recombination velocity S are more clearly exposed. It can be seen from figure 4.11 (b) that D mainly governs the lateral extension of the affected area while S is responsible for the decrease of the lifetime in the affected area.

More precisely, it is possible to get a approximation of the lifetime profile by studying the solution of the steady-state under constant excitation (see appendix 4.C for more details). We can define $\tau_{eff}(x)$ as

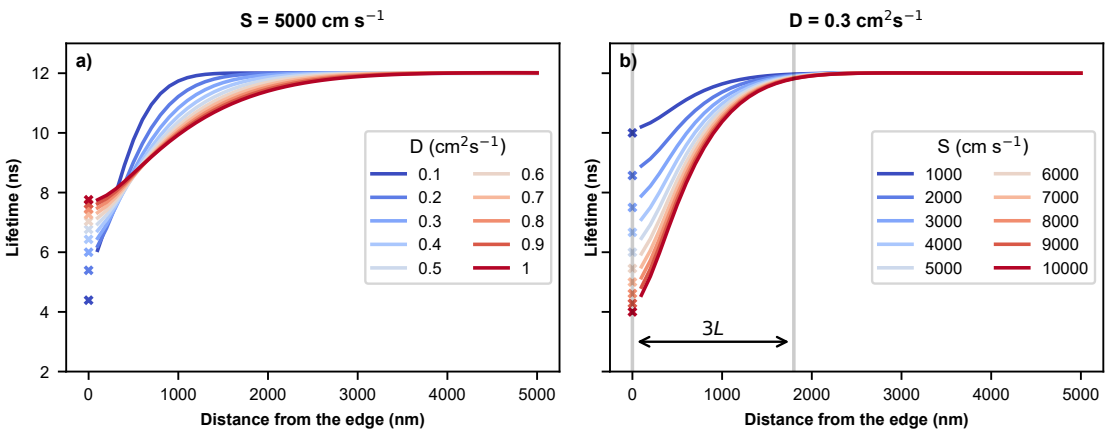

FIGURE 4.11: Lifetime profile as a function of the distance from the edge for (a) different value of D and a fixed S and (b) a fixed D and different value of S (solid lines). Approximation of lifetimes at the edge are displayed as crosses (see 4.C for more details).

$$\tau_{eff}(x) \approx \tau_{bulk}\left[1 - \frac{e^{-x/L}}{1 + \frac{L}{S\tau_{bulk}}}\right] \qquad \text{With } L = \sqrt{D\tau_{bulk}} \tag{4.7}$$
$$\implies \tau_{eff}(0) \approx \frac{\tau_{bulk}}{1 + \tau_{bulk}\frac{S}{L}}$$

In figure 4.11, approximations of the lifetimes at the edge are displayed as crosses. They are in relatively good agreement with the lifetimes obtained by simulations. Also, from (4.7) the lifetime profile should exhibit an exponential-like behavior with a characteristic length of L, which is also observed in the simulations. This tells us that the affected area is in the order of $3L$ (figure 4.11)

However, one should be careful by using it, as the difference between simulations and the approximation increases as D decreases (figure 4.11 (a)). Nevertheless, this approximation can be useful to obtain a first guess of the parameters, as simulations can quickly become computationally expensive:

- We can get D as the affected area is $\simeq 3L$
- From equation (4.7), $S \approx L({\tau_{eff}}^{-1}(0) - {\tau_{bulk}}^{-1})$

Furthermore, we observe that if D and τ_{bulk} are constant,*i.e.*, same bulk material, it implies that one can simply use the lifetime close to the edge to compare S in different samples. This would allow, for instance, a quick estimation of the effectiveness of different passivation techniques.

Now that our model is well defined, we can use it to extract D and S in our InGaN/GaN µLEDs.

4.1.5.2 Validation of the model

In order to validate our model, we passivated our sample by first performing a room-temperature KOH etching (10 min with a mass concentration of about 1 %) followed by an Al_2O_3 deposition by atomic layer deposition (30 H_2O/TMA cycles at 250 °C). A similar technique has already been reported in [Ley+20].

Note that the main point here is not the passivation technique but rather the characterization process. More detail about the passivation can be found in Corentin Le Maoult. "Etude et optimisation de l ' étape de passivation des µLED bleues GaN-InGaN". PhD thesis. 2021 (in french).

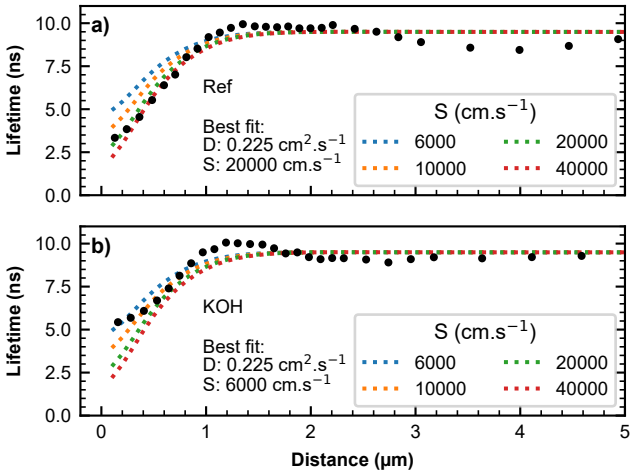

FIGURE 4.12: Lifetime profile of the untreated sample (a) and treated with a KOH etching followed by a deposition of Al_2O_3 by atomic layer deposition (b) (black dots). 1D diffusion simulations for different surface recombination velocities are also shown as dotted lines.

As expected, we observed in figure 4.12 (b) that the lifetime near the surface increases from 3.5 ns for the reference sample to 5.5 ns for the sample after KOH and Al_2O_3 treatment.

	τ_{eff} (ns)	S (10^3 cm s^{-1})	D (cm^2 s^{-1})
Ref	9.5 ± 0.5	14.8 ± 4.2	0.35 ± 0.11
KOH	9.7 ± 0.5	6.9 ± 1.4	0.34 ± 0.12

TABLE 4.1: Extracted model parameters for the reference sample (Ref) and passivated (KOH) sample. The uncertainty corresponds to one standard deviation.

A statistical study has been then performed on 7 different sidewalls for both the reference and the treated samples. We then applied the fitting procedure to extract D and S (table 4.1). As expected, we observed that only the surface recombination velocity changes from about $\sim 1.5 \times 10^4$ for the reference sample

to about $6.9 \times 10^3\,\mathrm{cm\,s^{-1}}$ for the sample after KOH and Al_2O_3 treatment while the diffusion coefficient remains around $0.34\,\mathrm{cm^2\,s^{-1}}$. These values are in line with previously published data obtained with other experimental techniques. Typical values of D can be found between 0.1 and $2\,\mathrm{cm^2\,s^{-1}}$ [Jar+05; SDS13; Ale+14] and S has been previously reported between 10^3 and $10^4\,\mathrm{cm\,s^{-1}}$ for etched III-nitride µLEDs [BK16; BKK18].

Summary We have developed a 1D model based on Fick's second law of diffusion. By fitting the lifetime profile close to an edge, we have demonstrated the possibility of extracting quantitative information on the fundamental parameters, which are the ambipolar diffusion coefficient D and the surface recombination velocity S, in agreement with the values found in the literature. This method could be used to characterize various surface passivation techniques, as the intensity could reflect changes in injection or light extraction efficiency.

4.1.5.3 IQE estimation using radial simulations

From our experimental results, we deduce the diffusion coefficient D and surface recombination velocities S for standard µLEDs. It is interesting now to see how the non-radiative surface recombinations affect the efficiency of electrically injected µLEDs.

Here, we consider now cylindrical devices of diameter d, with an initial carrier concentration n constant over the whole surface. Carriers are subject to diffusion to the surface where they recombine non-radiatively. This model is equivalent to evaporation from the surface of a cylinder, which has been solved analytically in [Cra75, p. 79]. The idea of using this solution to quantify surface recombination in semiconductors was first introduced by Daiminger et al. [Dai+94] to measure S and D in InGaAs/GaAs quantum dots, and later by Allen et al. [All+08] to show that surface recombination is a significant recombination path in Si nanowires. In these conditions, the effective carrier lifetime τ_{eff} is given by:

$$\frac{1}{\tau_{eff}} = \frac{4D\beta^2}{d} + \frac{1}{\tau_{bulk}} \tag{4.8}$$

where β is the solution of the transcendental equation:

$$\beta J_1(\beta) - \frac{Sd}{2D} J_0(\beta) = 0 \tag{4.9}$$

With J_0 and J_1, the Bessel functions of the first kind of zero and first order respectively.

Figure 4.13 shows relative IQE, defined as the ratio of the effective lifetime τ_{eff}

and bulk lifetime τ_{bulk}. It clearly illustrates the IQE reduction, from a large LED to an etched µLED.

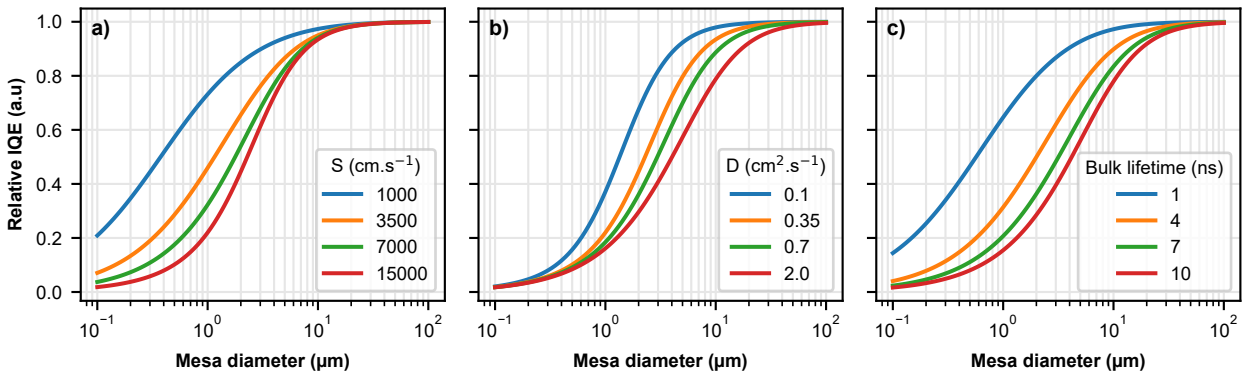

FIGURE 4.13: Relative IQE, defined as the ratio $\frac{\tau_{eff}}{\tau_{bulk}}$, showing the impact of (a) the surface recombination velocity, (b) the ambipolar diffusion coefficient, and (c) the bulk lifetime. When not explicitly specified $S = 15000\,\mathrm{cm\,s^{-1}}$, $D = 0.35\,\mathrm{cm^2\,s^{-1}}$ and $\tau = 9.5\,\mathrm{ns}$

First, in figure 4.13 (a), we set the diffusion coefficient $D = 0.35\,\mathrm{cm^2\,s^{-1}}$ and the bulk lifetime to $\tau = 9.5\,\mathrm{ns}$. We observe that the IQE remains unaffected by sidewall recombinations for diameter above ∼20 µm. However, below this limit, the IQE drops drastically. For small diameter, the IQE can be partially recovered if the surface recombination velocity is reduced.

In figure 4.13 (b), we set the recombination velocity to $S = 15000\,\mathrm{cm\,s^{-1}}$ and the bulk lifetime to $\tau = 9.5\,\mathrm{ns}$. In this case, we vary the diffusion coefficient from 0.1 to $2\,\mathrm{cm^2\,s^{-1}}$. We observe that by reducing the diffusion coefficient to $0.1\,\mathrm{cm^2\,s^{-1}}$, it is possible to maintain a good IQE for µLEDs with diameter of 3 µm.

Finally, in figure 4.13 (c), the influence of bulk effective lifetime is investigated. In this case, the recombination velocity is set to $S = 15000\,\mathrm{cm\,s^{-1}}$ and the diffusion coefficient to $D = 0.35\,\mathrm{cm^2\,s^{-1}}$. Thus, by increasing the recombination rate by one order of magnitude, it is possible to maintain the bulk IQE value for µLEDs with a diameter down to 2 µm. It should be noted that here, changing the lifetime has a more significant impact than changing the diffusion coefficient. This is understandable since the role of the lifetime is twofold. Not only does it reduce the diffusion length, but for an equal diffusion length, it also allows to favor the radiative processes and thus reduces the impact of surface recombination. In other words, there is competition between radiative and surface recombinations. Note that this point is valid only if surface recombinations are independent of the radiative lifetime, which is not necessarily the case.

4.1.5.4 Guidelines towards efficient µLEDs

From our experimental results and model, it is clear that non-radiative surface recombinations play an important role and cannot be neglected in µLEDs with a diameter in the micrometer range. However, we can draw some guidelines for the development of efficient µLEDs. Indeed, as shown in the previous section, three important parameters govern the IQE: the surface recombination velocity S, the diffusion coefficient D and the bulk effective lifetime τ_{bulk}. Thus, several directions are possible to mitigate the detrimental role of the surface.

First, starting with the most obvious, one way to improve the efficiency is to reduce S itself. Here again, this could be done in several ways, such as reducing the damages introduced by the etching process or even implementing damage-free etching processes. Among these techniques, atomic layer etching (ALE) [Ohb+17; Man+20] or neutral beam etching [Zhu+19] could be an alternative to reduce damages caused by ions bombardment in the commonly used ICP-reactive ion etching (RIE) etching. Particularly, Zhu et al. used this technique to demonstrate µLEDs with diameters ranging from 40 to 6 µm without significant EQE reduction [Zhu+19]. In addition, optimized post-treatment and surface passivation could be developed to recover from the etching process [Won+18; Ley+20].

Another way of reducing the influence of the surface is to reduce the diffusion length. Indeed, as we have seen, the affected area is proportional to the diffusion length. As the diffusion length depends on both the lifetime and the diffusion coefficient, two possibilities can be considered. One can consider to decrease the diffusion coefficient D by engineering the potential fluctuation landscape, as modeled by Shen et al. [She+21]. However, this technique is probably not the easiest to implement and may require considerable effort on the growth side. Finally, the last option is to enhance the recombination rate. This could be achieved by reducing the QW thickness [Wea+21], increasing the driving current [Dav21] or by using semi-polar or non-polar structures. Regarding all these aspects, core-shell microwire LEDs could also be an attractive solutions to produce efficient µLEDs with dimensions below 5 µm.

4.1.6 Conclusion of the study

In conclusion, in this section, we have highlighted variations in injection efficiency and probably in extraction efficiency. These variations prevent accurate measurement of the sidewall-induced IQE drop, a fundamental parameter for an early optimization of the µLED structure. Thanks to SRTC-CL, we were able to measure the evolution of the lifetime through mesas of different sizes. By coupling this analysis to a diffusion-recombination model taking into account the surface

recombinations, we extracted the fundamental parameters, namely D and S, in agreement with the typical values already published. We then gave some guidelines to reduce the impact of recombination on the IQE.

4.2 Extending the method to AlGaInP red µLED

In this section, we propose to study briefly surface recombinations in red AlInGaP based µLEDs. This study is more a demonstration of the applicability of the method to other materials and other wavelength ranges than a complete study. The µLEDs studied here have been realized in the framework of the PhD thesis of Younes Boussadi, a former PhD student of CEA-LETI. The reader can find a detailed characterization (SIMS, time-resolved photoluminescence, CL) of the etched LEDs in the following paper: "Investigation of sidewall damage induced by reactive ion etching on AlGaInP MESA for micro-LED application" [Bou+21].

4.2.1 Context

In order to achieve fully-functional micro-displays, it is necessary to have blue, green, and red µLEDs. Despite considerable efforts, III-nitrides-based LEDs still perform poorly in the red [Auf+16], whereas AlGaInP-based LEDs can have IQE exceeding 90% [Hor+18]. However, the miniaturization of these LEDs is less advanced than its III-nitride counterpart. One reason is that AlGaInP-based LEDs are known to suffer from higher surface recombination velocity and diffusion coefficient than III-nitride-based LEDs [Bor+00; BK16].

4.2.2 Studied sample

A schematic of the stack can be found in figure 4.14. It is commercially grown on lattice matched GaAs substrates. It consists of an undoped active region with five InGaP QWs separated by $Al_{x1}Ga_{1-x1}In_{0.48}P$ barriers. The active region is sandwiched between three undoped layers of $Al_{x1}Ga_{1-x1}In_{0.48}P$, $Al_{x2}Ga_{1-x2}In_{0.48}P$ (x2 > x1) and GaAs, respectively. This stack is then reported on a silicon substrate and squared mesa of various dimension are formed by BCl_3/Ar ICP-RIE.

Figure 4.15 (a) shows a secondary electron image of an etched mesa. We can see that the top surface, *i.e.*, the GaAs layer, is rough, probably due to the removal of the hard mask [Bou22]. Note that CL and secondary electron intensities are anticorrelated, *i.e.*, dark areas in secondary electron correspond to intense areas in CL and vice versa. This can be clearly seen by comparing the inverted version of

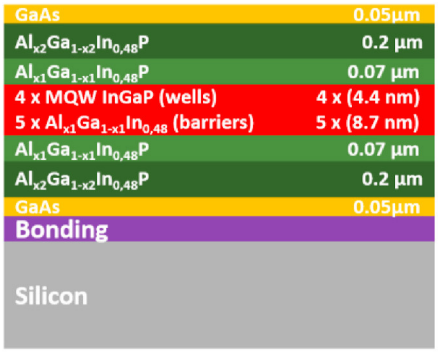

FIGURE 4.14: Schematic of the studied sample. [Bou+21]

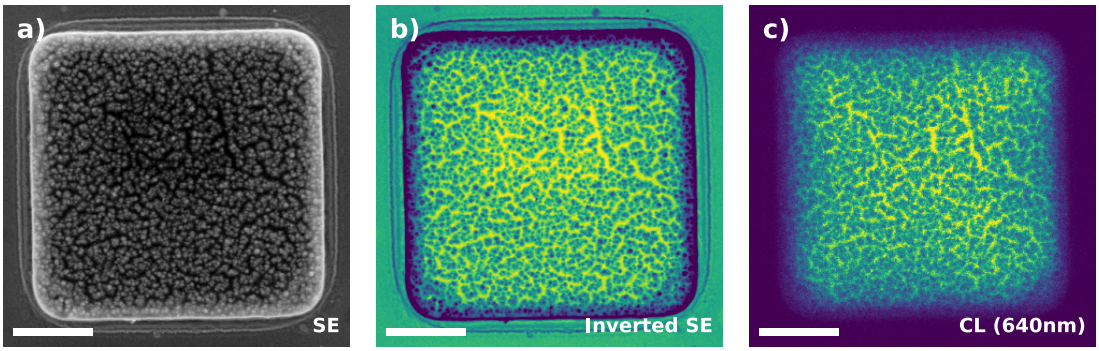

FIGURE 4.15: secondary electron image of an etched mesa (a) and its color-coded inverted version (b). CL image at the QWs energy (c). The anti-correlation between secondary electron and CL is visible when comparing images (b) and (c). The scale bar is 2 µm long and the measurements were performed at 10 kV

the secondary electron image displayed with the same colormap as the CL image figure 4.15 (b–c). This can be explained by a change in injection efficiency.

4.2.3 SRTC-CL measurements

To measure the surface recombination velocity, we used the same method as before. The significant difference here is the use of the setup optimized for the visible/red part of the spectrum. Concerning the experimental conditions, the current was set to 90 pA and the acceleration voltage to 10 kV to probe the QWs efficiently. The current may seem high to be in the single electron regime, but it must be taken into account that lifetimes are much shorter than in blue LEDs previously studied. Typically 90 pA corresponds to a mean time between electrons of 1.78 ns, compared to a bulk lifetime of ∼600 ps, as we will see later.

Figure 4.16 (a) shows a secondary electron image of a etched mesa with colored dots indicating the position of the spatially-resolved time-correlated cathodoluminescence measurements. The corresponding histograms are shown in fig-

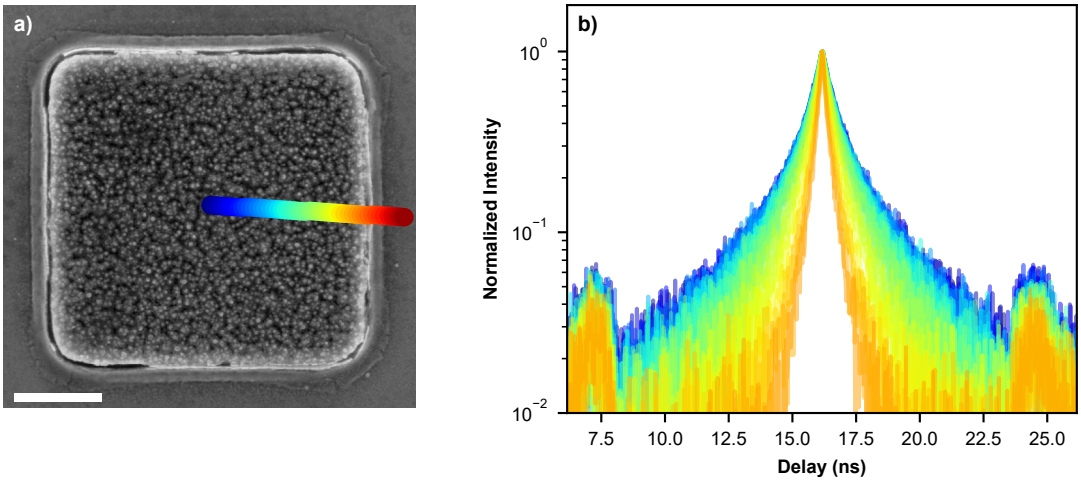

FIGURE 4.16: (a) SE image of a mesa, the scale bar is 2 µm long. (b) the corresponding normalized g^2 for different positions (colored dots in (a)) on the mesa.

ure 4.16 (b). We can directly see that the trend is as expected, identical to that of the blue µLEDs, with a lifetime decreasing near the edge due to surface recombinations. We also underline the presence of bumps at 16 ± 9 ns, attributed here to the afterglow of the detectors. Concretely, this corresponds to photons emitted after the detection of a photon by a SPAD detected by the second SPAD. It would eventually be possible to remove this artifact by adding a low pass filter in front of one of the two SPADs [Meu16, p. 32]. However, we did not need it here because the lifetimes are well below 9 ns.

By applying the same fitting procedure than used for the blue LEDs, we could extract lifetimes as a function of the distance to the edge figure 4.17. The bulk lifetime is roughly equal to 600 ps and drastically decreases to reach ∼200 ps close to the edge. The width of the affected area is approximately 1.1 µm. Then, using the 1D diffusion model developed previously with an initial carrier density following a Gaussian distribution with $\sigma = 170$ nm [Bou22], we could reproduce the trend followed by the lifetime.

However, as shown in figure 4.17, the uncertainties are more important here due to the large value of S and D. Indeed, even if a single set of parameters determines a lifetime profile, the variation induced by a change in D and S when D and S are large brings only a small variation in the lifetime profile. This is caused by the dependence in $(1 + \frac{\sqrt{D\tau}}{S\tau})^{-1}$ and was already pointed out earlier. According to our simulations, D should be between 4.5 to 7 $\mathrm{cm^2\,s^{-1}}$ and S in the 3×10^5–7×10^5 $\mathrm{cm\,s^{-1}}$ range. This was estimated by taking an arbitrary tolerance of 10% on the residuals of the best fit, namely D=5 $\mathrm{cm^2\,s^{-1}}$, S=5 $\times$ 10^5 $\mathrm{cm\,s^{-1}}$.

If we compare our values to published ones, Schultes et al. found a diffu-

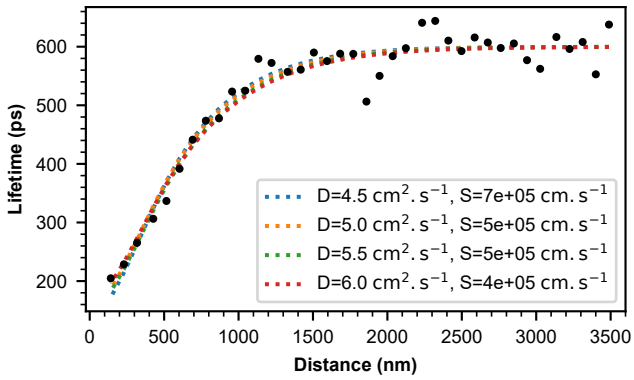

FIGURE 4.17: Lifetime profile (black dots) with 1D diffusion simulations for different surface recombination velocities and diffusion coefficient.

sion length of ∼3 µm in undoped GaInP sample for a corresponding lifetime of ∼15 ns [Sch+13]. This corresponds to a diffusion coefficient approximately equal to 6 $cm^2 s^{-1}$. Regarding the surface recombination velocity, values seem to be lower than what we have found, typically in the 2×10^4–10^5 $cm\,s^{-1}$ [Pea+93; Bor+00; BK16]. However, it is expected that this value depends very strongly on the surface quality and thus on the etching process.

We can also compare these results with those obtained previously on InGaN blue LEDs. First, here the lifetimes are ∼16 times shorter than for the blue InGaN wells (0.6 vs. 9.5 ns) but with a diffusion coefficient ∼14 times larger (∼5 vs. ∼0.35 $cm^2 s^{-1}$), resulting in an almost identical diffusion length. Then, we find that the surface recombination velocity is about 30 times larger (typically 5×10^5 vs. 1.5×10^4 $cm\,s^{-1}$). Therefore, one could expect the IQE to be more impacted than in InGaN LEDs. However, as shown in figure 4.18, which compares simulations of IQE as a function of mesa size for the blue and red LED, the difference between the two is relatively small. This is mainly due to the much shorter bulk lifetime, as discussed previously. Note, however, that this does not mean an identical IQE. Indeed, in the case of red LEDs, the intensity ratio between 300K and 30K is only 10% [Bou+21], suggesting a low IQE. Therefore, the short lifetime in bulk is possibly related to a short non-radiative lifetime. In other words, a similar LED with a higher IQE and, therefore, a longer bulk lifetime would be more impacted by surface recombination due to a longer diffusion length.

4.2.4 Conclusion

In conclusion, we have demonstrated that the methodology initially developed for blue InGaN/GaN µLEDs can also be applied to red AlInGaP µLEDs and more generally to other materials. Furthermore, we showed that despite a comparable diffusion length but a 33 times higher surface recombination velocity in InGaP

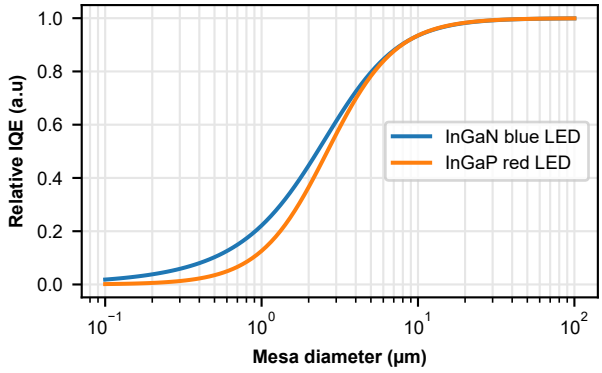

FIGURE 4.18: Simulated relative IQE for InGaN and InGaP µLED with the parameters extracted previously, *i.e.*, $S = 1.5 \times 10^4\,\mathrm{cm\,s^{-1}}$, $D = 0.35\,\mathrm{cm^2\,s^{-1}}$ and $\tau = 9.5\,\mathrm{ns}$ for InGaN blue LED and $S = 5 \times 10^5\,\mathrm{cm\,s^{-1}}$, $D = 5\,\mathrm{cm^2\,s^{-1}}$ and $\tau = 0.6\,\mathrm{ns}$ for InGaP LED.

LEDs compared to InGaN LEDs, a similar IQE reduction would be expected with mesa size due to a much shorter bulk lifetime. However, to remain critical, the uncertainties are larger. Therefore, unless it is essential to obtain a value of S and D, it is undoubtedly much simpler to compare only lifetime profiles or even bulk-to-edge lifetime ratios, provided that the lifetime and diffusion in bulk are identical from one sample to another. This is typically the case when studying etching or passivation processes.

4.3 Conclusion and perspectives

As a general conclusion, we have shown that it is possible to study surface recombination by measuring lifetimes at the nanoscale using a Hanbury Brown & Twiss interferometer coupled to a CL setup. This method offers the possibility to easily compare different etching and passivation methods without being sensitive to changes in injection or extraction efficiency.

Thus, with this new method, it could be interesting, for example, to study etching techniques not using ion bombardment, considered more gentle such as neutral beam etching [Zhu+19] or atomic layer etching [Man+20; Ohb+17]. Also, it could be interesting to study the effect of the etched shape. Indeed, etched mesas are traditionally squares or circles. However, in the case of III-nitride-based LEDs, the crystalline structure, *i.e.*, Wurtzite, has a hexagonal symmetry. Therefore, it can be assumed that this will have an impact on the surface termination and thus on dangling bonds. In addition, we have assumed that surface recombination velocity does not depend on bulk lifetime. It might be interesting to verify this, particularly as recombinations involving defects depend on the overlap of the electron and

hole wavefunction [Dav+20]. According to this hypothesis, S could also increase in thinner QWs, so the effect of the lifetime would only be to reduce the diffusion length and not twofold, as stated previously. Finally, if we consider a uniform defect surface density on the mesa sidewalls, the number of defects embedded in the QWs, or equivalently their linear density, depends on the QWs' thickness. Thus, it may be interesting to study this point as well.

Appendices

4.A Nextnano simulations

The idea here is to estimate the influence of a possible relaxation induced by the etching. The interpretation of the results should be taken with the greatest care as the simulated structure the one of a typical LED but does not necessarily match ours. Indeed, as our sample is a commercial LED, the exact epitaxy is unknown. We have based the simulated sample on assumptions from the optical study. As a result, it only gives us a qualitative picture of what the effect of strain on a typical µLED structure could be.

Simulation scheme and results

As shown in figure 4.A.1, we simulated a 1 µm wide mesa, constrained on GaN and surrounded by air to allow strain relaxation. From bottom to top, the simulated structure consists of a thin GaN buffer which imposes the strain, *i.e.*, considered as the substrate, a 200 nm n-GaN layer followed by five 3 nm-thick $In_0 \cdot 15\,Ga_0 \cdot 85\,N$ quantum wells. The GaN barriers are 15 nm thick. After the last barrier, there is a 15 nm $Al_{15}Ga_{85}N$ electron blocking layer. Finally, there is a 180 nm GaN layer. The entire structure is n-doped with a doping level of $10^{17}\,cm^{-3}$

The calculation scheme in nextnano is as follows, first, the strain is minimized. Then the new band structure taking into account the strain is calculated. Finally, the Schrödinger equation is solved in different regions for both electrons, using the effective mass model, and for holes using a 6×6 kp model. The parameters used can be found in Vurgaftman et al.[VM03].

Figure 4.A.2 (a) shows the normalized e-h) wavefunction spatial overlap defined in (4.10) as a function of the distance to the edge for the different quantum wells.

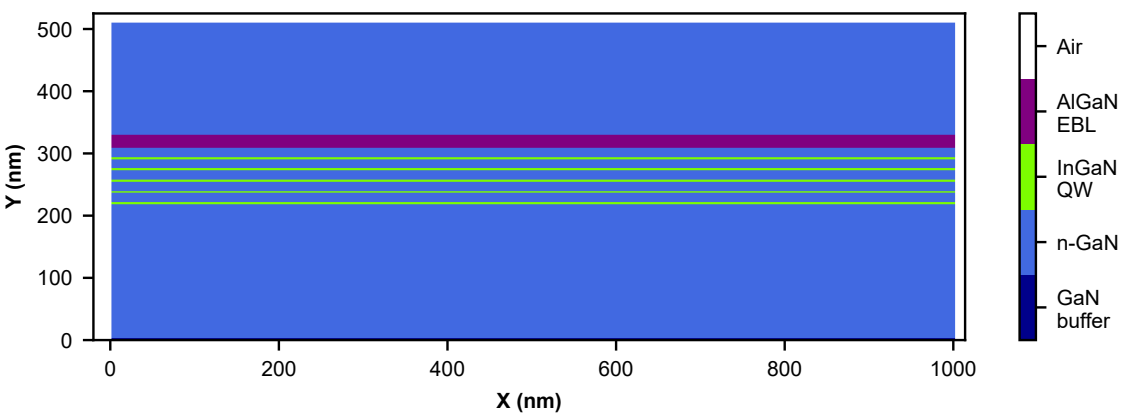

FIGURE 4.A.1: Schematic of the simulated structure

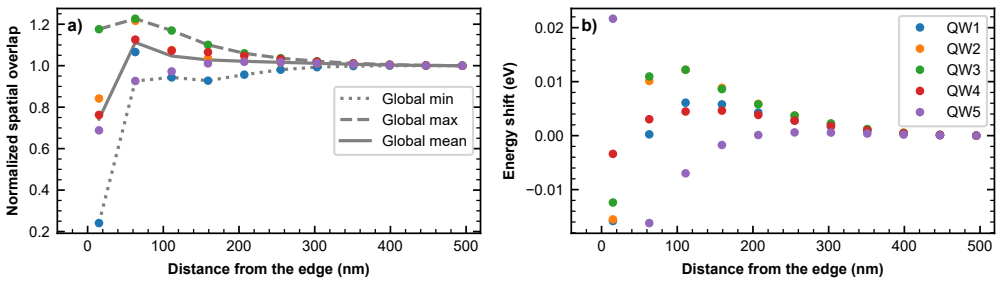

FIGURE 4.A.2: Normalized e-h wavefunction overlap (a) and energy shift (b) for the 5 QWs as a function of the distance to the edge

On average, the variation is contained within a 20 % interval, however, the overlap of the first QW, *i.e.* the furthest from the top surface, drops drastically in the vicinity of the edge. The energy shift, defined as the difference between the bulk energy and the energy at a given position is shown in figure 4.A.2 (b). This shift is maximal at the edge position, ranging from +22 to −16 meV depending on the QW. Note that, experimentally, no shift has been observed.

$$\text{Norm. spatial overlap} = \frac{|\langle \Psi_{hl}(x) | \Psi_{el}(x) \rangle|^2}{|\langle \Psi_{hl,bulk} | \Psi_{el,bulk} \rangle|^2} \tag{4.10}$$

$$\text{Energy shift} = E_{bulk} - E(x) \tag{4.11}$$

Influence of the e-h wavefunction overlap

The results presented in section 4.1.5 assumed a constant lifetime $\tau_{bulk}(x) \approx 12\,\text{ns}$. Here, as the lifetime should vary with the e-h wavefunction spatial overlap, we tried to use the spatial overlap calculated with nextnano3 (*cf* figure 4.A.2 (a)) as an input for the simulation. Basically we replaced the bulk lifetime τ_{eff} with :

$$\tau_{bulk}(x) = \frac{|\langle \Psi_{hl,bulk} | \Psi_{el,bulk} \rangle|^2}{|\langle \Psi_{hl}(x) | \Psi_{el}(x) \rangle|^2} \times \tau_{bulk,bulk}$$

As the spatial overlap did not follow the same trend in all quantum wells, we have chosen to compute only the extreme cases indicated in figure 4.A.2 as *global max*, *global min* and *global mean* which correspond respectively to the max, min and mean of the 5 quantum wells' e-h overlap at each position. The corresponding lifetime profiles are shown in figure 4.A.3 (a). Note that as the nextnano3 simulation was only 1 µm wide, the overlap is calculated only on the first 500 nm, *i.e.*, from the edge to the center of the mesa. Thus, normalized e-h wavefunction spatial overlaps are set to 1 for distances greater than 500 nm.

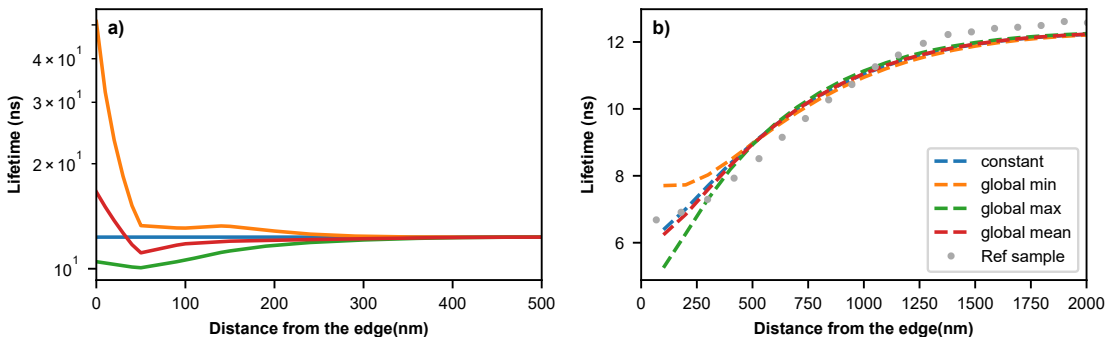

FIGURE 4.A.3: (a) Lifetime profile taking into account the e-h wavefunction spatial overlap calculated with nextnano3. (b) Diffusion model for various lifetime profiles with $D = 0.35\,\mathrm{cm}^2\,\mathrm{s}^{-1}$ and $S = 4750\,\mathrm{cm}\,\mathrm{s}^{-1}$

Figure 4.A.3 (b) shows results of the diffusion model for various lifetime profiles presented in figure 4.A.3 (a). Even when the lifetime is set to 50 ns near the edge (orange line), the corresponding lifetime profile obtained by fitting the carrier density with the stretched exponential only changes by about 1.5 ns, showing that non-radiative surface recombination prevails over change in radiative lifetime. Moreover, even taking into account the diffusion of the carriers, this effect is contained within the first 250 nm of the edge. Note, however, that a comparable trend with a much smaller amplitude is observed in the experimental data. This change of the bulk lifetime could be a second order effect.

4.B Carrier density independent lifetime

By performing a CASINO simulation, we could estimate the interaction volume. Here, for simplicity, we consider bulk GaN instead of the complete LED stack. This approximation should not be the main source of uncertainty as the quantum wells are thin (3 nm) compared to the total thickness of GaN. By taking as a criterion the volume where 90 % of the interactions occur, we estimate the volume V (see figure 4.B.1).

$$V = \frac{4\pi}{3} R_Z R_L^2 = \frac{4\pi}{3} \left(2.2 \times 10^{-5}\right)^2 \left(2.7 \times 10^{-5}\right) \approx 5.5 \times 10^{-14}\,\mathrm{cm}^{-3}$$

According to Tchernycheva et al.[TJP21], the number of e-h pairs generated in V per incident electron can be approximated by:

$$N_{e-h} \approx (1-f)\frac{E_b}{3E_G} = (1-0.24)\frac{10000}{3 \times 3.4} \approx 750\,\text{e-h pairs}$$

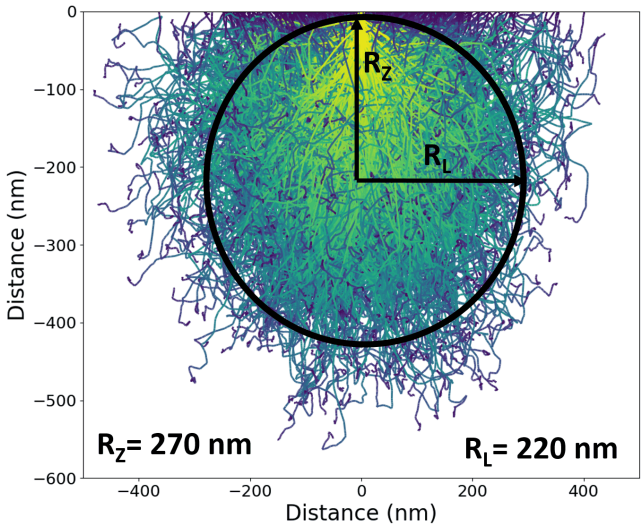

FIGURE 4.B.1: Generation volume of a 10 kV electron beam in GaN

Where f is the backscattered coefficient, E_b is the acceleration voltage and E_G is the bandgap. Thus, right after the creation of the e-h pairs, the maximum carrier density in our system is around:

$$n = \frac{N_{e-h}}{V} \approx 1.3 \times 10^{16}\,\mathrm{cm}^{-3}$$

We can thus estimate the contribution of radiative and Auger recombinations, through the ABC model.

$$R = An + Bn^2 + Cn^3 = \frac{n}{\tau_{eff}} \approx \frac{1.3 \times 10^{16}\,\mathrm{cm}^{-3}}{12\,\mathrm{ns}} \approx 1.1 \times 10^{24}\,\mathrm{cm}^{-3}\,\mathrm{s}^{-1}$$

According to [Dav+20], for an LED emitting at 440 nm, both radiative and Auger recombination coefficient are below:

$$B < 10^{-10}\,\mathrm{cm}^3\,\mathrm{s}^{-1} \text{ and } C < 10^{-29}\,\mathrm{cm}^6\,\mathrm{s}^{-1}$$

Thus, we can estimate an upper value to the contribution of the radiative and Auger terms to the recombination rate:

$$Bn^2 < 1.7 \times 10^{22}\,\mathrm{cm}^{-3}\,\mathrm{s}^{-1},\ Cn^3 < 2 \times 10^{19}\,\mathrm{cm}^{-3}\,\mathrm{s}^{-1} \ll\ R \approx 1.1 \times 10^{24}\,\mathrm{cm}^{-3}\,\mathrm{s}^{-1}$$

Therefore, given the low excitation density, we neglected B and C. Thus, the carrier dynamics is simply governed by the equation:

$$-\frac{dn}{dt} = An$$

For this reason, in our simulations, we considered a carrier independent lifetime.

4.C Derivation of the lifetime profile

Here, we first approximate the lifetime at the edge by simple dimensional analysis. Then, we will also derive an approximation of the lifetime profile taking into account surface recombinations by studying a steady-state version of the problem.

Dimensional analysis

As mentioned, it is possible to estimate the influence of the surface recombination velocity by performing a simple dimensional analysis. We first define a surface recombination lifetime τ_{surf} (4.13). Then, we calculate the edge lifetime $\tau_{eff}(0)$ taking into account the bulk lifetime τ_{bulk} and τ_{surf} (4.14).

$$L := \sqrt{D\tau_{bulk}} \tag{4.12}$$

$$\tau_{surf} := \frac{L}{S} \tag{4.13}$$

$$\tau_{eff}(0) = \left(\frac{1}{\tau_{bulk}} + \frac{1}{\tau_{surf}}\right)^{-1} \tag{4.14}$$

$$= \left(\frac{1}{\tau_{bulk}} + \frac{S}{L}\right)^{-1} \tag{4.15}$$

$$= \frac{L\tau_{bulk}}{L + S\tau_{bulk}} \tag{4.16}$$

$$\boxed{\tau_{eff}(0) = \frac{\tau_{bulk}}{1 + \tau_{bulk}\frac{S}{L}}} \tag{4.17}$$

Steady-state approximation

Here, we will study the steady-state equivalent of our model. Let us first recall the equations that govern our model

$$\begin{cases} \dfrac{dn}{dt} = D\left(\dfrac{\partial^2 n}{\partial x^2}\right) - \dfrac{n}{\tau_{bulk}} & (4.5) \\ D\left(\dfrac{dn}{dx}\right)_{x=0} = Sn(x=0) & (4.6) \end{cases}$$

If we instead consider steady-state under a constant excitation G (4.5) becomes

$$D\left(\frac{\partial^2 n}{\partial x^2}\right) - \frac{n}{\tau_{bulk}} + G = 0 \tag{4.18}$$

$$\iff \left(\frac{\partial^2 n}{\partial x^2}\right) - \frac{n}{L^2} + \frac{G}{D} = 0 \tag{4.19}$$

A solution to the homogeneous equation is

$$\boxed{n(x) = Ae^{-x/L} + Be^{+x/L}} \tag{4.20}$$

A particular solution is given by :

$$-\frac{n}{L^2} + \frac{G}{D} = 0 \tag{4.21}$$

$$\iff n = \frac{GL^2}{D} \tag{4.22}$$

$$\iff \boxed{n = G\tau_{bulk}} \tag{4.23}$$

Thus a general solution of (4.19) is

$$\boxed{n(x) = Ae^{-x/L} + Be^{+x/L} + G\tau_{bulk}} \tag{4.24}$$

As we consider a semi-infinite sample, to ensure convergence it is necessary that B=0.

$$\lim_{x\to\infty} e^{+x/L} = \infty \implies \boxed{B = 0} \tag{4.25}$$

Now if we consider the edge, we have to satisfy the boundary condition (4.5)

$$D\left(\frac{dn}{dx}\right)_{x=0} = Sn(x=0) \tag{4.6}$$

$$\iff \frac{-DA}{L} = S(A + G\tau_{bulk}) \tag{4.26}$$

$$\iff -A(S + \frac{D}{L}) = SG\tau_{bulk} \tag{4.27}$$

$$\iff A = \frac{-SG\tau_{bulk}}{S + \frac{D}{L}} \tag{4.28}$$

We can rearrange last expression to get $\boxed{A = \frac{-G\tau_{bulk}}{1 + \frac{L}{S\tau_{bulk}}}}$

This gives us:

$$n(x) = Ae^{-x/L} + G\tau_{bulk} \tag{4.29}$$

$$\boxed{n(x) = G\tau_{bulk}\left[1 - \frac{e^{-x/L}}{1 + \frac{L}{S\tau_{bulk}}}\right]} \tag{4.30}$$

Now if we define

$$n(x) \coloneqq G\tau(x) \tag{4.31}$$

$$\implies \boxed{\tau(x) = \tau_{bulk}\left[1 - \frac{e^{-x/L}}{1 + \frac{L}{S\tau_{bulk}}}\right]} \tag{4.32}$$

We can quickly check some limits, as expected:

- $\lim_{S\to\infty} \tau(x) = 0$
- $\lim_{S\to 0} \tau(x) = \tau_{bulk}$

Also, let's compute the lifetime at the edge $\tau_{eff}(0)$ from equation (4.32):

$$\tau_{eff}(0) = \tau_{bulk}\left[1 - \frac{1}{1 + \frac{L}{S\tau_{bulk}}}\right] \tag{4.33}$$

$$= \tau_{bulk}\frac{L}{S\tau_{bulk}\left(1 + \frac{L}{S\tau_{bulk}}\right)} \tag{4.34}$$

$$= \tau_{bulk}\frac{1}{1 + \frac{S\tau_{bulk}}{L}} \tag{4.35}$$

$$= \frac{\tau_{bulk}}{1 + \tau_{bulk}\frac{S}{L}} \tag{4.36}$$

Which is the same expression that we derived previously by dimensional analysis (4.17).

We can also compare this expression to the simulations. Figure 4.C.1 shows the lifetime profile obtained by simulations and the one derived here equation (4.32). Even though the problem is not the same, we can see that the steady-state gives us valuable information, especially if we keep in mind that simulations can be computationally expensive.

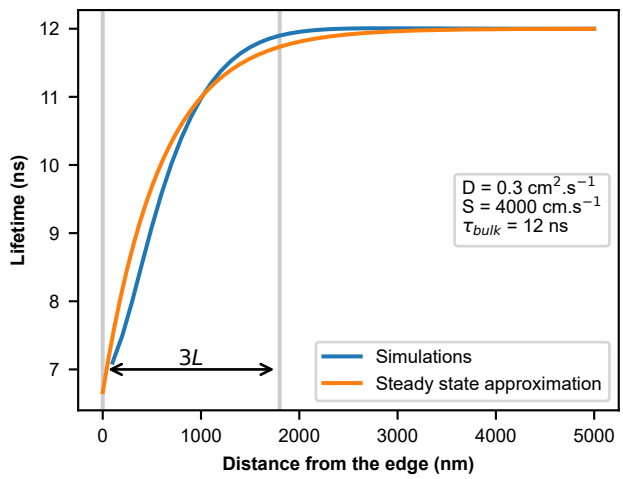

FIGURE 4.C.1: Comparison between the expression of the lifetime derived by considering a steady-state version of the problem and the simulations.

4.D Additional details about simulations

FTCS Scheme

To numerically integrate the model defined in equation (4.5) and equation (4.5), we first must discretized the equations. Here, for simplicity, the chosen integration scheme is the so called "Forward Time Centered Space".

$$\begin{cases} \dfrac{dn}{dt} = D\left(\dfrac{\partial^2 n}{\partial x^2}\right) - \dfrac{n}{\tau_{bulk}} & (4.5) \\ D\left(\dfrac{dn}{dx}\right)_{x=0} = Sn(x=0) & (4.6) \end{cases}$$

First, let us introduce a helpful notation $n_i^j := n(i\Delta x, j\Delta t)$. We can approximate the derivatives as :

$$\frac{\partial^2 n}{\partial x^2} \approx \frac{n_{i-1}^j - 2n_i^j + n_{i+1}^j}{\Delta x^2} \tag{4.37}$$

$$\frac{dn}{dt} \approx \frac{n_i^{j+1} - n_i^j}{\Delta t} \tag{4.38}$$

Hence, (4.5) becomes

$$\frac{n_i^{j+1} - n_i^j}{\Delta t} = D\frac{n_{i-1}^j - 2n_i^j + n_{i+1}^j}{\Delta x^2} - \frac{n_i^j}{\tau_{bulk}} \tag{4.39}$$

Equivalently,

$$\boxed{n_i^{j+1} = n_i^j \left(1 - \frac{\Delta t}{\tau_{bulk}}\right) + \frac{D\Delta t}{\Delta x^2}(n_{i-1}^j - 2n_i^j + n_{i+1}^j)} \tag{4.40}$$

Similarly, the boundary condition becomes :

$$\boxed{n_0^j = \frac{n_1^j}{1 + S\dfrac{\Delta x}{D}}} \tag{4.41}$$

This method has the main advantage to be explicit, *i.e.*, the state at n^{j+1} can be explicitly computed from the state at n^j, as shown in (4.40). However, the major drawback here is that to be stable, this method requires $\frac{D\Delta t}{\Delta x^2} \leq \frac{1}{2}$. Consequently, for high spatial resolution (*i.e.*, small Δx) or high diffusion coefficient D, the time step (Δt) has to be small, whatever the value of τ_{bulk}.

Example, for typical values:

$$\begin{aligned}\Delta t &\leq \frac{\Delta x^2}{2D} \\ &\leq \frac{(10\,\mathrm{nm})^2}{1\,\mathrm{cm^2s^{-1}}} \\ &\leq 1\,\mathrm{ps}\end{aligned}$$

Thus, generally $\Delta t \ll \tau_{bulk}$, which increases the simulation time.

2D simulations

Before doing 1D simulations, a 2D version of the model was initially implemented. Figure 4.D.1 (a) shows the normalized carrier density initially generated, following a Gaussian distribution at 900 nm from the edge and a standard deviation of 100 nm. Figure 4.D.1 (b) shows the normalized carrier density after 12 ns of evolution.

Note: 2D simulations are much more computationally expensive. However, one can take advantage of the high parallelization capability of the FTCS scheme. Indeed, as shown in equation (4.40), all nodes of n^{j+1} can be computed independently from n^j. This kind of computation can be extensively parallelized on a graphics processing unit (GPU). For this reason, I started to learn how to write python code designed for GPU with the library numba[3]. I will not go further into details. However, if interested, the reader can find more information about the

[3]Siu Kwan Lam et al. "Numba: A LLVM-based Python JIT Compiler". *Proceedings of the Second Workshop on the LLVM Compiler Infrastructure in HPC - LLVM '15*. New York, New York, USA: ACM Press, 2015, pp. 1–6. DOI: 10.1145/2833157

library, especially about writing CUDA kernels in python with numba here.[4]

In figure 4.D.2, 1D and 2D simulations are compared for identical parameters except Δt. Indeed, it can be shown that the stability conditions is different in 2D :

$$\Delta t_{2D} = \frac{\Delta x^2 \Delta y^2}{2D(\Delta x^2 + \Delta y^2)} \tag{4.42}$$

If $\Delta y = \Delta x$, then:

$$\boxed{\Delta t_{2D} = \frac{\Delta x^2}{4D} = 0.5\Delta t_{1D}} \tag{4.43}$$

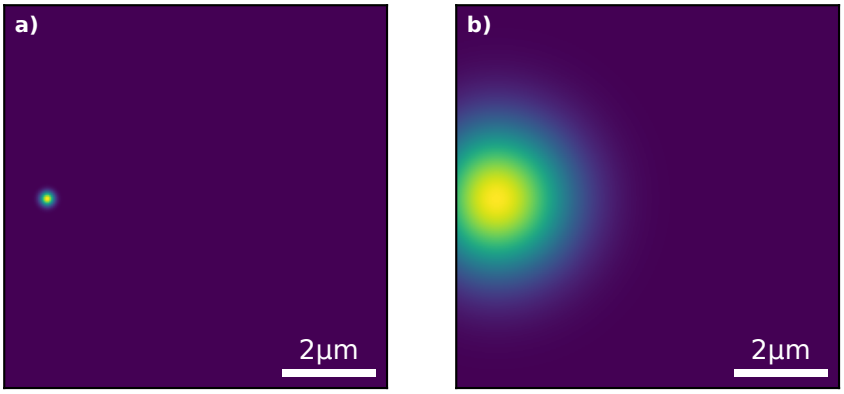

FIGURE 4.D.1: Normalized carrier density, (a) initially and (b) after 12 ns for $S = 5000\,\mathrm{cm\,s^{-1}}$, $D = 0.5\,\mathrm{cm^2 s^{-1}}$ and $\tau_{bulk} = 12\,\mathrm{ns}$. Here, only the left edge contributes to surface recombination

In this case, we can see that the simulations give the same results. For this reason, and as 2D simulations, even on GPU, take much more time to complete, only 1D simulations are considered. However, the implementation of the 2D simulation and the experimentation on GPU will not have been useless since this method could be used to adapt/parallelize 1D simulations.

1D simulations on GPU

Figure 4.D.3 illustrates how many simulations can be stacked to be processed concurrently by GPU. The main idea is to replace the spatial y-axis with a parameters axis. Here, the excitation position (x_0) and the surface recombination velocity (S) are combined to create this new y-axis. This allows for a massive gain in speed. More precisely, in this particular implementation, the CPU is faster if we consider

[4] https://numba.pydata.org/numba-doc/latest/cuda/index.html

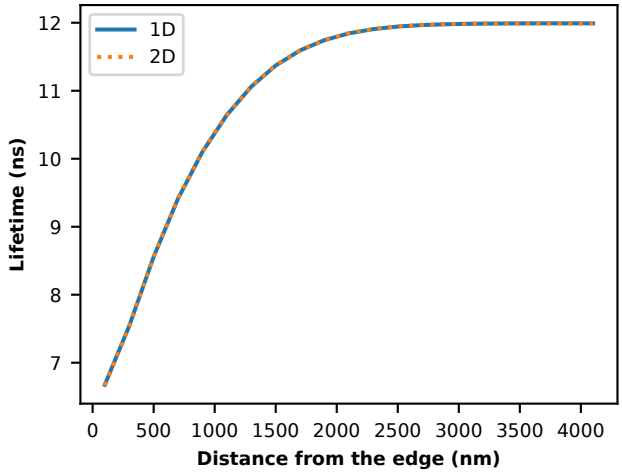

FIGURE 4.D.2: Comparison between a 1D and a 2D simulation both performed on a GPU. Note that only the left edge contribute to surface recombination. Also, all parameters are equal except $\Delta t_{1D} = 2\Delta t_{2D}$ (as shown in (4.43))

a single 1D simulation. On the other hand, the GPU becomes very quickly advantageous when we want to test many parameter sets. Indeed, at fixed Δt, while the simulation time increases with the number of parameters set (typically $N_{x_0} \times N_S$) on the CPU, the time on GPU remains almost constant. Therefore, the simulation time mainly depends on Δt (and thus on D and Δx).

Example, $D = 0.5\,\mathrm{cm^2s^{-1}}$, $\Delta x = 40\,\mathrm{nm}$, it takes about 500 ms to complete between 1 and 4000 simulations for a simulation domain of about 8 µm. It probably means that the 500 ms come for latency when launching kernels (see GPU launch overhead).

Possible improvements

As stated in the previous section, the choice of the FTCS scheme limits the choice of the time step. An alternative could be to change the integration scheme to an unconditionally stable one, such as Crank-Nicolson's method.

There are several advantages to this method, the first one is being unconditionally stable, so no relation exists between Δt and Δx. The second one is that this method is now second order in both time and space, meaning that the error scales as :

$$\epsilon = \alpha \Delta t^2 + \beta \Delta x^2$$

However, this comes with a cost. Indeed, this method is not explicit. At each time step, to get n_i^{j+1}, one has to solve a system of equations. This method is thus not as straightforward as FTCS to implement.

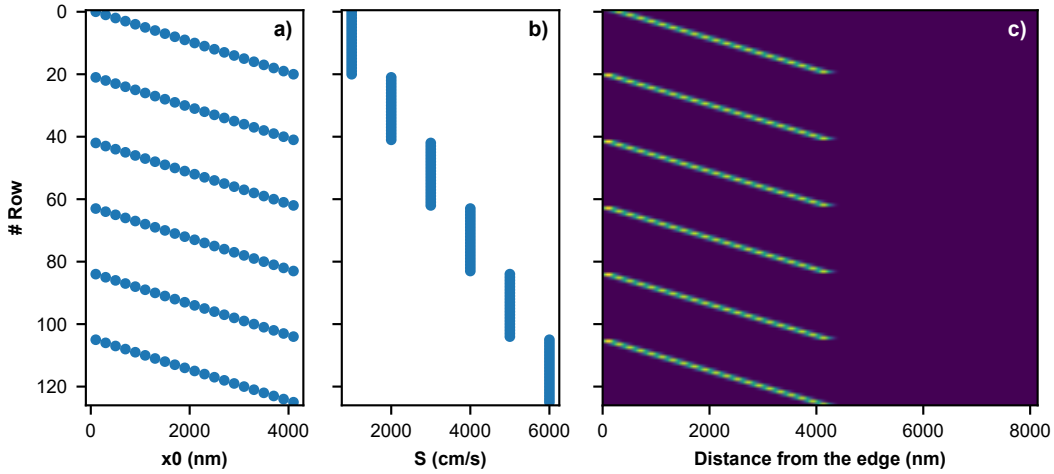

FIGURE 4.D.3: (a) Distribution of x_0, and (b) S along the y axis. (c) The resulting grid, allowing to take advantage of the GPU parallelization capability. Each line is treated as an independent 1D simulation and thus allows to simulate a set of parameters (x_0, S).

References

[Ale+14] R. Aleksiejunas et al. "Diffusion-driven and excitation-dependent recombination rate in blue InGaN/GaN quantum well structures". *Applied Physics Letters* 104.2 (Jan. 2014), 022114. DOI: 10.1063/1.4862026.

[All+08] Jonathan E. Allen et al. "High-resolution detection of Au catalyst atoms in Si nanowires". *Nature Nanotechnology* 3.3 (Feb. 2008), 168–173. DOI: 10.1038/nnano.2008.5.

[Auf+16] Matthias Auf Der Maur et al. "Efficiency Drop in Green InGaN/GaN Light Emitting Diodes: The Role of Random Alloy Fluctuations". *Physical Review Letters* 116.2 (2016). DOI: 10.1103/PhysRevLett.116.027401.

[Bir+07] Stefan Birner et al. "Nextnano: General purpose 3-D simulations". *IEEE Transactions on Electron Devices* 54.9 (Sept. 2007), 2137–2142. DOI: 10.1109/TED.2007.902871.

[BK16] Kirill A. Bulashevich and Sergey Yu Karpov. "Impact of surface recombination on efficiency of III-nitride light-emitting diodes". *Physica Status Solidi - Rapid Research Letters* 10.6 (June 2016), 480–484. DOI: 10.1002/pssr.201600059.

[BKK18] Kirill Bulashevich, Sergey Konoplev, and Sergey Karpov. "Effect of Die Shape and Size on Performance of III-Nitride Micro-LEDs: A Modeling Study". *Photonics* 5.4 (Oct. 2018), 41. DOI: 10.3390/photonics5040041.

[Bor+00] M. Boroditsky et al. "Surface recombination measurements on III-V candidate materials for nanostructure light-emitting diodes". *Journal of Applied Physics* 87.7 (Apr. 2000), 3497–3504. DOI: 10.1063/1.372372.

[Bou+21] Younes Boussadi et al. "Investigation of sidewall damage induced by reactive ion etching on AlGaInP MESA for micro-LED application". *Journal of Luminescence* 234.July 2020 (June 2021), 117937. DOI: 10.1016/j.jlumin.2021.117937.

[Bou22] Younes Boussadi. "Corrélation de mesures électro-optiques en température dans les micro-structures LED à puits quantiques pour applications micro-écrans Younes". PhD thesis. Université de Lyon, 2022.

[Cho+03] H. W. Choi et al. "Mechanism of enhanced light output efficiency in InGaN-based microlight emitting diodes". *Journal of Applied Physics* 93.10 1 (May 2003), 5978–5982. DOI: 10.1063/1.1567803.

[Cho+14] Won Hyuck Choi et al. "Sidewall passivation for InGaN/GaN nanopillar light emitting diodes". *Journal of Applied Physics* 116.1 (July 2014), 013103. DOI: 10.1063/1.4885455.

[Cra75] J Crank. *The Mathematics of Diffusion*. Clarendon Press Oxford, 1975.

[Dai+94] Franz X. Daiminger et al. "Picosecond time-resolved investigations of carrier lifetime and carrier capture in InGaAs/GaAs quantum dots". *Quantum Well and Superlattice Physics V*. Ed. by Gottfried H. Doehler and Emil S. Koteles. Vol. 2139. May 1994. May 1994, pp. 213–221. DOI: 10.1117/12.175717.

[Dav+20] Aurelien David et al. "Review—The Physics of Recombinations in III-Nitride Emitters". *ECS Journal of Solid State Science and Technology* 9.1 (2020), 016021. DOI: 10.1149/2.0372001jss.

[Dav21] Aurelien David. "Long-Range Carrier Diffusion in (In,Ga) N Quantum Wells and Implications from Fundamentals to Devices". *Physical Review Applied* 15.5 (May 2021), 054015. DOI: 10.1103/PhysRevApplied.15.054015.

[Dem+11] Hendrix Demers et al. "Three-dimensional electron microscopy simulation with the CASINO Monte Carlo software". *Scanning* 33.3 (May 2011), 135–146. DOI: 10.1002/sca.20262.

[Fin+22] Sylvain Finot et al. "Surface Recombinations in III-Nitride Micro-LEDs Probed by Photon-Correlation Cathodoluminescence". *ACS Photonics* 9.1 (Jan. 2022), 173–178. DOI: 10.1021/acsphotonics.1c01339.

[Hor+18] Ray Hua Horng et al. "Development and Fabrication of AlGaInP-Based Flip-Chip Micro-LEDs". *IEEE Journal of the Electron Devices Society* 6.April (2018), 475–479. DOI: 10.1109/JEDS.2018.2823981.

[Jar+05] K. Jarašiunas et al. "Carrier diffusion and recombination in highly excited InGaN/GaN heterostructures". *Physica Status Solidi (A) Applications and Materials Science* 202.5 (Apr. 2005), 820–823. DOI: 10.1002/pssa.200461351.

[Jin+00] S. X. Jin et al. "InGaN/GaN quantum well interconnected microdisk light emitting diodes". *Applied Physics Letters* 77.20 (Nov. 2000), 3236–3238. DOI: 10.1063/1.1326479.

[Le 21] Corentin Le Maoult. "Etude et optimisation de l ' étape de passivation des µLED bleues GaN-InGaN". PhD thesis. 2021.

[Ley+20] Ryan T. Ley et al. "Revealing the importance of light extraction efficiency in InGaN/GaN microLEDs via chemical treatment and dielectric passivation". *Applied Physics Letters* 116.25 (June 2020), 251104. DOI: 10.1063/5.0011651.

[LPS15] Siu Kwan Lam, Antoine Pitrou, and Stanley Seibert. "Numba: A LLVM-based Python JIT Compiler". *Proceedings of the Second Workshop on the LLVM Compiler Infrastructure in HPC - LLVM '15*. New York, New York, USA: ACM Press, 2015, pp. 1–6. DOI: 10.1145/2833157.

[Ma+12] Ming Ma et al. "Strong light-extraction enhancement in GaInN light-emitting diodes patterned with TiO 2 micro-pillars with tapered sidewalls". *Applied Physics Letters* 101.14 (Oct. 2012), 141105. DOI: 10.1063/1.4756797.

[Man+20] Cédric Mannequin et al. "Comparative study of two atomic layer etching processes for GaN". *Journal of Vacuum Science & Technology A* 38.3 (2020), 032602. DOI: 10.1116/1.5134130.

[Meu16] Sophie Meuret. "Expérience de Hanbury Brown et Twiss dans un microscope électronique à transmission à balayage : sa physique et ses applications". PhD thesis. UNIVERSITE PARIS-SACLAY, 2016.

[Mon+14] B. Monemar et al. "Properties of the main Mg-related acceptors in GaN from optical and structural studies". *Journal of Applied Physics* 115.5 (Feb. 2014), 053507. DOI: 10.1063/1.4862928.

[Ohb+17] Tomihito Ohba et al. "Atomic layer etching of GaN and AlGaN using directional plasma-enhanced approach". *Japanese Journal of Applied Physics* 56.6S2 (June 2017), 06HB06. DOI: 10.7567/JJAP.56.06HB06.

[Oli+17a] Francois Olivier et al. "Shockley-Read-Hall and Auger non-radiative recombination in GaN based LEDs: A size effect study". *Applied Physics Letters* 111.2 (July 2017), 022104. DOI: 10.1063/1.4993741.

[Oli+17b] François Olivier et al. "Investigation and improvement of 10μm pixel-pitch GaN-based micro-LED arrays with very high brightness". *Digest of Technical Papers - SID International Symposium* 48.1 (May 2017), 353–356. DOI: 10.1002/sdtp.11615.

[Ott+15] I. Otto et al. "Micro-pixel light emitting diodes: Impact of the chip process on microscopic electro- and photoluminescence". *Applied Physics Letters* 106.15 (Apr. 2015), 151108. DOI: 10.1063/1.4918678.

[Pea+93] S J Pearton et al. "Surface recombination velocities on processed InGaP p-n junctions". *Applied Physics Letters* 63.26 (1993), 3610–3612. DOI: 10.1063/1.110064.

[Pop+00] M. Pophristic et al. "Time-resolved photoluminescence measurements of InGaN light-emitting diodes". *Materials Science Forum* 338.24 (May 2000), 1623–1626. DOI: 10.4028/www.scientific.net/msf.338-342.1623.

[RGD18] M A Reshchikov, P Ghimire, and D O Demchenko. "Magnesium acceptor in gallium nitride. I. Photoluminescence from Mg-doped GaN". *Physical Review B* 97.20 (2018), 205204. DOI: 10.1103/PhysRevB.97.205204.

[RM05] Michael A. Reshchikov and Hadis Morko. "Luminescence properties of defects in GaN". *Journal of Applied Physics* 97.6 (Mar. 2005), 061301. DOI: 10.1063/1.1868059.

[Sch+13] F J Schultes et al. "Temperature dependence of diffusion length, lifetime and minority electron mobility in GaInP". *Applied Physics Letters* 103.24 (2013), 242106. DOI: 10.1063/1.4847635.

[SDS13] Hans Michael Solowan, Julia Danhof, and Ulrich T. Schwarz. "Direct observation of charge carrier diffusion and localization in an InGaN multi quantum well". *Japanese Journal of Applied Physics* 52.8 PART 2 (Aug. 2013), 08JK07. DOI: 10.7567/JJAP.52.08JK07.

[She+21] Huan-Ting Shen et al. "Three-dimensional modeling of minority carrier lateral diffusion length in InGaN blue/green and AlGaN ultraviolet C single quantum wells including random alloy fluctuations" (May 2021), 1–7.

[Sol+21] Magdalena Sola-Garcia et al. "Photon Statistics of Incoherent Cathodoluminescence with Continuous and Pulsed Electron Beams". *ACS Photonics* (Dec. 2021). DOI: 10.1021/acsphotonics.0c01939.

[Tia+12] Pengfei Tian et al. "Size-dependent efficiency and efficiency droop of blue InGaN micro-light emitting diodes". *Applied Physics Letters* 101.23 (Dec. 2012), 231110. DOI: 10.1063/1.4769835.

[TJP21] Maria Tchernycheva, Gwénolé Jacopin, and Valerio Piazza. "Characterisation of Semiconductor Nanowires by Electron Beam Induced Microscopy and Cathodoluminescence". *Fundamental Properties of Semiconductor Nanowires*. Springer Singapore, 2021, pp. 251–288. DOI: 10.1007/978-981-15-9050-4_5.

[VM03] I. Vurgaftman and J. R. Meyer. "Band parameters for nitrogen-containing semiconductors". *Journal of Applied Physics* 94.6 (Sept. 2003), 3675–3696. DOI: 10.1063/1.1600519.

[Wea+21] Thomas F.K. Weatherley et al. "Imaging Nonradiative Point Defects Buried in Quantum Wells Using Cathodoluminescence". *Nano Letters* 21.12 (June 2021), 5217–5224. DOI: 10.1021/acs.nanolett.1c01295.

[Won+18] Matthew S. Wong et al. "High efficiency of III-nitride micro-light-emitting diodes by sidewall passivation using atomic layer deposition". *Optics Express* 26.16 (Aug. 2018), 21324. DOI: 10.1364/OE.26.021324.

[Won+19] Matthew S. Wong et al. "Size-independent peak efficiency of III-nitride micro-light-emitting-diodes using chemical treatment and sidewall passivation". *Applied Physics Express* 12.9 (Sept. 2019), 097004. DOI: 10.7567/1882-0786/ab3949.

[Xie+12] E. Y. Xie et al. "Strain relaxation in InGaN/GaN micro-pillars evidenced by high resolution cathodoluminescence hyperspectral imaging". *Journal of Applied Physics* 112.1 (July 2012), 013107. DOI: 10.1063/1.4733335.

[Zhu+19] Jun Zhu et al. "Near-Complete Elimination of Size-Dependent Efficiency Decrease in GaN Micro-Light-Emitting Diodes". *physica status solidi (a)* 216.22 (Nov. 2019), 1900380. DOI: 10.1002/pssa.201900380.

Chapter 5

Core-shell GaN microwires for UV emitters

5.1 III-Nitride UV Emitters . . . 138
5.1.1 Applications of UV LEDs . . . 138
5.1.2 State of the Art and Challenges . . . 139
5.1.3 Microwires for UV emission . . . 143
5.2 Effect of cracks on the optical properties . . . 144
5.2.1 Studied samples . . . 144
5.2.2 Optical characterization of cracks . . . 146
5.2.2.1 CL . . . 146
5.2.2.2 Simulations of a crack . . . 147
5.2.2.3 Carrier dynamics near a crack . . . 150
5.2.2.4 Conclusion . . . 152
5.3 Mitigation of cracks . . . 153
5.4 Realization and characterization of single wire LEDs . . . 156
5.4.1 EBID Contacts . . . 156
5.4.1.1 Contact deposition . . . 156
5.4.1.2 Study of GaN and AlGaN *p-n* junction . . . 157
5.4.1.3 Electrical properties of UV-A LED microwires . . . 160
5.4.1.4 Optical properties of UV-A LED microwires . . . 164
5.4.1.5 Towards UV-B LED . . . 166
5.4.1.6 Origin of the violet band . . . 168
5.4.1.7 Improved electrical properties of UV-B LEDs . . . 169
5.4.1.8 Conclusion . . . 169
5.4.2 Realization and characterization of Ni/Au contacts . . . 171
5.4.2.1 Ohmic contact on GaN . . . 171
5.4.2.2 Fabrication process . . . 172
5.4.2.3 Electro-optical properties of the wires . . . 174
5.4.2.4 Conclusion . . . 177
5.4.3 Conclusion and perspectives . . . 177
Appendices . . . 179

This chapter will discuss the problem of UV emitters. We will first present the context with a general introduction of III-nitrides for UV emitters, their applications, state of the art, and the main limitations. Then, we will see how III-nitride microwires are attractive for this application. Next, we will study a type of extended defect in this type of structure and how to reduce its occurrence. Finally, we will focus on the realization and electro-optical characterization of single microwire LEDs.

5.1 III-Nitride UV Emitters

Nowadays, GaN-based white LEDs are the most efficient man-made light source. Despite this, only a small part of the broad spectrum that III-nitrides can cover is currently exploited. In particular, an area of great interest is that of UV emitters. As shown in figure 5.1, by alloying AlN with GaN, it is possible to cover almost the entire UV spectral range[1]. Moreover, the emission energy can be finely tuned as it depends mainly on the composition of the alloy. This would make it possible to replace mercury lamps that are bulky, fragile, toxic and emit specific lines with compact, durable, environmentally friendly and tunable emission UV-LEDs. However, many challenges remain to be overcome before they can match their visible wavelength counterparts. Motivated by the incredible potential of this technology, research in this field is constantly increasing.

The following is a brief summary of the current status and challenges of UV-LEDs development and is extensively based on these three publications Kneissl and Rass. *III-Nitride Ultraviolet Emitters*, 2016; Kneissl et al. "The emergence and prospects of deep-ultraviolet light-emitting diode technologies", 2019; Amano et al. "The 2020 UV emitter roadmap", 2020.

5.1.1 Applications of UV LEDs

A particularly interesting feature of UV LEDs is their tunable emission. In particular, the interaction of UV with organisms and matter is highly dependent on wavelength and power, making this technology a first-choice candidate for applications from security, medical treatment, disinfection and purification to communication and sensing.

The UV spectrum is commonly divided into three spectral bands defined by the Global Solar UV Index: UV-A (400–315 nm), UV-B (315–280 nm) and UV-C

[1]The UV spectral range here refers to 200–400 nm which corresponds on one hand to the end of vacuum UV (200 nm) and one the other hand the limit between visible and UV (above 400 nm)

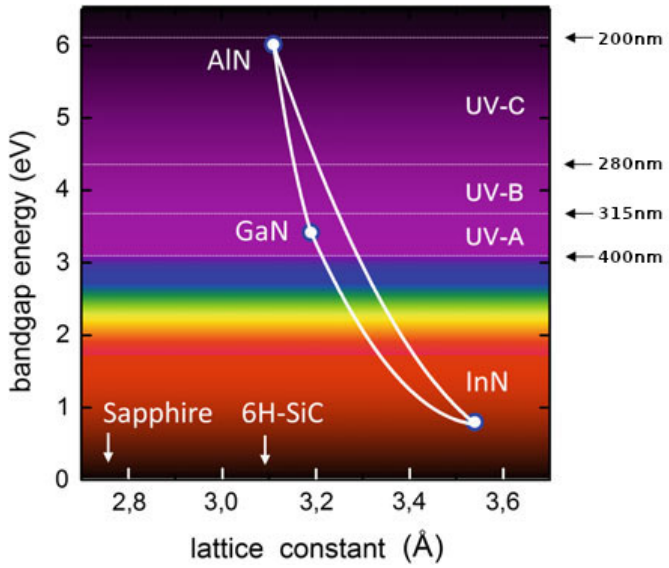

FIGURE 5.1: Bandgap energies and emission wavelength of InN, GaN, AlN and other III–V and II–VI compound semiconductor materials plotted versus their lattice spacing [KR16]

(280–100 nm). Figure 5.2 shows an overview of the numerous applications depending on the power and the emission wavelength. The most widespread applications of UV-A are mainly focused on curing inks, resins, and polymers with, for example, 3D printing or photolithography technologies. There are also applications related to security, where UV light is used to reveal fluorescent markers (banknotes, ID cards) and medical applications like blood gas analysis. The noticeable applications of UV-B are phototherapy, including the treatment of psoriasis and vitiligo, and plant-growth lighting. Regarding UV-C, one of the main applications is disinfection and purification. Indeed, most organisms are sensitive to UV-C. In particular, studies have shown that it was possible to inhibit the ability to multiply in bacteria and viruses. This topic has been of particular interest during the COVID-19 global pandemic [RA20; Hei+20; Kit+21].

5.1.2 State of the Art and Challenges

State of the Art

Currently, the efficiency of UV LEDs rapidly decreases with the emission wavelength. A compilation of EQE of UV LEDs as a function of the emission wavelength is shown in figure 5.3. The significant drop in EQE below 365 nm corresponds to the transition from InGaN-based to AlGaN-based LEDs. Since InGaN-based near-UV emitters (400–365 nm) use the same materials and device technologies as blue LEDs, they have benefited from many years of large-scale industrial development.

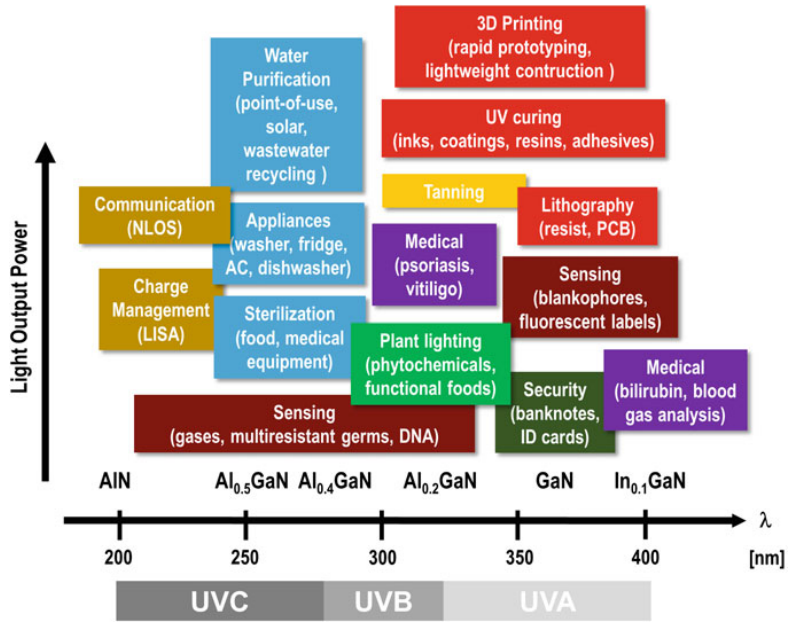

FIGURE 5.2: Key applications for UV-A, UV-B, and UV-C LEDs. [Ama+20]

As a result, near-UV LEDs exhibit performance levels close to those of blue LEDs, with EQEs typically above 50% [Kne+19]. Below 365 nm, the situation is radically different. With efficiencies of the order of a few percent, AlGaN-based UV LEDs are still far from the efficiency of InGaN-based LEDs.

This difference comes from a combination of different factors. To understand it, let us first detail the expression of the EQE:

$$\eta_{\mathrm{EQE}} = \eta_{\mathrm{rad}} \cdot \eta_{\mathrm{inj}} \cdot \eta_{\mathrm{ext}} = \eta_{\mathrm{IQE}} \cdot \eta_{\mathrm{ext}}$$

Where η_{rad} is the radiative efficiency, η_{inj} the injection efficiency, and η_{ext} the light extraction efficiency[2].

While all these efficiencies are well in the 90% range for blue LEDs, leading to a ∼80 % EQE, it is far from being the case in UV LEDs. According to Amano et al., although it is difficult to precisely estimate the different contribution to the overall efficiencies, the radiative efficiency, the injection efficiency and the the extraction efficiency should be around 40%, 80% and 20% resulting in an EQE typically below 10% [Ama+20].[3] In addition, when considering the large voltage drop in the device, the WPE is further reduced.[4] We will now discuss the cause of these efficiency drops.

[2]Note that this definition is based on [Ama+20]. In other publications, the IQE may refer to the radiative efficiency.

[3]This was estimated on a commercial 280 nm LED with a record EQE of 6.4%.

[4]Nichia announced in September 2022 the commercialization of their new 110 mW UV-C (280 nm) LED with a WPE of 5.4% https://www.nichia.co.jp/en/newsroom/2022/2022_090601.html

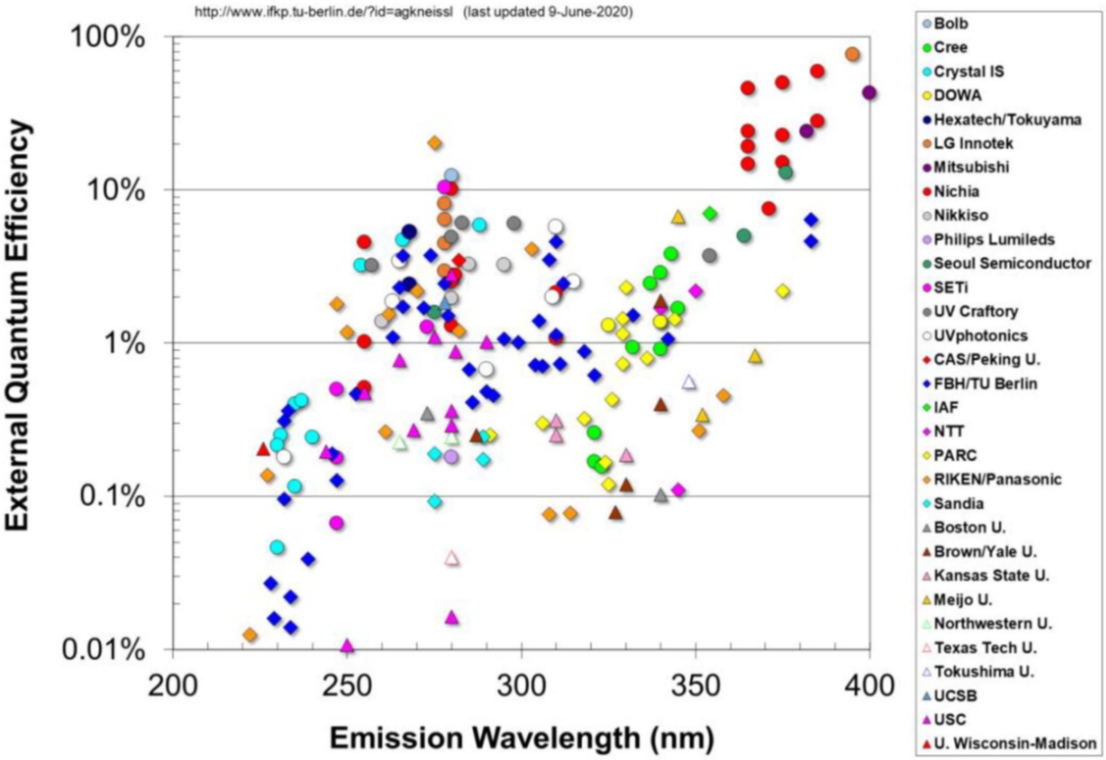

FIGURE 5.3: Reported external quantum efficiencies for AlGaN, InAlGaN, and InGaN QW LEDs emitting in the UV spectral range [Ama+20]

Internal Quantum Efficiency

UV-LEDs are generally grown on *c*-plane sapphire due to the availability of large volume and low price resulting from the development of visible LEDs. Moreover, sapphire is transparent to UV due to its large bandgap of 8.8 eV. However, due to the significant lattice mismatch between sapphire and III-nitrides, a large number of threading dislocations, typically between 10^8 and $10^{10}\,\mathrm{cm}^{-2}$, are generated. As shown in figure 5.4, this is a considerable issue as threading dislocations is one of the main causes of non-radiative recombinations in UV LEDs when the density is typically above $10^8\,\mathrm{cm}^{-2}$ [Ama+20; Ban+11; Sha+12].

Thus, one of the main challenges would be to reduce the threading dislocation density below $10^8\,\mathrm{cm}^{-2}$ to increase the IQE significantly. Below this value, the main limiting factor is the presence of point defects, which tend to pin the IQE whatever the dislocation density.

Light Extraction Efficiency

As mentioned previously, the light extraction efficiency (LEE) is typically around 10–20% for UV-LEDs. This is because most of the methods used for improving LEE in the case of blue LEDs cannot be transposed to UV. For example, the high

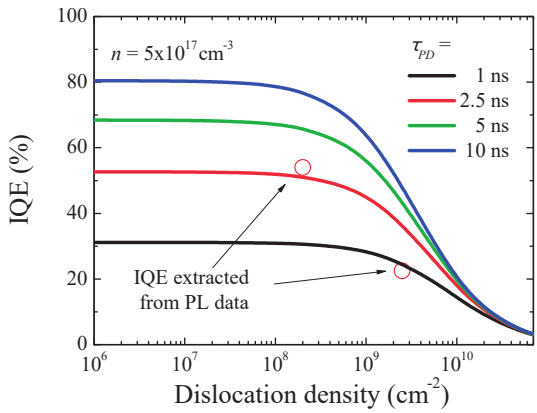

FIGURE 5.4: Calculated IQE as a function of threading dislocation density for different values of non-radiative carrier lifetime via point defects. [Sha+12]

refractive index polymers on which encapsulation and packaging are based are not stable when exposed to high-energy UV photons. In addition, silver commonly used to make reflective contacts has a rapid drop in reflectivity below 350 nm and therefore cannot be used for UV-LEDs below this limit. Aluminum would be a good metal in terms of reflectivity, but it normally does not form a good ohmic contact on *p*-AlGaN due to its low work function. Therefore, it is necessary to develop new techniques to increase the LEE, which massively contributes to the EQE drop. Several approaches have been investigated, such as surface roughening/texturing, substrate patterning, LED array shaping, micro-pixel LEDs and flip-chip LEDs [Sha+12].

An additional complication arises from the negative crystal field splitting in AlGaN alloys. This leads to a rearrangement of the valence bands at a higher aluminum content, resulting in a polarization change from transverse electric (TE) to transverse magnetic (TM) at a shorter wavelength ($\lambda \lesssim 240$ nm). As a result, fewer photons are extracted from the top surface or substrate, and most of them are emitted in-plane [Rei+15].

Injection Efficiency

UV LEDs tend to suffer from poor injection efficiencies mainly due to the poor conductivity of Mg-doped *p*-AlGaN. Indeed, the ionization energy of Mg increases with the Al content. Therefore, only a small fraction of the Mg acceptors are ionized at room temperature in an Al-rich structure, resulting in very low free hole concentrations. Another major challenge is the efficient injection of holes into the AlGaN QWs and the electron leakage from the active region. These two parameters are difficult to estimate, but according to Kneissl and Rass the resulting efficiency typically spreads between less than 10% for deep UV emitters

to more than 90% for UV-A LEDs [KR16].

Wall-plug efficiency

Finally, as we said, the ionization energy of impurities increases with the Al content. Thus the resistivity of the AlGaN layer increases, which increases the voltage drop in the devices. In addition, it becomes more difficult to form ohmic contacts, forming Schottky contact at high Al content. Therefore the operating voltage increases, resulting in a lower WPE [Ama+20].

5.1.3 Microwires for UV emission

To overcome some of the inherent limitations of planar *c*-plane LED architectures, the use of nanowire-based UV LEDs has recently emerged [Zha+14]. They already offer some key advantages: higher Mg solubility leading to a more efficient *p*-doping in the deep-UV [Tra+17] and a drastic reduction of extended defects either due to better strain management [Lan+10] or dislocation filtering [KI15]. A particularly promising approach is based on *m*-plane core-shell wires [Cou+18a; Bru+19; Cou+18b; Gre+20]. In this geometry, the absence of the QCSE and the increased emitting area contribute to the mitigation of the detrimental effects that appear at high carrier densities. Moreover, in the absence of QCSE, the emission energy will typically be higher than for an equivalent *c*-plane structure.

In a core-shell microwire, the emitting dipole is usually coupled to a guided mode where the wire itself acts as a waveguide [Tch+14b]. As a consequence, for UV emitters, the light extraction could be severely altered due to the detrimental GaN core parasitic absorption. To circumvent this issue, one approach is to use an AlN inner core [Cou+18a]. However, with such a design, the electrical injection is challenging. Hence, to combine electrical injection and low absorption losses, a solution is to grow an AlGaN cladding shell to protect the guided mode from inner core absorption losses.[5] This cladding layer has to be both Al-rich and thick enough to be efficient in the deep UV emission. Under these conditions, and as observed for planar layers, this often leads to crack formation [Ein+00]. Therefore, it is crucial to investigate the influence of cracks on the optical properties of the active region. This will be the subject of the next section.

[5]Note that a more recent approach could be to remove the GaN wire core by in-situ selective etching at the end of the growth, as demonstrated by Durand et al. [Dur+17].

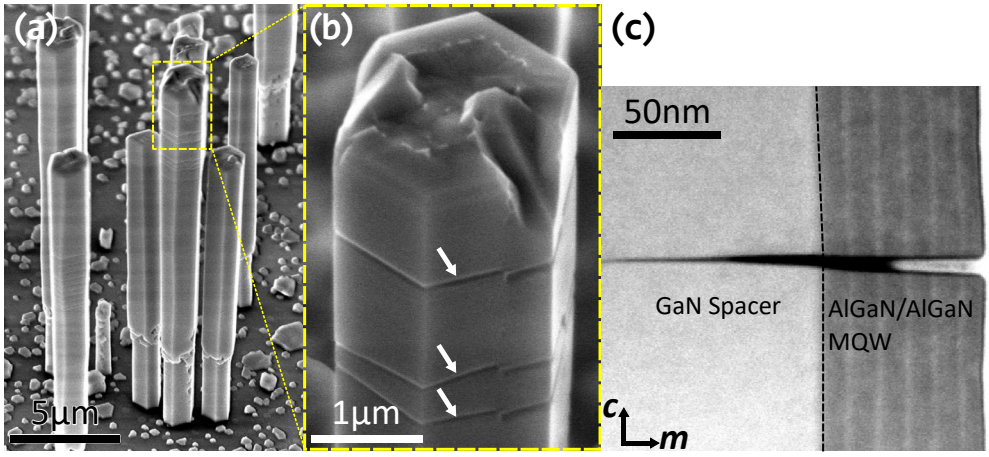

FIGURE 5.5: (a)-(b) 45°-tilted SE image of GaN wires covered with Al-based MQWs grown on *c*-sapphire substrate. (b) Enlarged view near the wire top with the presence of multiple cracks. (c) HAADF-STEM longitudinal cross-section near a radial crack. [Fin+20]

5.2 Effect of cracks on the optical properties

5.2.1 Studied samples

The studied GaN microwires with a core-shell AlGaN heterostructure have been realized by Vincent Grenier and Christophe Durand. They were grown on *c*-plane sapphire substrates by metal-organic vapor phase epitaxy. The wires are mainly N-polar but may exhibit polarity mixing. The growth is initiated with a heavily *n*-doped GaN wire core ([Si]$\sim 10^{20}\,\mathrm{cm}^{-3}$) grown under high silane flux ($\sim$ 200 nmol.min^{-1}), which favors the vertical growth [Koe+10]. Then, an undoped GaN section is grown. The shell, which preferentially grows on the undoped GaN core, starts from an unintentionally doped GaN spacer ($\sim$150 nm) to bury the contamination surface layer, as shown in chapter 3. Then, the active region containing five AlGaN/AlGaN QWs is grown at 950 °C under N_2 (100 mbar) with a V/III ratio close to 1000. The Al-content was estimated to be around $70 \pm 10\,\%$ in the barriers, and $45 \pm 5\,\%$ in the QWs. It should be noted that the estimations were based on X-ray diffraction performed on *c*-plane AlGaN layers grown under identical conditions. According to Dinh et al., the Al incorporation is comparable on polar, semi- and non-polar planes [Din+19]. Figure 5.5 (a) displays a 45°-tilted secondary electron image of typical as-grown wires.

Due to the large lattice mismatch between the GaN core and the Al-rich AlGaN shell, we observe the formation of cracks for most of the wires (figure 5.5 (b)). In a core-shell geometry, the strain is mainly enhanced along the *c*-axis (ϵ_{zz}) [Hes+10; Dur+14]. For this reason, these cracks preferentially form perpendicular to the

c-axis, along the a-axis. To precisely determine the structural properties of these defects, longitudinal cross-sections have been prepared by focused Ga-ion beam using a STRATA 400S equipment and observed by STEM using an FEI-Tecnai microscope operated at 200 kV[6]. Figure 5.5 (c) shows a cross-section STEM image allowing to deduce the QW and barrier thicknesses, respectively equal to 4 ± 1 nm and 10 ± 1 nm. We observe that the crack runs through the entire AlGaN heterostructure and terminates in the GaN spacer. The thickness of the heterostructure does not seem to be affected by the presence of the crack.

Additionally, as shown in figure 5.6, qualitative EDX measurements were performed with an FEI THEMIS TEM operated at 200 kV and equipped with super X detectors.[7] In the intensity profile of the Al- and Ga-Kα lines shown in figure 5.6 (d), we can see that Al and Ga intensities vary simultaneously; thus, no significant change in Al content can be identified near a crack.

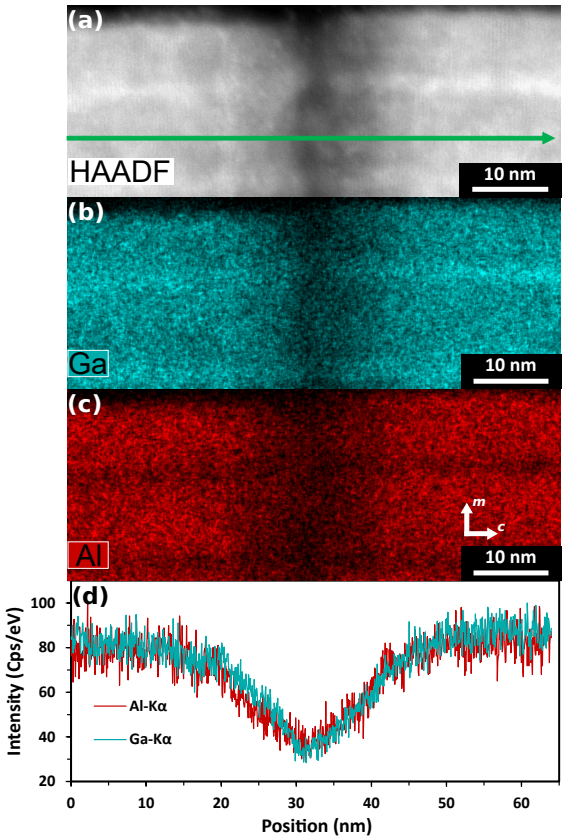

FIGURE 5.6: (a) HAADF-TEM longitudinal cross-section near a crack and the corresponding EDX intensity map of Ga and Al (b) and (c). (d) Intensity profile of Al- and Ga-Kα lines along the c-axis. Adapted from [Fin+20]

[6]The FIB slices have been prepared by Vincent Grenier and the STEM observations performed by Catherine Bougerol

[7]EDX measurements have been performed by Hanako Okuno

5.2.2 Optical characterization of cracks

5.2.2.1 CL

To probe the influence of cracks on the optical properties, we first performed 5 K-CL measurements. First, microwires were mechanically dispersed on SiO_2/Si substrates. Then, a spectrum was acquired in the 2–4.5 eV range, showing the different contributions.

For example, figure 5.7 shows a 30 kV CL spectrum acquired in a 0.25 µm^2 region on the core-shell part of the wire. Note the choice of a high acceleration voltage to excite all layers, including the GaN core. In addition to the MQW emission centered at 4.13 eV with a FWHM of 150 meV, we can identify three common signatures of GaN samples: the broad yellow luminescence (YL) band at 2.24 eV, the DAP band around 3.26 eV with the typical ∼90 meV LO phonon replicas and lastly, the near band edge emission (NBE) of GaN at 3.5 eV.

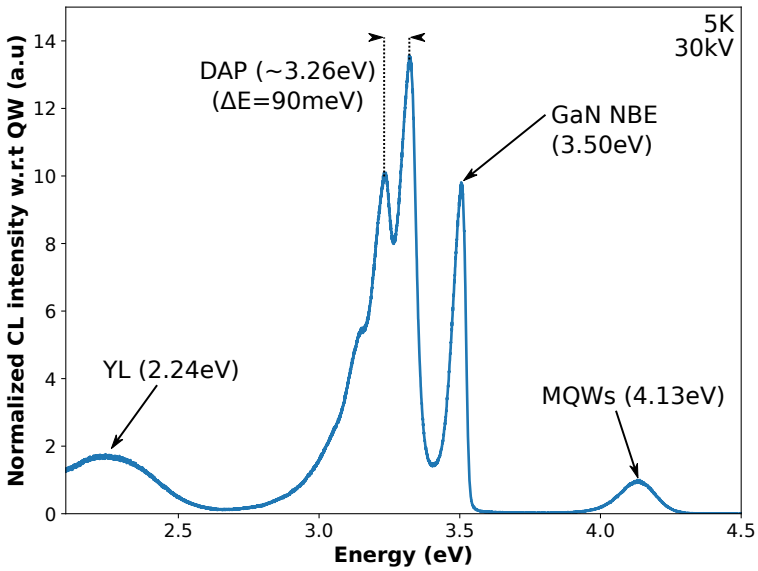

FIGURE 5.7: Spectrum acquired in a 0.25 µm^2 area with a 30 kV acceleration voltage at $T = 5$ K. Adapted from [Fin+20]

For each wire, we also performed a CL spectra mapping focused on the QW emission, *i.e.*, in the 3.7–4.9 eV energy range, with a 2 kV acceleration voltage and a dwell time of 10 ms.

An SE image of a typical wire with multiple cracks is shown in figure 5.8 (a). Figure 5.8 (b) shows the corresponding CL map integrated over the wire's width in the MQWs energy region. The MQWs' emission energy is slightly shifting to higher emission energy from the bottom to the top, probably due to an Al gradient along the wire or a change in QWs thickness. Even if cracks can be difficult to locate on SE images, they can easily be seen on the CL spectra map. Indeed, the

presence of a crack systematically leads to an energy blue-shift of about 100 meV associated with a significant increase in CL intensity.

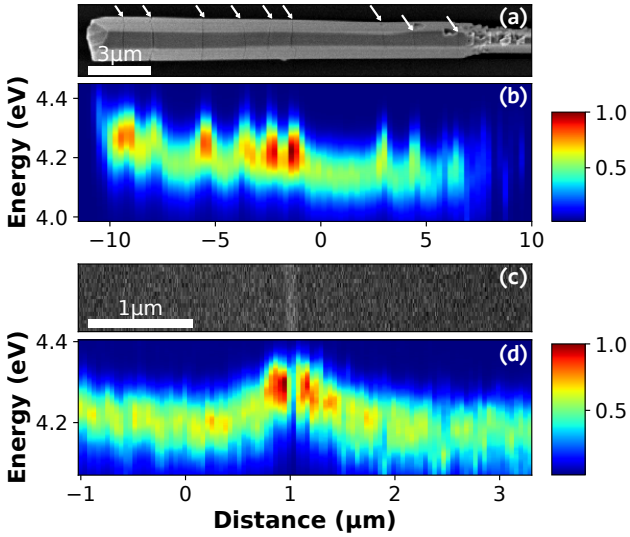

FIGURE 5.8: (a) SE image of a wire and (b) the corresponding mapping of the CL spectra. (c) Close-view SE image near a crack on a different wire and its corresponding CL spectra map (d). The measurements were done at 5 K with a 5 kV acceleration voltage for (a) and (b) and 2 kV for (c) and (d). The horizontal axis corresponds to the *c*-axis. The color bars indicate the normalized CL intensity. Adapted from [Fin+20]

This increase in intensity can be better seen on monochromatic images with better resolution (see figure 5.9). The origin of this increase is attributed here to an improvement in the LEE and will be discussed in more detail later. Also, note a higher intensity at the edges of the wire, which may also suggest an increase in LEE for geometrical reasons.

5.2.2.2 Simulations of a crack

As we have seen previously, the Al content seems constant near the cracks. Thus, this energy shift could be explained by a change in strain. To verify this hypothesis, we performed two-dimensional 6x6 k.p simulations with the software nextnano3 [Bir+07]. The parameters used can be found in Vurgaftman and Meyer. "Band parameters for nitrogen-containing semiconductors", 2003 [VM03]. The simulated system replicates the observed stacking in the TEM cross-sections. To reproduce the experimental transition energies, the Al content in the MQWs has been adjusted to 40 % and 60 % in the barrier. The MQWs structure is assumed to be pseudomorphic on a *m*-plane GaN substrate. We first perform strain minimization to estimate the strain state of each layer. Then, we compute the band edges profiles to take into account the influence of strain on the valence and conduction bands.

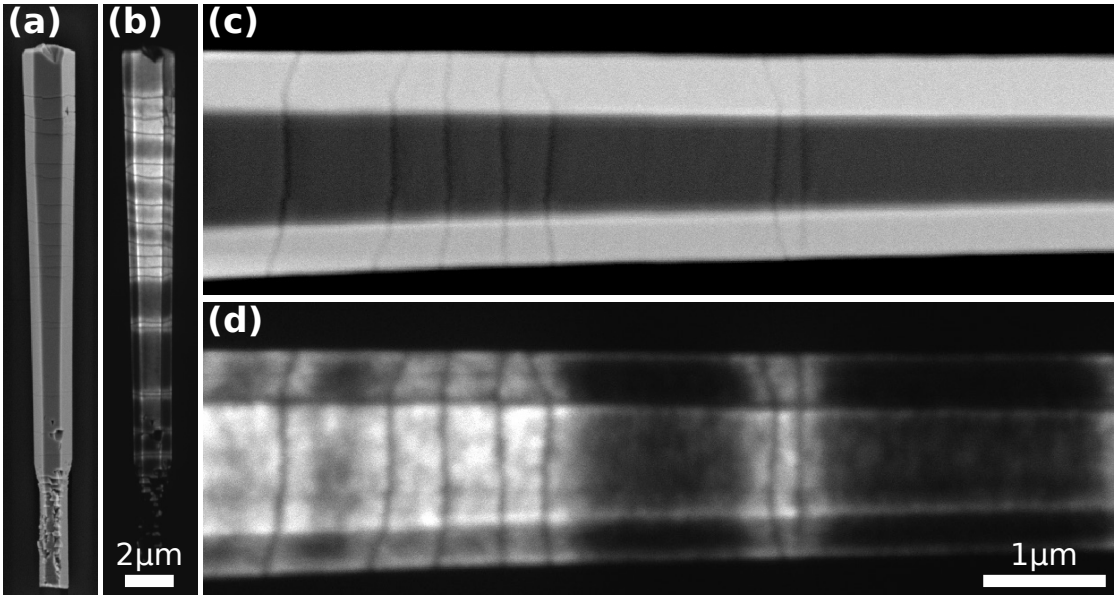

FIGURE 5.9: SE images of a wire with multiple cracks (a, c) and their corresponding CL images at the MQWs emission (b, d). Both CL and SE images have been acquired with a 5 kV acceleration voltage, at $T = 5$ K. Adapted from [Fin+20]

Finally, the Schrödinger equation is solved for electrons and holes in the five QWs at different positions. Figure 5.10 (a) shows the simulated bandgap energy. 500 nm away from the crack, the energy of the bandgap tends towards the crack-free value (4.24 eV). As we get closer to the crack, the strain is relaxed thanks to the free surface and the bandgap energy increases. We then solve the Schrödinger equation to take into account the influence of strain on confined states.

It should be noted that the energy obtained via simulations is higher than our observations by about 170 meV. This is why we compare the energy shift and not directly the energy in what follows. Different factors could explain this offset. First, our model does not consider the exciton binding energy, which could be of the order of 30-50 meV [Big+99], nor the effects of localization which could also introduce a shift of the order of 50-60 meV, as observed by Frankerl et al. [Fra+20]. This difference may also be attributed to the uncertainty on the Al content in the heterostructure. Finally, to remain critical, there is uncertainty in the simulation input parameters, especially in the elements of the k.p matrix. This can also be responsible for this discrepancy.

In figure 5.10 (b), the experimental CL energy shift is compared to the shift of the transition energy obtained by simulations. The error bars of the experimental data are set to 11 meV, which corresponds to the standard deviation of CL mean energy at more than one micron away from the crack. As the energy of the QWs depends on their distance to the GaN spacer due to strain relaxation, only the minimum and maximum energy are indicated by crosses, the intermediate values

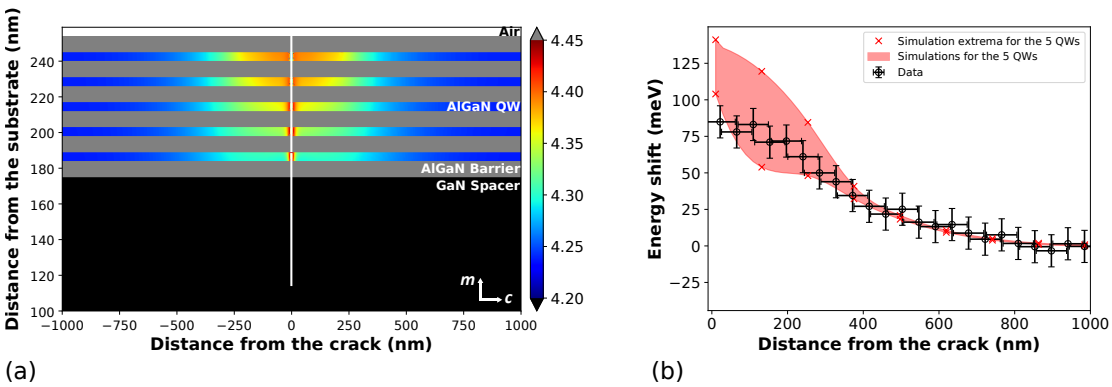

FIGURE 5.10: (a) Mapping of the local bandgap energy in the five QWs near a crack with nextnano3 calculations. The air appears in white, the AlGaN barriers in grey, and the GaN spacer in black. (b) Comparison between simulated and experimental energy shift as a function of the distance to the crack. The simulations correspond to the lowest energy transitions in the MQWs obtained by solving the Schrödinger equation for both holes and electrons. Both (a) and (b) were simulated with an Al content of 40 % in the MQWs and 60 % in the barriers. [Fin+20]

are contained in the red ribbon.

As mentioned, the Al content here is subject to uncertainties. Therefore, identical simulations with different Al contents were performed to estimate the effect of this parameter. Figure 5.11 (a) shows the simulated bandgap energy for 50 % Al content in the QW and 75 % in the barriers. Similarly, figure 5.11 (b) shows the energy shift. The same trend is observed for the simulations performed with 40 % and 60 %, but the simulated energy shift is larger and thus less in agreement with the CL observations.

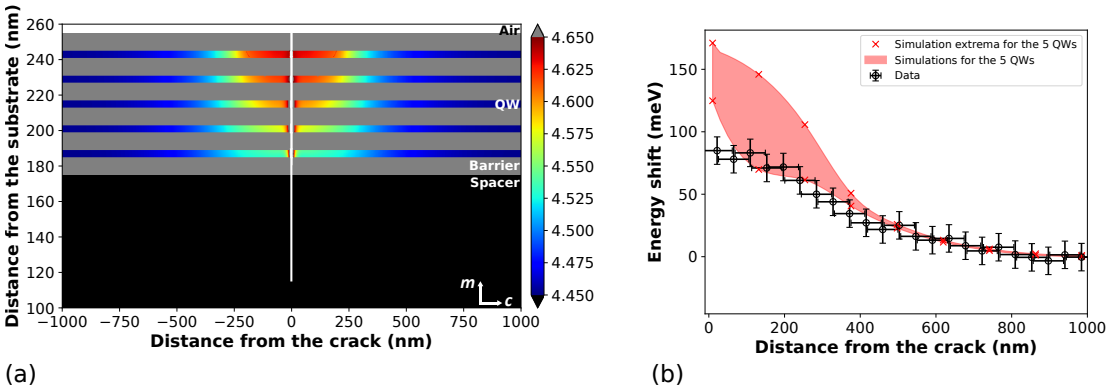

FIGURE 5.11: Same as in figure 5.10 but with an Al content of 50 % in the MQWs and 75 % in the barriers. [Fin+20]

5.2.2.3 Carrier dynamics near a crack

As already mentioned, the study of CL intensity does not allow to decorrelate LEE and IQE. Therefore, here, we will measure the evolution of the CL lifetime compared to the distance to a crack thanks to the spatially-resolved time-correlated cathodoluminescence setup (UV-HBT) previously described. The measurements are done at liquid helium temperature, with an acceleration voltage of 2 kV, and a probe current of about 5 pA.

Note: As the HBT setup is not at the output of the spectrometer, and as we did not have an adequate filter (ideally a low-pass filter with a cut-off wavelength of 350 nm, which is hard to find), we decided to work at a low acceleration voltage. Indeed, at 2 kV, the GaN intensity is negligible. In addition, it reduces the interaction volume and thus improves spatial resolution. The only other contribution apart from the MQW is the DAP band, with an intensity about three times lower than the MQW and a long lifetime ($\sim 10^2$–10^3 ns) [Fis+08; Res14], hence the choice of the acceleration voltage.

To extract quantitative information, we then fitted the decay of the autocorrelation function with an exponential decay:

$$g^2(t) = 1 + g_0 \exp(-|t - t_0|/\tau_{eff}) \tag{5.1}$$

$${\tau_{eff}}^{-1} = {\tau_r}^{-1} + {\tau_{nr}}^{-1} \tag{5.2}$$

Figure 5.12 (a), shows $g^2 - 1$ and the corresponding fits at a distance of 100 nm and 1500 nm from the crack. We can see that the lifetime is much shorter close to the crack. To study the effect of the crack on the lifetime in more detail, we then measured the lifetime evolution as a function of the distance to the crack.

In figure 5.12 (b), the normalized CL intensity and the effective lifetime are shown as a function of the distance to the crack. The CL intensity has been obtained by acquiring a CL mapping similar to the one presented earlier in figure 5.8 (d), here integrated in a window of 35 nm centered on the MQW emission.

Note: With a dwell time of 10 ms, the acquisition time of this type of profile is of the order of a few seconds (typically about 2 s). The drift is, therefore, negligible during this time. Now, concerning the lifetime profile, the dwell time is much longer, typically around 100 s. Because of the drift, it is impossible to do the whole profile (here 18 points) at once. Thus, the sample was realigned between each acquisition thanks to SE images. Intensity and lifetime profiles have been later aligned, again thanks to SE images.

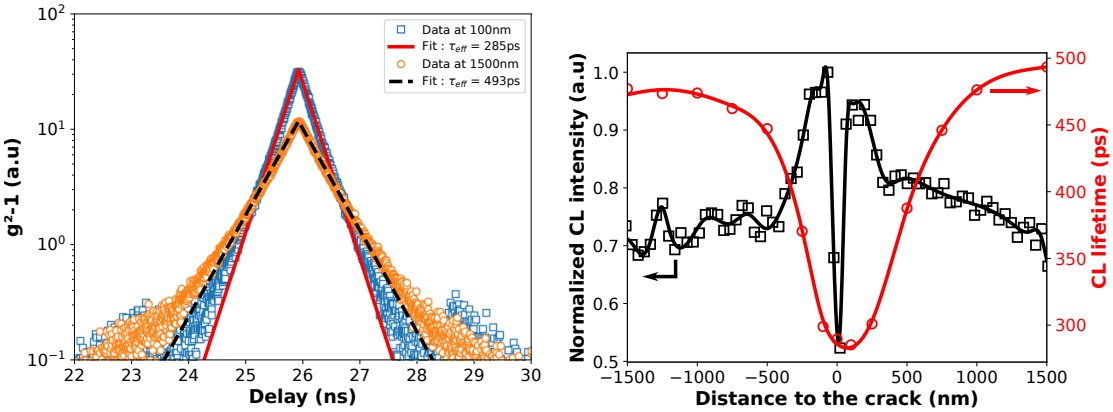

(a) (b)

FIGURE 5.12: (a) Measurement of $g^2 - 1$ at two different distances from the crack (data point) and their corresponding fit (lines). (b) Normalized CL intensity of the MQW (black squares) and CL lifetime (red circles) as a distance to the crack acquired at T = 5 K. The lifetime has been acquired with an spatially-resolved time-correlated cathodoluminescence setup. Adapted from [Fin+20]

About 400 nm away from the crack, the CL intensity starts to increase to reach 1.4 times the intensity of the crack-free region at 100 nm. Under 100 nm, the intensity quickly decreases to its minimum, which corresponds to 0.7 times the crack-free region. The lifetime is strictly decreasing with distance. It ranges from 475 ps at one micron away from the crack to 285 ps near the crack.

We can consider that this lifetime reduction is driven either by the radiative or the non-radiative lifetime.

If we consider the first hypothesis, where only the radiative lifetime is modified, we can write this as a system of equations:

$$\begin{cases} \tau_{r,bulk}^{-1} + \tau_{nr}^{-1} = \tau_{eff,bulk}^{-1} \\ \tau_{r,crack}^{-1} + \tau_{nr}^{-1} = \tau_{eff,crack}^{-1} \\ \mathrm{IQE}_{crack} = \dfrac{I_{CL,crack}}{I_{CL,bulk}} \mathrm{IQE}_{bulk} \end{cases} \tag{5.3}$$

By solving this system, it is possible to extract the non-radiative lifetime $\tau_{nr} = 920 \pm 88$ ps, the radiative lifetime near the crack $\tau_{r,crack} = 410 \pm 42$ ps and far from the crack $\tau_{r,bulk} = 980 \pm 135$ ps. Such an improvement would correspond to a significant increase in oscillator strength (more than a factor of 2), which is not seen in our simulations and not expected for m-plane QWs. In addition, we performed similar measurements at room temperature. Effective lifetimes between 65 and 80 ps were found in uncracked regions, compared to ∼40 ps at a crack location (probably limited by the time resolution). Such a reduction in effective lifetime,

even far from a crack, indicates that non-radiative recombinations dominate. To recall, the radiative lifetime is expected to increase with temperature. Thus, the observed decrease in effective lifetime near a crack is necessarily due to a further decrease in non-radiative lifetime.

Therefore, the reduction of effective lifetime near the crack is here assigned to the increasing influence of non-radiative recombinations near the surface. This lifetime reduction could originate from a strong electric field at the surface due to Fermi level pinning and piezoelectric fields [Kag+19]. Such a field dissociates excitons and spatially separates e-h pairs, preventing them from radiative recombinations. This shortening of the lifetime could also be related to the formation of non-radiative centers in the near-surface region, associated with the generation of cracks. However, this hypothesis alone is less likely. Indeed, as observed in CL, an energy shift reflects the presence of a potential barrier, impeding the carriers' diffusion towards the surface.

If the IQE decreases near cracks, the increase in CL intensity has to be related to a local enhancement of LEE. This local LEE increase could have two origins. First, by locally breaking the symmetry of the structure, the crack could act as a scattering center for the emitted light, which thus offers a possible coupling to the free space. Due to the GaN core parasitic absorption ($\alpha_{\mathrm{GaN}}(4.2 - 4.4\mathrm{eV}) \approx 2 \times 10^5\,\mathrm{cm}^{-1}$ [Kaw+97]) UV photons emitted in the wire can only propagate on few hundreds of nanometers. As a consequence, only the light generated close to the crack would benefit from a better extraction efficiency, which is consistent with our observations. Second, according to our simulations (not shown here), the change of strain state near the crack could induce a reordering of the valence bands at around 250 nm from the crack [Rig+11; Jac+12]. Due to their different selection rules, it should result in a change of polarization direction of the emitted light [Bry+15; Rei+15]. Since LEE drastically depends on the light polarization [Ama+20; KR16], such crossover could locally increase the observed CL intensity. In order to confirm this hypothesis, it could be interesting to perform polarization-dependent CL measurements, as presented by Fouchier et al. [Fou+19].

5.2.2.4 Conclusion

In conclusion, by probing the optical properties of GaN wires with Al-rich core-shell MQWs using spatially-resolved time-correlated cathodoluminescence, we demonstrate the influence of cracks on the active region efficiency. Under the effect of strain relaxation, the emission energy of MQWs increases near the crack by about 100 meV. In addition, we observed an increase in CL intensity near the crack, which was attributed to a local increase in LEE. This indicates that light extrac-

tion is a severe problem in this type of structure. Finally, the carrier lifetime undergoes a pronounced decrease near the extended defect, reflecting a reduction of the IQE.

Although the general trend indicates an increase in intensity and therefore in EQE, these cracks could be a real problem when it comes to electrical injection. Especially, as they extend deep into the wires, they could shunt the active region. It is, therefore, necessary to prevent their formation.

5.3 Mitigation of cracks

Now that we have seen the effects of cracks on optical properties, it is important to understand under what conditions they form. The following is a brief summary of the material published in Grenier et al. "Toward Crack-Free Core-Shell GaN/AlGaN Quantum Wells", 2021 [Gre+21].

As we have seen, crack formation is related to the difference in lattice parameters between the Al-rich layers in the shell and the GaN wire core. Therefore, a first approach to reduce their formation would be to reduce the Al content in the shell. For that, we will focus here on structures relatively similar to the one presented previously, except for the AlGaN QWs, that have been replaced by GaN QWs. A schematic of the studied structure can be found in figure 5.13 (a). The upper part, *i.e.*, the core-shell region, is composed of a 100 nm-thick GaN spacer followed by five GaN QWs with 5 nm-thick $Al_{0.6}Ga_{0.4}N$ barriers. Finally, the growth is capped by 2 nm of GaN.

In this type of structure, the emission energy is mainly determined by the thickness of the wells. Therefore, it is necessary to have very thin QWs to emit in the deep UV. Despite the absence of Al in the QWs, we observed the formations of cracks for the thinner QWs. As shown in figure 5.13 (b) and (c) the crack density increases by decreasing the thickness of the QWs. To understand under which conditions these cracks form, elastic calculations have been performed by Vincent Grenier. Without going into details, these calculations rely on the fact that, here, the wire's diameter is in the micrometer range. Thus, the GaN core can be considered quasi-bulk and calculations are similar to those for planar structures. For simplicity, the heterostructure is approximated by a single AlGaN layer of thickness L and average Al composition $\bar{x}$.

$$L = 6L_{\text{barrier}} + 5L_{\text{QW}}$$
$$\bar{x} = \frac{6L_{\text{barrier}} \times \bar{x}_{\text{barrier}}}{L}$$

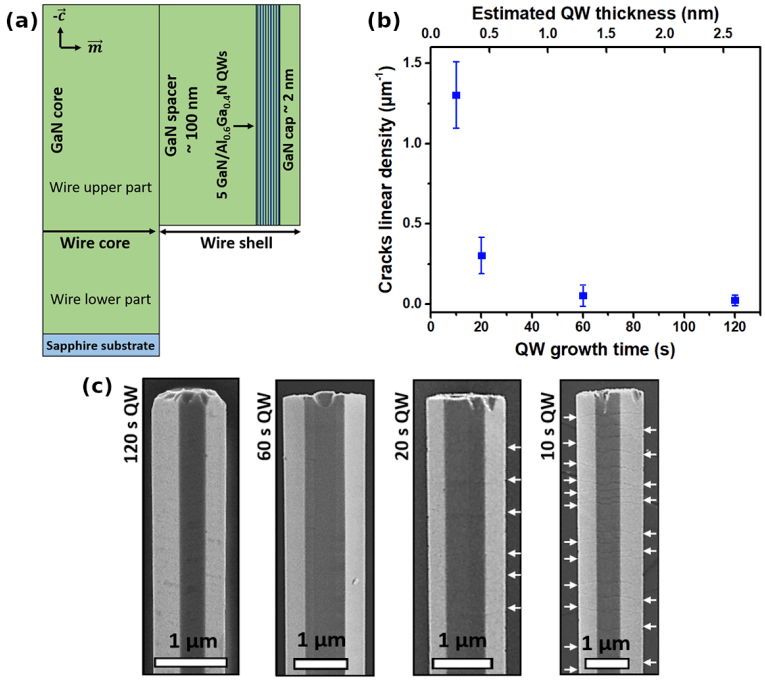

FIGURE 5.13: (a) Schematic of a typical wire. (b) Measured crack linear density as a function of the GaN QW thickness. For each sample, 50 wires are considered, and the error bar corresponds to a 95% deviation from the mean value. (c) Top-view SE image of the upper part wire with QW thickness changing from 2.6 to 0.2 nm (corresponding growth time between 120 and 10 s). White arrows indicate the presence of cracks. Adapted from [Gre+21]

Figure 5.14a shows the linear crack density as a function of the calculated strain energy density. The interested reader may find more details in [Gre+21; Dur+14]. The energy threshold of $4\,\mathrm{J\,m^{-2}}$ above which planar structure tends to form cracks found by Einfeldt et al. is indicated by a dashed line [Ein+00]. We can see that crack density rapidly increases above this threshold.

To confirm this hypothesis, we grew two additional samples with the thinnest QWs (*i.e.*, samples that presented cracks). However, the barrier thickness was reduced from 5 nm to 3 nm to reduce the surface energy. As indicated by the red dots in figure 5.14a, these samples are free of cracks.

In addition, by adding an Al gradient between the spacer and the QWs, the crack density appears to be further reduced, and the emission energy increases. An overview of the PL emission of the different samples as a function of the estimated QWs thickness can be found in figure 5.14b. Results are compared to one-dimensional 8x8 k.p calculations performed with nextnano3 [Bir+07]. Two cases have been considered to estimate the influence of the strain, a pseudomorphic growth on: GaN, *i.e.*, $Al_{0.6}Ga_{0.4}N$ is fully strained and on $Al_{0.6}Ga_{0.4}N$, *i.e.*, GaN is fully strained. From these data, we cannot safely draw conclusions about the

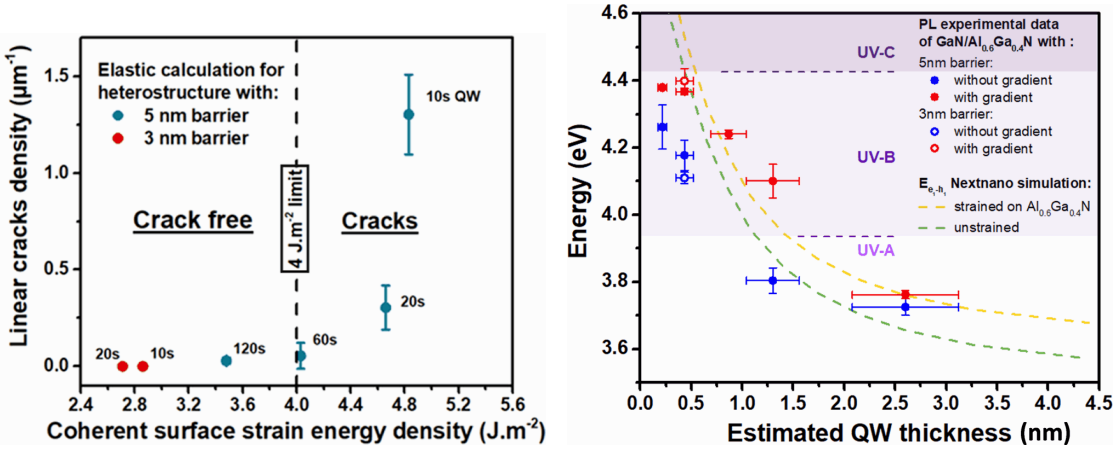

(a) (b)

FIGURE 5.14: (a) Linear crack density as a function of the surface elastic energy calculated for a single Al_xGa_xN layer having QW growth times varying from 120 to 10 s and two barrier thicknesses (5 nm, blue dots; 3 nm, red dots). The experimental elastic energy density threshold ($4\,J\,m^{-2}$) found by Einfeldt et al. is indicated by a vertical dashed line. (b) PL emission energy of GaN QWs as a function of their estimated thickness with (red dots) and without (blue dots) Al gradient. Measurements are performed at 5 K on wire assemblies dispersed on silicon. Done with a 244 nm laser at about $50\,W\,cm^{-2}$. Adapted from [Gre+21]

strain state of the wire. However, the energy shift induced by the gradient suggests that it partially relaxes the strain induced by the core, thus inducing strain in the GaN QWs.

It would be interesting to perform TEM analysis to verify if this gradient favors dislocation formation, thus allowing relaxation without crack formation.

Conclusion

In conclusion, the apparition of cracks seems to be related to a surface energy threshold. By growing different samples and calculating their respective surface energy density, a threshold of $\sim 4\,J\,m^{-2}$ was found. The same value has already been reported by Einfeldt et al. in the case of planar structures [Ein+00]. New samples have been grown with thinner barriers to stay below this threshold, resulting in crack-free microwires. In addition, by adding an Al gradient before realizing the active region, we observed a systematic decrease in the crack density as well as an increase in the PL emission energy. As a result, emission as low as 4.4 eV (280 nm) corresponding to the UV-B/C limit was achieved.

These results open the way to a first component fabrication in order to characterize the electrical properties of AlGaN/GaN microwires. This study will be the

subject of the next section.

5.4 Realization and characterization of single wire LEDs

We are now interested in the realization of a single-wire UV-LED device. This study was carried out in collaboration with Vincent Grenier and Christophe Durand. In particular, Vincent has grown the samples, made the electron-beam-induced deposition contacts, and performed part of the I-V measurements.

5.4.1 EBID Contacts

We first decided to contact the wires by electron-beam-induced deposition as it is a single-step in situ process, requiring no planarization layer or lithography. Thus, it is adapted for contacting dispersed core-shell wires. In this technique, a volatile precursor is decomposed by a focused electron beam, typically of a SEM or STEM, leading to the deposition of the desired compound on the substrate.

5.4.1.1 Contact deposition

Here, microwires were mechanically dispersed on silicon thermal oxide wafer (500 nm of SiO_2) with Ni/Au patterns. Figure 5.15 (a, b) illustrate the possibility of moving the selected wire (green) between two Ni/Au contacts (yellow) using a micromanipulator. Once the wire is in place, an injector is inserted near the sample and releases tungsten hexacarbonyl ($W(CO)_6$), a precursor of tungsten. During the deposition, the electron beam current is set to 17 nA with a 3 kV acceleration voltage. To contact only the desired part, the scanning area is narrowed to the two regions outlined by red rectangles in figure 5.15 (c). Also, the n contacts were done by rotating and tilting the stage to have a direct view of the GaN core. This process has been performed by Vincent Grenier.

Note : Ion-beam-induced deposition (IBID), a similar technique except that electrons are replaced by ions, has already been reported to produce higher-quality contact [An+19; Wil+14]. It appears that the contacts made in IBID have a lower percentage of carbon and oxygen than those made by electron-beam-induced deposition. One of the reasons could be the higher energy of the ions, leading to a better dissociation of the precursor ($W(CO)_6$). However, similar observations have been made for precursors containing neither carbon nor oxygen (WF_6) [Wil+14]. Anyway, considering the damage caused by ions, we still preferred electron-beam-induced deposition, as advised by An et al. [An+19].

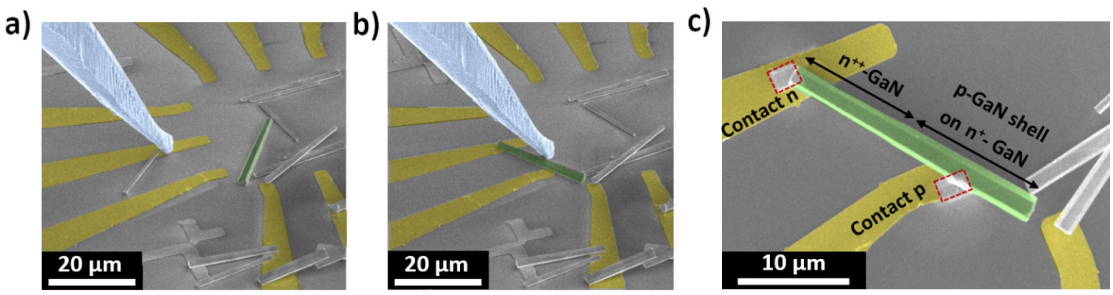

FIGURE 5.15: (a) and (b) SE images of a microwire (green) moved on Ni/Au contacts (yellow) using a micromanipulator (light blue). (c) SE image of tungsten deposition (red rectangle) by electron-beam-induced deposition (3 kV, 17 nA) to perform n and p contacts of a core-shell GaN microwire (green). [Gre+22]

5.4.1.2 Study of GaN and AlGaN *p-n* junction

Usually, the Al-rich active part of deep UV-LED devices is embedded in an AlGaN p-n junction. Here, the core-shell active layer is buried under a Mg p-doped layer, as it has already been demonstrated in microwire LEDs for visible emission [Tch+14b; Lav+14; Kap+18]. However, extending this doping procedure to AlGaN alloys is still challenging, and only a few studies investigated it on m-plane surfaces.

As a first step, it is crucial to characterize the electrical properties of AlGaN p-n junction embedded in GaN p-n junction. For this purpose, two structures without QWs have been realized (see figure 5.16 (a)): the first structure (structure 1) is a GaN p-n junction, and structure 2 embeds an $Al_{0.3}Ga_{0.7}N$ p-n junction.

Figure 5.16 (b) shows I-V measurements performed on several wires of each type. A clear rectifying profile is observed for both structures with standard diode-like behavior. Note, however, that the first measurement on some wires shows rectifying behavior but with a low forward current. It could be due to a thin insulating layer, e.g., native oxide or passivation layer, that breaks under a strong electric field. All subsequent measurements seemed identical.

We can see that structure 2, *i.e.*, with an AlGaN junction, has a higher threshold voltage. To quantify this, we introduce the Schockley diode model, which gives the I-V characteristics of an idealized diode, *i.e.*, in the absence of parasitic resistance:

$$I = I_S \left[\exp\left(\frac{qV}{\eta k_B T} \right) - 1 \right] \tag{5.4}$$

With I the diode current, I_S the reverse bias saturation current, V the voltage across the diode, k_B the Boltzmann constant, T the temperature, q the elementary charge, and η the ideality/quality factor.

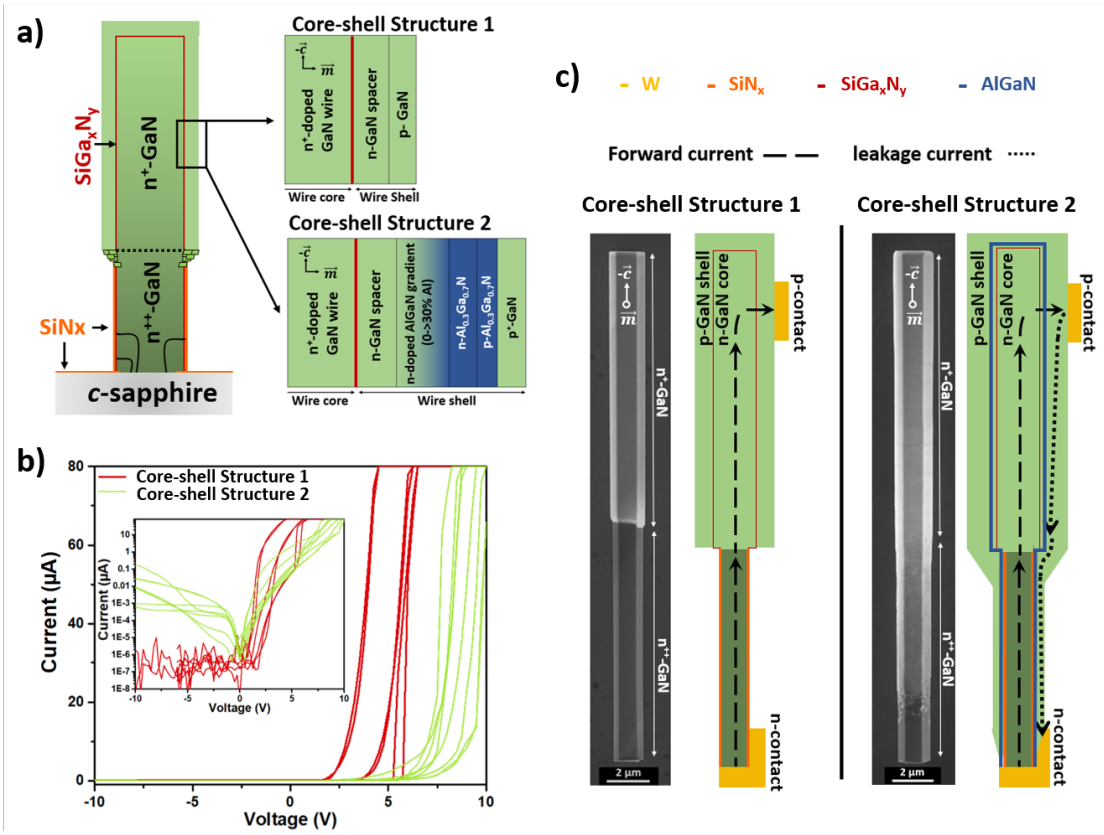

FIGURE 5.16: a) Schematic of core-shell structures with GaN single p-n junction (structure 1) and GaN/AlGaN p-n junction (structure 2). b) Room temperature I-V curves of structures 1 (red) and 2 (green). The inset shows the I-V curves in logarithmic scale. c) Schematics and SE images of structures 1 and 2. In the SE images, the p-GaN layer that finishes the shell growth of both structures appears brighter. The schematics show a single core-shell wire contacted with tungsten. When growth involves AlGaN layer(s) (right), the supposed leakage and forward current paths are represented by dotted lines. Adapted from [Gre+22]

In order to extract the ideality factor, we make some assumptions. First, we assume that the Joule effect is negligible because the measurements are brief. Thus, the wires remain at room temperature. This sets k_BT to ~26 meV. Then, to simplify the expression, we want to ideally place ourselves in the case where $qV/(\eta k_BT) \gg 1$. Here we assume that the ideality factor will typically be of the order of 10. Thus, for a voltage greater than 1 V, we here neglect the -1 in equation (5.4), so the expression of the current becomes:

$$I \approx I_S \exp\left(\frac{qV}{\eta k_B T}\right) \tag{5.5}$$

From this expression, we can easily get the ideality factor which gives insight into the diode's quality.

$$\eta \approx \frac{q}{k_B T} \left(\frac{\partial \ln I}{\partial V} \right)^{-1} \tag{5.6}$$

Note: The ideality factor can also be extracted numerically without assuming $qV/(\eta k_B T) \gg 1$. This gives very similar results above 1 V. More details on the derivation of η with and without this approximation can be found in appendix 5.A.

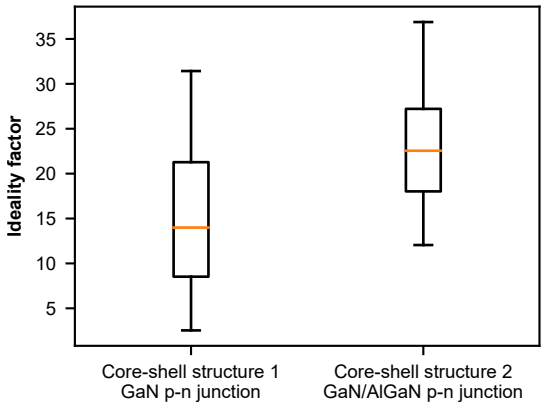

FIGURE 5.17: Comparison of ideality factors for structures 1 and 2 extracted at a forward bias greater than 1 V

Figure 5.17 shows the ideality factor for 5 devices of each structure for a forward bias greater than 1 V. We can see that overall η is greater in the case of structure 2, embedding an AlGaN p-n junction. This is probably related to a higher bandgap energy and a lower hole injection efficiency due to the doping of AlGaN.

The relatively high ideality factor, even in the case of a simple GaN p-n junction, has already been reported for a similar core-shell structure [Tch15; Lav+14]. Several explanations have been proposed: trap-assisted tunneling, current crowding, as well as carrier leakage [Bin+13]. A model assuming multiple rectifying junctions in series in a device can also explain a high ideality factor [Sha+03]. The latter assumption probably applies in our case. Indeed, the contacts are not optimized. In particular, the realization of ohmic contact on p-GaN is challenging. Moreover, tungsten is not the best metal for making p-GaN contacts. With a work function of 4.6 eV against 5.2 eV for Ni, which is commonly used, the Schottky barrier can be estimated to be 2.2 and 1.6 eV in W/p-GaN and Ni/p-GaN contacts, respectively, leading to an increased ideality factor as observed by Hwang et al. [Hwa+13]. Furthermore, no surface treatment was performed before deposition, and no annealing was performed after deposition. For all these reasons, p-contacts may not be ohmic.

Although we have not verified it, the injection on the n side should be of better quality because the core is heavily doped, well above the Mott transition[8]

[8]The Mott transition corresponds to the non-metal metal transition. Beyond a certain con-

([Si]$\sim 10^{20} \gg 2 \times 10^{18}\,\mathrm{cm}^{-3}$) [Wol+11]. In addition, the n contacts were made with a certain angle of incidence, which allows direct contact with the core and not through a possible SiN_x layer. It has already been shown that this residual layer prevents the realization of ohmic contacts and requires an etching before metal deposition [Tch15].

In addition to the higher ideality factor, we observe a larger leakage current in structure 2. To understand its origin, it is necessary to take a closer look at the actual structure of the device. As observed in the SE images of figure 5.16 (c), the delimitation between the core and the core-shell region is well defined in structure 1 (*i.e.*, without Al), while it is not the case for structure 2. Indeed, the realization of a shell only on the upper part of the wire relies on the presence of a SiN_x passivation layer that prevents the lateral growth of GaN [Eym+12]. However, it turns out that this passivation layer is not as effective in preventing the growth of Al-containing layers [Gre+20]. Therefore, the p-doped shell may extend to the bottom of the wire, creating an additional conduction path (see *"leakage current path"* in figure 5.16 (c)).

It is probably possible to mitigate this problem by making longer GaN wires since, as observed in the SE image (figure 5.16 (c)), the thickness of the p-GaN shell decreases as we get closer to the base of the wire.

Conclusion This preliminary study shows that, although the contacts made by electron-beam-induced deposition and the doping of AlGaN have not been optimized, it is possible to make core-shell GaN microwires containing an AlGaN p-n junction with diode-like electrical properties.

5.4.1.3 Electrical properties of UV-A LED microwires

As we have seen that it is possible to realize GaN/AlGaN p-n junctions with a diode behavior, we have realized structures, including this time QWs, in order to obtain single wire UV-A LEDs.

This structure was realized by inserting 5 GaN (2.6 nm)/$Al_{0.3}Ga_{0.7}N$ (3 nm) QWs into the GaN/$Al_{0.3}Ga_{0.7}N$ p-n junction (see figure 5.18 (a)). The electrical contacts were made by electron-beam-induced deposition as described previously. Figure 5.18 (b) shows the I-V measurements at room temperature for this new structure. We can see that the addition of the five QWs does not significantly change the electrical properties, with a forward current close to $\sim$100 µA at 10 V and a leakage current around $\sim$0.1 nA at 5 V.

centration of dopant n (p), the ionization energy drops to zero, all dopants are ionized, and the Fermi level enters the conduction (valence) band. The semiconductor then becomes metallic.

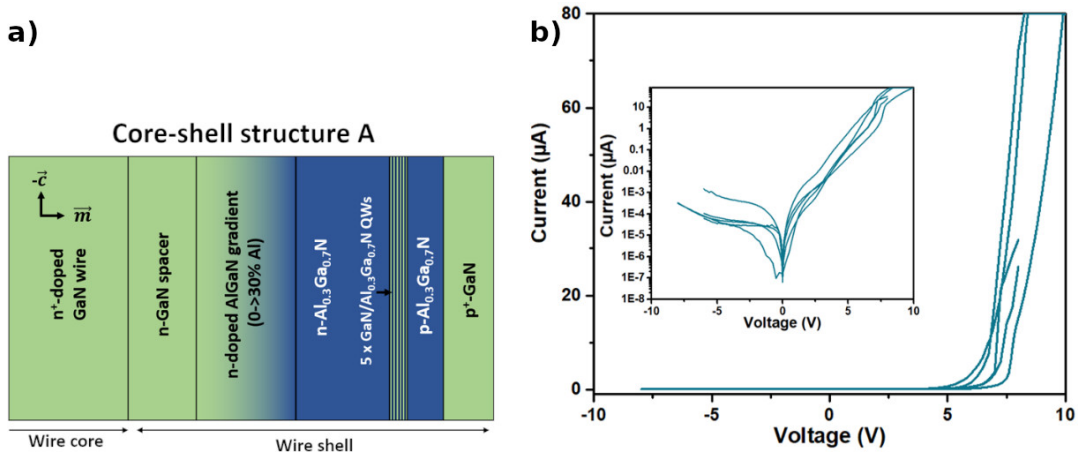

FIGURE 5.18: a) Schematic of the core-shell structure wire for UV-A emission with 5 GaN (2.6 nm)/$Al_{0.3}Ga_{0.7}N$ (3 nm) QWs integrated in a GaN/$Al_{0.3}Ga_{0.7}N$ *p-n* junction. b) Room temperature I-V curves on several single wires with core-shell structure A connected by electron-beam-induced deposition. Adapted from [Gre+22]

We will now focus on their electro-optical properties. To do so, the wires are placed in our CL setup. Inside the SEM, micromanipulators are inserted in such a way that they can contact the Ni/Au patterns while keeping the sample at the focal plane of the parabolic mirror figure 5.19.

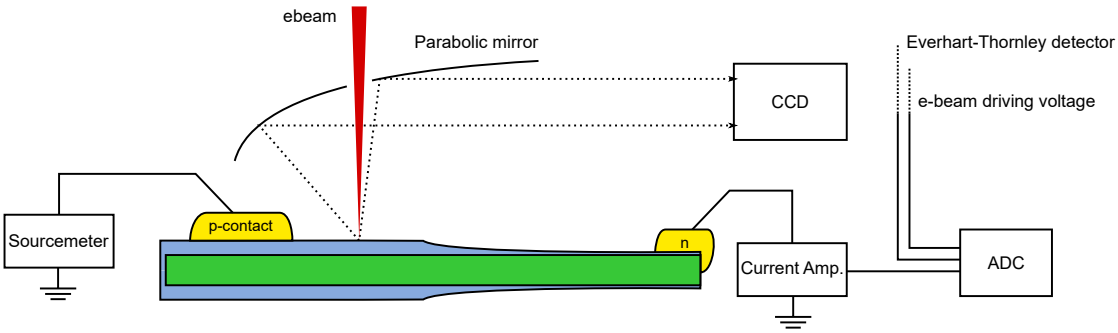

FIGURE 5.19: Schematic of the experimental setup. Note that the current amplifier is bypassed when the sourcemeter is used to perform I-V measurements. In addition, the CCD can be replaced by a PMT + current amplifier connected to another channel of an ADC to measure CL intensity at the same time.

We first check that we obtain the same electrical properties with this new setup. A sourcemeter is used to bias the device and perform I-V measurements. It can be seen in figure 5.20 (a) that the first I-V measurement is similar to the previous ones. However, we also notice that the current level is sensitive to electron beam irradiation and current stressing. In particular, we have often observed that a large leakage current appears especially after current stressing.

Several hypotheses can explain these phenomena: it has already been observed

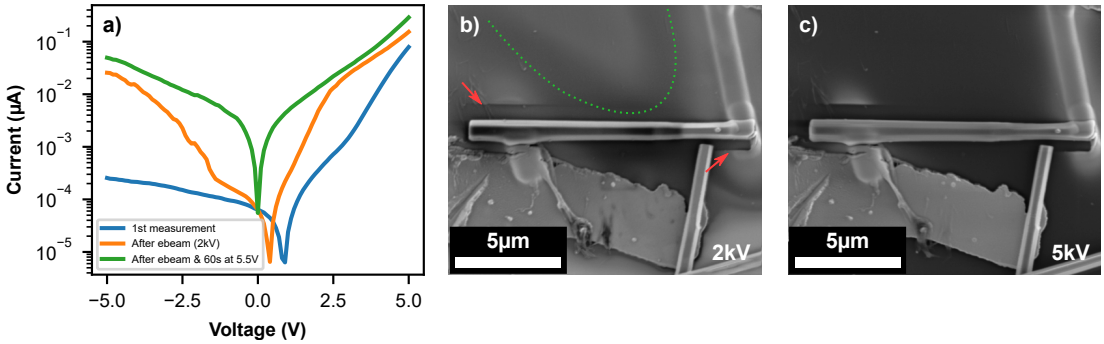

FIGURE 5.20: a) IV measurements, performed on the same wire: first measurement (blue), after ∼1 min under 2 kV electron beam irradiation (orange), and finally after 60 seconds with a forward bias of 5.5 V (green). b) and c) SE images of a wire acquired at 2 and 5 kV respectively. Both images show a diffuse tungsten deposit. On the 2 kV image, the shadowing effect of the electron-beam-induced deposition deposit is highlighted by red arrows. We also observe a changing SE contrast, delimited by a green dotted line.

that the conductivity of electron-beam-induced deposition contacts increases after current stressing. This would be partly due to a change in composition, more precisely to a decrease in the amount of oxygen and carbon in the contacts. Identical results were observed after annealing, suggesting a thermal effect [Wil+14].

Concerning the sensitivity under electron beam irradiation, the tungsten precursor ($W(CO)_6$) may be deposited on a larger area than desired. Figure 5.20 (b) and (c) shading effects suggest a very large and diffuse deposit. This can be seen very well at low acceleration voltage (figure 5.20 (b)), where the surface and charge effects are important. This deposit may be formed by precursors that are not entirely decomposed. Under the effect of the electron beam, this layer may become conductive, thus creating new conduction paths, which is the underlying principle of electron-beam-induced deposition.

In this setup, it is also possible to perform electron-beam-induced current (EBIC) mapping. This technique consists in generating e-h pairs with an electron beam, here of a SEM. If the carriers are generated in a region with an electric field, or if they can diffuse to such a region before recombining, they can be separated by the electric field. The resulting current is measured. This technique allows, for example, to directly image the SCR [Tch+14c] and measure minority carriers' diffusion length. Note that here, due to the core-shell geometry, it is not possible to image the extension of the SCR. However, this type of measurement does provide information on the transport efficiency of majority carriers (*i.e.*, holes in the p and electron in the n region) and the location of the core-shell region [Lav+14].

As observed in figure 5.21 (a) and (b), the EBIC signal originates only from

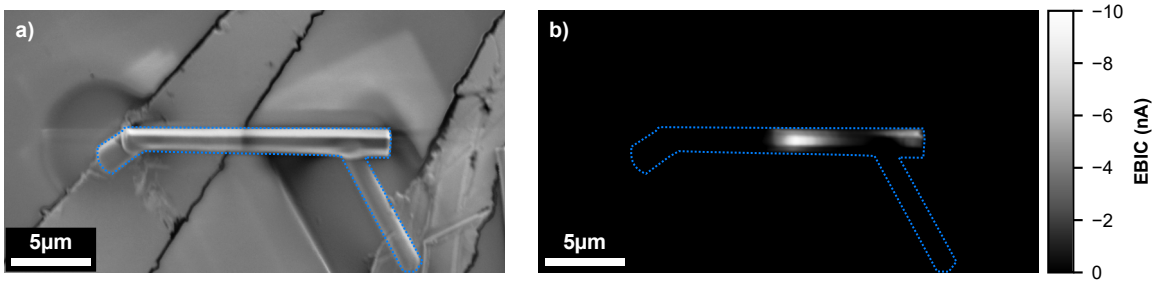

FIGURE 5.21: (a) SE image and (b) 0 V EBIC mapping acquired with an acceleration voltage of 2 kV. A blue dotted line indicates the outline of the wire and contacts.

the upper part of the wire. This suggests that the *p*-*n* junction is localized only in the core-shell region, as previously observed on InGaN/GaN core-shell microwires [Tch+14c; Lav+14]. We can also notice the absence of EBIC signal at the location of the *p*-GaN contact, due to the absorption of the electron beam by the metal. The fact that the signal extends relatively far from the contact position may reflect an efficient transport of the majority carriers. However, it could also be a sign of a very large *p*-contact on the shell.[9] This is probably the case here, as a weak electron-beam-absorbed current (EBAC) was observed in the circular region close to the *n* contact in figure 5.21 (a). This is an additional clue that the tungsten deposit is broader than expected and thus could be partly responsible for the leakage/instability. The origin of this current will not be discussed here to keep the message clear but details can be found in appendix 5.B.

For completeness, from these measurements, we can estimate the current density. Assuming that the current is injected only below the thick part of the contact ($\sim$1 µm^2), the current density is estimated to be about $\sim 10^4$ A cm^{-2} at 10 V. On the contrary, if we assume that the current is distributed on the whole shell ($\sim$40 µm^2, delimited by the EBIC signal), the current density should be around $\sim 2.5 \times 10^2$ A cm^{-2}. This is somewhat comparable to planar blue/UV-A LEDs, which often present a current density in the 10^2–10^4 A cm^{-2} range slightly above threshold [Oli+17b; Fan+19]. This reflects a relatively efficient injection of the carriers.

Note 1: It is important not to confuse the e-beam current (of the order of a few hundred pA) and the EBIC of some nA. This difference is explained by the fact that the incident electrons are very energetic ($E_{beam} = 2$ keV) compared to the energy of creation of an e-h pair ($E_{eh} \sim 10$ eV). Therefore each incident electron generates hundreds of carriers [Lav+14]. Also, the sign of the EBIC is here negative according to the standard convention (*i.e.*, positive current when a

[9] Note that the two hypotheses are not mutually exclusive.

positive bias is applied). Indeed, due to the electric field of the SCR, we collect electrons (holes) on the n-side (p-side).

Note 2: As demonstrated by Lavenus et al., it is possible to observe a change in the sign of the EBIC signal at low acceleration voltage in the vicinity of the p-contact, reflecting the presence of a Schottky barrier [Lav+14]. However, we did not observe such a phenomenon down to 2 kV. Below 2 kV, charging effects are important, and the signal is too weak to be properly measured.

Again, the interested reader may find additional details about EBIC in appendix 5.B

5.4.1.4 Optical properties of UV-A LED microwires

We are now interested in the optical properties of microwires. As mentioned before, an important leakage current (or even short circuits) often appears after sustained bias probably due to thermal effects. To prevent this, measurements will be carried out under pulsed bias with a duty cycle of 1 % at 10 kHz.

Figure 5.22 shows electroluminescence spectra at various peak voltage ranging from 12 to 18 V. Three main contributions can be identified.

- the broad yellow band (YL) emission at around 2.25 eV related to deep defects in GaN [RM05]. Note that this contribution is observed in the unintentionally-doped part in this type of sample in CL [Koe+11; Kap+20].
- an asymmetric contribution at 3.35 eV called violet band (VB), that could be attributed to a defect band in AlGaN [Nam+05; Yan+14], to DAP present in AlGaN [Nak+09] or in the p-doped GaN shell [RYW99]. A more recent study also suggests that it could be related to surface defects in GaN [Fuj+22]. A hypothesis about its origin in our case will be given in a later section (section 5.4.1.6)
- the GaN QWs UV-A emission centered at 3.65 eV (340 nm) with a FWHM of ∼150 meV.

We can see that the VB emission dominates at low voltage, but the QWs/VB intensity ratio reverses between 17 and 18 V. Note that even though we mitigate the apparition of leakage current using a pulsed excitation, the wire and the p-contact broke at 18 V. This breakage seems to appear systematically at the p-contact and has been observed in many wires, typically between 15 and 20 V, see figure 5.23. Note that the contact breaking systematically on the p-side is probably correlated with the fact that it is the most resistive area of the wire and, therefore, the one where both the electric field and the Joule heating are the most important.

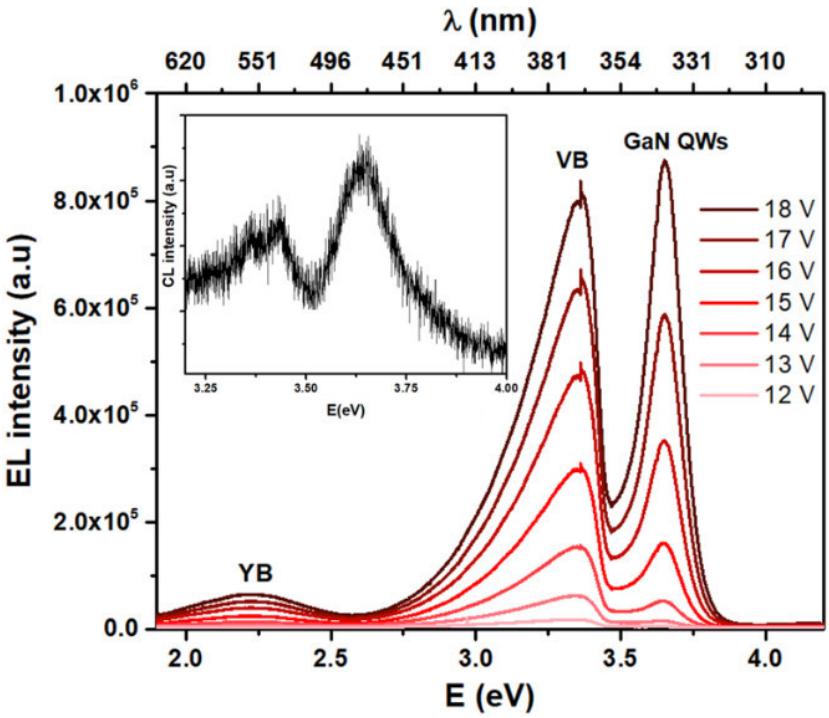

FIGURE 5.22: Electroluminescence spectra of a single wire obtained at room under pulsed bias. The inset shows the CL spectrum of the same wire, acquired with a 2 kV acceleration voltage. Adapted from [Gre+22]

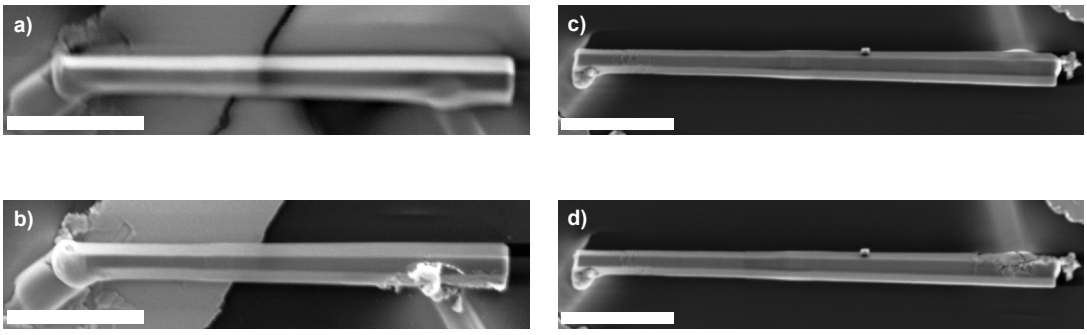

FIGURE 5.23: Image of contacted wires before (a and c) and after breakage (b and d). The scale bar are 5 µm wide.

The inset of figure 5.22 shows a CL spectra acquired on the same wire with a 2 kV acceleration voltage. In contrast to the electroluminescence measurements, the main CL emission comes from the QWs, and the observed peak at 3.35 eV (370 nm) attributed to the VB emission is weaker. Note that the VB emission is quite difficult to observe in CL while it appears systematically in electroluminescence. This VB emission is mainly visible in the CL spectra for low acceleration voltage. Therefore, we suspect it originates from the outer shell layers and most likely from DAP contributions in *p*-GaN.

The intense VB emission and the high voltages required for QW emission could be a sign of poor hole injection in the active region combined with poor electrical injection at the metal contact. Moreover, here, in the absence of EBL, an electron overflow is suspected, inducing important recombinations in the *p*-shell.

5.4.1.5 Towards UV-B LED

A structure similar to the one presented earlier has been designed to target UV-B emission (see figure 5.24 (a)). To do so, the growth time of the QWs has been divided by three. Thus, assuming an identical growth rate, the thickness of the QWs is estimated to be 0.85 nm. In addition, to ensure quantum confinement in these thinner QWs, the Al content of the barriers was increased to 60%. Also, note the presence of a *p*-doped linear AlGaN gradient between the active part and the *p*-$Al_{0.3}Ga_{0.7}N$ layer. Similar layers have already been used in planar UV structures to improve the hole injection [Kuo+16; Yan+11].

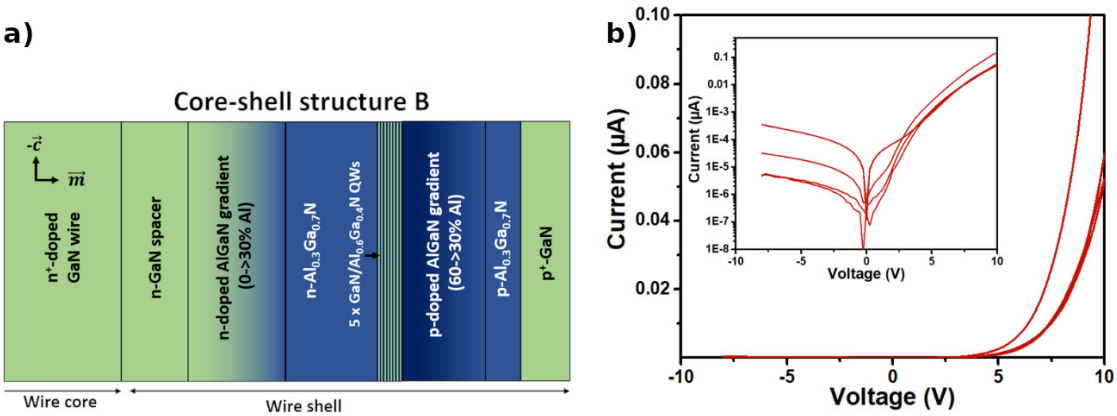

FIGURE 5.24: a) Schematic of the core-shell structure wire for UV-B emission with 5 GaN (0.85 nm)/$Al_{0.4}Ga_{0.6}N$ (3 nm) QWs integrated in a GaN/$Al_{0.3}Ga_{0.7}N$ *p*-*n* junction. b) Room temperature I-V curves on several single wires with core-shell structure B connected by electron-beam-induced deposition. Adapted from [Gre+22]

Figure 5.24 (b) shows preliminar I-V measurements performed on several wires.

As expected, the UV-B devices have degraded electrical characteristics compared to UV-A devices. Typically, at a 10 V forward bias, the current is 3 to 4 orders of magnitude lower. However, it should be noted that the reverse leakage current is comparable to that of the UV-A devices. This suggests that the leakage does not depend on quantity but rather on the presence or not of Al in the structure. This observation is consistent with the hypothesis that the leakage current is primarily caused by the *p*-GaN shell extending to the bottom of the wire, as the Al-containing layers bury the passivation layer.

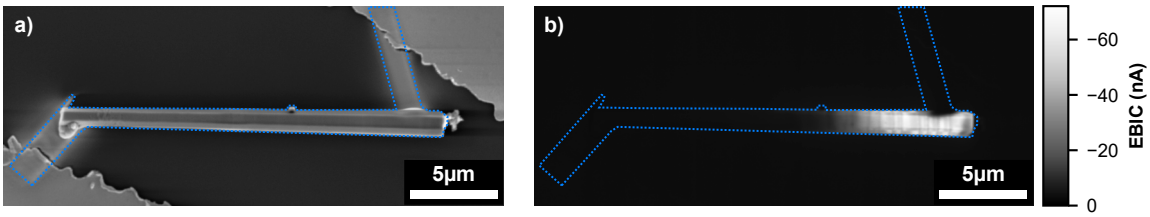

FIGURE 5.25: (a) SE image and (b) 0 V EBIC mapping acquired with an acceleration voltage of 5 kV. A blue dotted line indicates the outline of the wire and contacts.

Figure 5.25 shows a SE image of a single microwire (a) with its corresponding EBIC signal mapping at 0 V (b). Similar to the UV-A structure, the EBIC signal is only present on the upper part of the wire, where the GaN/AlGaN *p*-*n* junction is located. In the EBIC image, dark lines indicate the presence of cracks in the wire. This suggests that they have a detrimental effect on the electrical injection. However, since the forward current is much lower and the reverse one is comparable to the UV-A sample, *i.e.*, without cracks, they probably do not introduce significant leakage paths.

We can again estimate a current density as we did for the UV-A wires. If the injection were done only beneath the contact ($\sim$1 µm^2), the current density would be about $\sim$10 A cm^{-2} at 10 V. Conversely, if the injection takes place on the entire shell ($\sim$40 µm^2), the current density would be $\sim$0.25 A cm^{-2}. These values are far from those obtained previously, underlining a drastic decrease in injection efficiency.

As shown in figure 5.26, electroluminescence was observed despite the low forward current and the presence of cracks. Spectra are here very similar to the ones of the UV-A devices. The same contributions can be identified: the yellow band YL, the violet band VB, and the QWs emitting here at 4 eV (310 nm). Interestingly, we can note that the VB emission is here slightly red-shifted. It could be a sign that VB does not originate from an Al-containing layer but rather from GaN, as one could naturally expect a blue shift with increasing Al content. Here again, the intensity of the QWs increases faster than the VB one. However, we could not

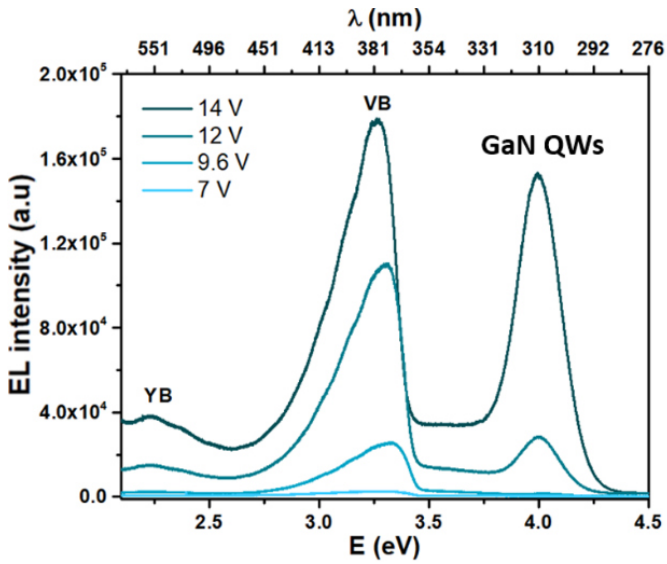

FIGURE 5.26: Electroluminescence spectra of a single wire obtained at room with a pulsed voltage. [Gre+22]

go higher in voltage because the wire broke at 15 V, as for the UV-A sample. Note that, at the time of writing, this emission energy is the highest ever reported in the literature for core-shell QWs.

Regarding the CL spectra, the three usual contributions were observed: the yellow band, the QWs, and the GaN NBE. However, particular attention should be paid because the SiO_2 substrate on which the wires were dispersed showed UV (285 nm), blue (460 nm), and red (650 nm) emissions. These emission lines were previously reported by Goldberg et al. and appear to be activated/enhanced by electron beam irradiation (see details in appendix 5.C) [GTF96].

5.4.1.6 Origin of the violet band

Finally, to determine the origin of the VB emission, we performed EL measurements in the same experimental conditions on a GaN *p*-*n* junction studied earlier (structure 1). Figure 5.27 shows electroluminescence spectra for the three studied structures: GaN *p*-*n* junction (a), UV-A (b), and UV-B LED (c). All three samples have in common YL and VB, confirming that they originate from GaN. It is well known that YL comes from the unintentionally-doped GaN core in this type of structure [Koe+11; Kap+18]. Concerning VB, as we only observed it on LED structures, *i.e.*, with a *p*-GaN shell, and the fact that a quite similar line is visible in CL spectra at low acceleration voltages (between 1.5 and 3 kV) suggests that it comes from the *p*-GaN layer. Moreover, a band with a maximum at ∼3.25 eV is commonly reported in PL spectra of Mg-doped GaN [Res+14]. We could also add that its energy is in relatively good agreement with an electron-to-neutral acceptor

transition or with a DAP transition ($E \approx 3.25 \approx E_G - E_{\mathrm{Mg}} + \frac{1}{2}k_B T$)

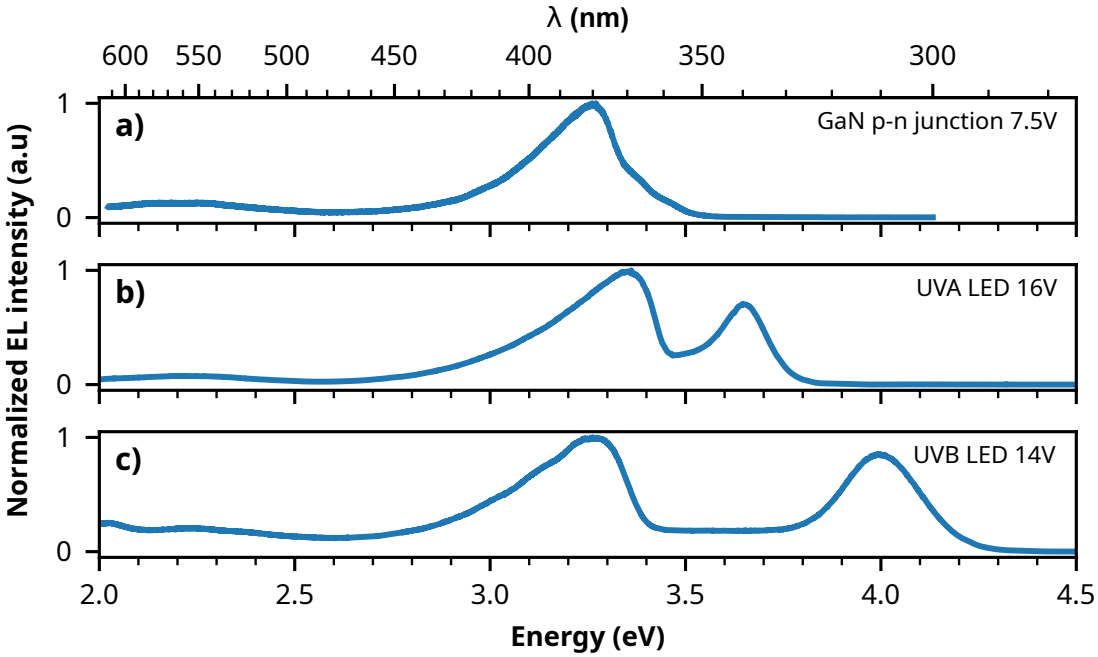

FIGURE 5.27: EL spectra for (a) GaN *p*-*n* junction (structure 1), (b) UV-A and (c) UV-B LED.

5.4.1.7 Improved electrical properties of UV-B LEDs.

A third LED structure was realized to improve the electrical properties and, in particular, the injection. It includes an additional *n*-doped Al gradient from 30% to 60% [Kuo+16; Yan+11]. Also, the thickness of the barriers was reduced from 3 nm to 1 nm. By following the same experimental procedure, we observed a significant increase in the forward current (typically three orders of magnitude at 10 V, *i.e.*, ∼100 µA at 10 V) while the leakage current remained similar, see figure 5.28. In other words, this new sample has electrical characteristics close to the UV-A sample despite containing layers with a higher Al content. This new sample will be used as a starting point for the next section about the realization of contacts by optical lithography.

5.4.1.8 Conclusion

In conclusion, we have shown that it is possible to obtain diode characteristics with AlGaN *p*-*n* junctions embedded in GaN core-shell microwires contacted with tungsten EBID contacts. However, the use of Al buries the passivation layer at the base of the wire, allowing the *p*-GaN shell to extend close to the *n*-contact. Consequently, these structures tend to have a larger leakage current than their Al-free counterpart.

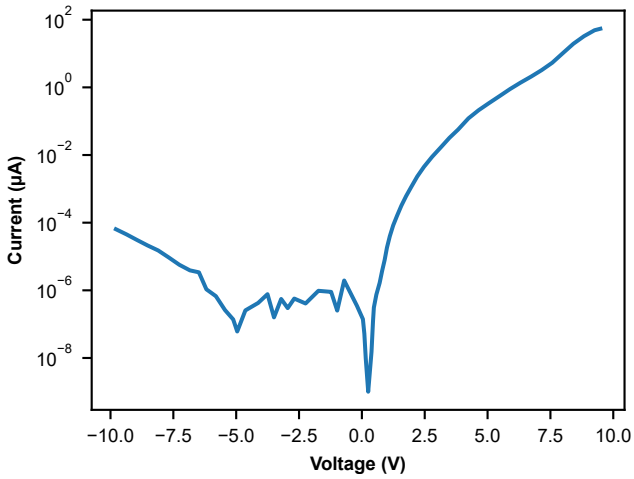

FIGURE 5.28: Single wire I-V measurement of the new sample with thinner barriers and Al gradient

Then, two similar structures designed for UV-A and UV-B emission were grown. The UV-B device has a much lower forward current (3 orders of magnitude) at 10 V, probably due to the increase in Al content, making hole injection more difficult. Both structures have a comparable leakage current level. We observed that the electrical properties of these devices are not stable under irradiation and current stress. In particular, significant leakage occurs after prolonged current stress. Based on secondary electron images and EBIC mapping, the proposed hypothesis is the presence of a parasitic tungsten deposit, activated mainly by Joule effect but also by e-beam irradiation. These leaks seem avoidable by reducing the current, typically by performing pulsed measurements.

Then, we have highlighted the presence of the *p*-*n* junction on the upper part of the wires with EBIC mapping for each device. It is to be noted that cracks are visible in EBIC on the upper part of the wires and thus near the *p* contact. Therefore, we can deduce that they play a role in the injection and luminescence without introducing noticeable leakage.

We also observed electroluminescence on both structures, with very similar spectra: a yellow band at about 2.25 eV, a violet band close to 3.35 eV, and the QWs emitting at 3.65 and 4 eV for the UV-A and B structures. By performing electroluminescence measurements on a simple GaN *p*-*n* junction, without any Al-containing layers, we could observe the presence of the yellow and violet bands that we attributed to recombination in *u*-GaN and *p*-GaN, respectively.

Finally, we obtained a much better electrical injection, comparable to the UV-A sample, by designing a new UV-B structure with an additional aluminum gradient and thinner barriers. This new structure will be used as a starting point for the next section concerning the realization of contact by optical lithography.

5.4.2 Realization and characterization of Ni/Au contacts

In order to obtain better and more reliable contacts, we decided to replace the tungsten-EBID contacts with Ni/Au contacts realized by photolithography and e-beam evaporation. To understand the choice of metals, we first need to analyze the creation of ohmic contact on GaN.

5.4.2.1 Ohmic contact on GaN

The metal stacks to produce ohmic contacts on n and p-GaN are well established in the literature.

On the n side, the stack is composed of four metals divided into two bilayers, typically Ti/Al/metal/Au. The first bilayer (Ti/Al) is responsible for forming the contact, while the second one (metal/Au) is a capping layer. Au is used to prevent oxidation of the Ti/Al bilayer and the metal is meant to keep in-diffusion of Au and out-diffusion of Al and Ti as low as possible [Van+05]. Concerning the choice of metal, the most commonly used are Ni and Ti, but Mo and Pt are also found in the literature. The role of the first Ti layer would be to extract the nitrogen from GaN by forming a TiN layer, thus, leaving nitrogen vacancies that act as donors in GaN. As a result, a heavily n-doped thin layer is formed at the interface, thus pinning the Fermi level and reducing the barrier's thickness. The resulting tunnel junction is responsible for ohmic contact behavior [Van+05; Ruv+96; Mot+03]. Concerning the Al layer, two explanations are found in the literature. The first would be to form a Ti-Al intermetallic phase with a low work function, thus reducing the barrier's height [Lut+97]. A more recent explanation is that Al would reduce the reactivity between Ti and Ga. This would explain the existence of an optimal Ti/Al ratio, as too much Ti would lead to the formation of voids below the TiN, and too much Al would prevent the formation of the TiN layer [Van+05].

On the p side, the creation of an ohmic contact is more complicated due to a lack of metal with a high work function and less efficient doping. The most commonly used stack is Ni/Au.

In our case, to simplify the technological steps, we decided to deposit the same metal stack (Ni/Au) on the n and p sides. Based on the assumption that the mechanism responsible for the ohmic behavior of the n-contact involves the formation of a heavily n-doped layer at the interface, the electrical injection is probably much easier on the n side as the wire core is metallic ([Si] $\sim 10^{20}\,\mathrm{cm}^{-3}$).

5.4.2.2 Fabrication process

To realize contacts by evaporation, lithography is an essential step. This step can be done either optically or electronically. As the resolution is not a limiting criterion, we have decided to use optical lithography for simplicity.

Here, as the wire diameter is typically between 1 and 3 µm, a planarization layer is required to ensure continuity of contact between the substrate and the wire.

Planarization The planarization process is very similar to the one described in [Tch15]. First, the wires are mechanically dispersed on a Si substrate coated with 500 nm of SiO_2. Then, about 500 nm of UV photoresist S1805 from Shipley is deposited and soft baked. These 500 nm may seem too thin compared to the diameter of the wires, but they correspond to the average thickness. In reality, there is an accumulation of resist near the wires, perceptible thanks to interference patterns. Then the resist is fully exposed in a UV-KUB3 from Kloé (7 s at 20%) and developed ∼4 s in a 1:1 mixture of microposite developer concentrate and deionized (DI) water, which removes about 70 nm (measured by interferometry). Then the resist is stabilized by baking at 200 °C for 10 min. Note that the evaporation of the solvents reduces the thickness. Finally, the sample is washed for a few minutes in acetone, then rinsed in isopropyl alcohol (IPA) and dried with N_2. Although the resist is cured, the thickness decreases by a few tens of nanometers during this cleaning to leave only the acetone insoluble part (∼300 nm).
A quick O_2 plasma etching could have been performed to ensure that the wires were uncovered. However, we wanted to avoid this step because it may deteriorate the electrical property of the *p*-GaN shell, as observed by Yan et al. [Yan+04].

Lithography & development The sample is first spin-coated with 1.8 µm of Shipley's S1818 resist with standard deposition parameters. Then, to avoid locating the position of the wires to design a mask, we decided not to use the commonly used laser lithography. Instead, we use a rapid prototyping system (Smart Print from microlight3d), consisting of a UV projector with interchangeable microscope objective lenses (see figure 5.29 (a)). The writing field and the resolution depend on the choice of the objective. In our case, we choose the objective with the highest magnification, a x25 objective. This objective is well adapted here, with a resolution of about 1-2 microns and a writing field of $544 \times 306\,\mu m^2$. Thus, as shown in figure 5.29 (b) and (c), the wire contacts and the large pad where the tips will be placed can be exposed simultaneously. Note that here the mask consists of a bitmap of 1920 by 1080 pixels, where each pixel measures ∼283 nm. Therefore the diagonals are necessarily converted into steps as seen in the zoomed-in view of fig-

ure 5.29 (b). This effect must be kept in mind when designing masks with patterns in the micrometer range. Additional details about the setup and the process can be found in appendix 5.D

Finally, after exposing several wires, the mask is developed for about 1 min in a 1:1 mixture of DI water and microposite developer concentrate, then rinsed in DI and dried with N_2. The development stage is checked under a microscope, and the time is adjusted if needed.

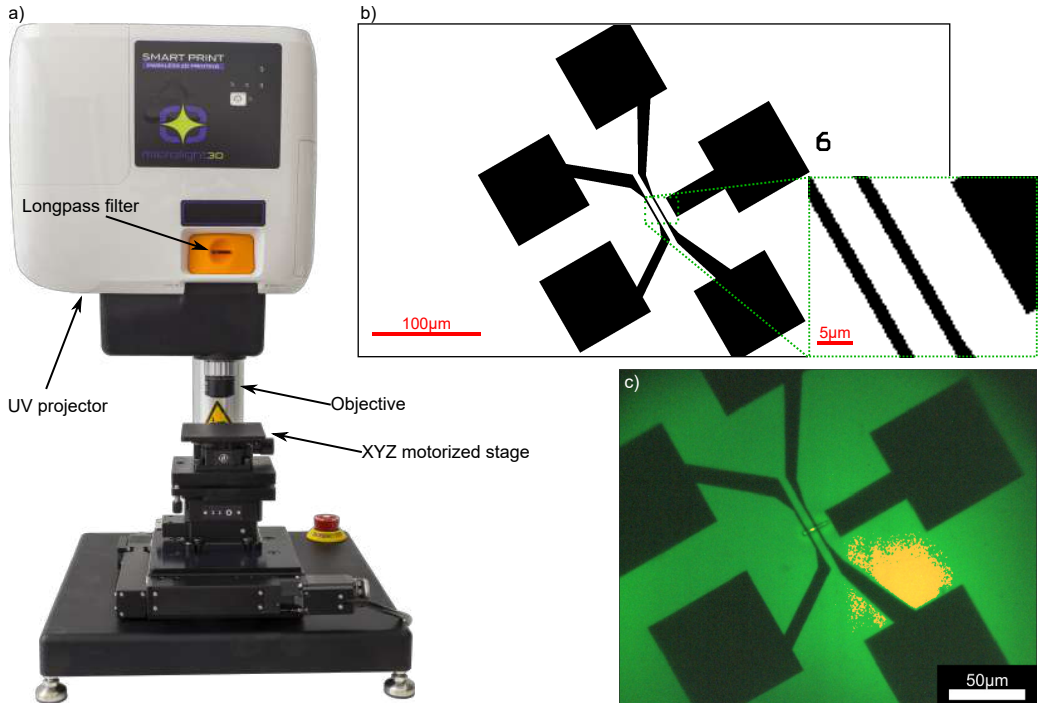

FIGURE 5.29: (a) The Smart Print setup. (b) A typical mask. A black border delimits the entire writing field. A zoomed-in view shows a staircase pattern due to the resolution limit. (c) The inverted mask aligned on the microwire with a 525 nm light source before exposition.

Metal deposition & lift-off After the lithography, 20 nm of Ni and 80 nm of Au are deposited with an e-beam evaporator MEB550S. Then, the lift-off simply consists in leaving the sample in acetone for a few hours. The quality of the lift-off is then checked under the microscope while the sample is still immersed in IPA. If necessary, the sample is again placed in fresh acetone. At the end of the process, the sample is rinsed in IPA and dried with N_2.

Figure 5.30 shows images of wires after the complete process. A problem can be spotted immediately: after the lift-off, the edges of the contacts remain attached to the wire as thin metallic filaments (indicated by arrows). This is a problem because, as seen in figure 5.30 (b), these filaments could short-circuit the n and p contacts. To solve this problem, we tried longer lift-offs as well as sonication.

Unfortunately, the former did not change anything, while the latter damaged the devices before removing these unwanted filaments. We will see later that they are, in fact, not an issue when it comes to electrical injection, as they burn under a small bias.

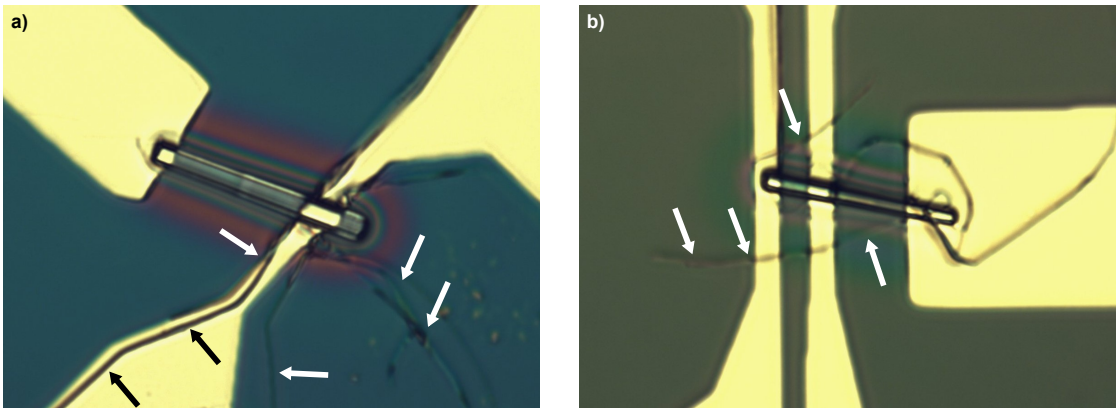

FIGURE 5.30: Image of the wires after the complete process. It can be seen that the contours of the contacts are peeling off while still attached to the wires (indicated by arrows).

5.4.2.3 Electro-optical properties of the wires

We will now focus on the electrical and optical properties of our devices. For this, the same setup as previously described is used.

Figure 5.31 (a) shows an SE image of the wire shown in figure 5.30 (b). The two *p*-contacts, named p_1 (top) and p_2 (middle of the shell), are highlighted in blue and green. Figure 5.31 (b) shows the I-V measurements acquired on this wire for the two *p*-contacts.

First, let us consider the measurements acquired between p_1 and n, *i.e.*, blue solid lines in figure 5.31 (b).

1. We can see a short circuit in the first measurement. This is due to the presence of thin filaments after the lift-off. However, by applying a small continuous bias (∼2 V) for a few seconds, it is possible to burn them off. Indeed, we can see that the filament indicated by the topmost arrow in figure 5.30 (b) is now broken in figure 5.31 (b).

2. The measurement done right after shows a small and erratic current level in both forward and reverse bias, between −3 V and 3 V. This could be due to filament leftovers.

3. On the next measurement, no current is observed between -9 and ∼5 V, confirming that the filaments are totally removed. After 5 V, the current

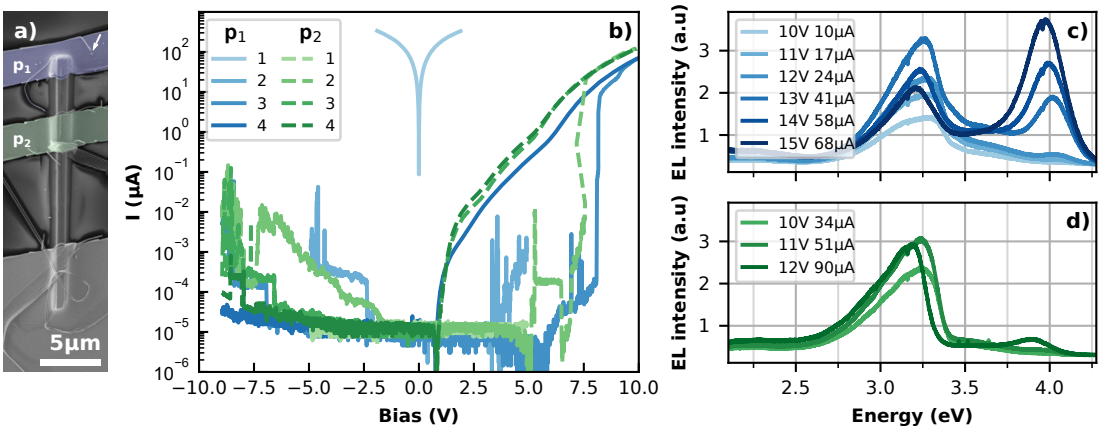

FIGURE 5.31: (a) SE image of a contacted wire. The two *p*-contacts are highlighted: p_1 in blue and p_2 in green, and an arrow indicates a burned filament. (b) I-V measurements of the corresponding wire for the two *p*-contacts with the same color code. (c) (*resp.* d) EL spectra obtained by contacting p_1 (*resp.* p_2)

slowly increases and abruptly jumps from 2×10^{-4} µA to almost 10 µA at 5 V.

4. The last measurement done on p_1 shows an excellent rectifying behavior with saturation current in the picoamp range and ∼100 µA at 10 V. Subsequent measurements are very similar.

The current jump could be explained by the presence of an insulating layer on the surface of the wire, which would eventually break in the presence of a strong electric field. This layer is most probably a residue of the resist used during the planarization or lithography process but might also be a layer of native oxide.

Also, note the presence of bumps in the final, *i.e.,* stabilized, I-V characteristics. These kinds of bumps have been observed in InGaN/GaN core-shell microwires and were well described by a model discretizing the wire into elementary cells composed of a diode and resistors [Tch+14a].

Measurements performed on the second *p*-contact, *i.e.*, p_2, show similar characteristics. Especially we can see on the second measurement that a similar current jump appears around 7.5 V. It indicates that the insulating layer is present on the *p*-shell. Subsequent measurements are similar to the last one obtained on p_1 except for a slightly higher forward current.

To verify the reproducibility of the measurements, additional measurements were performed on 20 wires. Except for 6 that showed little or no current, they all showed the same characteristics after breaking the insulating layer. Regarding the stability of the contacts, we observed that the forward current generally increased after current stress while the reverse current remained unchanged. It

indicates an improvement of the contacts, which can be explained by the formation of conduction channels due to the breakdown of the insulating layer. It could also originate from an improvement of the Ni/GaN interface quality, perhaps via thermal annealing if the current density is locally important.

We also observed that the current drops rapidly in the first few seconds before stabilizing when a DC bias is applied. For example, at 11 V, we observed the current started at ∼90 µA and then stabilized around 70 µA. A similar effect was observed with pulsed bias. Typically, the peak current at 11 V was ∼15 µA, while the DC current was 5 µA. This effect seems to be fully reversible and could be a sign that thermal effects are non-negligible in this type of structure.

We will now look at the electroluminescence spectra. Here again, we decided to reduce the average current by performing the measurements with a pulsed bias. Figure 5.31 (c) and (d) show electroluminescence spectra acquired while applying a forward bias on p_1 and p_2 respectively. Although the current is three to four times higher on p_2 at a given voltage, the QWs emission is very low, and the luminescence comes almost exclusively from VB. By comparing the spectra obtained on p_1 and p_2, we can see that the emission of QWs is red-shifted on p_2. It could be a variation of the thickness of the wells along the wire. This kind of shift has already been observed in this type of sample [Sha+16; Liu+18].

Looking now at the QWs emission when the injection is done on p_1, we see a redshift as the voltage increases. It is possible that the injection occurs mainly under the contact at low voltage. Then, with increasing voltages, the injection could extend toward the bottom of the wire.

In addition, to confirm that the shell is conducting and to eliminate the ambiguity related to the very diffuse EBID contacts, we also performed EBIC mapping. Figure 5.32 shows a SE image of the same microwire (a) with its corresponding EBIC signal mapping at 0 V (b) acquired at 7 kV. Here, the charge collection on the *p*-side was done at the top of the wire (rightmost contact, p_1). Hence, as no short circuit is present between p_1 and p_2 and the EBIC signal extends up to ∼10 µm from the contact, we can conclude that transport of the majority carriers is not limited by the *p*-shell.

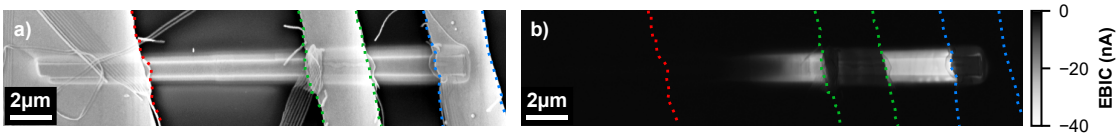

FIGURE 5.32: (a) SE image and (b) 0 V EBIC mapping acquired with an acceleration voltage of 7 kV. Note that the charge collection on the *p*-side was done at the top of the wire (rightmost contact, p_1). Dotted lines indicate the outline of each contact.

5.4.2.4 Conclusion

In conclusion, the Ni/Au contacts made by lithography and e-beam evaporation showed better stability under current stress and were insensitive to e-beam irradiation. Also, in electron-beam-induced deposition, there was a significant wire-to-wire dispersion, typically between 10^{-4} and $\sim 10^{-2}$ µA at -10 V, contrary to contacts fabricated by lithography, where the average leakage is about $\sim 10^{-4}$ µA up to -10 V. This further incriminates the electron-beam-induced deposition contacts as the main cause of instability and leakage. However, replacing W with Ni/Au contacts showed no significant improvement in the forward current, with typically $\sim 10^{2}$ µA at 10 V with both contacts. Several hypotheses can explain this. First, the *p*-contact would not be the limiting factor for the current injection. Indeed, as we have observed, the reduction of the barriers' thickness has significantly increased the current density. Thus, the injection would be mainly governed by the resistivity of AlGaN. Another possible hypothesis is that W and Ni/Au contacts are comparable. According to Greco et al., no clear correlation exists between the metal work function and the resulting contact resistance on *p*-type GaN [GIR16]. Furthermore, annealing seems to be an essential step to obtain good *p*-type contacts, which we did not do here because of the planarization layer. Note that the resist could have been replaced by an hydrogen silsesquioxane (HSQ) layer, as described in [Bug+11; Lav+14]. This planarization layer would have been compatible with thermal annealing. However, we did not use it due to difficult access to HF to wet-etch the HSQ and uncover the wires.

5.4.3 Conclusion and perspectives

We have demonstrated that it is possible to obtain a diode profile in the case of GaN/AlGaN core-shell wires. At first, the contacts made in electron-beam-induced deposition allowed us to obtain good I-V profiles but were unstable under electron beam irradiation and current stress. Despite this, we obtained electroluminescence in UV-A (3.65 eV) and then in UV-B (4 eV) with a sample with thinner wells and barriers richer in Al. However, this new sample showed degraded electrical properties, probably due to poor hole injection. By decreasing the thickness of the barriers, we observed a clear increase in the forward current. Concerning electroluminescence, a strong violet band was systematically observed. By performing EL measurements on a single *p*-*n* GaN junction, we could attribute its origin to the *p*-GaN shell. The presence of this band at low injection in LED devices suggests a low injection efficiency. Here, the cause could be the difficult hole injection, requiring a higher voltage to reach the wells. Therefore, recombinations would occur in the *p*-GaN at low bias and then in the wells at higher bias. Further inves-

tigations are required to understand and prevent its apparition. A good starting point could be implementing an electron blocking layer to reduce the injection of electrons in the *p*-GaN. Also, the doping level and Al content of *p*-AlGaN require further study. These are undoubtedly key parameters for improving hole injection.

With the aim of improving the stability and quality of the contacts, an in-situ optical lithography process was developed, and Ni/Au contacts were deposited by electron beam evaporation. The resulting contacts did not suffer from instability under e-beam irradiation, thus incriminating the electron-beam-induced deposition deposits. However, the electro-optical characteristics were quite similar to those obtained with electron-beam-induced deposition contacts. Therefore, it could be interesting to characterize the electrical properties of these contacts after thermal annealing; however, this requires modifying the planarization process to use a layer that can withstand high temperatures.

Finally, to reach UV-C, it seems necessary to develop and optimize the growth of GaN monolayers. Moreover, to alleviate absorption losses, developing core-shell tubes by in-situ GaN core etching, as presented by Durand et al., could be a promising approach.

Appendices

5.A Ideality factor of an ideal diode

We recall the model of the ideal diode:

$$I = I_S \left[\exp\left(\frac{qV}{\eta k_B T} \right) - 1 \right] \tag{5.4}$$

From this expression, we can get the ideality factor as follows:

$$\begin{aligned} \ln I &= \ln I_S + \ln\left(e^{\frac{qV}{\eta k_B T}} - 1 \right) \\ \implies \frac{\partial \ln I}{\partial V} &= \frac{e^{\frac{qV}{\eta k_B T}}}{e^{\frac{qV}{\eta k_B T}} - 1} \frac{q}{\eta k_B T} \\ \iff \boxed{\frac{\partial \ln I}{\partial V} = \frac{1}{1 - e^{\frac{-qV}{\eta k_B T}}} \frac{q}{\eta k_B T}} \end{aligned} \tag{5.7}$$

If $\frac{qV}{\eta k_B T} \gg 1$, we can then approximate:

$$\boxed{\eta \approx \frac{q}{k_B T} \left(\frac{\partial \ln I}{\partial V} \right)^{-1}} \tag{5.8}$$

Otherwise, it is possible to solve equation (5.7) numerically.

Figure 5.A.1 (a) shows a typical I-V curve for a wire of structure 2, *i.e.,* with an AlGaN embedded. In figure 5.A.1 (b), we can see that the difference in ideality factor obtained numerically (with (5.7)) and by the approximated expression ((5.8)) are identical above 2 V and very close above 1 V.

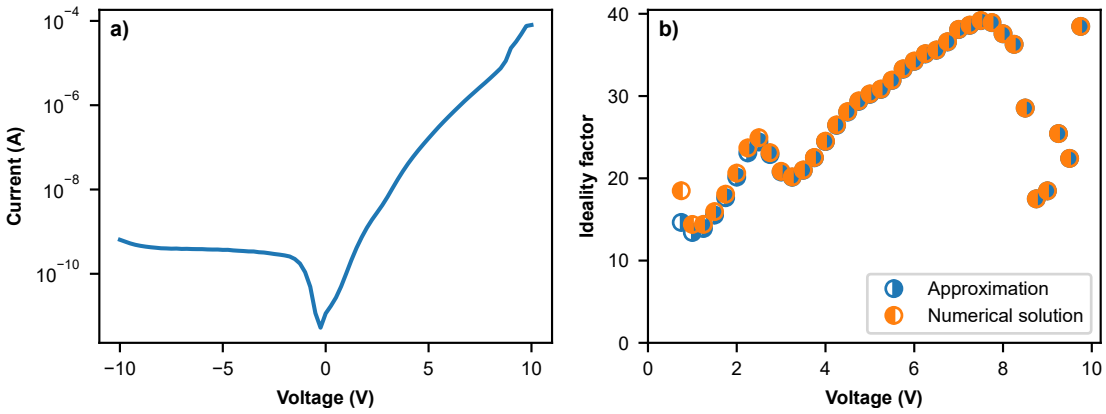

FIGURE 5.A.1: (a) Typical I-V curve for a sample containing an AlGaN *p-n* junction embedded in a GaN *p-n* junction. (b) Ideality factor extracted thanks to the approximation or numerically

5.B Additional details on EBIC

Setup and mapping

The EBIC setup consists of a low noise current amplifier SR570 from Standford Research connected to an ADC NI-5734 mounted in a NI PXIe-1073 from National Instrument. Also, the beam driving voltage and the output of an Everhart-Thornley detector are connected to the ADC. The driving voltage is used to get the pixels' coordinates and form an image, and the ETD allows the acquisition of a SE image simultaneously. Here, fast inline dB attenuators were used to limit the voltage and protect the ADC.

From the acquired 16bit greyscale image, one can retrieve the current using the following expression:

$$I = g \times \frac{\text{ADC input range}}{\text{ADC output range}} \times A_f \times S - \Delta$$

Where :

- g is the greyscale value between 0 and $2^{16} - 1$
- A_f the attenuation factor
- S the sensitivity in A/V of the low noise current amplifier
- Δ the offset in A of the low noise current amplifier

The ADC input range is here in volt.

Current generation

Now, to understand the main mechanism responsible for the current generation, we need to take a look at a simplified band diagram figure 5.B.1. Two important regions can be identified, first, the space charge region (SCR) of the p-n junction (region II in figure 5.B.1). Because of the band bending, electrons (holes) are accelerated toward the n-side (p-side). According to the commonly used current convention, this corresponds to a negative current. This is the current that we observed on the core-shell region of the wires in figure 5.21 and figure 5.25. As demonstrated by Lavenus et al., it is also possible to observe a positive current when carriers are generated or diffuse close to a Schottky p-contact. Indeed, because of band bending induced by the barrier (region III), electrons (holes) are

this time attracted (repulsed) to the p-contact. Note that in the case of a Schottky n-contact the sign would be identical as electrons (holes) would be repulsed (attracted) from the contact (region I).

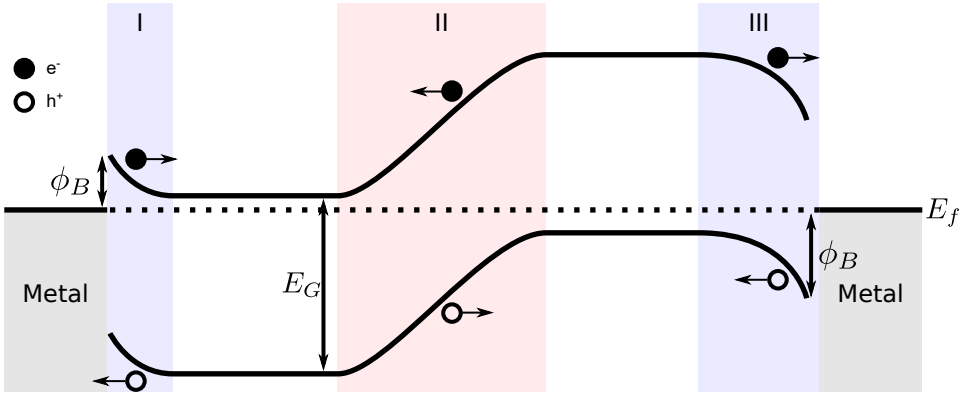

FIGURE 5.B.1: Band diagram of a p-n junction (II) with Schottky contacts (I & III). Arrows indicate the directions in which the carriers are accelerated. According to the current convention, the resulting current is positive for the Schottky contacts and negative for the p-n junction.

In addition, we can also observe second-order effects. However, because of the contrast, these effects were not visible on the previously shown EBIC mapping. Indeed, as shown in figure 5.B.2, a low negative current is visible on the metallic contact on the n-side (in red) and a low positive current on the sidewalls at the base of the wire (in white and blue).

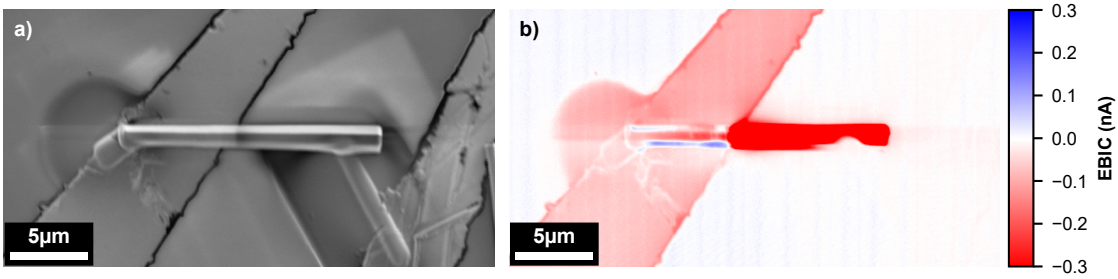

FIGURE 5.B.2: (a) SE image and (b) 0 V EBIC image acquired with an acceleration voltage of 2 kV.

To understand their origin, let us first detail the different mechanisms that can induce a current under electron beam irradiation:

EBIC for electron-beam induced current. It is based on the presence of a SCR in a semiconductor (either from a Schottky contact or p-n junction). Due to the large energy difference between the electron beam and the energy required to create an e-h pair, the current generated is several orders of magnitude greater than that of the beam. The sign of this current depends on the band

bending, typically negative for a *p-n* junction and positive for a Schottky contact. Figure 5.B.3 (a)

EBAC for electron-beam absorbed current. As the electrons are absorbed by the metal, this generates an electron current from the contact to the ground. This current is approximately equal to that of the electron beam. Figure 5.B.3 (b)

SEEBIC for secondary electron EBIC. This current arises from holes generated by the emission of secondary electrons. This hole current will be measured as a positive current, and its intensity depends on the specimen's SE yield (both material and geometry have to be considered). Figure 5.B.3 (c)

The interested reader may find additional details and other mechanisms, such as recapture and secondary electron EBAC (SEEBAC) that will not be discussed here in [Dyc+22].

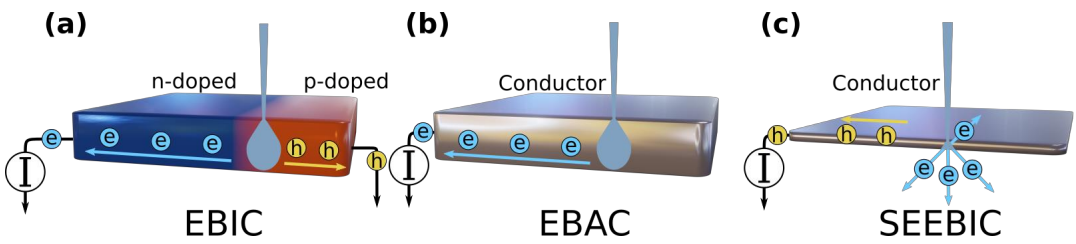

FIGURE 5.B.3: Schematics of the most common EBIC concepts. (a) An incident e-beam excites holes and carriers in the depletion region of a *p-n* junction, resulting in a current through the transimpedance amplifier. (b) An incident e-beam is absorbed by a conductive specimen resulting in a current through the amplifier. (c) An incident e-beam generates SE emission from a thin specimen resulting in a hole current through the amplifier. [Dyc+22]

Thus, in figure 5.B.3 (b), we can identify the large EBIC signal coming from the core-shell region of the wire. In addition, an EBAC signal is observed on the contact connected to the current amplifier. From this signal, we can deduce that the tungsten deposit on the *n* side is very diffuse and broad, which supports the hypothesis that it is responsible for the short circuits. Lastly, the positive current observed on the sidewalls is probably a SEEBIC signal, enhanced by the geometry of the sample.

5.C SiO_2 CL emission

Figure 5.C.1 shows a luminescence spectrum of the substrate (SiO_2/Si). We can see three emission lines: one centered at 286 nm, one at 460 nm, and finally, one at 650 nm. It is important to note that these emissions can be present initially

on some substrates but can also be activated under irradiation. Figure 5.C.2 (a) shows a SE image of a substrate and the corresponding CL image centered at 285 nm (b). We can spot an area that we have irradiated thanks to a change in contrast related to a contamination deposit. On the corresponding CL image, this area shows a stronger luminescence. These three same emissions have already been reported by Goldberg et al. The ultraviolet and blue emissions are present in the thermal SiO_2 and are attributed to an intrinsic defect (two-fold coordinated silicon center). Note that we also observed the UV band in PL.

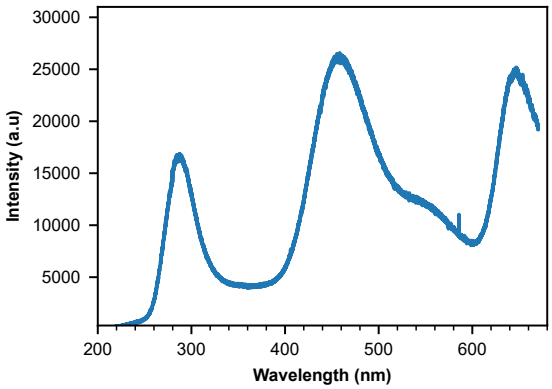

FIGURE 5.C.1: Room temperature CL spectrum of the SiO_2 substrate acquired with a 10 kV acceleration voltage.

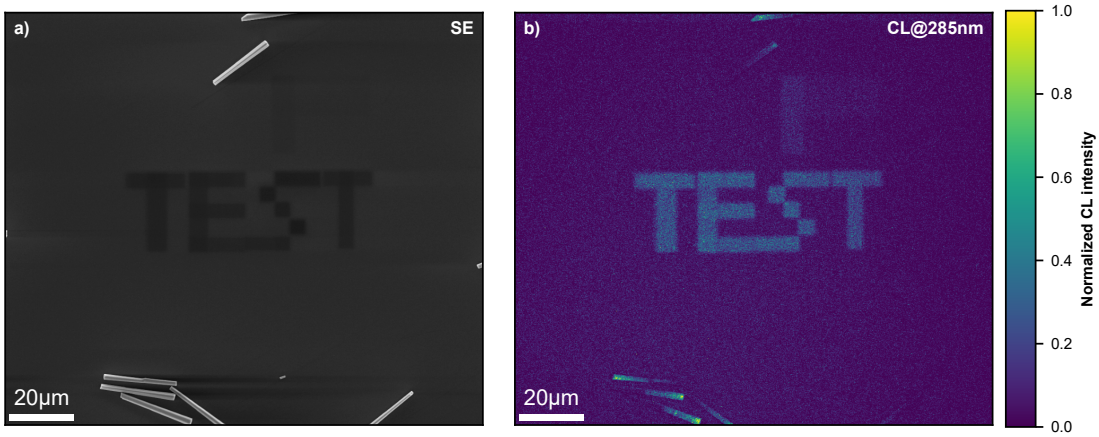

FIGURE 5.C.2: (a) SE image of the SiO_2 substrate on which microwires have been dispersed. (b) The corresponding CL image centered at $\lambda = 285$ nm.

5.D Practical details on the lithography process

At the time of writing, the conversion software of the smartprint transformed the GDS files into "stitch" files containing one or more bitmaps with their relative positions. This format allows to divide a large mask into sub-masks if the writing field is not big enough to contain the entire mask.

This process was not very convenient in our case. First, the conversion was relatively long, several tens of seconds. This is a problem since the software does not allow drawing directly on the feedback camera or measuring distances. Thus realizing a mask is a trial and error process, and it can be tedious to align the p and n contacts on the wire. Note that even if this can be improved, it is not a software problem, but simply that our usage is probably a bit off its designated purpose. More importantly, after alignment, the software that drives the stage moves to the coordinates indicated in the "stitch file. It is very unpractical in our case where only one exposure is necessary because the stage moves to return almost to the same position, introducing a 1 to 2 µm shift. Maybe these problems were/will be corrected in a future release.[10]

To circumvent this, a Klayout macro has been developed to do the conversion using the same functions as the provided software (which uses Klayout internally). The two advantages here in the case of a one-shot exposure: the stage does not move anymore between the alignment and the exposure. The conversion is instantaneous, which allows to draw and adjust the mask in real-time. Of course, masks produced by the macro and the software were compared to ensure they were strictly identical. Note that without the macro, it is still possible to avoid the stage movement by extracting the bitmap in the "stitch" file with a software opening zip files.

Also, although the mask alignment was done in green light (525 nm) and with a high pass filter, aligned but unexposed patterns (during the mask creation process) were visible after development. This problem was observed only with the x25 objective. The hypothesis is that the resist is a bit sensitive at 525 nm. The combination of a long exposure time during the creation and alignment of the mask and a dose that is probably high due to the objective used ends up transforming the resist. It was enough to reduce the brightness of the green light from 100% to 50% in the settings and turn the light off whenever possible to make this problem disappear.

References

[Ama+20] Hiroshi Amano et al. "The 2020 UV emitter roadmap". *Journal of Physics D: Applied Physics* 53.50 (Dec. 2020), 503001. DOI: 10.1088/1361-6463/aba64c.

[10] To be precise, the version of the smartprint present in our cleanroom was not the latest. Improvements have probably been made since then. See https://www.microlight3d.com/our-products/smartprint-uv for an up to date datasheet

[An+19] Byeong Seon An et al. "Evaluation of ion/electron beam induced deposition for electrical connection using a modern focused ion beam system". *Applied Microscopy* 49.1 (2019). DOI: 10.1186/s42649-019-0008-2.

[Ban+11] Kazuhito Ban et al. "Internal quantum efficiency of whole-composition-range AlGaN multiquantum wells". *Applied Physics Express* 4.5 (May 2011). DOI: 10.1143/APEX.4.052101.

[Big+99] P. Bigenwald et al. "Confined excitons in GaN-AlGaN quantum wells". *Physica Status Solidi (B) Basic Research* 216.1 (1999), 371–374. DOI: 10.1002/(SICI)1521-3951(199911)216:1<371::AID-PSSB371>3.0.CO;2-S.

[Bin+13] M. Binder et al. "Investigations on correlation between I-V characteristic and internal quantum efficiency of blue (AlGaIn)N light-emitting diodes". *Applied Physics Letters* 103.22 (2013), 221110. DOI: 10.1063/1.4833895.

[Bir+07] Stefan Birner et al. "Nextnano: General purpose 3-D simulations". *IEEE Transactions on Electron Devices* 54.9 (Sept. 2007), 2137–2142. DOI: 10.1109/TED.2007.902871.

[Bru+19] Matt D. Brubaker et al. "UV LEDs based on p-i-n core-shell AlGaN/GaN nanowire heterostructures grown by N-polar selective area epitaxy". *Nanotechnology* 30.23 (2019), 234001. DOI: 10.1088/1361-6528/ab07ed.

[Bry+15] Zachary Bryan et al. "Strain dependence on polarization properties of AlGaN and AlGaN-based ultraviolet lasers grown on AlN substrates". *Applied Physics Letters* 106.23 (June 2015), 232101. DOI: 10.1063/1.4922385.

[Bug+11] A. De Luna Bugallo et al. "Single-wire photodetectors based on InGaN/GaN radial quantum wells in GaN wires grown by catalyst-free metal-organic vapor phase epitaxy". *Applied Physics Letters* 98.23 (June 2011), 233107. DOI: 10.1063/1.3596446.

[Cou+18a] Pierre Marie Coulon et al. "Deep UV Emission from Highly Ordered AlGaN/AlN Core-Shell Nanorods". *ACS Applied Materials and Interfaces* 10.39 (Oct. 2018), 33441–33449. DOI: 10.1021/acsami.8b10605.

[Cou+18b] Pierre Marie Coulon et al. "Hybrid Top-Down/Bottom-Up Fabrication of Regular Arrays of AlN Nanorods for Deep-UV Core–Shell LEDs". *Physica Status Solidi (B) Basic Research* 255.5 (2018), 1700445. DOI: 10.1002/pssb.201700445.

[Din+19] Duc V. Dinh et al. "Aluminium incorporation in polar, semi- and non-polar AlGaN layers: a comparative study of x-ray diffraction and optical properties". *Scientific Reports* 9.1 (Dec. 2019), 15802. DOI: 10.1038/s41598-019-52067-y.

[Dur+14] Christophe Durand et al. "M-Plane GaN/InAlN Multiple Quantum Wells in Core-Shell Wire Structure for UV Emission". *ACS Photonics* 1.1 (Jan. 2014), 38–46. DOI: 10.1021/ph400031x.

[Dur+17] Christophe Durand et al. "Thin-Wall GaN/InAlN Multiple Quantum Well Tubes". *Nano Letters* 17.6 (2017), 3347–3355. DOI: 10.1021/acs.nanolett.6b04852.

[Dyc+22] Ondrej Dyck et al. "Contrast mechanisms in secondary electron e-beam induced current (SEEBIC) imaging" (Mar. 2022), 1–49.

[Ein+00] S. Einfeldt et al. "Strain relaxation in AlGaN under tensile plane stress". *Journal of Applied Physics* 88.12 (2000), 7029–7036. DOI: 10.1063/1.1326852.

[Eym+12] J Eymery et al. *Process for catalyst-free selective growth on a semiconductor structure*. 2012.

[Fan+19] V. Fan Arcara et al. "Ge doped GaN and Al0.5Ga0.5N-based tunnel junctions on top of visible and UV light emitting diodes". *Journal of Applied Physics* 126.22 (2019). DOI: 10.1063/1.5121379.

[Fin+20] Sylvain Finot et al. "Carrier dynamics near a crack in GaN microwires with AlGaN multiple quantum wells". *Applied Physics Letters* 117.22 (Nov. 2020), 221105. DOI: 10.1063/5.0023545.

[Fis+08] A M Fischer et al. "Time-resolved cathodoluminescence of Mg-doped GaN". *Applied Physics Letters* 93.15 (2008), 151901. DOI: 10.1063/1.3000383.

[Fou+19] M. Fouchier et al. "Polarized cathodoluminescence for strain measurement". *Review of Scientific Instruments* 90.4 (Apr. 2019), 043701. DOI: 10.1063/1.5078506.

[Fra+20] Christian Frankerl et al. "Strongly localized carriers in Al-rich AlGaN/AlN single quantum wells grown on sapphire substrates". *Journal of Applied Physics* 127.9 (Mar. 2020), 095701. DOI: 10.1063/1.5144152.

[Fuj+22] Ryoto Fujiki et al. "Hydrogen in-situ etching of GaN surface to reduce non-radiative recombination centers in 510-nm GaInN/GaN quantum-wells". *Journal of Crystal Growth* 593 (2022), 126751. DOI: 10.1016/j.jcrysgro.2022.126751.

[GIR16] Giuseppe Greco, Ferdinando Iucolano, and Fabrizio Roccaforte. "Ohmic contacts to Gallium Nitride materials". *Applied Surface Science* 383 (2016), 324–345. DOI: 10.1016/j.apsusc.2016.04.016.

[Gre+20] Vincent Grenier et al. "UV Emission from GaN Wires with m-Plane Core-Shell GaN/AlGaN Multiple Quantum Wells". *ACS Applied Materials and Interfaces* 12.39 (Sept. 2020), 44007–44016. DOI: 10.1021/acsami.0c08765.

[Gre+21] Vincent Grenier et al. "Toward Crack-Free Core-Shell GaN/AlGaN Quantum Wells". *Crystal Growth and Design* 21.11 (2021), 6504–6511. DOI: 10.1021/acs.cgd.1c00943.

[Gre+22] Vincent Grenier et al. "UV-A to UV-B Electroluminescence of Core-Shell GaN/AlGaN Wire Heterostructures". *Applied Physics Letters* (2022). Submitted.

[GTF96] M. Goldberg, A. Trukhin, and H. J. Fitting. "Dose effects of cathodoluminescence in SiO2 layers on Si". *Materials Science and Engineering B* 42.1-3 (1996), 293–296. DOI: 10.1016/S0921-5107(96)01724-2.

[Hei+20] Christiane Silke Heilingloh et al. "Susceptibility of SARS-CoV-2 to UV irradiation". *American Journal of Infection Control* 48.10 (2020), 1273–1275. DOI: 10.1016/j.ajic.2020.07.031.

[Hes+10] K. Hestroffer et al. "The structural properties of GaN/AlN core-shell nanocolumn heterostructures". *Nanotechnology* 21.41 (Oct. 2010), 415702. DOI: 10.1088/0957-4484/21/41/415702.

[Hwa+13] Injun Hwang et al. "P-GaN Gate HEMTs with tungsten gate metal for high threshold voltage and low gate current". *IEEE Electron Device Letters* 34.2 (Feb. 2013), 202–204. DOI: 10.1109/LED.2012.2230312.

[Jac+12] G. Jacopin et al. "Photoluminescence polarization in strained GaN/AlGaN core/shell nanowires". *Nanotechnology* 23.32 (Aug. 2012), 325701. DOI: 10.1088/0957-4484/23/32/325701.

[Kag+19] Vladimir M. Kaganer et al. "Determination of the Carrier Diffusion Length in Ga N from Cathodoluminescence Maps Around Threading Dislocations: Fallacies and Opportunities". *Physical Review Applied* 12.5 (2019), 1. DOI: 10.1103/PhysRevApplied.12.054038.

[Kap+18] Akanksha Kapoor et al. "Green Electroluminescence from Radial m-Plane InGaN Quantum Wells Grown on GaN Wire Sidewalls by Metal-Organic Vapor Phase Epitaxy". *ACS Photonics* 5.11 (2018), 4330–4337. DOI: 10.1021/acsphotonics.8b00520.

[Kap+20] Akanksha Kapoor et al. "Role of Underlayer for Efficient Core-Shell InGaN QWs Grown on m-plane GaN Wire Sidewalls". *ACS Applied Materials and Interfaces* 12.16 (Apr. 2020), 19092–19101. DOI: 10.1021/acsami.9b19314.

[Kaw+97] Takahiro Kawashima et al. "Optical properties of hexagonal GaN". *Journal of Applied Physics* 82.7 (Oct. 1997), 3528–3535. DOI: 10.1063/1.365671.

[KI15] Katsumi Kishino and Shunsuke Ishizawa. "Selective-area growth of GaN nanocolumns on Si(111) substrates for application to nanocolumn emitters with systematic analysis of dislocation filtering effect of nanocolumns". *Nanotechnology* 26.22 (June 2015). DOI: 10.1088/0957-4484/26/22/225602.

[Kit+21] Hiroki Kitagawa et al. "Effectiveness of 222-nm ultraviolet light on disinfecting SARS-CoV-2 surface contamination". *American Journal of Infection Control* 49.3 (2021), 299–301. DOI: 10.1016/j.ajic.2020.08.022.

[Kne+19] Michael Kneissl et al. "The emergence and prospects of deep-ultraviolet light-emitting diode technologies". *Nature Photonics* 13.4 (Apr. 2019), 233–244. DOI: 10.1038/s41566-019-0359-9.

[Koe+10] R. Koester et al. "Self-assembled growth of catalyst-free GaN wires by metal-organic vapour phase epitaxy". *Nanotechnology* 21.1 (Jan. 2010), 015602. DOI: 10.1088/0957-4484/21/1/015602.

[Koe+11] Robert Koester et al. "M-plane core-shell InGaN/GaN multiple-quantum-wells on GaN wires for electroluminescent devices". *Nano Letters* 11.11 (2011), 4839–4845. DOI: 10.1021/nl202686n.

[KR16] Michael Kneissl and Jens Rass, eds. *III-Nitride Ultraviolet Emitters*. Vol. 227. Springer Series in Materials Science. Springer International Publishing, 2016. DOI: 10.1007/978-3-319-24100-5.

[Kuo+16] Yen Kuang Kuo et al. "Numerical investigation on the carrier transport characteristics of AlGaN deep-UV light-emitting diodes". *IEEE Journal of Quantum Electronics* 52.4 (2016), 1343–1348. DOI: 10.1109/JQE.2016.2535252.

[Lan+10] O. Landré et al. "Elastic strain relaxation in GaN/AlN nanowire superlattice". *Physical Review B* 81.15 (Apr. 2010), 153306. DOI: 10.1103/PhysRevB.81.153306.

[Lav+14] P. Lavenus et al. "Experimental and theoretical analysis of transport properties of core-shell wire light emitting diodes probed by electron beam induced current microscopy". *Nanotechnology* 25.25 (2014). DOI: 10.1088/0957-4484/25/25/255201.

[Liu+18] W. Liu et al. "Spatially dependent carrier dynamics in single InGaN/GaN core-shell microrod by time-resolved cathodoluminescence". *Applied Physics Letters* 112.5 (Jan. 2018), 052106. DOI: 10.1063/1.5009728.

[Lut+97] B. P. Luther et al. "Investigation of the mechanism for Ohmic contact formation in Al and Ti/Al contacts to n-type GaN". *Applied Physics Letters* 70.1 (1997), 57–59. DOI: 10.1063/1.119305.

[Mot+03] Abhishek Motayed et al. "Electrical, thermal, and microstructural characteristics of Ti/Al/Ti/Au multilayer Ohmic contacts to n-type GaN". *Journal of Applied Physics* 93.2 (2003), 1087–1094. DOI: 10.1063/1.1528294.

[Nak+09] M. L. Nakarmi et al. "Photoluminescence studies of impurity transitions in Mg-doped AlGaN alloys". *Applied Physics Letters* 94.9 (Mar. 2009), 091903. DOI: 10.1063/1.3094754.

[Nam+05] K. B. Nam et al. "Deep impurity transitions involving cation vacancies and complexes in AlGaN alloys". *Applied Physics Letters* 86.22 (May 2005), 222108. DOI: 10.1063/1.1943489.

[Oli+17b] François Olivier et al. "Investigation and improvement of 10μm pixel-pitch GaN-based micro-LED arrays with very high brightness". *Digest of Technical Papers - SID International Symposium* 48.1 (May 2017), 353–356. DOI: 10.1002/sdtp.11615.

[RA20] Milad Raeiszadeh and Babak Adeli. *A Critical Review on Ultraviolet Disinfection Systems against COVID-19 Outbreak: Applicability, Validation, and Safety Considerations*. Nov. 2020. DOI: 10.1021/acsphotonics.0c01245.

[Rei+15] Christoph Reich et al. "Strongly transverse-electric-polarized emission from deep ultraviolet AlGaN quantum well light emitting diodes". *Applied Physics Letters* 107.14 (2015), 142101. DOI: 10.1063/1.4932651.

[Res+14] M. A. Reshchikov et al. "Green luminescence in Mg-doped GaN". *Physical Review B - Condensed Matter and Materials Physics* 90.3 (2014), 1–14. DOI: 10.1103/PhysRevB.90.035207.

[Res14] M A Reshchikov. "Time-resolved photoluminescence from defects in n -type GaN". *Journal of Applied Physics* 115.10 (2014), 103503. DOI: 10.1063/1.4867043.

[Rig+11] L. Rigutti et al. "Correlation of optical and structural properties of GaN/AlN core-shell nanowires". *Physical Review B - Condensed Matter and Materials Physics* 83.15 (Apr. 2011), 155320. DOI: 10.1103/PhysRevB.83.155320.

[RM05] Michael A. Reshchikov and Hadis Morko. "Luminescence properties of defects in GaN". *Journal of Applied Physics* 97.6 (Mar. 2005), 061301. DOI: 10.1063/1.1868059.

[Ruv+96] S. Ruvimov et al. "Microstructure of Ti/Al and Ti/Al/Ni/Au Ohmic contacts for n-GaN". *Applied Physics Letters* 69.11 (1996), 1556–1558. DOI: 10.1063/1.117060.

[RYW99] M. A. Reshchikov, G.-C. Yi, and B. W. Wessels. "Behavior of 2.8- and 3.2-eV photoluminescence bands in Mg-doped GaN at different temperatures and excitation densities". *Physical Review B* 59.20 (May 1999), 13176–13183. DOI: 10.1103/PhysRevB.59.13176.

[Sha+03] Jay M. Shah et al. "Experimental analysis and theoretical model for anomalously high ideality factors (n≫2.0) in AlGaN/GaN p-n junction diodes". *Journal of Applied Physics* 94.4 (2003), 2627–2630. DOI: 10.1063/1.1593218.

[Sha+12] Max Shatalov et al. "AlGaN deep-ultraviolet light-emitting diodes with external quantum efficiency above 10%". *Applied Physics Express* 5.8 (2012), 82101. DOI: 10.1143/APEX.5.082101.

[Sha+16] M. Shahmohammadi et al. "Excitonic Diffusion in InGaN/GaN Core-Shell Nanowires". *Nano Letters* 16.1 (Jan. 2016), 243–249. DOI: 10.1021/acs.nanolett.5b03611.

[Tch+14a] M. Tchernycheva et al. "InGaN/GaN core-shell single nanowire light emitting diodes with graphene-based P-contact". *Nano Letters* 14.5 (2014), 2456–2465. DOI: 10.1021/nl5001295.

[Tch+14b] M. Tchernycheva et al. "Integrated photonic platform based on InGaN/GaN nanowire emitters and detectors". *Nano Letters* 14.6 (2014), 3515–3520. DOI: 10.1021/nl501124s.

[Tch+14c] P. Tchoulfian et al. "Direct imaging of p-n junction in core-shell GaN wires". *Nano Letters* 14.6 (2014), 3491–3498. DOI: 10.1021/nl5010493.

[Tch15] Pierre Tchoulfian. "Propriétés électriques, optiques et électro-optiques de microfils GaN pour la réalisation de LEDs". PhD thesis. 2015.

[Tra+17] Nhung Hong Tran et al. "On the mechanism of highly efficient p-type conduction of Mg-doped ultra-wide-bandgap AlN nanostructures". *Applied Physics Letters* 110.3 (Jan. 2017), 32102. DOI: 10.1063/1.4973999.

[Van+05] B. Van Daele et al. "The role of Al on Ohmic contact formation on n-type GaN and AlGaN/GaN". *Applied Physics Letters* 87.6 (Aug. 2005), 061905. DOI: 10.1063/1.2008361.

[VM03] I. Vurgaftman and J. R. Meyer. "Band parameters for nitrogen-containing semiconductors". *Journal of Applied Physics* 94.6 (Sept. 2003), 3675–3696. DOI: 10.1063/1.1600519.

[Wil+14] Patrick Wilhite et al. "Electron-beam and ion-beam-induced deposited tungsten contacts for carbon nanofiber interconnects". *Nanotechnology* 25.37 (Aug. 2014), 375702. DOI: 10.1088/0957-4484/25/37/375702.

[Wol+11] A. Wolos et al. "Properties of metal-insulator transition and electron spin relaxation in GaN:Si". *Physical Review B - Condensed Matter and Materials Physics* 83.16 (2011), 165206. DOI: 10.1103/PhysRevB.83.165206.

[Yan+04] J Yan et al. "Effects of oxygen plasma treatments on the formation of ohmic contacts to GaN". *Applied Surface Science*. Vol. 234. 1-4. 2004, pp. 328–332. DOI: 10.1016/j.apsusc.2004.05.066.

[Yan+11] Jianchang Yan et al. "Improved performance of UV-LED by p-AlGaN with graded composition". *Physica Status Solidi (C) Current Topics in Solid State Physics* 8.2 (Feb. 2011), 461–463. DOI: 10.1002/pssc.201000458.

[Yan+14] Qimin Yan et al. "Origins of optical absorption and emission lines in AlN". *Applied Physics Letters* 105.11 (Sept. 2014), 111104. DOI: 10.1063/1.4895786.

[Zha+14] S. Zhao et al. "Aluminum nitride nanowire light emitting diodes: Breaking the fundamental bottleneck of deep ultraviolet light sources". *Scientific Reports* 5.1 (July 2014), 8332. DOI: 10.1038/srep08332.

Conclusion

In this thesis, we have studied different LED structures based on time-resolved and time-correlated cathodoluminescence. In particular, in order to have a sufficient spatial resolution, we have developed a setup based on the Hanbury Brown & Twiss interferometer. This latter allows to measure the unique photon generation statistic in CL: the photon bunching and thus to measure the lifetime. Moreover, this setup is relatively inexpensive, works in a standard CL setup, and has an excellent spatial resolution at the expense of a lower signal-to-noise ratio than time-resolved techniques.

As a first study, we investigated the use of indium-containing ULs to reduce the defect density in InGaN QWs grown on *c*-plane sapphire. We observed a reduction in non-radiative recombinations by performing lifetime measurements as a function of temperature, reflecting an increase in efficiency when an InGaN UL is grown prior to the QW. By performing a similar study on samples grown on silicon, we were able to highlight that the impact of these defects on efficiency is relatively important. Indeed, we have shown that point defects continue to play a significant role and appear to be the limiting factor, even if their density is estimated to be 1–2 orders of magnitude lower than that of threading dislocations. We then showed that an InGaN UL is not needed to improve the efficiency of *m*-plane InGaN QWs grown on the sidewalls of GaN microwires. This work has, however, pointed out that a GaN spacer is needed to bury a SiGaN layer presumably formed because of the strong silane injection to promote wire growth. Without this spacer, the QWs are of poor crystalline quality and defects created at the QW/SiGaN interface propagate in the upper layers, thereby suppressing luminescence. Concerning the role of the UL, we have also performed a study on planar *m*-plane QWs to discriminate the particular growth conditions of the wires. This study showed a similar and relatively high efficiency with and without UL. We have therefore concluded that ULs are not necessary for *m*-plane QWs.

Perspectives: In the long term, it would be, of course, interesting to elucidate the nature and formation mechanism of these point defects. In the short term, a study to confirm the potential role of thermal stability of GaN could be considered. For this purpose, it would be possible to study the role of the UL by replacing the high-temperature GaN buffer with an AlGaN buffer with a low Al content (∼5 %), or by studying the impact of the UL for different orientations, in particular N-polar or Ga-polar.

We then focused on surface recombinations at the sidewalls of etched µLEDs. In particular, we have shown the benefit of the Hanbury Brown & Twiss interfer-

ometer to measure lifetimes at the nanoscale. The main advantage is the possibility of comparing different etching and passivation methods without being sensitive to changes in injection or extraction efficiency. By fitting our data with a 1D diffusion model taking into account surface recombination, we were able to extract the surface recombination velocity and the diffusion coefficient in these µLEDs. Moreover, we showed a reduction in the surface recombination velocity by applying a passivation process consisting in a KOH etching and an Al_2O_3 deposition. Finally, we briefly investigated AlInGaP-based red LEDs, demonstrating the method's applicability with a setup designed for visible light.
Perspectives: This technique can be used to study the impact of other etching or passivation processes on the efficiency. We can mention here in particular two not very common techniques: neutral beam etching and atomic layer etching. Also, as mentioned, it could be worthwhile to study the effect of a shorter radiative lifetime. Indeed, first, it will reduce the diffusion length. Thus the surface will affect a smaller area. Second, assuming that the non-radiative lifetime associated with surface recombinations does not depend on the radiative lifetime, a shorter radiative lifetime would improve the IQE by making radiative recombinations more favorable.

Finally, we were interested in the problem of UV LEDs and the possibility of using core-shell microwires. We first showed that the strain generated by the Al-rich AlGaN layers could form cracks, similar to the observations reported on planar *c*-plane samples. By studying these cracks, we could observe a twofold effect. First, the CL energy is blue-shifted near a crack due to strain relaxation. Then the intensity profile is modified with an increase near the crack and the extinction of the luminescence at the crack location. This profile was attributed to a local increase in LEE. We also observed a significant reduction in lifetime near the crack, attributed to non-radiative recombinations, reflecting a decrease in IQE and demonstrating once again the importance of lifetime measurements.
Perspectives: It could be interesting to perform polarization-dependent CL or µPL measurements. This could help to better understand the strain state in this type of sample and also give clues to improve the LEE.

We then realized and characterized single microwire UV-A and UV-B LEDs. In this study, we first highlighted the appearance of a leakage current due to the non-selectivity of AlGaN, allowing the *p*-shell to extend close to the *n*-contact. We also noticed that the tungsten contacts initially made by electron-beam-induced deposition were a source of instability in the electrical characteristics. Nevertheless, we observed electroluminescence at 3.65 and 4 eV for the UV-A and UV-B samples, respectively. In addition to the MQWs emission, both samples showed a defect band due to recombinations in the Mg-doped GaN, underlining poor injection

efficiency. Concerning the UV-B samples, a drastic reduction of the current density was initially observed, which could be mitigated by reducing the barrier width, as well as the presence of buried cracks, which did not induce any significant leakage current. We then replaced the electron-beam-induced deposition contacts with Ni/Au contacts realized by lithography and e-beam evaporation. These contacts had similar electrical characteristics except for improved stability.

Perspectives: Further studies are needed to optimize these devices. First, it is essential to characterize and control the n and p-type doping of AlGaN to decrease resistivity. Then, to improve the injection efficiency, it is necessary to understand and suppress the recombination in the p-GaN. A first approach could be to introduce an EBL. In the future, it would be interesting to develop structures with single GaN monolayer QWs to target UV-C emission. Also, as a way to reduce the parasitic absorption of the GaN core, an exciting approach could be to etch the GaN core in situ to form tubes.

Final words With their remarkable efficiency, GaN-based blue LEDs have already revolutionized the field of lighting and improved the quality of life of mankind. In the near future, III-nitrides will probably contribute to the next generation of displays but also offer compact, efficient and environmentally friendly disinfection and purification solutions.

Résumé en français

Au cours des vingt dernières années, les diodes électroluminescentes (light-emitting diodes (LEDs) en anglais) à base de nitrure de gallium (GaN) ont révolutionné le domaine de l'éclairage en devenant la source de lumière la plus efficace créée par l'Homme. Aujourd'hui, leurs applications sont nombreuses, allant de l'éclairage public à l'éclairage automobile en passant par le rétroéclairage des écrans à cristaux liquides. Afin d'exploiter le plein potentiel de cette technologie, deux axes de recherche ont reçu une attention particulière. D'une part, la miniaturisation des LEDs bleues motivée par la volonté de développer une nouvelle génération d'écrans et de micro-écrans, plus lumineux, avec un meilleur contraste et plus performants, notamment pour les smartphones, les smartwatches et les applications de réalité virtuelle et augmentée [Wu+18; Din+19]. Il est intéressant de noter que ces efforts de recherche pourraient également permettre de remplacer les connexions électriques entre puces électroniques de courte et moyenne portée par des connexions optiques pour une communication plus efficace, bénéfique pour les centres de données et de calculs [Pez+22].

Afin de réduire la taille de ces dispositifs, deux approches sont considérées:

- L'approche *'top-down'* qui consiste à graver les µLEDs à partir d'une épitaxie 2D traditionnelle. Cette approche tire profit de la maturité des couches 2D utilisée pour l'éclairage. Cependant, comme le montre la figure 5.1, les procédés de gravure introduisent généralement des défauts de surface qui réduisent drastiquement l'efficacité au fur et à mesure que le rapport surface/périmètre diminue. Le but est donc de limiter l'impact de ces défauts de surface en développant de nouveaux procédés de gravure ou en passivant les surfaces après gravure [Oli+17].

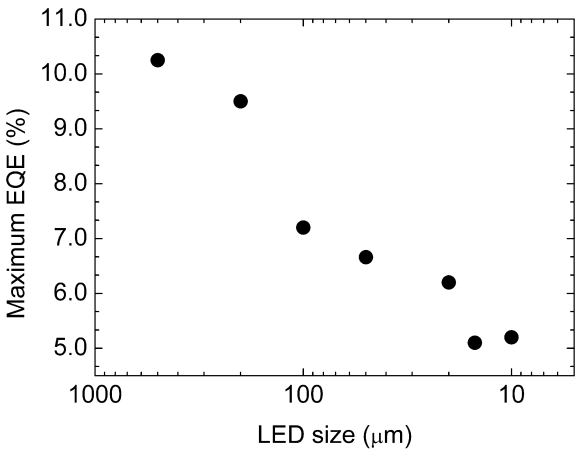

FIGURE 5.1: Influence de la réduction de la taille sur l'EQE maximal de µLEDs gravées. Adapté de [Din+19].

- La seconde approche, appelée *'bottom-up'*, consiste à former des pixels à partir d'assemblages de micro ou nanofils. L'un des avantages considérables est la possibilité de faire croître ces fils sur des substrats de silicium, ce qui facilite l'intégration technologique. Plus important encore, l'efficacité ne dépend plus de la taille du pixel mais de l'efficacité individuelle de chaque fil. Le défi est donc d'optimiser l'efficacité de ces fils, qui n'ont pas bénéficié de nombreuses années d'optimisation industrielle [Liu+22].

D'autre part, bien qu'il soit possible de faire varier le gap des nitrures de l'ultraviolet (UV) à l'infrarouge en alliant AlN, GaN et InN, seules les LEDs émettant du proche UV au vert sont efficaces, comme le montre la figure 5.2. Du côté des grandes longueurs d'onde, le développement se heurte au *"green gap"*, faisant historiquement référence au fait que l'efficacité des LEDs diminuait considérablement dans le vert. Aujourd'hui, ce terme est plus largement utilisé pour décrire la tendance générale à la réduction de l'efficacité quantique interne (internal quantum efficiency (IQE) en anglais) pour les émetteurs à base de nitrures aux plus grandes longueurs d'onde, en particulier dans la gamme jaune-rouge (*cf* figure 5.2 (a)). L'origine de ce phénomène est encore contestée. Récemment, David et al. ont suggéré que l'incorporation plus importante de défauts dans les puits à haute teneur en indium pourrait être à l'origine de ce phénomène [Dav+20].

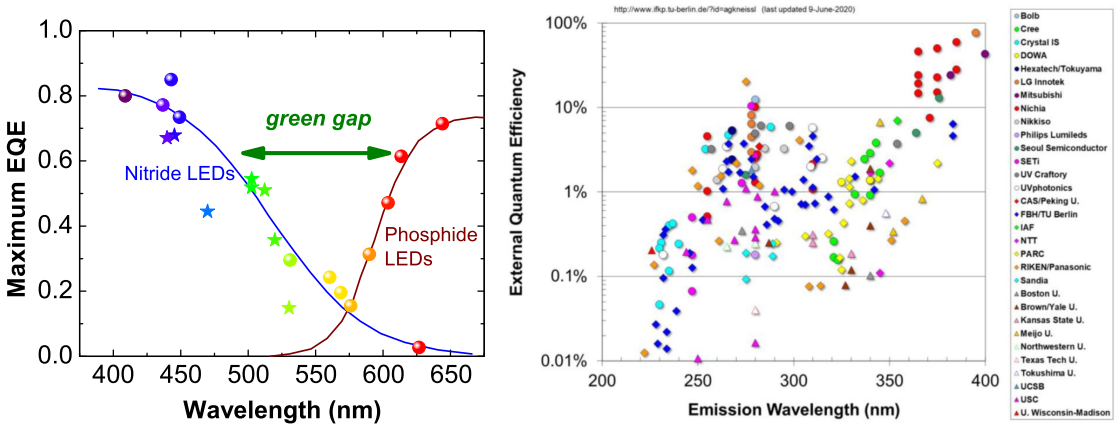

(a) (b)

FIGURE 5.2: Efficacité quantique externe en fonction de la longueur d'onde dans le visible (a) et l'UV (b). Adapté de [Auf+16] et [Kne+19].

Du côté de l'UV, un effort de recherche considérable est consacré pour faire face à la demande croissante de sources efficaces, compactes et respectueuses de l'environnement [Ama+20]. En effet, l'une des caractéristiques les plus importantes de la lumière UV est sa forte interaction avec l'ADN des bactéries, virus et autres pathogènes. Ces émetteurs sont donc particulièrement intéressants pour

un large éventail d'applications biomédicales, notamment la désinfection, la décontamination, la purification de l'eau et de l'air [Ama+20; RA20; Kit+21]. Malheureusement, comme le montre la figure 5.2 (b), à l'heure actuelle, l'efficacité s'effondre pour les longueurs d'onde inférieures à ∼360 nm en raison de multiples problèmes, notamment la difficulté à doper l'AlGaN et à former des contacts ohmiques transparents dans l'UV.

Par conséquent, la diminution de la taille des dispositifs et la nécessité d'étudier les défauts ont mis en évidence le besoin de caractérisation optoélectronique à l'échelle nanométrique, bien en dessous de la limite imposée par la diffraction de la lumière. Dans cette thèse, nous avons utilisé la cathodoluminescence (CL), une technique tirant profit de la petite longueur d'onde des électrons accélérés pour dépasser la limite de diffraction de la lumière.

Cependant, lorsque la taille de l'émetteur devient comparable à la longueur d'onde ou à la longueur de propagation de la lumière, il est difficile de distinguer la variation de l'extraction de lumière de l'IQE liée à la qualité du matériau. Pour cela, des techniques résolues en temps sont souvent utilisées pour étudier le temps de vie des porteurs, permettant d'estimer la contribution relative des processus radiatifs et non radiatifs sans être sensible aux variations de l'efficacité d'extraction de la lumière. Ainsi, ce type de mesure est particulièrement adapté à l'étude de l'impact de divers défauts, tels que les défauts ponctuels, les dislocations, les fissures ou encore les défauts de surface, ce qui est fondamental pour l'optimisation amont des dispositifs.

Dans ce contexte, cette thèse se concentre sur l'étude de l'efficacité des émetteurs à base de nitrure d'élément III. En particulier, nous avons développé une méthode basée sur l'étude de la statistique d'émission des photons caractéristique à la CL. Le principal avantage de cette technique est la possibilité de mesurer le temps de vie dans un montage CL conventionnel, *i.e.*, sans modification du microscope électronique tout en ayant une excellente résolution temporelle et la meilleure résolution spatiale possible.

Un bref aperçu du contenu de cette thèse est présenté dans les sections suivantes.

Nitrures d'élément III, QCSE et efficacités

Dans le premier chapitre de cette thèse nous introduisons tout d'abord les nitrures d'élément III. Ce sont des semiconducteurs à gap direct très largement utilisés pour la fabrication de composants optoélectroniques. Dans leur forme stable, ces composés cristallisent dans une structure wurtzite et sont composés d'éléments du troisième groupe du tableau périodique, à savoir aluminium (Al), gallium (Ga)

ou indium (In) ainsi que d'azote (N). Il est possible de les retrouver sous leur forme binaire (AlN, GaN ou InN), ternaire ($Al_xGa_{1-x}N$, $In_xGa_{1-x}N$ et $Al_xIn_{1-x}N$) ou encore quaternaire ($Al_xIn_yGa_{1-x-y}N$). Ce dernier point est tout particulièrement intéressant puisque les propriétés d'un alliage peuvent, au premier ordre, s'approximer par une loi de Vegard. Par exemple, le gap, et donc *in fine* la "couleur" d'émission d'un ternaire peut s'écrire:

$$E_{G,\mathrm{A}_x\mathrm{B}_{1-x}\mathrm{N}} = xE_{G,\mathrm{AN}} + (1-x)E_{G,\mathrm{BN}} - x(1-x)b_{\mathrm{ABN}} \tag{5.9}$$

Où b_{ABN} est le paramètre de courbure pour le ternaire ABN. Ainsi, il est en théorie possible de faire varier le gap continûment de l'UV à l'infrarouge, comme le montre la figure 5.3

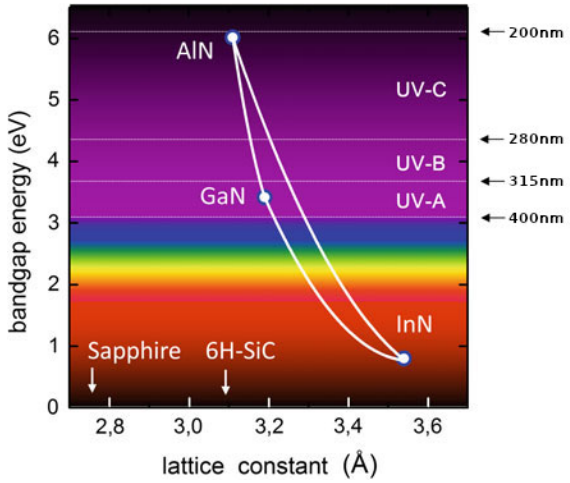

FIGURE 5.3: Energie de bande interdite en fonction du paramètre de maille a pour les nitrures d'élément III en phase wurtzite. Adapté de [KR16]

Nous avons également discuté d'une propriété importante des nitrures: l'absence de symétrie d'inversion le long d'un axe cristallographique, l'axe c. Ainsi, les nitrures sont des matériaux pyro- et piézoélectriques. Il en résulte une polarisation électrique alignée avec l'axe c. Dans le cas d'un puits quantique aligné avec cet axe, la discontinuité de polarisation entre le puits et les barrières entraîne une densité de charge aux interfaces et donc, un champ électrique. Ce champ a pour effet de modifier le profil des bandes, séparant ainsi les électrons et les trous aux deux interfaces correspondant à leurs minima d'énergie respectifs. Cette modification du profil de bande à principalement deux effets notables: des temps de recombinaisons radiatifs plus longs du à la séparation des porteurset un décalage de l'émission vers les plus hautes longueurs d'onde. Cet effet s'appelle l'effet Stark confiné quantiquement (ou quantum-confined Stark effect (QCSE) en anglais) et impacte considérablement les propriétés des LEDs à base de nitrures.

Dans ce chapitre, nous avons aussi introduit les différentes notions d'efficacité,

essentielles à la bonne compréhension de cette thèse. En effet, comme nous l'avons mentionné précédemment, nous cherchons à mesurer l'efficacité quantique interne (IQE) sans être influencés par les variations d'efficacité d'extraction de lumière (light extraction efficiency (LEE)) ou d'injection de porteurs (injection efficiency (IE)). Il est donc important de préciser ces notions:

IE L'efficacité d'injection est définie comme la fraction de paires électron-trou (e-h) injectées dans le dispositif qui vont finir par se recombiner dans la zone active. Cette grandeur peut être affectée par le courant de fuite, le dépassement de la zone active par les électrons (*overflow*) et les recombinaisons en dehors de la zone active.

$$IE = \frac{\text{\# paires e-h se recombinant dans la zone active}}{\text{\# de paires e-h injectées dans la structure}} \tag{5.10}$$

IQE L'efficacité quantique interne est définie comme le nombre de photons émis par rapport au nombre de paires electron-hole (e-h) se recombinant dans la zone active. Cette quantité reflète l'impact des recombinaisons non-radiatives dans la zone active.

$$IQE = \frac{\text{\# photons émis}}{\text{\# paires e-h se recombinant dans la zone active}} \tag{5.11}$$

LEE L'efficacité d'extraction de la lumière est définie comme le rapport entre le nombre de photons s'échappant de l'échantillon et ceux émis par la zone active. Cette quantité peut être sévèrement affectée par la réflexion totale interne et l'absorption des substrats ou d'autres couches selon la conception de la LED.

$$LEE = \frac{\text{\# photons s'échappant de la structure}}{\text{\# photons émis}} \tag{5.12}$$

External quantum efficiency (EQE) L'efficacité quantique externe est le rapport entre le nombre de photons émis et le nombre de paires e-h injectées dans le dispositif. Il peut être exprimé comme le produit de IE, IQE et LEE.

$$EQE = \frac{\text{\# photons s'échappant de la structure}}{\text{\# de paires e-h injectées dans la structure}} = IE \times IQE \times LEE \tag{5.13}$$

Wall-plug efficiency (WPE) L'efficacité à la prise est une quantité utile pour tenir compte de la perte de puissance. Elle est définie comme le rapport entre la puissance optique émise par la LED et la puissance électrique injectée.

$$WPE = \frac{P_{opt}}{P_{elec}} = \frac{E_\gamma (I/q) EQE}{IV} = \frac{E_\gamma}{qV} \times EQE \tag{5.14}$$

Où E_γ est l'énergie du photon, q est la charge de l'électron, I et V sont respectivement le courant et la tension de fonctionnement. Un exemple typique permettant de constater l'importance de la WPE est le cas des LEDs UV, qui peuvent avoir des tensions de seuil allant jusqu'à 10–20 V pour une énergie de photon de 4–6 eV.

Mesure du temps de vie à l'échelle nanométrique

Le deuxième chapitre de cette thèse présente brièvement différentes techniques de caractérisation couramment utilisées, telles que la photoluminescence (PL), la CL et leurs équivalents dites "résolues" en temps (TRPL et TRCL). Parmi ces deux dernière, seule la TRCL permet de mesurer le temps de vie à l'échelle nanométrique, grâce à la plus petite longueur d'onde des électrons accélérés. Pour effectuer de telles mesures, il faut pouvoir générer des pulses d'électrons. Pour ce faire, deux approches sont communément employées:

- L'utilisation d'un canon à électron pulsé. En quelques mots, le principe est d'abaisser la température de fonctionnement de la pointe d'un field emission gun, diminuant ainsi la probabilité d'extraction. Il est alors possible d'extraire les porteurs par effet photoélectrique, typiquement en focalisant un laser UV pulsé sur la pointe du canon à électron. Ainsi, l'émission d'électron est pilotée par les pulses du laser. Le principal avantage de cette technique est de procurer une excellente résolution temporelle tout en préservant la résolution spatiale du microscope. Cependant, cela nécessite d'avoir une fenêtre optique sur la pointe et un laser UV pulsé très coûteux. De plus, l'alignement du laser sur la pointe n'est pas chose aisée.

- Une autre possibilité est l'utilisation d'un "beam blanker". Le principe est d'introduire des électrodes dans la colonne du microscope. En modulant la polarisation, il est possible de dévier le faisceau d'électrons. Le principal avantage de cette technique est sa facilité d'utilisation et la possibilité de passer du mode pulsé au mode continu en arrêtant la modulation. En revanche, cette technique présente une résolution temporelle plus faible et une résolution spatiale dégradée principalement à cause du déplacement du faisceau sur l'échantillon. Note: Il est possible de minimiser ce déplacement de faisceau lors de l'obturation, en faisant coïncider le plan médian du beam blanker avec le plan focal conjugué.

Dans notre cas, nous utiliserons un beam blanker pour certaines mesures, mais celui-ci ne peut être positionné de manière idéale, ce qui induit un déplacement important du faisceau sur l'échantillon. Pour outrepasser cette limitation et améliorer

la résolution spatiale, nous avons développé un interféromètre de Hanbury Brown et Twiss (HBT) basé sur les travaux de Meuret et al.

L'interféromètre de Hanbury Brown & Twiss

L'introduction de cette technique constitue l'essentiel du second chapitre et n'est que rapidement présentée ci-dessous.

L'interféromètre de Hanbury Brown & Twiss, du nom de ses inventeurs Robert Hanbury Brown et Richard Quintin Twiss, ou plus communément appelé HBT, est un interféromètre d'intensité. Celui-ci est composé d'une lame séparatrice dirigeant la lumière vers deux photodétecteurs reliés à un corrélateur. Il permet de mesurer la fonction autocorrélation de second ordre $g^2(\tau)$ qui est proportionnelle à la probabilité conditionnelle d'observer un photon à un temps t sur un détecteur sachant qu'un photon a été détecté à un temps $t+\tau$ sur l'autre détecteur.

$$g^2(\tau) = \frac{\langle I(t)I(t+\tau)\rangle}{\langle I(t)\rangle^2} \tag{5.15}$$

Cette quantité est utile pour caractériser la nature de la lumière. En effet, on peut distinguer 3 cas, comme illustré en figure 5.4 :

Lumière poissonnienne Cela correspond typiquement à un faisceau laser. La statistique d'émission des photons est un processus de Poisson, c'est-à-dire que le temps moyen entre deux émissions consécutives est constant et indépendant du temps écoulé depuis la dernière émission. Dans ce cas, $g^2(\tau) = 1\ \forall\tau$

Lumière super-poissonienne lumière dite classique ou chaotique. Ici, l'émission de photons tend à former des paquets qui s'étalent sur un temps τ_c appelé temps de cohérence. Ainsi, la probabilité de détection jointe augmente pour les faibles délais. Dans ce cas, $g^2(\tau)_{\tau\lesssim\tau_c} > 1$ et $g^2(\tau)_{\tau\gg\tau_c} = 1$. Notez que si expérimentalement la résolution temporelle n'est pas meilleure que τ_c, ce comportement de regroupement ne peut pas être observé, *i.e*, $g^2(\tau) = 1\ \forall\tau$.

Lumière sub-poissonienne correspond typiquement à des émetteurs de photons uniques. La probabilité d'avoir une détection jointe à délais nul est nulle et reste faible pour des délais inférieurs au temps de vie de l'émetteur, car celui-ci doit se relaxer avant de pouvoir être excité à nouveau et émettre un photon. Cela se traduit par $g^2(\tau)_{\tau\lesssim\tau_c} < 1$ et en particulier, $g^2(0) = 0$.

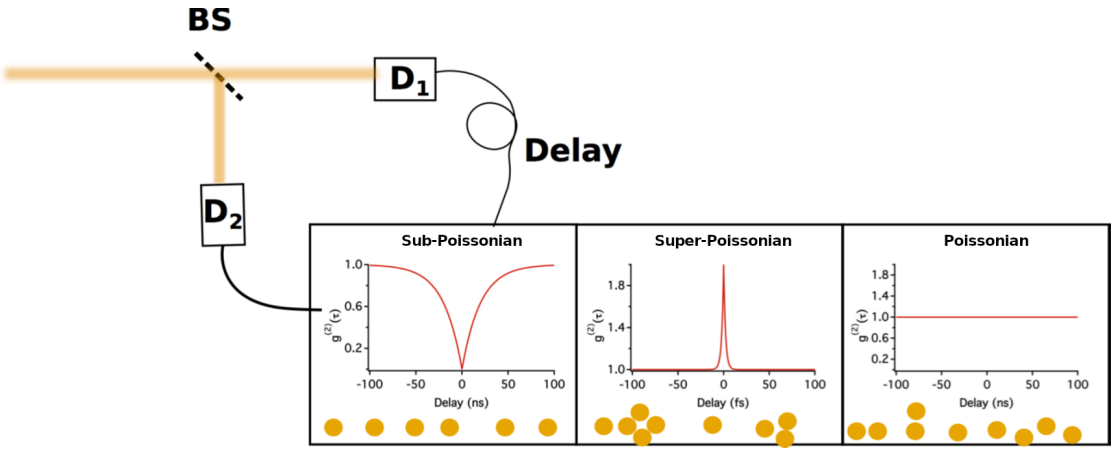

FIGURE 5.4: Schéma de base d'un montage HBT illustrant différentes statistiques d'émission. Adapté de [Meu16]

Photon bunching en cathodoluminescence

Une des différence fondamentale entre la PL et la CL réside dans la différence de la statistique de génération des porteurs. En effet, en raison de la haute énergie des électrons accélérés, chacun d'entre eux peut générer de nombreuses paires électron-trou, là où, en PL, un photon entraîne au maximum la génération d'une paire. Ces paires vont ensuite se recombiner et émettre des photons, typiquement suivant une loi exponentielle.

Par conséquent, pour chaque électron primaire, plusieurs photons peuvent être émis. En utilisant un HBT, il est possible d'observer cette statistique qui se traduit ici par

$$g^2(\tau) = 1 + g_0 \exp\left(-\frac{|\tau|}{\tau_{eff}}\right) \tag{5.16}$$

Ainsi, en ajustant la décroissance de la fonction d'autocorrélation, il est possible d'accéder au temps de vie des porteurs τ_{eff} [BL99; Meu+16; Meu+18].

Afin d'observer ce phénomène, il est nécessaire de se trouver dans un régime où le temps entre chaque électron primaire est typiquement plus grand que la largeur d'un bunch de photons, tout comme la fréquence d'excitation doit être suffisamment basse pour permettre la relaxation du système en TRCL ou TRPL. Cependant, ici les électrons ne sont pas émis à intervalles réguliers mais suivant un processus de Poisson avec un paramètre dépendant du courant du faisceau d'électrons.

Il est donc possible d'établir un critère de sélection sur le courant en fonction du temps de vie que l'on souhaite mesurer. En supposant que l'essentiel des photons est contenu dans un temps égale à 3τ après l'excitation, nous avons ici décidé de respecter le critère suivant :

$$I \lesssim q/3\tau_{eff} \tag{5.17}$$

La table 5.1 présente quelques valeurs de courant pour différents temps de vie.

τ (ns)	0.1	1	10	100
I (pA)	534	53.4	5.3	0.5

TABLE 5.1: Suggestion de courant maximal du faisceau d'électron en fonction du temps de vie.

En plus de ce critère, il existe comme dans toute mesure de corrélation, une limitation sur le nombre de coups par excitation à ne pas dépasser afin ne pas déformer la statistique que l'on souhaite mesurer. Cette limitation provient essentiellement du fait que l'électronique d'acquisition possède un temps mort après une mesure pendant lequel le système est "aveugle". En prenant en compte cette limitation, il est possible d'obtenir un critère supplémentaire reliant taux de comptage et courant. Ces deux critères sont résumés en figure 5.5 (a) et (b).[11]

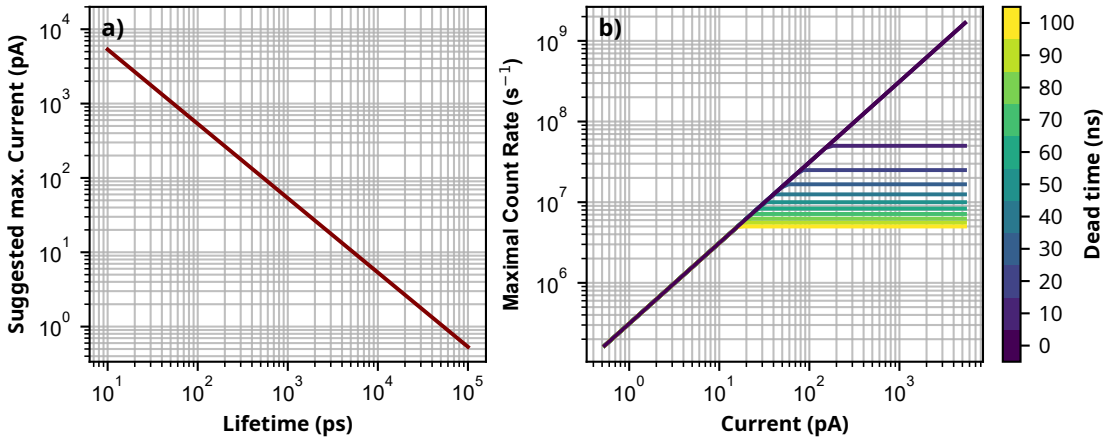

FIGURE 5.5: (a) Courant maximal du faisceau d'électrons suggéré pour des temps de vie allant de 10 ps à 100 ns. (b) Taux de comptage utile maximal par canal en tenant compte du temps mort et du pile-up pour différents temps morts.

Dans ce chapitre, nous avons également présenter un modèle Monte-Carlo extrêmement simple permettant de reproduire les résultats obtenus. Pour plus de détails, le lecteur est invité à consulter le chapitre.

Pour finir, ce chapitre présente le setup expérimental utilisé et développé pendant cette thèse. Seul un schéma est présenté ici (figure 5.6), le lecteur intéressé est invité consulter à la section correspondante.

[11] La figure 5.5 (b) tient compte d'un critère supplémentaire fixant taux de comptage maximal en fonction de la durée du temps mort, voir chapter 2 pour plus d'information.

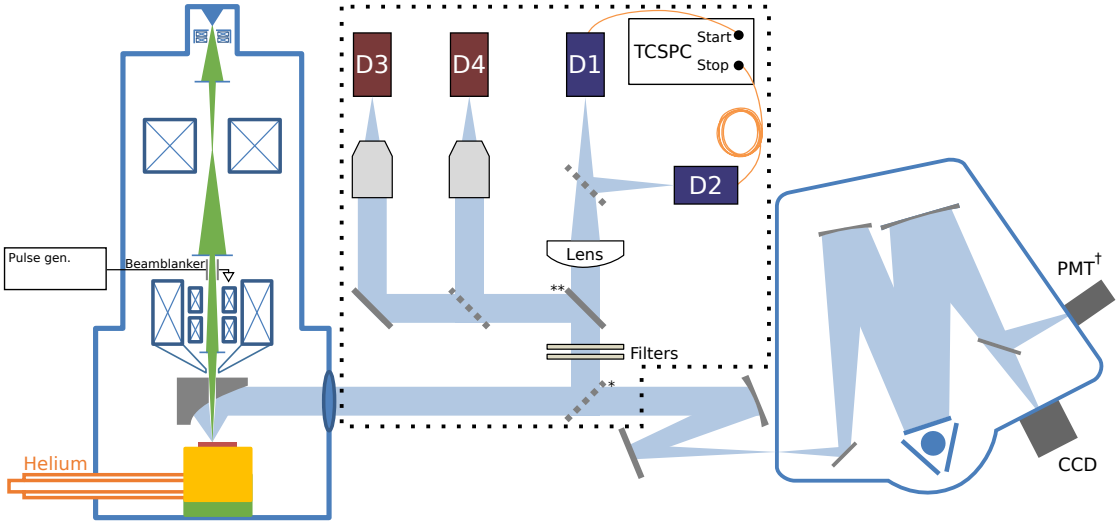

FIGURE 5.6: Schéma du setup. La partie développée au cours de cette thèse est encadrée en pointillés. * Lame séparatrice présente que lors de l'utilisation d'un des deux Hanbury Brown & Twiss interferometers et peut être remplacée par un miroir si l'échantillon n'est pas assez lumineux. ** Miroir amovible pour passer de l'HBT visible à l'HBT UV. † PMT facilement remplaçable par un PMT hybride (D2) pour effectuer des mesures de TRCL. Notez que le beamblanker n'est présent que lors des mesures de TRCL.

Des sous-couches pour des LEDs bleues plus efficaces

Le troisième chapitre est dédié à l'étude des effets des underlayers (ULs) sur l'efficacité des puits quantiques (quantum wells (QWs) en anglais) InGaN/GaN. En particulier, l'étude se concentre sur le rôle des ULs contenant de l'indium (In) pour la suppression des défauts ponctuels créés pendant la croissance à haute température du GaN.

De nos jours, les LEDs bleues à nitrure d'éléments III sont largement commercialisées pour l'éclairage et peuvent avoir un IQE bien supérieur à 80% [Dav+20]. Pour atteindre de telles performances, il est bien connu qu'un UL d'InGaN avant la croissance du QWs augmente considérablement l'efficacité de la région active [Dav+20].

Bien que cette pratique empirique soit connue depuis longtemps, la physique sous-jacente n'a été étudiée en détail que récemment et fait encore l'objet de débats. Plusieurs mécanismes ont été proposés pour expliquer l'amélioration de l'efficacité des LEDs. Récemment, Haller et al. ont montré que des défauts ponctuels sont générés pendant la croissance du GaN à haute température (typiquement $T > 900\,°\mathrm{C}$) et restent à la surface du GaN même après une recroissance à basse tem-

pérature [Hal+18]. Cependant, ces défauts sont incorporés dans les couches, et ce proportionnellement à la teneur en indium pour former des centres non radiatifs. Le rôle d'un UL contenant de l'indium est donc de piéger ces défauts avant la croissance des QWs d'InGaN. Jusqu'à ce jour, la nature de ces défauts fait toujours l'objet de débats. Récemment, Chen et al. ont proposé que ces défauts soient probablement des lacunes d'azote [Che+21].

Ce chapitre est organisé en quatre études résumées ci-dessous.

Puits quantiques sur substrat de saphir plan *c*

Dans un premier temps, nous nous sommes intéressés à la reproduction et à l'étude de l'effet reporté dans la littérature. Pour cela, nous avons réalisés deux échantillons similaires. Ils consistent en un buffer de GaN réalisé à haute température sur un substrat de GaN. La croissance se poursuit par la réalisation d'un puits quantique d'InGaN réalisé à plus basse température. Le deuxième échantillon diffère par l'ajout d'un UL d'InGaN du 50 nm avant la croissance du puits quantique.

Après une rapide comparaison par PL, nous avons constaté que l'intensité de l'échantillon sans UL était inférieure de près de deux ordres de grandeur, en accord avec les observations de Haller et al. [Hal+17].

Nous avons ensuite étudié l'évolution du temps de vie effectif en fonction de la température grace à des mesures de TRCL réalisées avec le beam blanker. Cette mesure permet de déterminer quel mécanisme est prépondérant. En effet, la dépendance en température des temps de vie radiatif et non-radiatif diffère. Dans le premier cas, le temps de vie radiatif pour un puits quantique augmente linéairement avec la température.[12] A l'inverse, comme les processus non radiatifs sont activés thermiquement, le temps de vie non radiatif diminue avec la température.

Comme on pouvait s'y attendre, le profil de temps de vie est radicalement différent entre les deux échantillons. Pour l'échantillon avec UL, le temps de vie effectif passe de 86 ns à 127 ns entre 5 K et 300 K. A l'inverse, en l'absence d'UL, le temps de vie chute drastiquement entre 5 K et 300 K de 68 ns à 7 ns. Cette mesure à donc permis de mettre en évidence une importante réduction des processus non radiatifs grace à l'ajout d'un UL d'InGaN.

Croissances sur silicium

Après que l'effet de l'UL ait été rapporté pour des structures planaires réalisées par croissance sur saphir et sur GaN free-standing, cette étude vise à étudier l'effet

[12] Les effets de la localisation sont omis ici pour des raisons de simplicité, voir le chapitre pour plus de détails.

de l'UL d'InGaN dans le cas d'échantillons planaires réalisés par croissance sur silicium.

En particulier, nous avons étudié le rôle relatif des défauts ponctuels et des dislocations sur l'efficacité des puits quantique plan c réalisés sur des substrats de Si (111). En comparant à la fois l'IQE relatif en fonction de la puissance d'excitation et le temps de vie effectif en fonction de la température, nous avons pu mettre en évidence que les défauts ponctuels continuent à jouer un rôle important même si leur densité est typiquement de 1 à 2 ordres de grandeur inférieure à celle des dislocations. Ainsi, bien que le rôle des dislocations en tant que centres non radiatifs soit bien établi et ne puisse être négligé, il semble être moins critique que celui des défauts ponctuels.

Etude de microfils coeur-coquille InGaN/GaN

Après avoir montré que les ULs étaient efficaces pour diverses structures planaires (plan c), nous nous sommes penchés sur leur effet sur l'efficacité de puits quantiques coeur-coquilles InGaN/GaN réalisés sur les parois latérales (plan m) de microfils de GaN. Sans entrer dans les détails, l'une des principale motivations de cette étude est le fait que ce type de structure est prometteur pour la réalisation de microLEDs. L'étude étant relativement conséquente, nous nous contenterons d'énoncer les principaux résultats.

Nous avons tout d'abord constaté grace à des cartographies CL qu'il était nécessaire d'introduire un espaceur (spacer en anglais) de GaN juste après la croissance du coeur de GaN pour obtenir de la luminescence sur les plans m. Des analyses STEM et EDX ont démontré que le rôle de ce spacer est d'enterrer une fine couche de SiGaN formée probablement à cause de la forte injection de silane afin de promouvoir la croissance verticale des fils. Sans ce spacer, les QWs sont de mauvaise qualité cristalline et les défauts créés à l'interface entre le premier QW et le SiGaN se propagent dans les couches supérieures, empêchant ainsi la luminescence.

Ensuite, concernant les ULs d'InGaN, nous n'avons observé aucune différence significative en PL, CL, TRPL et TRCL. Il semblerait donc que contrairement au cas planaire (plan c), l'ajout d'un UL d'InGaN avant le puits quantique n'augmente pas son efficacité. A ce stade, nous ne pouvons pas conclure si cela est dû aux conditions de croissance particulières des fils, en particulier un rapport V/III très faible pour la croissance du coeur GaN, ainsi qu'une forte injection de silane.

Afin de répondre à cette question, nous avons étudié des puits quantiques réalisés sur des substrats de GaN plan m. Les résultats sont présentés dans la prochaine section.

Puits quantiques plan *m* sur substrat de GaN

Afin de dissocier les éventuels effets liés aux conditions de croissance des fils de GaN, nous nous sommes intéressés à l'effet d'un ULs d'InGaN sur l'efficacité de puits quantiques crûs par metal-organic vapor phase epitaxy sur des substrats de GaN plan *m*, permettant ainsi de comparer l'effet de l'orientation du substrat.

Nous avons d'abord observé par analyse SIMS que l'incorporation des impuretés diffère entre les plans *m* et *c*. En particulier, pour le plan *m*, la concentration en oxygène était d'un ordre de grandeur plus élevé dans la couche d'InGaN que dans le GaN. Ensuite, nous avons étudié deux échantillons plan *m* avec et sans UL par analyse CL et TRCL en fonction de la température. Nous avons pu montrer que les deux échantillons avaient des propriétés similaires. En particulier, le rapport d'intensité entre la basse et la haute température est d'environ 55%. Bien que ce ratio ne reflète pas rigoureusement l'IQE, il fournit une première estimation. De plus, les temps de vie augmentent avec la température pour les deux échantillons, suggérant que les recombinaisons radiatives prévalent même en l'absence d'UL. Ces deux signes indiquent un IQE relativement élevé et suggèrent que la présence de l'UL pour les échantillons plan *m* n'est pas aussi critique que pour les échantillons plan *c*.

Le chapitre se termine par quelques hypothèses qui pourraient expliquer la différence de comportement entre les deux orientations cristallines. En particulier, il est souligné que la croissance du GaN en MOVPE se produit à une température proche de la température de décomposition thermique. Il est important de préciser que diverses études ont montré que la décomposition thermique est anisotrope, ce qui pourrait expliquer la différence de comportement entre plan *m* et *c*. Pour vérifier cette hypothèse, il pourrait être intéressant d'essayer de remplacer la croissance de GaN par de l'AlGaN qui ne se décompose pas et ce même avec une concentration en Al de seulement 5%.

Recombinaisons de surface dans les µLEDs

Ce chapitre est dédié à l'étude des recombinaisons de surface dans les µLEDs gravées. Comme déjà mentionné, la réalisation de µLEDs par l'approche dite *'top-down'* a pour principale limitation l'introduction de défauts aux surfaces gravées. La diminution du rapport surface/périmètre s'accompagne d'une sévère perte d'efficacité. L'enjeu est de réduire cet effet en travaillant sur de nouvelles techniques de gravure ou encore en passivant les surfaces par traitement chimique ou dépôt d'oxyde par exemple. Pour développer ces solutions, il est nécessaire de quantifier l'impact des recombinaisons de surface. Pour cela différentes tech-

nique de caractérisation peuvent être employées comme l'électroluminescence ou la micro-photoluminescence. Cependant, si ces technique sont bien adaptées pour mesurer des variations d'EQE, elles ne permettent pas de distinguer des variations d'IQE, LEE ou encore IE. Ainsi, pour avoir accès à l'IQE, des mesures résolues en temps peuvent être effectuée, comme la TRPL. Cependant, le résolution spatial de cette technique est limitée et ne permet pas de quantifier la vitesse de recombinaison. Dans ce chapitre, nous introduisons une méthode pour mesurer les grandeurs essentielles que sont le coefficient de diffusion D et la vitesse de recombinaison de surface S au sein d'une µLED. Cette méthode est basée sur la mesure du temps de vie à l'échelle nanométrique, effectuée grace au setup HBT développé, combinée à model de diffusion.

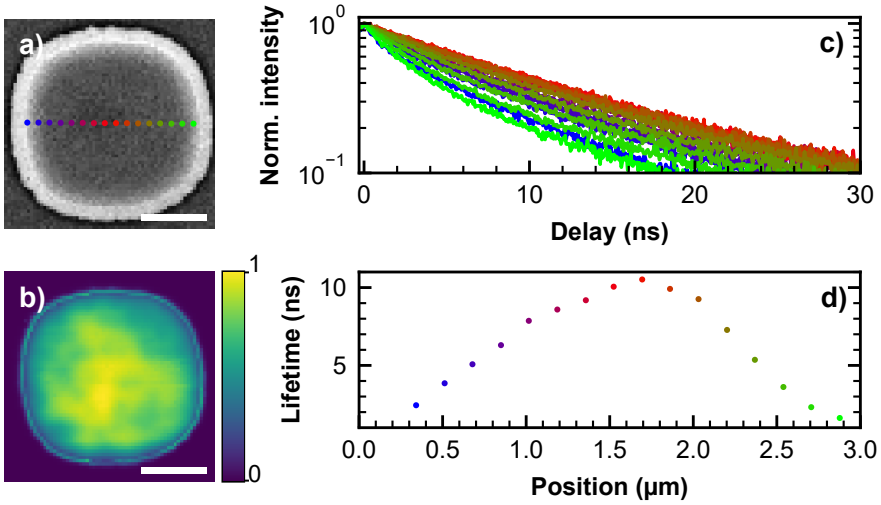

FIGURE 5.7: (a) Image MEB d'un mesa de 3 µm de large et (b) l'image CL correspondante à l'énergie du MQW. La barre d'échelle mesure 1 µm. (c) g^2 normalisé pour différentes positions (points colorés en (a)) sur la mesa. (d) Temps de vie CL en fonction de la position sur la mesa.

La figure 5.7 (a) montre l'image MEB d'un mesa gravé de 3 µm ainsi que son image CL acquise simultanément (b). Par analogie avec les mesures résolues en temps, nous montrons les fonctions d'autocorrélation normalisées pour les délais positifs dans la figure 5.7 (c). Les points de mesure correspondants sont indiqués par un code couleur sur les figure 5.7 (a) et (d). Le profil du temps de vie du CL à travers la mesa est représenté en figure 5.7 (d). Il suit approximativement une courbe en forme de cloche avec un maximum de ∼10.5 ns au centre du mesa. Lorsque le faisceau d'électrons s'approche des parois latérales, le temps de vie CL diminue. Près des parois latérales, le temps de vie des porteurs est inférieur à 3 ns, ce qui met en évidence le rôle néfaste des recombinaisons de surface non radiatives.

Afin de quantifier les recombinaisons de surface, nous avons ensuite développé un model basée sur la deuxième loi de diffusion de Fick avec un terme supplémen-

taire pour prendre en compte les recombinaisons dans le bulk. Pour le valider, nous avons passivé notre échantillon en effectuant d'abord une gravure au KOH à température ambiante suivie d'un dépôt d'Al_2O_3 par ALD. Une technique similaire a déjà été rapportée dans [Ley+20].

Comme attendu, nous avons pu observer que le temps de vie près de la surface passe de 3.5 ns pour l'échantillon de référence à 5.5 ns pour l'échantillon après traitement au KOH et Al_2O_3 figure 5.8.

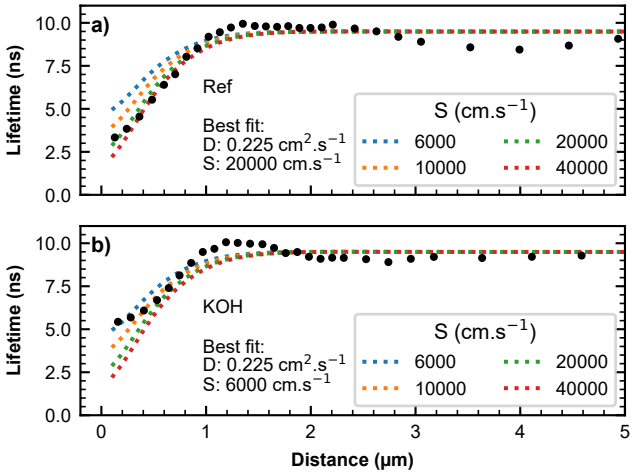

FIGURE 5.8: Profil de temps de vie de l'échantillon non traité (a) et traité avec une gravure KOH suivie d'un dépôt d'Al_2O_3 par ALD (b) (points noirs). Les simulations de diffusion 1D pour différentes vitesses de recombinaison en surface sont également représentées par des lignes en pointillés.

Une étude statistique a ensuite été réalisée sur 7 mesa pour les échantillons de référence et les échantillons traités. Nous avons ensuite extrait D et S en utilisant notre model. Nous avons observé, que seule la vitesse de recombinaison de surface change, passant d'environ $\sim 1.5 \times 10^4$ pour l'échantillon de référence à environ $6.9 \times 10^3\,\mathrm{cm\,s^{-1}}$ pour l'échantillon après traitement par KOH et Al_2O_3, tandis que le coefficient de diffusion reste autour de $0.34\,\mathrm{cm^2\,s^{-1}}$. Ces valeurs sont en accord avec les données publiées précédemment et obtenues avec d'autres techniques expérimentales. Pour finir, nous avons brièvement étudié des LED rouges à base d'AlInGaP, démontrant ainsi l'applicabilité de la méthode avec un montage développé pour le domaine du visible.

LEDs UV à base de microfils de GaN coeur-coquille

Le dernier chapitre de cette thèse est consacré à la caractérisation et réalisation de LEDs UV à base de microfils de GaN. En effet, pour surmonter certaines limita-

tions inhérentes aux architectures de LEDs planaires plan c, l'utilisation de LED UV à base de nanofils a récemment fait son apparition [Zha+14]. Elles offrent déjà quelques avantages clés : une plus grande solubilité du Mg conduisant à un dopage p plus efficace dans l'UV profond [Tra+17] et une réduction drastique des défauts étendus, soit en raison d'une meilleure gestion des contraintes [Lan+10] ou du filtrage des dislocations [KI15]. Une approche prometteuse est basée sur des fils de type coeur-coquille plan m [Cou+18a; Bru+19; Cou+18b; Gre+20]. Dans cette géométrie, l'absence de QCSE et l'augmentation de la surface d'émission contribuent à l'atténuation des effets néfastes qui apparaissent à des densités élevées de porteurs. De plus, en l'absence de QCSE, l'énergie d'émission sera généralement plus élevée que pour une structure équivalente en plan c.

Dans un micro-fil coeur-coquille, le dipôle émetteur est généralement couplé à un mode guidé où le fil lui-même agit comme un guide d'ondes [Tch+14]. En conséquence, pour les émetteurs UV, l'extraction de la lumière pourrait être sévèrement altérée en raison de l'absorption du coeur en GaN. Pour éviter ce problème, l'une des approches consiste à utiliser un coeur en AlN interne [Cou+18a]. Cependant, avec une telle conception, l'injection électrique est un défi. Par conséquent, pour combiner injection électrique et faibles pertes d'absorption, une solution consiste à faire croître une coque de revêtement en AlGaN pour protéger le mode guidé des pertes d'absorption du coeur. Cette couche de protection doit être à la fois riche en Al et suffisamment épaisse pour être efficace dans les UV profonds. Dans ces conditions, et comme observé pour les couches planaires, cela conduit souvent à la formation de fissures [Ein+00]. Il est donc crucial d'étudier l'influence des fissures sur les propriétés optiques de la région active. Cette problématique est abordée dans la première partie du chapitre et est résumée ci-après.

Effet des fissures sur les propriétés optiques

En raison de la grande différence de paramètre de maille entre le coeur de GaN et la coquille d'AlGaN riche en Al, nous pouvons observer la formation de fissures (figure 5.9 (a, b)). Dans une géométrie coeur-coquille, la contrainte est principalement concentrée le long de l'axe c. Pour cette raison, ces fissures se forment préférentiellement perpendiculairement à l'axe c, le long de l'axe a (figure 5.9 (b)). Nous avons pu observer par STEM que la fissure traverse toute l'hétérostructure AlGaN et se termine dans une couche de GaN (figure 5.9 (c)).

Pour étudier l'influence des fissures sur les propriétés optiques, nous avons effectué des cartographies des spectres CL centrées sur l'émission des QWs, *i.e*, dans la plage d'énergie 3,7–4.9 eV pour chaque fil. L'image MEB typique d'un fil typique présentant plusieurs fissures est présentée en figure 5.10 (a). La figure 5.10 (b)

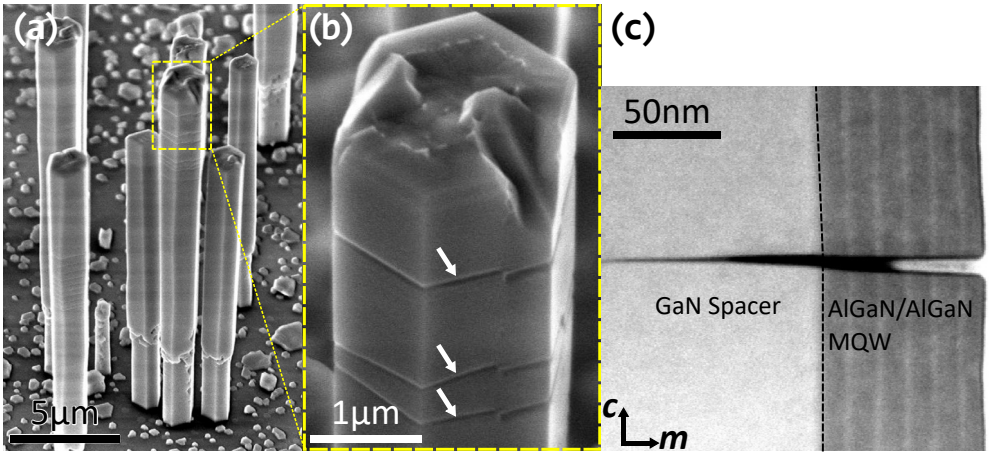

FIGURE 5.9: (a) Image SE inclinée de fils de GaN recouverts de MQWs à base d'Al réalisés sur substrat de saphir. (b) Vue rapprochée d'un fil avec plusieurs fissures. (c) Vue HAADF-STEM en coupe. Adaptée de [Fin+20]

montre la cartographie CL correspondante, intégrée sur la largeur du fil dans la région d'énergie des QWs. Nous pouvons voir que l'énergie d'émission des QWs augmente légèrement de bas en haut, probablement en raison d'un gradient d'Al le long du fil ou d'un changement d'épaisseur des QWs. Même si les fissures peuvent être difficiles à localiser sur les images MEB, elles sont facilement visibles sur les cartographies des spectres CL. En effet, la présence d'une fissure entraîne systématiquement un décalage vers le bleu de l'énergie d'environ 100 meV accompagné d'une augmentation significative de l'intensité CL.

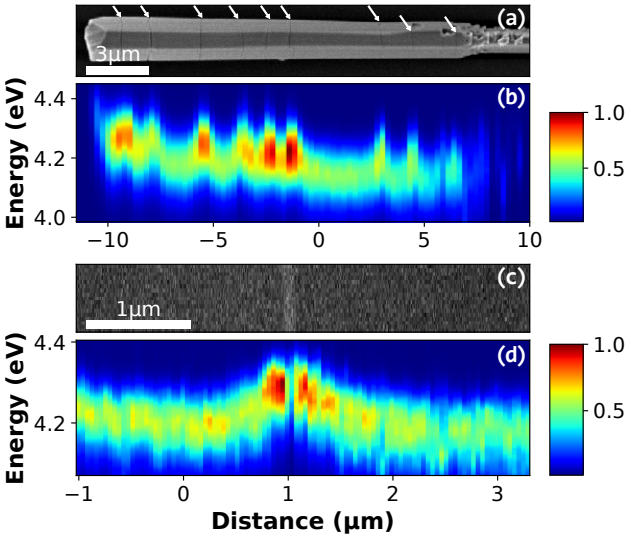

FIGURE 5.10: (a) Image SE d'un fil et (b) la cartographie des spectres CL correspondante. (c) Vue rapprochée de l'image SE près d'une fissure sur un fil différent et sa cartographie des spectres CL correspondante (d). Adaptée de [Fin+20]

Dans un premier temps, nous nous sommes concentrés à l'augmentation de

l'énergie. En effectuant des simulations basées sur la relaxation de la contrainte induite par le crack suivi du calcul des niveaux d'énergie en prenant en compte la modification des bandes, nous avons pu reproduire le blueshift observé. Au vu de l'excellente concordance entre les données et les simulations, nous avons attribué le changement d'énergie à la relaxation locale de la contrainte.

Ensuite, comme déjà mentionné, l'étude de l'intensité de CL ne permet pas de décorréler LEE et IQE. Par conséquent, ici, nous avons mesuré l'évolution du temps de vie de la CL en fonction de la distance à une fissure grâce au dispositif de développé dans cette thèse (UV-HBT). Les mesures ont été effectuées à 5K, avec une tension d'accélération de 2 kV, et un courant de sonde d'environ 5 pA.

La figure 5.11 (a), montre $g^2 - 1$ et les fits correspondants à une distance de 100 nm et 1500 nm d'une fissure. Nous pouvons voir que le temps de vie est beaucoup plus court à proximité de la fissure. Pour étudier plus en détail cet effet, nous avons ensuite mesuré l'évolution du temps de vie en fonction de la distance à la fissure. Dans la figure 5.11 (b), l'intensité CL normalisée et le temps de vie effectif sont représentés en fonction de la distance à la fissure.

À environ 400 nm de la fissure, l'intensité CL commence à augmenter pour atteindre 1,4 fois l'intensité de la région sans fissure à 100 nm. En deçà de 100 nm, l'intensité diminue rapidement jusqu'à son minimum, qui correspond à 0,7 fois l'intensité de la région sans fissure. Le temps de vie est strictement décroissant avec la distance. Elle varie de 475 ps à un micron à 285 ps près de la fissure.

Nous pouvons considérer que cette réduction de temps de vie est due soit au temps de vie radiatif, soit au temps de vie non radiatif. Pour diverses raisons, il est possible d'écarter la première hypothèse (voir chapter 5 pour plus d'informations).

Par conséquent, la réduction du temps de vie effectif près de la fissure est ici attribuée à l'influence croissante des recombinaisons non radiatives près de la surface. Cette réduction du temps de vie pourrait provenir d'un fort champ électrique à la surface dû au pinning du niveau de Fermi et aux champs piézoélectriques . Si l'IQE diminue près des fissures, l'augmentation de l'intensité de la CL doit être liée à une augmentation locale de LEE. Cette augmentation locale de LEE pourrait avoir deux origines. Premièrement, en brisant localement la symétrie de la structure, la fissure pourrait agir comme un centre de diffusion pour la lumière émise. Notez qu'en raison de l'absorption du coeur de GaN les photons UV émis dans le fil ne peuvent se propager que sur quelques centaines de nanomètres. En conséquence, seule la lumière générée à proximité de la fissure bénéficierait d'une meilleure efficacité d'extraction, ce qui est cohérent avec nos observations. Deuxièmement, selon nos simulations (non présentées ici) , le changement d'état de contrainte près de la fissure pourrait induire un réarrangement des bandes de valence à environ 250 nm de la fissure . En raison de leurs règles de sélection dif-

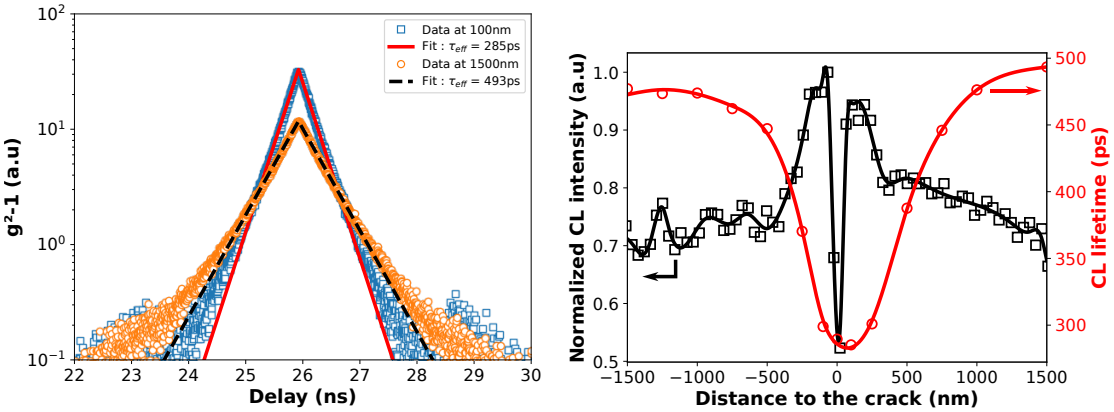

(a) (b)

FIGURE 5.11: (a) Measurement of $g^2 - 1$ at two different distances from the crack (data point) and their corresponding fit (lines). (b) Normalized CL intensity of the MQW (black squares) and CL lifetime (red circles) as a distance to the crack acquired at T = 5 K. The lifetime has been acquired with an spatially-resolved time-correlated cathodoluminescence setup. Adapted from [Fin+20]

férentes, cela devrait entraîner un changement de direction de la polarisation de la lumière émise . Puisque la LEE dépend drastiquement de la polarisation de la lumière , un tel croisement pourrait localement augmenter l'intensité observée. Afin de confirmer cette hypothèse, il pourrait être intéressant de réaliser des mesures de CL dépendantes de la polarisation, comme présenté par Fouchier et al. [Fou+19].

Pour résumer, en sondant les propriétés optiques de fils de GaN avec des QWs coeur-coquille riches en Al, nous mettons en évidence l'influence des fissures sur l'efficacité de la région active. Sous l'effet de la relaxation de la contrainte, l'énergie d'émission des QWs augmente près des fissures d'environ 100 meV. De plus, nous avons observé une augmentation de l'intensité de CL, qui a été attribuée à une augmentation locale de l'efficacité d'extraction de la lumière. Cela indique que l'extraction est un problème important dans ce type de structure. Enfin, le temps de vie des porteurs subit une diminution significative près des fissures, reflétant une réduction de l'IQE.

Réalisation et caractérisation de LEDs UV à fil unique

La deuxième partie du chapter 5 présente les résultats obtenus concernant la réalisation de µLEDs UV à base de microfils coeur-coquille GaN/AlGaN.

Dans un premier temps, nous avons réalisé des contacts en tungsten en electron-beam-induced deposition. Grace à ces contacts, nous avons montré qu'il est possible d'obtenir des caractéristiques de diode avec des jonctions AlGaN intégrées dans des microfils coeur-coquille. Cependant, à la différence des microfils étudié dans

le chapter 3, l'utilisation d'Al enterre la couche de passivation à la base du fil, ce qui permet à la coquille de p-GaN de s'étendre près du contact n. Par conséquent, ces structures ont tendance à avoir un courant de fuite plus important que leur homologue sans Al.

Ensuite, nous avons réalisé la croissance de deux structures similaires conçues pour une émission dans l'UV-A et l'UV-B. Après caractérisation électrique des deux structures, nous avons constaté que le dispositif UV-B présente un courant direct bien inférieur (3 ordres de grandeur) à 10 V, probablement en raison de l'augmentation de la teneur en Al, rendant l'injection de trous plus difficile. En revanche, les deux structures présentent un niveau de courant de fuite comparable. A ce stade il est important de souligner que ces dispositifs ne sont pas stables sous irradiation et sous contrainte de courant. En particulier, des fuites importantes se produisent après une contrainte de courant prolongée. Sur la base d'images secondary electron et de cartographie electron-beam-induced current (EBIC), l'hypothèse proposée est la présence d'un dépôt de tungstène parasite, activé principalement par effet Joule mais aussi par irradiation par faisceau d'électrons. Ces fuites semblent pouvoir être évitées en réduisant le courant, typiquement en effectuant des mesures pulsées.

Nous avons ensuite mis en évidence la présence de la jonction p-n sur la partie supérieure des fils avec une cartographie EBIC pour chaque dispositif. Il est à noter que des fissures sont visibles en EBIC sur la partie supérieure des fils et donc à proximité du contact p. On peut donc en déduire qu'elles jouent un rôle dans l'injection et la luminescence sans pour autant introduire de fuites.

Enfin, nous avons pu observer de l'electroluminescence sur les deux structures, avec des spectres très similaires (*cf* figure 5.12):

- Une large bande jaune à environ 2.25 eV liée aux défauts profonds dans le GaN.
- Une bande violette asymétrique piquée entre 3.25 et 3.35 eV que nous avons pu attribuer à des transitions electron-accepteur ou donneur-accepteur dans la coquille de p-GaN grace à des mesures sur une simple jonction p-n de GaN.
- Enfin, la contribution des puits quantiques à 3.65 et 4 eV pour les dispositifs UV-A et UV-B respectivement.

La présence de la bande violette suggère des problèmes d'injection. Des études supplémentaires sont nécessaires pour comprendre et prévenir son apparition. Il pourrait être intéressant d'étudier l'effet d'une couche de blocage des électrons pour réduire l'injection d'électrons dans le p-GaN.

Par la suite, nous avons réussis à obtenir une meilleure injection électrique, comparable à celle de l'échantillon UV-A, en concevant une nouvelle structure

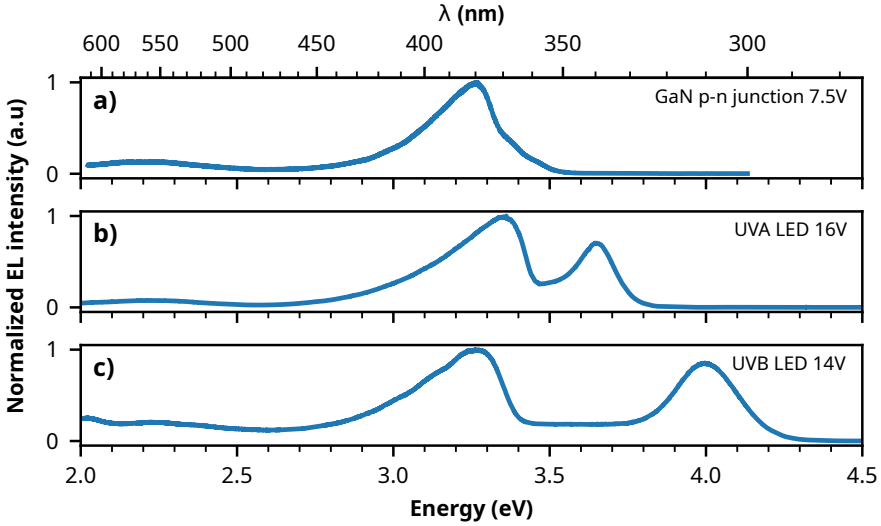

FIGURE 5.12: Spectres EL pour (a) une jonction *p-n* en GaN, (b) une LED UV-A et (c) une LED UV-B.

UV-B avec un gradient d'aluminium supplémentaire et des barrières plus fines. Cette nouvelle structure a ensuite été utilisée pour la réalisation de contacts Ni/Au par lithographie optique. Comme nous pouvions nous y attendre, ces nouveaux contacts ont montré une meilleure stabilité sous contrainte de courant et étaient insensibles à l'irradiation par faisceau d'électrons. Cependant, ces nouveaux contacts n'ont montré aucune amélioration significative du courant direct, avec typiquement $\sim 10^2$ µA à 10 V. Plusieurs hypothèses peuvent expliquer cela, notamment, il est possible que le facteur limitant ne soit pas le contact mais la résistivité des couches d'AlGaN. Nous pouvons également mentionner que nous n'avons pas effectué de recuit après le dépôt, un point qu'il serait intéressant d'étudier.

Enfin, pour conclure ce chapitre, nous évoquons quelques perspectives telles que le développement et l'optimisation de monocouches de GaN pour atteindre les UV-C. Ou encore le développement de tubes coeur-coquille par gravure in-situ du coeur en GaN pour réduire les pertes par absorption comme présenté par Durand et al.

[Ama+20] Hiroshi Amano et al. "The 2020 UV emitter roadmap". *Journal of Physics D: Applied Physics* 53.50 (Dec. 2020), 503001. DOI: 10.1088/1361-6463/aba64c.

[Auf+16] Matthias Auf Der Maur et al. "Efficiency Drop in Green InGaN/GaN Light Emitting Diodes: The Role of Random Alloy Fluctuations". *Physical Review Letters* 116.2 (2016). DOI: 10.1103/PhysRevLett.116.027401.

[BL99] Walter L. Borst and Lin I. Liu. "Time-autocorrelated two-photon counting technique for time-resolved fluorescence measurements". *Review of Scientific Instruments* 70.1 PART II (1999), 41–49. DOI: 10.1063/1.1149540.

[Bru+19] Matt D. Brubaker et al. "UV LEDs based on p-i-n core-shell AlGaN/GaN nanowire heterostructures grown by N-polar selective area epitaxy". *Nanotechnology* 30.23 (2019), 234001. DOI: 10.1088/1361-6528/ab07ed.

[Che+21] Yao Chen et al. "GaN buffer growth temperature and efficiency of InGaN/GaN quantum wells: The critical role of nitrogen vacancies at the GaN surface". *Applied Physics Letters* 118.11 (2021), 111102. DOI: 10.1063/5.0040326.

[Cou+18a] Pierre Marie Coulon et al. "Deep UV Emission from Highly Ordered AlGaN/AlN Core-Shell Nanorods". *ACS Applied Materials and Interfaces* 10.39 (Oct. 2018), 33441–33449. DOI: 10.1021/acsami.8b10605.

[Cou+18b] Pierre Marie Coulon et al. "Hybrid Top-Down/Bottom-Up Fabrication of Regular Arrays of AlN Nanorods for Deep-UV Core–Shell LEDs". *Physica Status Solidi (B) Basic Research* 255.5 (2018), 1700445. DOI: 10.1002/pssb.201700445.

[Dav+20] Aurelien David et al. "Review—The Physics of Recombinations in III-Nitride Emitters". *ECS Journal of Solid State Science and Technology* 9.1 (2020), 016021. DOI: 10.1149/2.0372001jss.

[Din+19] Kai Ding et al. *Micro-LEDs, a manufacturability perspective*. 2019. DOI: 10.3390/app9061206.

[Dur+17] Christophe Durand et al. "Thin-Wall GaN/InAlN Multiple Quantum Well Tubes". *Nano Letters* 17.6 (2017), 3347–3355. DOI: 10.1021/acs.nanolett.6b04852.

[Ein+00] S. Einfeldt et al. "Strain relaxation in AlGaN under tensile plane stress". *Journal of Applied Physics* 88.12 (2000), 7029–7036. DOI: 10.1063/1.1326852.

[Fin+20] Sylvain Finot et al. "Carrier dynamics near a crack in GaN microwires with AlGaN multiple quantum wells". *Applied Physics Letters* 117.22 (Nov. 2020), 221105. DOI: 10.1063/5.0023545.

[Fou+19] M. Fouchier et al. "Polarized cathodoluminescence for strain measurement". *Review of Scientific Instruments* 90.4 (Apr. 2019), 043701. DOI: 10.1063/1.5078506.

[Gre+20] Vincent Grenier et al. "UV Emission from GaN Wires with m-Plane Core-Shell GaN/AlGaN Multiple Quantum Wells". *ACS Applied Materials and Interfaces* 12.39 (Sept. 2020), 44007–44016. DOI: 10.1021/acsami.0c08765.

[Hal+17] C. Haller et al. "Burying non-radiative defects in InGaN underlayer to increase InGaN/GaN quantum well efficiency". *Applied Physics Letters* 111.26 (Dec. 2017). DOI: 10.1063/1.5007616.

[Hal+18] C. Haller et al. "GaN surface as the source of non-radiative defects in InGaN/GaN quantum wells". *Applied Physics Letters* 113.11 (Sept. 2018), 111106. DOI: 10.1063/1.5048010.

[KI15] Katsumi Kishino and Shunsuke Ishizawa. "Selective-area growth of GaN nanocolumns on Si(111) substrates for application to nanocolumn emitters with systematic analysis of dislocation filtering effect of nanocolumns". *Nanotechnology* 26.22 (June 2015). DOI: 10.1088/0957-4484/26/22/225602.

[Kit+21] Hiroki Kitagawa et al. "Effectiveness of 222-nm ultraviolet light on disinfecting SARS-CoV-2 surface contamination". *American Journal of Infection Control* 49.3 (2021), 299–301. DOI: 10.1016/j.ajic.2020.08.022.

[Kne+19] Michael Kneissl et al. "The emergence and prospects of deep-ultraviolet light-emitting diode technologies". *Nature Photonics* 13.4 (Apr. 2019), 233–244. DOI: 10.1038/s41566-019-0359-9.

[KR16] Michael Kneissl and Jens Rass, eds. *III-Nitride Ultraviolet Emitters*. Vol. 227. Springer Series in Materials Science. Springer International Publishing, 2016. DOI: 10.1007/978-3-319-24100-5.

[Lan+10] O. Landré et al. "Elastic strain relaxation in GaN/AlN nanowire superlattice". *Physical Review B* 81.15 (Apr. 2010), 153306. DOI: 10.1103/PhysRevB.81.153306.

[Ley+20] Ryan T. Ley et al. "Revealing the importance of light extraction efficiency in InGaN/GaN microLEDs via chemical treatment and dielectric passivation". *Applied Physics Letters* 116.25 (June 2020), 251104. DOI: 10.1063/5.0011651.

[Liu+22] Xianhe Liu et al. "N-polar InGaN nanowires: breaking the efficiency bottleneck of nano and micro LEDs". *Photonics Research* 10.2 (2022), 587. DOI: 10.1364/prj.443165.

[Meu+16] Sophie Meuret et al. "Lifetime Measurements Well below the Optical Diffraction Limit". *ACS Photonics* 3.7 (July 2016), 1157–1163. DOI: 10.1021/acsphotonics.6b00212.

[Meu+18] Sophie Meuret et al. "Nanoscale Relative Emission Efficiency Mapping Using Cathodoluminescence g(2) Imaging". *Nano Letters* 18.4 (Apr. 2018), 2288–2293. DOI: 10.1021/acs.nanolett.7b04891.

[Meu16] Sophie Meuret. "Expérience de Hanbury Brown et Twiss dans un microscope électronique à transmission à balayage : sa physique et ses applications". PhD thesis. UNIVERSITE PARIS-SACLAY, 2016.

[Oli+17] François Olivier et al. "Influence of size-reduction on the performances of GaN-based micro-LEDs for display application". *Journal of Luminescence* 191 (Nov. 2017), 112–116. DOI: 10.1016/j.jlumin.2016.09.052.

[Pez+22] Bardia Pezeshki et al. "LED-array based optical interconnects for chip-to-chip communications with integrated CMOS drivers, detectors, and circuitry". 1200707.March (2022), 11. DOI: 10.1117/12.2614547.

[RA20] Milad Raeiszadeh and Babak Adeli. *A Critical Review on Ultraviolet Disinfection Systems against COVID-19 Outbreak: Applicability, Validation, and Safety Considerations*. Nov. 2020. DOI: 10.1021/acsphotonics.0c01245.

[Tch+14] M. Tchernycheva et al. "Integrated photonic platform based on InGaN/GaN nanowire emitters and detectors". *Nano Letters* 14.6 (2014), 3515–3520. DOI: 10.1021/nl501124s.

[Tra+17] Nhung Hong Tran et al. "On the mechanism of highly efficient p-type conduction of Mg-doped ultra-wide-bandgap AlN nanostructures". *Applied Physics Letters* 110.3 (Jan. 2017), 32102. DOI: 10.1063/1.4973999.

[Wu+18] Tingzhu Wu et al. "Mini-LED and Micro-LED: Promising candidates for the next generation display technology". *Applied Sciences (Switzerland)* 8.9 (2018). DOI: 10.3390/app8091557.

[Zha+14] S. Zhao et al. "Aluminum nitride nanowire light emitting diodes: Breaking the fundamental bottleneck of deep ultraviolet light sources". *Scientific Reports* 5.1 (July 2014), 8332. DOI: 10.1038/srep08332.

Résumé

Au cours des vingt dernières années, les diodes électroluminescentes (LED) à base de nitrure de gallium (GaN) ont révolutionné le domaine de l'éclairage en devenant la source de lumière la plus efficace créée par l'Homme. Afin d'exploiter le plein potentiel de cette technologie, deux axes de recherche ont reçu une attention particulière. D'une part, la miniaturisation pour produire, entre autres, des dispositifs d'affichage efficaces, et d'autre part, le développement de LEDs émettant dans l'ultraviolet (UV) pour répondre à la demande croissante de sources UV efficaces, compactes et respectueuses de l'environnement. La diminution de la taille des dispositifs et la nécessité d'étudier les défauts à fait apparaître le besoin de caractérisation optoélectronique à l'échelle nanométrique, bien en deçà de la limite imposée par la diffraction de la lumière. Un outil particulièrement adapté, la cathodoluminescence (CL) utilise des électrons pour sonder la matière et permet d'atteindre une résolution spatiale de quelques dizaines de nanomètres. De plus, la grande énergie des électrons devant l'énergie de bande interdite des semiconducteurs en font une source d'excitation non-résonante universelle. Dans cette thèse, on se propose d'étudier différents systèmes grâce à la CL et CL résolue en temps (TR-CL pour time-resolved cathodoluminescence). L'avantage premier de la TR-CL est qu'elle permet de sonder l'efficacité quantique interne, grandeur fondamentale pour l'optimisation de dispositifs, indépendamment de l'efficacité d'injection, ou d'extraction. Premièrement, nous nous sommes intéressés à l'effet des sous-couches (UL pour underlayer) contenant de l'indium. Ces ULs sont utilisés dans les LEDs commerciales pour supprimer des défauts formés lors de la croissance du GaN à haute température, augmentant ainsi considérablement l'efficacité des puits quantiques (QW pour quantum well). Nous avons montré que ces défauts sont des centres non-radiatifs très efficaces. Même avec une densité cent fois plus faible que celle des dislocations, connues pour diminuer fortement le rendement, ils restent la principale source de recombinaison non-radiative. Ensuite, bien que ces ULs soient très efficaces pour les LEDs planaires plan c, aucune amélioration n'a pu être observée pour des QWs crus sur les parois (plan m) de microfils de GaN. Afin de dissocier les conditions de croissances de l'orientation cristallographique, nous avons étudier les ULs pour des QWs crus sur des substrats de GaN plan m. Les résultats obtenus suggèrent une efficacité comparable et relativement élevée même sans UL. Ainsi, la formation de ces défauts semble dépendre du plan cristallographique. Nous avons ensuite étudié les recombinaisons de surface dans les µLEDs. Afin d'avoir la résolution spatiale nécessaire, nous avons développé un interféromètre de Hanbury Brown & Twiss (HBT) couplé à notre montage de CL. Ce dispositif permet de mesurer la statistique d'émission des photons, et de mesurer le temps de vie des porteurs sans utiliser d'obturateur de faisceau qui détériore la résolution spatiale ou de laser pulsé onéreux. Grâce à ce montage, nous avons mesurer le coefficient de diffusion et la vitesse de recombinaison de surface dans des µLEDs. Nous avons pu montrer que cette vitesse de recombinaisons est réduite de moitié après passivation des surfaces. Afin de compléter le premier montage optimisé pour l'UV et le bleu, un deuxième interféromètre a été désigné pour couvrir le reste du visible et étudier des µLEDs rouges. Enfin, nous avons étudié des LEDs UV basées sur des microfils AlGaN/GaN. L'un des problèmes majeurs est la présence de fissures dues à la relaxation des contraintes. Grâce au HBT nous avons montré que bien que ces fissures favorisent localement l'extraction de la lumière, elles sont en réalité des centres non radiatifs. Enfin, en contactant ces microfils nous avons pu mesurer les caractéristiques électro-optiques et obtenir une électroluminescence record de 302 nm pour ce type de structure.

Abstract

Over the past two decades, gallium nitride (GaN) based light-emitting diodes (LEDs) have revolutionized the lighting field by becoming the most efficient man-made light source. In order to exploit the full potential of this technology, two main areas of research have received particular attention. On the one hand, miniaturization for producing, among other things, efficient display devices, and on the other hand, the development of ultraviolet (UV) LEDs to meet the growing demand for efficient, compact, and environmentally friendly UV sources. The decrease in the size of devices and the need to study defects has highlighted the need for optoelectronic characterization at the nanoscale, well below the diffraction limit of light. A particularly adapted tool, cathodoluminescence (CL), uses electrons to probe the matter and allows to reach a spatial resolution of a few tens of nanometers. Moreover, the high energy of electrons compared to the bandgap energy of semiconductors makes it a universal non-resonant excitation source. This thesis proposes to study different systems using CL and time-resolved cathodoluminescence (TR-CL). The main advantage of TR-CL is that it allows probing the internal quantum efficiency (IQE), a fundamental parameter for the early optimization of devices, independently of the injection or extraction efficiency. First, we focused on the effect of indium-containing underlayers (ULs). These ULs are commonly used in commercial LEDs to suppress defects formed during the growth of high-temperature GaN, thus considerably increasing the efficiency of quantum wells (QWs). By studying QWs grown on silicon, we have shown that these defects are very efficient non-radiative centers. Indeed, even with density hundreds of times lower than that of dislocations, known to strongly decrease efficiency, they remain the primary source of non-radiative recombination. Then, although these ULs are very efficient for planar *c*-plane LEDs, no improvement could be observed for QWs grown on *m*-plane sidewalls of GaN microwires. To dissociate the effect of the particular growth condition of wires from the crystallographic orientation, we have studied ULs for QWs grown on *m*-plane GaN substrates. The results obtained suggest a comparable and relatively high efficiency even without UL. Thus, the formation of these defects seems to depend on the crystallographic plane. We then studied the surface recombinations in µLEDs. In order to have the desired spatial resolution, we developed a Hanbury Brown & Twiss (HBT) interferometer coupled to our CL setup. This instrument allows to measure the photon emission statistics and thus measure the carrier lifetime without needing a beam blanker, which deteriorates the spatial resolution or an expensive pulsed laser. Thanks to this setup, we have measured the diffusion coefficient and the surface recombination velocity in blue µLEDs. Furthermore, we could show that this recombination velocity is reduced by half after passivating the surfaces. In order to complement the first setup optimized for UV and blue photons, a second interferometer was designed to cover the rest of the visible spectrum. Finally, we studied UV LEDs based on AlGaN/GaN microwires. One of the major issues of these wires is the presence of cracks due to strain relaxation. Thanks to the HBT, we have shown that although these cracks locally enhance light extraction, they are non-radiative centers, thus decreasing the IQE. Finally, by contacting these microwires individually, we could measure the electro-optical characteristics and obtain record electroluminescence at 302 nm for this type of structure.